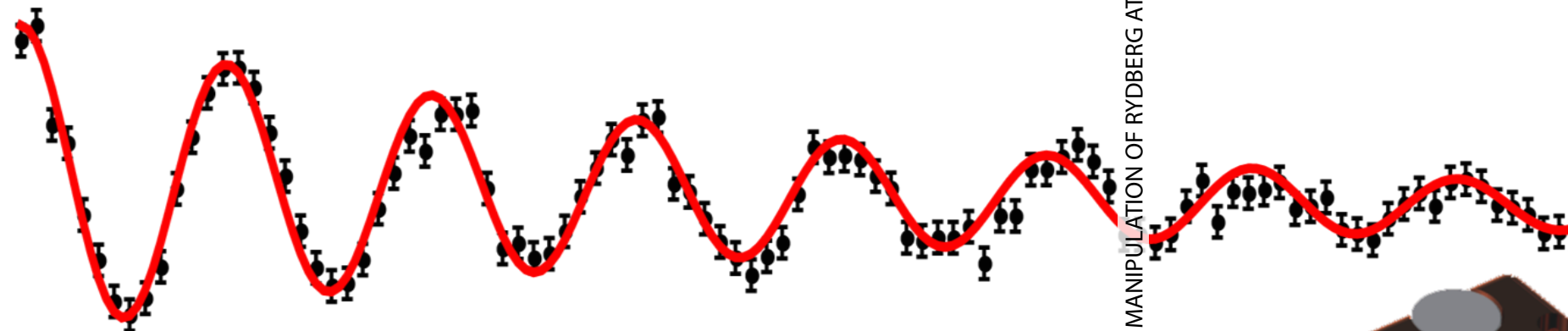


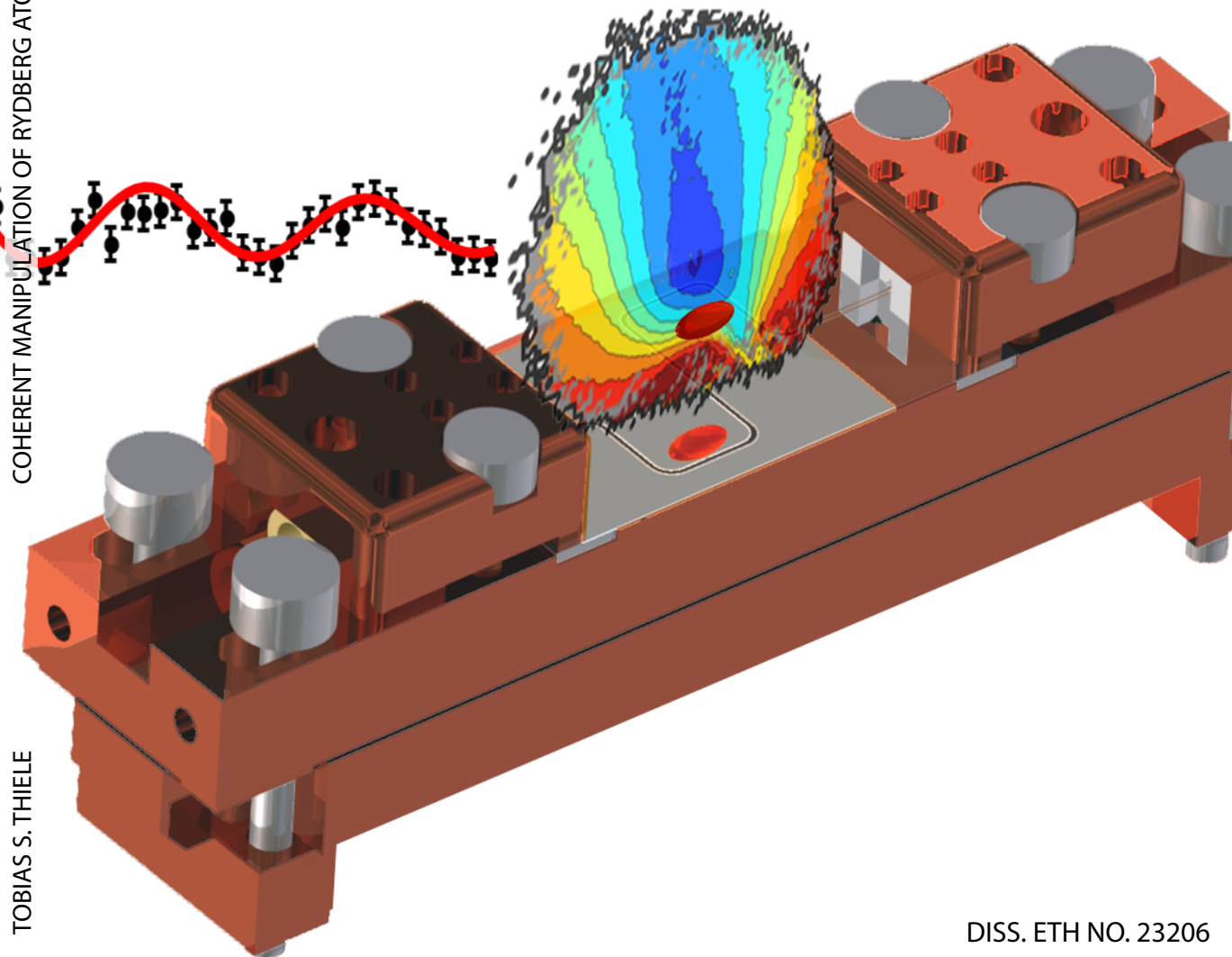
COHERENT MANIPULATION OF RYDBERG ATOMS CLOSE TO SURFACES AT CRYOGENIC TEMPERATURES

TOBIAS S. THIELE



COHERENT MANIPULATION OF RYDBERG ATOMS CLOSE TO SURFACES AT CRYOGENIC TEMPERATURES

TOBIAS S. THIELE



DISS. ETH NO. 23206

COHERENT MANIPULATION OF RYDBERG ATOMS CLOSE TO SURFACES AT CRYOGENIC TEMPERATURES

A thesis submitted to attain the degree of
DOCTOR OF SCIENCES of ETH ZURICH
(Dr. sc. ETH Zurich)

presented by
Tobias Sebastian Thiele
MSc ETH Physics, ETH Zurich
born on 24.10.1986
citizen of Germany

accepted on the recommendation of
Prof. Dr. Andreas Wallraff, examiner
Prof. Dr. Frédéric Merkt, co-examiner
Prof. Dr. Michel Brune, co-examiner

2016

ABSTRACT

In recent years, the field of cavity quantum electrodynamics has become increasingly important in the area of quantum information science and technology. The ability to interface single, stationary two-level systems with single, flying photons in a cavity is nowadays exploited in many experiments that aim for a future world, in which quantum technology is used to process and transfer quantum information. So far, several physically different schemes have been identified that perform very well in a small subset of all processing or transfer tasks only. Therefore, the concept of a hybrid system was developed, merging two or more physical implementations into a new system that exhibits optimal performance in a larger set of tasks than the individual entities.

In this thesis we present pioneering works toward a hybrid system, that combines the best of the worlds of atom and solid-state systems. Specifically, we aim at interfacing single or ensembles of atoms in Rydberg states to chip-based microwave photons in a circuit quantum electrodynamics system (circuit QED) operating at cryogenic temperatures. The combined system may exploit the fast processing rate and scalability of circuit QED systems, and the optical interface and long coherence times of Rydberg atoms. The realization of such a hybrid systems has been a longstanding goal, but could not be achieved so far because of fundamental and technical challenges that are linked to the sensitivity of Rydberg atoms to surface imperfections such as patches of adsorbates, local charges or potential differences. Static and time-dependent inhomogeneous stray electric fields emanating from these imperfections result in strong decoherence of the atom cloud and tools to avoid or characterize and compensate these fields need to be developed. We have built a new setup in which decoherence due to stray electric fields that emanate from surfaces at cryogenic temperatures can be measured and reduced. In the new setup, we do not have to rely on specific modifications of the surface to observe coherent population transfer between Rydberg states.

Specifically, helium atoms in Rydberg states have been manipulated coherently with microwave radiation pulses near planar gold surfaces, and near transmission lines patterned onto either a printed-circuit board or onto a superconducting NbTiN surface. All surfaces were cooled to cryogenic temperatures. The

experiments were carried out with a collimated supersonic beam of metastable $(1s)^1(2s)^1\ ^1S_0$ helium atoms excited with laser radiation to np Rydberg levels with principal quantum number n between 30 and 40. The separation between the cold surface and the center of the collimated beam was adjustable between $250\ \mu\text{m}$ and 2 mm. Short-lived np Rydberg states were coherently transferred to the long-lived ns state to avoid radiative decay of the Rydberg atoms between the photoexcitation region and the region above the cold surfaces. Further coherent manipulation of the ns Rydberg states with pulsed microwave radiation above the surfaces enabled measurements of stray electric fields and allowed studying the decoherence of the atomic ensemble. Adsorption of residual gas onto the surfaces and the resulting slow buildup of stray fields was minimized by controlling the temperature of the surface and monitoring the partial pressures of residual gases in the experimental chamber during the cooldown procedure. Compensation of the stray electric fields to levels below $100\ \text{mV/cm}$ was achieved over a region of 6 mm along the beam-propagation direction and below $20\ \text{mV/cm}$ over a region of 1 mm.

Furthermore, static and time-dependent electric fields were measured in situ with a new technique. Here, we determined stray-electric-field distributions at distances of less than 2 mm from patterned surfaces using coherent spectroscopy on Stark shifts in the beam of helium atoms. We demonstrate the capabilities of this technique by characterizing the electric stray field emanating from a structured superconducting coplanar waveguide and exploit coherent population transfer with microwave radiation from the same structure. Modification of this technique also allowed the characterization of the microwave-field distribution above the surface.

The results of this thesis represent important milestones toward a working hybrid system with Rydberg atoms and coplanar microwave resonators. The techniques to avoid and compensate stray electric fields allowed to preserve coherence of the atomic sample for several microseconds above cold, patterned surfaces for the first time without specific modifications of the surface properties. This opens a clear path toward a non-destructive detection of Rydberg atoms using a small number of microwave photons in the waveguide resonator.

Additionally, the developed techniques could be used to build a characterization apparatus that exploits quantum effects to detect static and microwave stray electric fields above planar samples. The detection can be on a mm-scale, with resolutions on the μm -scale, without additional demands for the sample and for temperatures varying from room temperature down to cryogenic levels.

KURZFASSUNG

In den letzten Jahren hat das Feld der Resonator-Quanten-Elektrodynamik mehr und mehr an Bedeutung im Feld der Quanteninformations-Wissenschaften und -Technologien gewonnen. Heutzutage wird die Möglichkeit einzelne, stationäre Zwei-Level Systeme mit einzelnen, fliegenden Photonen in einem Resonator zu koppeln in vielen Experimenten rege genutzt. Diese Experimente haben das erklärte Ziel in Zukunft Quantentechnologie für die Verarbeitung und Übertragung von Quanteninformation zu benutzen. Diverse physikalische Systeme wurden bereits identifiziert, welche allerdings nur jeweils einen kleinen Satz aller möglichen Prozess- und Transferaufgaben gut bewältigen. Deswegen wurde das Konzept der Hybridsysteme entwickelt, die zwei oder mehrere physikalische Systeme in eine neue Anwendung zusammenfassen, welche einem grösseren Satz von Aufgaben gewachsen ist als die jeweils einzelnen Teile.

In dieser Arbeit präsentieren wir Pionierarbeiten für ein Hybridsystem, welches das Beste aus den zwei Welten der Atom- und Festkörperphysik kombinieren soll. Das Ziel der Arbeit ist die Kopplung von Einzelnen oder Ensembles von Atomen in Rydberg-Zuständen an Photonen in einem Schaltkreis-Quanten-Elektrodynamik System (Schaltkreis-QED), das bei tiefkalten Temperaturen funktioniert. Das kombinierte System besitzt sowohl die schnelle Prozessier-Rate und Skalierbarkeit der Schaltkreis-QED, als auch die optische Schnittstelle und die langen Kohärenzzeiten der Rydbergatome. Das Ziel, die Realisierung eines solchen Hybridsystems, konnte bis heute noch nicht erreicht werden aufgrund technischer und fundamentaler Schwierigkeiten, die in direktem Zusammenhang mit der Sensitivität von (Rydberg)atomen auf Oberflächendefekte stehen. Heterogene elektrische Streufelder können beispielsweise durch Adsorbate, lokale Ladungen oder Potentialdifferenzen verursacht werden und verursachen starke Dekohärenz in der Atomwolke. Für ein erfolgreiches Experiment ist es deshalb unumgänglich, Werkzeuge zu entwickeln, welche diese Defekte verhindern, charakterisieren oder deren Effekte kompensieren können. Wir haben einen neuen Aufbau entwickelt, welcher es erlaubt, Streufelder an tiefkalten Oberflächen zu messen und zu reduzieren. Dadurch konnten wir kohärenten Besetzungstransfer zwischen Rydbergzuständen beobachten ohne die Oberfläche modifizieren zu müssen.

In den Experimenten wurden Heliumatome in Rydbergzuständen nahe an Oberflächen kohärent mit Mikrowellenstrahlung manipuliert. Sowohl planare Goldoberflächen als auch Platinen und supraleitende NbTiN Oberflächen, in welche eine Transmissionslinie eingelassen waren, wurden verwendet. Die Oberflächen wurden jeweils auf tiefkalte Temperaturen abgekühlt. Die Experimente wurden mit einem kollimierten Überschallstrahl aus metastabilen $(1s)^1(2s)^1\ ^1S_0$ Heliumatomen durchgeführt. Die Atome wurden in np -Rydbergzustände angeregt, wobei n zwischen 30 und 35 lag. Der Abstand zwischen der kalten Oberfläche und dem Mittelpunkt des kollimierten Strahls konnte zwischen $250\ \mu\text{m}$ und $2\ \text{mm}$ variiert werden. Kurzlebige np -Rydbergzustände wurden kohärent zu langlebigen ns -Rydbergzuständen transferiert, um den radiativen Zerfall der Rydbergatome zwischen der Photo-Anregungsregion und der Region über der kalten Oberfläche zu verhindern.

Kohärente Manipulation der ns -Rydbergzustände mit gepulster Mikrowellenstrahlung über der Oberfläche ermöglichte (ausserdem) die Messung des elektrischen Streufeldes und erlaubte die Bestimmung der Dekohärenzzeit des Atomensembles. Die Adsorption von Restgas auf der Oberfläche und der daraus resultierende Aufbau von Streufeldern während des Abkühlprozesses wurden durch Regelung der Oberflächentemperatur und durch Überwachen des Partialdruckes des Restgases in der Experimentierkammer minimiert. Durch diese Massnahmen konnten elektrische Streufelder über einen Bereich von $6\ \text{mm}$ Länge entlang der Flugrichtung des Atomstrahls auf unter $100\ \text{mV/cm}$ reduziert werden. Des Weiteren erlaubte die Korrektur eine Kompensation auf unter $20\ \text{mV/cm}$ über einen Bereich von $1\ \text{mm}$.

Des Weiteren wurde eine neue Technik zur Messung statischer und zeitabhängiger elektrischer Streufelder entwickelt. Mit Hilfe von kohärenter Spektroskopie von Starkzuständen im Heliumstrahl konnten elektrische Streufeldverteilungen in Distanzen von weniger als $2\ \text{mm}$ von geprägten Oberflächen gemessen werden. Durch die Charakterisierung von elektrischen Streufeldern, die von einem supraleitenden, koplanaren Wellenleiter ausgehen, zeigen wir die Möglichkeiten dieser Technik auf, indem wir kohärenten Populationstransfer ausnutzen. Dieser wird durch Mikrowellenstrahlung getrieben, die von derselben Struktur ausgeht.

Die Resultate dieser Arbeit setzen neue Meilensteine bezüglich eines funktionierenden Hybridsystems aus Rydbergatomen und koplanaren Mikrowellenleitern. Die Kohärenz von Atomwolken nahe kalten, geprägten Oberflächen während einiger Mikrosekunden wurde durch die beschriebenen Techniken zur Verhinderung oder Kompensierung elektrischer Streufelder erstmals ermöglicht ohne die spezifische Anpassung der Oberflächeneigenschaften. Dies eröffnet einen

klaren Weg hin zu einer nicht-destruktiven Detektion von Rydbergatomen mit einer kleinen Anzahl von Mikrowellenphotonen in einem Mikrowellenleiter.

Zusätzlich können die in dieser Arbeit entwickelten Techniken genutzt werden um statische elektrische Felder und elektrische Mikrowellenfelder mithilfe von Quanteneffekten zu detektieren. Diese Methode erlaubt eine Feldcharakterisierung über mehrere Millimeter mit einer Auflösung im Mikrometerbereich ohne zusätzliche Anforderungen an die zu untersuchenden Oberflächen. Zudem ist sie in erster Ordnung temperaturunabhängig, sodass die Temperatur der Oberfläche zwischen Raumtemperatur und tiefkalten Leveln variieren kann.

ACKNOWLEDGEMENTS

During the time I spent at ETH, I met and collaborated with many people and they all contributed to the success of the experiment and to my personal development. To thank all of them with the appropriate length and depth would probably add another 100 pages to this (already long) thesis. Therefore, I mention only the most important ones here.

First, I would like to thank my supervisor: *Andreas Wallraff*. Of course, I am happy that you accepted me as a PhD-student in your group in the first place. However, I thank you more for the freedom and trust you gave me during my PhD ... and for removing my Latte-Macchiato glasses from my working places. It was always enlightening when interacting with you scientifically and I learned a lot from you; e.g. on the scientific side about cavity QED, or the important soft-skill of how to give good talks. Working in your group was a unique and formative experience with many good moments.

Then I thank my second supervisor: *Frédéric Merkt*. I am really grateful that you welcomed me as an additional member of your group. This warm atmosphere made interaction with you at scientific and non-scientific occasions very pleasant. I really enjoyed our paper-writing sessions and the scientific discussions we had, and it was always fun and illuminative working with you in the lab, especially when observing Rabi-oscillations for the first time.

In general, the collaboration and interaction between both groups taught me a lot and contributed significantly to the scientist I am today, especially because of the (very) different approaches in doing research, or the interaction between group members. In general one says that working in collaborations can be very difficult and/or distressful. However, this was not the case here. In contrast, interaction with both groups at least doubled the satisfaction during good times and more than compensated the difficult times when one had to cope with or manage small problems that can appear in every collaboration.

I specifically thank *Seppi (A.-J. Agner)*. Without your relentless effort, dedication and commitment also during times when other technicians and PhD students have long left ETH, the experiment would not be in the good state it is now. I admire your innovative ideas and the technical and scientific knowledge you have. It

was always more than fun interacting with you and I will always remember skiing with Christian Seiler and you in St. Luc. You truly made my time here at ETH an exceptional experience for which I thank you.

Similarly, I thank *Hansjürg Schmutz*. Your electronic expertise is great, and I learned a lot from you in this direction. But I find it even more amazing that one could approach you with almost any electronic problem, and then you opened some drawer or cupboard and took out a home-built device that either directly or with little changes was a perfect solution.

I thank the three post-docs, *Stephen Hogan*, *Stefan Filipp* and *Johannes Deiglmayr*, with which I interacted most of the time during my PhD. Stephen, during my first 1.5 years I learned all I need to know from you about performing Rydberg-atom experiments in supersonic beams. Also it is always a pleasure to meet with you and talk about science when you visit ETH. Stefan, from you I not only learned everything about microwave techniques, superconducting chips and cryogenics, but also how to properly program LabView. It was always fun to contemplate with you about atom-surface interactions and their various causes. Johannes, I am still learning a lot from you about Rydberg atoms and their interactions, especially when excited from ground-state alkali-atoms. Your advice is always appreciated and it is fun measuring with you artistic-valuable Rabi- and Ramseyoscillations between Rydberg states in cesium.

Also I thank the people that shared the office and the lab with me for an extended period of time, my co-PhD student *Mathias Stammeier*, and the two post-docs *Klaus Reim* and *Sébastien Garcia*. It was great working with you and I hope, that my taste of music didn't annoy you too much.

I thank all the semester-, master-, and summerstudents that I supervised during my work here at ETH: *Ants Remm*, *Raphael Barmettler*, *Dominik Waldburger*, *Mario Könz*, *Marten Seeman*, *Reshad Ebert*, *Matthias Mergenthaler*, *Florian Lüthi*, *Valentin Goblot*, *Anna Hambitzer*, *Lukas Gerster*, *Dominik Friese*, *Max Melchner*, *Marie-Therese Phillip* and *Lukas Möller*. You not only taught me how to improve on supervising one or many students at the same time, but also often surprised me with new possibilities on how to solve a problem and you always showed a lot of effort and interest. You have since gone different paths in your personal and professional life, and I am sure you do well. Specifically, I would like to highlight *Joannis Köpsell*, who started out as a semesterstudent, then stayed as a research assistant and recently finished with his master studies from Cambridge university. From all the students I had, we interacted over the longest period (and still do). I am convinced that you will be a great scientist, not only because of your strive and success for learning new physics or operating the experiment, but also because of your time and patience to sit down and think properly through a scientific problem and your care when performing experiments.

I am grateful to the group-members that keep everything running and who make working here a real pleasure. *Gaby Strahm*, as Andreas most expensive grad student, I ordered a lot (and expensive) equipment. You did an extraordinary job managing and handling all orders, invoices and customs documents and fighting with the (sometimes annoying) shipping companies. Also I am sure that I am not the only one who appreciates that you use your insight into the leaving/coming dynamics of the group to organise the good-bye gifts and cards, and it will be hard for any other member of the group to do this in time and with similar care or thought. Also, I would like to thank *Francesca Bay* for managing the project and filling out the time-sheets. *Janis Lütolf*, you took care of renovating the lab, building a nice crane for the experiment, and making sure (together with *Melvin Frey*) that the workshop is always nice and tidy. All that is extremely important when working experimentally and cannot be appreciated too much.

In general, I want to say thank you to the rest of the current and former group members of the *QuDev-team* and of the *Molecular Physics and Spectroscopy group* that have not been mentioned (but would surely deserve it) and which made working here at ETH a wonderful time, not only due to their various contributions on the technical and scientific side to the experiment, but also on the personal side.

I also thank all my other *friends* from high-school or studies, that motivated and/or managed on many occasions to get me out of the lab and into different adventures, holidays or visits and therefore contributed to a healthy work-life balance.

One of the two fixpoints in my life next to ETH were the frequent visits to my *family: Isa, Lothar, Florian and Frédéric*. Ich weiss nicht, ob ihr auch nur ahnt, wieviel mir die Besuche bei euch bedeutet haben. Ausserdem habe ich die selbstlose Unterstützung in Rat und Tat von euch allen sehr geschätzt, ob in Krisen- oder Freudenzeiten. Die mit (manchmal hitzigen) Diskussionen am Tisch gespickten Abendessen, die schönen Geburtstags- und Weihnachtsfeiern, die Ferien in Jordanien, oder die Wochenenden mit diversen Spielevents waren sehr wichtig für mich und ich werde sie nie vergessen. Ich bin wirklich froh, dass ich euch habe.

And last, but by far not least: *Yolanda*. Du bist jetzt seit mehr als 10 Jahren an meiner Seite. Mehr als die Hälfte dieser Zeit habe ich an meiner Dissertation gearbeitet, und du hast mich jede Sekunde, während meinen guten und schlechten Zeiten und Stimmungen, unterstützt. Selten hast du meine langen Arbeitstage und Nachtschichten kritisiert; und wenn, dann nur weil du (zu Recht) gefunden hast, dass etwas mehr Schlaf oder Sonnenlicht nützlich sein könnten. Tatsächlich warst du immer der Hauptgrund für mich um nach Hause zu kommen. Ich bin dir von Herzen dankbar, dass wir unsere Reise in Zukunft zusammen weitergehen werden, wohin auch immer sie uns führen wird... Ich liebe dich.

CONTENTS

Abstract	i
Kurzfassung	iii
Acknowledgements	vii
Contents	xi
1 Introduction	1
1.1 From free-space atom-photon interactions to cavity QED	4
1.1.1 Two-level atom interacting with a photon in free-space	6
1.1.2 Qubit interacting with a photon in an ideal cavity	8
1.1.3 Modifications in a transmissive cavity	10
1.1.4 Coupling ratios for different excitation states and scaling laws	13
1.2 Cavity QED systems in solid state devices	19
1.2.1 The role of cavity QED systems in applications of quantum information science	21
1.3 A potential quantum network of hybrid systems	25
1.4 A hybrid system of Rydberg atoms coupled to a circuit QED archi- tecture and an optical cavity	28
1.5 Thesis contributions and outline	36
I Experimental Setup and Measurement Procedure	41
2 Experimental setup and measurement procedures	43
2.1 Internal state manipulations of atomic beam	46
3 Dynamics of atomic beam	49
3.1 A source of a supersonic metastable helium beam	50
3.2 Longitudinal dynamics of metastable and Rydberg atom pulse	57

4	Spectroscopy of Rydberg atoms	65
4.1	Laser spectroscopy	65
4.1.1	Spectroscopy of Rydberg atoms in a field-free environment	66
4.1.2	Spectroscopy of Rydberg atoms in an electric field	71
4.2	Microwave spectroscopy - A sensitive way of measuring electric fields	76
4.2.1	Coherent microwave spectroscopy	77
4.2.2	Spatially resolved measurement of electric fields	80
4.3	Important experimental methods and characterizations	83
4.3.1	Rydberg state excitation laser	83
4.3.2	Pulsed field ionization	90
4.3.3	Atom beam detection techniques	94
4.3.3.1	The microchannel plate detector	94
4.3.3.2	Detection of time traces of Rydberg atoms	96
4.3.3.3	Detection of spatial atom distributions	101
5	Design of vacuum chamber and cryostat	113
5.1	Design of vacuum chamber	114
5.2	Design of cryostat	120
5.2.1	Mechanical design of the 3-K stage	120
5.2.2	Wires and connections	123
5.2.3	Heat loads	127
5.2.4	Adsorption-free cooldown of samples	129
5.2.4.1	Warmup of the cryostat	135
5.2.5	Fast temperature stabilization of the sample holder	138
5.3	Magnetic field compensation for optimal detection of atom distributions	140
5.3.1	Magnetic field controller	141
5.3.2	Measured deflections of an electron beam for different Rydberg atom states	145
5.4	Electronic control of the experiment and data acquisition programs	147
6	Important samples	155
6.1	From printed circuit boards to superconducting chips	155
6.1.1	An optimized sample holder for Rydberg beam experiments	158
6.1.2	Stray-field characterization of samples	160
6.2	Characterization of under and overcoupled NbTiN resonators	163

II	Measurements	173
7	Driving Rydberg-Rydberg transitions from a printed-circuit-board-based coplanar microwave waveguide	177
7.1	Determination of stray field strength using microwave spectra . . .	177
7.2	Coherent population transfer with small contrast	180
8	Manipulating Rydberg atoms close to surfaces at cryogenic temperatures	183
8.1	Optimal compensation of static stray electric fields	184
8.2	Coherent population transfer to determine electric field distributions	188
8.3	Rabi oscillations with optimized coherence	191
8.4	Conclusions	200
9	Imaging electric fields in the vicinity of cryogenic surfaces using Rydberg atoms	201
9.1	Measurement of stray electric field distributions	203
9.2	Measurement of microwave electric field mode	207
9.3	Conclusions	211
III	Conclusions and Outlook	213
10	Non-destructive detection of Rydberg atoms using chip-based microwave resonators	219
10.1	An optimized metastable helium source for Rydberg experiments close to cryogenic surfaces	222
10.1.1	A cryogenically cooled, pulsed valve for high repetition rates	223
10.1.2	Collimation of metastable 2^3S_1 helium atoms using laser cooling techniques	225
10.1.3	Deflection and separation of metastable 2^3S_1 helium atoms from a supersonic helium beam	226
10.1.4	Important properties and two-photon excitation of 2^3S_1 helium	228
10.1.5	Conclusions	229
	Bibliography	231
	Curriculum vitae	259

INTRODUCTION

The theory of *quantum mechanics* has experienced an exceptional success since the beginning of the 20th century, when Max Planck postulated that the energy of light is quantized. According to Planck, light can only be emitted in multiples of a basic energy unit: $h\nu$, ν being the frequency of the light and h Planck's constant [*Planck (1900, 1901)*]. Motivated by this work, Albert Einstein, Arthur H. Compton and others identified these "quanta of light" (ger: "Lichtquanta") as individual entities that can only be fully absorbed or emitted by matter [*Einstein (1905); Compton (1923)*]. In the following, a particle-like character was attributed to these quanta ("photons"), a clear contradiction to the classical wave model of light described by Maxwell's equations [*Maxwell (1865)*]. Nowadays, the property of quantum particles exhibiting both, wave and particle character, (wave-particle duality) is a key-ingredient of the fundamental framework of quantum mechanics.

Meanwhile, the concept of energy quantization and wave-particle duality was adapted to matter particles by Louis de Broglie [*de Broglie (1924)*] and later Erwin Schrödinger [*Schrödinger (1926, 1935)*]. An important breakthrough for quantum mechanics was the first atom model formulated by Arthur E. Haas and Niels Bohr [*Haas (1910); Bohr (1913)*] based on observations by Ernest Rutherford [*Rutherford (1911)*]. The Bohr model suggested that negatively charged electrons are bound by positively charged nuclei with quantized energy states. The model was able to predict the physical (Rydberg) constant R_∞ from more fundamental constants. It is part of the empirically found Rydberg equation describing the spectrum of many chemical elements. It was described 1888 by Johannes Ry-

berg [Rydberg (1890)] as a generalization of the empirically found equation for a series of spectral lines of hydrogen, formulated by Johann J. Balmer 3 years before [Balmer (1885)].

In the early 20th century people realized that manipulation of atomic hydrogen and other simple atomic species with electromagnetic radiation provided an ideal testbed to study the interaction of matter and light in the framework of quantum mechanics. Motivated to explain small deviations from Rydberg's equation such as the Lamb shift [Lamb and Retherford (1947)] and the anomalous electron moment [Schwinger (1958)], the theory of *quantum electrodynamics* (QED) was developed in the middle of the 20th century. Combining quantum mechanics and special relativity in a converging field theory, QED describes the interaction between charged particles by means of photons and is today one of the most stringently tested theories in physics [Schwinger (1958)].

From the early beginning, the fundamental differences in the physical concepts between quantum mechanics and classical theories have led to a plethora philosophical questions. Because of the lack of suitable experimental methods, these questions were typically addressed using the formulation of a "*Gedankenexperiment*" (thought-experiment), i.e. thinking through an experiment which is difficult or impossible to conduct. For example, the famous "Gedankenexperiment" of 'Schrödinger's cat' illustrates the alienation of the fundamental quantum mechanical concept of superposition, where a particle can be in two states at the same time (e.g. a radioactive nucleus *has* and *has not* decayed), to macroscopic (classical) objects (a cat is *dead* and *alive*) [Schrödinger (1935)]. Another famous "Gedankenexperiment" was the EPR-paradoxon formulated by Albert Einstein, Boris Podolsky and Nathan Rosen showing that quantum mechanics violates locality [Einstein *et al.* (1935)]. It describes two quantum mechanically entangled two-level systems, that are space-like separated, by a single state. The (classical) paradox enters where two complementary measurement variables, fulfilling Heisenberg's uncertainty relationship [Heisenberg (1927)], are strongly correlated. Alain Aspect was able to experimentally verify the non-locality of quantum mechanics in an EPR-experiment [Aspect *et al.* (1982)] by violating Bell's inequality [Bell (1964)] using latest advances in laser technology at the time.

The possibility to trap, cool and manipulate single atoms or ensembles of atoms, and to generate single photons and control their properties with laser radiation triggered a variety of ground-breaking new experiments. Thanks to the laser, it was possible to realize "Gedankenexperimente" that study the interaction of only a few elementary particles of light (photons) and matter (atoms); experiments considered impossible at earlier times. Serge Haroche and David Wineland received the 2012 nobel prize in physics "for ground-breaking experimental methods that enable measuring and manipulation of individual quantum

systems." [*Class for Physics of the Royal Swedish Academy of Sciences (2012)*]. Serge Haroche (for microwave frequencies) and H. Jeffrey Kimble (for optical frequencies) were pioneers in the new field of *cavity QED*, which studies the fundamental interaction of n -level systems ($n = 2$ typically) and a single (maybe unoccupied) light mode in a cavity. In both systems the fundamental interaction between a single atom and a single photon could be observed [*Thompson et al. (1992)*; *Brune et al. (1996)*].

Nowadays, cavity QED systems are promising systems for realizing applications in the field of quantum information science. The most promising examples of possible, future applications are *quantum computers* and *quantum networks*. Simply spoken, a quantum computer, contrary to a classical computer, uses the additional resource of entanglement between two quantum objects [*Nielsen and Chuang (2000)*]. For some specific problems, e.g. prime-number factorization, quantum algorithms have been found that are exponentially faster than classical algorithms. Quantum networks are used to distribute (quantum) entanglement and information between distant nodes, e.g. in or between quantum computers [*Kimble (2008)*]. Possible applications are, for example, secure communication channels [*Gisin et al. (2002)*].

Today, there is a number of different physical systems that implement cavity QED systems. The most promising example for realizing quantum networks are (ground-state) atoms and photons that operate in the optical regime, e.g. the system used by H. Jeff Kimble [*Kimble (1998)*; *Aoki et al. (2006)*]. For a quantum computer, however, a promising candidate are solid-state, *circuit-QED*-systems that interface microwave photons with artificial atoms [*Blais et al. (2004)*; *Wallraff et al. (2004)*], but with comparatively short coherence times. Although both systems perform very well on their own they cannot be interfaced currently, because of their difference in frequency ($\gtrsim 100$ THz for atoms versus ~ 10 GHz for circuit QED). A future, successful quantum technology, however, needs to include both, quantum computers that can communicate via quantum networks.

So far, no physical system is known that has the definite potential to perform well in both subareas of quantum information. One can, however, envision a combination of a system with optical properties and long coherence times and a (circuit-QED) system with microwave properties, a 'hybrid system'. Hybrid systems combine the best properties of two or more physical systems by interfacing them using an interaction that creates an energetic excitation in one system, while deexciting another system. For a cleverly chosen interaction, the new combined system exploits the 'best of both worlds' [*Kurizki et al. (2015)*].

A possible quantum-mechanical link between the chip-based microwave photons of a future quantum computer and optical photons in a quantum network is the system we work toward in the experiments discussed in this thesis. The sys-

tem aims to interface highly excited atoms (called 'Rydberg atoms')¹ in free-space and with long coherence times, and microwave photons in a chip-based (i.e. solid-state) cavity QED experiment. As will be shown this system maximizes the single-atom-single-photon interaction combining the best of both worlds (Sec. 1.4). Therefore, a Rydberg atom strongly coupled to microwave photons in a chip-based microwave cavity could serve either as a microwave-to-optical-converter if the atom is also coupled to an optical cavity, or it could serve as a quantum memory if the microwave cavity is coupled to a superconducting qubit. Therefore, I will first introduce both cavity QED systems (free-space and solid-state) in the remainder of this chapter and then discuss their combination.

Specifically, I relate to experiments that were done by using atoms in Fabry-Perot cavities (Sec. 1.1), by means of a parameter η , called the coupling ratio. Simply spoken, η is a general measure of how well a system can be isolated from the environment. η is used to discuss the fundamental limitation of free-space cavity QED with single atoms and single photons as a function of their excitation state. As a result, Rydberg atoms are identified as the best system in which the single-atom-single-photon coupling dominates all other couplings (Sec. 1.1.4). Sec. 1.2 describes recent advances of cavity QED in solid-state devices. Solid-state cavity QED systems allow to beat the fundamental limits of free-space cavity QED and become increasingly important in the field of quantum information processing (Sec. 1.2.1). The Rydberg-atom-circuit-QED system is introduced as the hybrid system which may play a central role in a future quantum network (Sec. 1.3). The thesis contributions to the current fields of (hybrid) systems and an overview of the rest of this document are presented in Sec. 1.5.

1.1 From free-space atom-photon interactions to cavity QED

A qubit (*quantum bit*) is a two level system which consists of a ground state $|g\rangle$ and an excited state $|e\rangle$. It has a dipole \mathbf{d} and is described by the qubit Hamiltonian

$$H_q = \frac{1}{2} \hbar \omega_q \sigma^z \quad (1.1)$$

with ω_q the resonance frequency of the qubit and σ^z the third Pauli operator. A light mode m is described as an electric field \mathbf{F}_m oscillating at a rate ω_m . The Hamiltonian of a mode m is described as a harmonic oscillator, i.e.

$$H_m = \hbar \omega_m \left(a_m^\dagger a_m + \frac{1}{2} \right), \quad (1.2)$$

¹Rydberg atoms in free-space-microwave cavities is the system studied by Serge Haroche.

a_m being the photon annihilation operator of the radiation mode.

The combined system of a qubit interacting with a light mode by $H_{\text{int}} = \mathbf{d}\mathbf{F}_m$ is described by the Jaynes-Cummings Hamiltonian [Jaynes and Cummings (1963)] in the rotating wave approximation:

$$\begin{aligned} H_{\text{JC}} &= H_q + H_m + H_{\text{int}} \\ &= \frac{1}{2}\hbar\omega_q\sigma^z + \hbar\omega_m\left(a_m^\dagger a_m + \frac{1}{2}\right) + \hbar g\left(a_m^\dagger\sigma^- + a_m\sigma^+\right). \end{aligned} \quad (1.3)$$

The spin-flip operators σ^\pm describe emission ($a_m^\dagger\sigma^-$) and absorption ($a_m\sigma^+$) of a photon by decay and excitation of the qubit, respectively. The coupling rate

$$\mathbf{g} = \frac{\mathbf{d}\mathbf{F}_m(\mathbf{r}, t)}{\hbar}, \quad (1.4)$$

is given by the electric $\mathbf{F}_m(\mathbf{r}, t)$ of the mode at the position of the qubit \mathbf{r} . The population of the dipole oscillates with Rabi rate $\Omega = 2g\sqrt{N}$ between $|g\rangle$ and $|e\rangle$ for $\omega_m = \omega_q$, and N photons in the mode. The coherent population transfer of a qubit in the presence of a single photon ($N = 1$) can only be observed under the specific condition that g exceeds the combined coupling to all other modes (Γ). Γ is typically a combination of direct coupling to other modes (spontaneous decay), and indirect coupling via the mode m . Here, we define a parameter, called coupling ratio hereafter, as a measure of how well a qubit-mode system can be decoupled from other modes, i.e.

$$\eta = g/\Gamma. \quad (1.5)$$

Coherent interaction of a single qubit and a single photon according to Eq. (1.3) can be observed if $\eta > 1$. In the following we will calculate or discuss η for four exemplary situations with atoms as qubits:

1. a two-level atom interacting with a photon in (3-dimensional) free-space (typically $\eta < 1$),
2. a two-level atom interacting with a photon in a perfectly reflecting Fabry-Perot cavity ($\eta \gg 1$),
3. an atom interacting with a photon in a partially reflecting Fabry-Perot cavity ($\eta > 1$),
4. generalization of situation 2 to different atom excitation levels (principal quantum numbers $n \leq 100$) and comparison with experiments.

From now on, we will always assume an interaction with a single photon ($N = 1$), the atom being polarized parallel to the photon's field, i.e. $\mathbf{dF}_m = dF_m$, and that $\omega_m = \omega_q$. We also assume that we only excite electrons from the valence shell of the atom. Except for item 3, technical constraints or imperfections (e.g. finite transmissivity of mirrors) are not taken into account.

1.1.1 Two-level atom interacting with a photon in free-space

To estimate the coupling ratio η for an atom in free space, we consider a single photon of frequency ω_m in a specific light mode. The mode is resonant with the cycling transition of the D₁ line ($6^2S_{1/2} \rightarrow 6^2P_{1/2}$) of cesium. A single cesium atom is placed in the waist of the mode and we consider a transition dipole parallel to the electric field of the photon.

We assume that the electric field of the single photon is distributed over the mode volume V_m . Therefore, we describe the coupling rate between the atom at position \mathbf{r} and the photon by [Beth and Leuchs (2005)]

$$g(\mathbf{r}) = \frac{dF_m(\mathbf{r})}{\hbar} = \frac{d}{\hbar} \sqrt{\frac{\hbar\omega_m}{2\epsilon_0 V_m}} f(\mathbf{r}) = \sqrt{\frac{d^2\omega_m}{2\epsilon_0 \hbar V_m}} f(\mathbf{r}), \quad (1.6)$$

where $f(\mathbf{r})$ is the mode's spatial distribution.

The calculation of the mode volume V_m of a flying photon depends on the specific experimental conditions. A possible experimental setup would be to focus single photons from single-mode fiber onto the atom [van Enk and Kimble (2000); Tey et al. (2008)]. We assume that the photon occupies a Gaussian TEM₀₀-mode of waist w_0 , which is always larger than the diffraction limit, i.e. $w_0 \approx \lambda/2$. The free-space Gaussian mode distribution is given by [Svelto (1998)]

$$f_{\text{fs}}(\mathbf{r}) = f(z, r, \phi) = \frac{w_0}{w(z)} \exp\left(-\frac{r^2}{w(z)^2} - ikz - ik\frac{r^2}{2R(z)} + i\xi(z)\right) \quad (1.7)$$

where

$$w(z) = w_0 \sqrt{1 + \left(\frac{z}{z_R}\right)^2} \quad (1.8)$$

$$z_R = \frac{\pi w_0^2}{\lambda} \quad (1.9)$$

$$R(z) = z \left[1 + \left(\frac{z_R}{z}\right)^2\right] \quad (1.10)$$

$$\xi(z) = \arctan\left(\frac{z}{z_R}\right) \quad (1.11)$$

are the expressions for the mode diameter $w(z)$, the Rayleigh range z_R , the radius of curvature $R(z)$ and the Gouy phase $\xi(z)$, respectively, and $\lambda = 2\pi c/\omega_m$ the wavelength of the mode. $f_{\text{fs}}(\mathbf{r}) = 1$, for the atom positioned in the focus $[\mathbf{r} = (z, r, \phi) = (0, 0, \phi)]$ of the Gaussian beam. The mode volume is given by integration of f_{fs} over the photon length l in the propagation direction (z direction) and its orthogonal plane, i.e.

$$\begin{aligned} V_m(w_0) &= \int_{\mathbb{R}^3} |f_{\text{fs}}(\mathbf{r})|^2 d\mathbf{r} = \int_{-l/2}^{l/2} \frac{w_0^2}{w^2(z)} \left(\int_{\mathbb{R}^2} e^{-2\left(\frac{r}{w(z)}\right)^2} r dr d\phi \right) dz \\ &= \int_{-l/2}^{l/2} \frac{\pi w_0^2}{2} dz = \frac{\pi}{2} w_0^2 l, \end{aligned} \quad (1.12)$$

In the propagation direction, the photon has an effective length of $l = c\tau$, τ being the inverse bandwidth of the single photon source. As single photon source we assume another cesium atom spontaneously decaying from the $6^2P_{1/2}$ state into the fiber mode, i.e. $\tau = \Gamma_0^{-1} \approx 34.9$ ns [Rafac *et al.* (1999)] and $l \approx 10.5$ m. Considering a constant stream of single photons, the only decay rate Γ in the system is the atomic free-space decay rate Γ_0 . To obtain an analytic expression for the coupling ratio η for a free-space system, we approximate Γ_0 with the expression for a two-level atom [Haroche and Raimond (2006)], i.e.

$$\Gamma = \Gamma_0 = \frac{d^2 \omega_q^3}{3\pi \epsilon_0 \hbar c^3} \approx 2\pi \cdot 4.56 \text{ MHz}. \quad (1.13)$$

This approximation gives the exact free-space decay rate for the $6^2P_{1/2}$ state. As a result, the coupling ratio

$$\eta = \frac{g}{\Gamma} = \sqrt{\frac{\hbar \epsilon_0}{2V_m(w_0)}} \frac{3c^3 \pi}{\omega_0^{\frac{5}{2}} d} \quad (1.14)$$

is maximal for a diffraction limited beam waist of $w_0 = \frac{\lambda}{2}$ with $\lambda \approx 894$ nm, the photon wavelength of the cesium D₁ line [Steck (2010a)]. Therefore, the mode volume is $\sim 3.3 \times 10^{-12}$ m³, and because

$$\max(\eta) = \frac{2\pi \cdot 2.5 \text{ MHz}}{2\pi \cdot 4.56 \text{ MHz}} \approx 0.55 < 1, \quad (1.15)$$

coherent dynamics according to the Jaynes-Cummings Hamiltonian [Eq. (1.3)] are hard to observe.

1.1.2 Qubit interacting with a photon in an ideal cavity

To observe coherent dynamics of a single atom with a single photon in a specific mode, it is necessary either to protect the atom from decaying into other modes (decreasing Γ) or to increase the coupling strength g . In this section, we present the best way to increase the coupling rate g by placing the atom in a perfectly reflecting, resonant cavity, e.g. an ideal Fabry-Perot cavity for atoms in vacuum (Fig. 1.1). The main effect of the cavity is a change of mode structure at the position of the atom. On the one hand, it modifies the spontaneous decay rate Γ_{ac} such that $\Gamma_{ac} \neq \Gamma_0$. On the other hand, the coupling rate g is increased by the reduction of the mode volume to a few multiples of the mode's wavelength λ .

We consider the fundamental TEM_{00} mode of a symmetric, perfectly reflecting ($\kappa = 0$) Fabry-Perot cavity. To approach the limit of perfect mirrors may be technically hard to achieve in some cases, or is not intended because of experimental motivations, e.g. to probe the cavity transmission. However, it is ideally suited to study the fundamental limits of η in a cavity QED system. The cavity we consider

has curved mirrors of radius R and a mirror separation of l . The separation of the mirrors defines the spatial extension of the photons in the cavity mode along the photon propagation direction (compare with photon length l in Sec. 1.1.1).

The largest coupling rate g is achieved for the smallest mirror separation $l = \lambda/2$, i.e. the smallest mode volume V_m [Eq. (1.6)], and the atom positioned in the center of the mode. The radius of the mirror is chosen to be $R \approx 5l$, such that the beam waist of the TEM_{00} mode in the cavity is diffraction limited, i.e.

$$w_0^2 = \frac{\lambda}{2\pi} \sqrt{l(2R-l)} \approx \left(\frac{\lambda}{2}\right)^2, \quad (1.16)$$

and the cavity is in its stable regime [Kogelnik and Li (1966)]. The standing wave along the cavity axis (z direction) that forms because of the photon's reflection

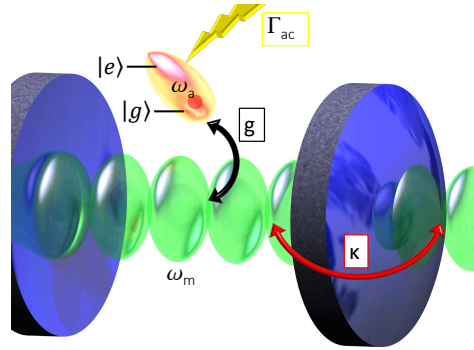


Figure 1.1: Sketch of a typical cavity QED system. A two-level system (orange, resonance frequency ω_a) with decay rate Γ_{ac} is coupled by the rate g to the mode (green, resonance frequency ω_m) of a cavity (blue). The cavity mode is coupled by a cavity coupling rate κ to the environment.

from the mirrors, modifies the mode distribution, i.e.

$$|f_c(\mathbf{r})|^2 = \left| f_{\text{fs}}(\mathbf{r}) \sin\left(\frac{2\pi}{\lambda}z\right) \right|^2. \quad (1.17)$$

For a photon of $\lambda = 894$ nm, the mode volume [using Eq. (1.12) and Eq. (1.17)]

$$V_m = \frac{\pi}{4} w_0^2 l - \frac{\lambda w_0^2}{8} \sin\left(\frac{2\pi}{\lambda}l\right) \approx \frac{\pi}{4} \left(\frac{\lambda}{2}\right)^2 \frac{\lambda}{2} \approx 7 \times 10^{-20} \text{ m}^3 \quad (1.18)$$

is strongly reduced with respect to the calculated mode volume of a photon in free-space ($\sim 3.3 \times 10^{-12} \text{ m}^3$), see last section (Sec. 1.1.1). As a result, a cesium atom is coupled via the D₁ line with a coupling rate $g \approx 2\pi \cdot 17.6$ GHz [Eq. (1.6)] that is higher by a factor ~ 7000 with respect to the free-space coupling rate ($\sim 2\pi \cdot 2.5$ MHz).

However, a small mode volume also modifies the (free-space) radiative decay Γ_0 depending on the parallel or perpendicular orientation of the atom's transition dipole with respect to the mirrors. For the case of two parallel, perfectly reflecting mirrors [Dutra and Knight (1996)],

$$\begin{aligned} \frac{\Gamma_{\text{ac},\parallel}}{\Gamma_0} &= \sum_{n=0}^{\lfloor 2l/\lambda \rfloor} \frac{3\lambda}{4l} \left[1 + \left(\frac{n\lambda}{2l}\right)^2 \right] \sin^2\left(\frac{n\pi}{l}z_a\right) \quad \text{and} \\ \frac{\Gamma_{\text{ac},\perp}}{\Gamma_0} &= \left\{ \frac{3\lambda}{4l} + \sum_{n=1}^{\lfloor 2l/\lambda \rfloor} \frac{3\lambda}{2l} \left[1 - \left(\frac{n\lambda}{2l}\right)^2 \right] \cos^2\left(\frac{n\pi}{l}z_a\right) \right\}, \end{aligned} \quad (1.19)$$

respectively. Here, z_a indicates the position of the atom within the cavity and $\lfloor 2l/\lambda \rfloor$ the largest integer number of half wavelengths that can fit into the mirror separation l . The parallel and perpendicular decay rates describe different processes. A decay according to $\Gamma_{\text{ac},\perp}$ (dipole oriented perpendicular to the mirror plane) corresponds to a radiative decay out of the cavity ($T_1 = \Gamma_{\text{ac},\perp}^{-1}$). Because it causes the relaxation of the Bloch vector along the z -axis, it is called the 'longitudinal' decay rate [Kimble (1998)].

An atom that decays into an intra-cavity mode with the rate $\Gamma_{\text{ac},\parallel}$ (dipole oriented parallel to the mirror plane) can reabsorb the photon coherently. For a mode m this happens with the rate² g , which relates to $\Gamma_{\text{ac},\parallel}$ by [Spillane et al. (2005); Alton (2013)]

$$g(\mathbf{r}) = \Gamma_{\text{ac},\parallel} \left| \frac{\mathbf{F}_m(\mathbf{r})}{\mathbf{F}_m^{\text{max}}} \right| \sqrt{\frac{V_a(\mathbf{r})}{V_m}} = \Gamma_{\text{ac},\parallel} f_c(\mathbf{r}) \sqrt{\frac{V_a(\mathbf{r})}{V_m}}, \quad (1.20)$$

with $\mathbf{F}_m(\mathbf{r})$ the electric field at the position of the atom, $\mathbf{F}_m^{\text{max}}$, the mode's maximum field, and $V_a(\mathbf{r})$ a characteristic atom interaction volume that depends on atomic

²For a number N of photons, this absorption and emission process happens with $\sim g\sqrt{N}$

parameters (d, λ) only. The coherent coupling to many other modes, e.g. higher transverse modes of a Fabry-Perot cavity may lead to dephasing ($T_2 = \Gamma_{ac,\parallel}^{-1}$) [Kimble (1998); Spillane et al. (2005)]. Because it may cause the relaxation of the Bloch vector transverse to the z -axis, $\Gamma_{ac,\parallel}$ is called the 'transverse' decay rate.

For a mirror separation $l < \lambda/2$ spontaneous decay into the cavity is fully suppressed because no modes can form within the cavity (black traces in Fig. 1.2), as calculated using Eq. (1.19). For $z_a = l/2$ (solid line), the peaks at positions $(n + 0.5)\lambda$, $n \in \mathbb{N}_0$ correspond to new modes that form in the cavity. This structure depends strongly on the position of the atom within the cavity (compare dashed line in Fig. 1.2 for $z_a = l/4$). The spontaneous decay out of the cavity diverges for small mirror separations because of the energy density in these modes ($n = 0$) being proportional to the volume between the mirrors (blue traces). For long cavities, the decay of the atom into all modes approaches the free-space limit.

The modification of spontaneous decay rate was described by [Kleppner (1981)] and enhancement was observed by [Goy et al. (1983); Rempe et al. (1990)], and inhibition by [Drexhage (1974); Hulet et al. (1985); Gabrielse and Dehmelt (1985)].

Because g is largest for $l = \lambda/2$, the total decay rate of the considered system is in the worst case $\Gamma = \Gamma_{ac} \approx 2\Gamma_0$, when averaged over all possible directions of the dipole, i.e. the spontaneous decay into perpendicular and parallel modes. This increase of Γ with respect to free-space is negligible compared to the increase in g . In fact, the smaller mode volume dominates the increase in coupling ratio of more than 3 orders of magnitude for a cesium atom from free-space to a $\lambda/2$ -Fabry-Perot cavity, i.e.

$$\max(\eta) = \frac{g}{\Gamma} = \frac{g}{\Gamma_{ac}} \approx \frac{g}{2\Gamma_0} = \frac{17.6 \text{ GHz}}{2 \cdot 4.56 \text{ MHz}} = 1930. \quad (1.21)$$

In conclusion, we have seen that by interfacing an atom and a well-defined mode in a cavity with small mode volume, the coupling rate g , and as consequence the coupling ratio η , can be increased by orders of magnitude.

1.1.3 Modifications in a transmissive cavity

As discussed in the last section, the coupling ratio η can be very large if an atom is placed in an ideal cavity with a small mode volume. However, perfect cavities are impossible to fabricate. In fact, the design of good enough cavities to observe single-atom-single-photon interactions was a major technical hurdle to overcome in the experiments of S. Haroche and J. Kimble (Sec. 1). In this section we sketch the consequences of a non-ideal cavity.

In fact, a coupling ratio of $\eta \approx 2000$ for a typical ground-state atom (here cesium) in a Fabry-Perot cavity is impossible to achieve if the mode leakage through

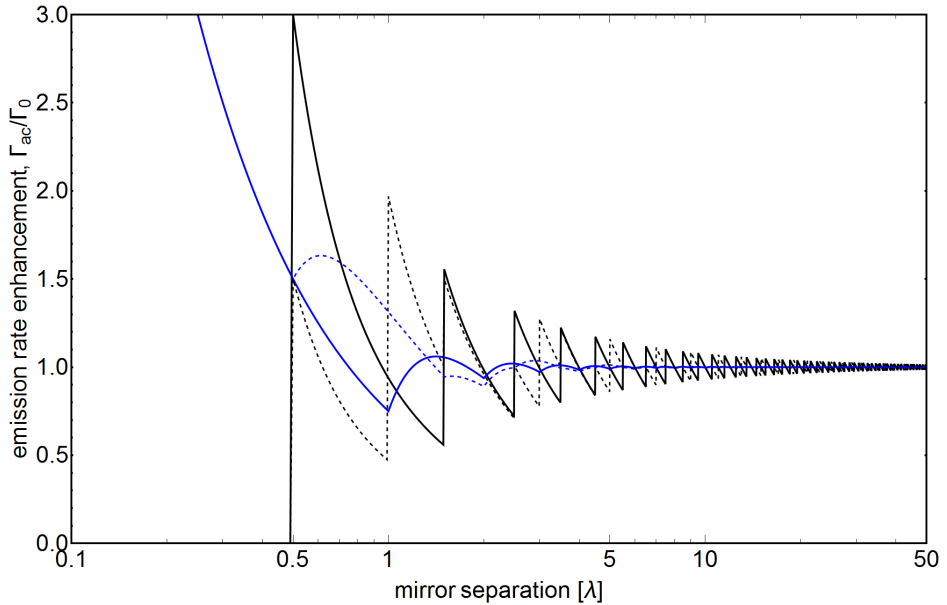


Figure 1.2: Enhancement of radiative decay rate Γ_{ac} with respect to free-space decay rate Γ_0 of a dipole between two perfectly reflecting mirrors as a function of mirror separation. The black and blue traces show the enhancement for a dipole parallel and normal to the mirrors, respectively. Solid lines indicate decay rates for an atom at $z_a = l/2$, dashed lines for $z_a = l/4$. The traces were simulated using Eq. (1.19).

the mirrors is finite, i.e. cavity loss rate $\kappa \neq 0$. A finite κ strongly affects spontaneous emission through the mirrors and, as consequence, the optimal cavity length. As *Dutra and Knight (1996)* show, the inhibition of the decay into the cavity mode (black traces in Fig. 1.2) is lifted and diverges for small cavity length l if one of the mirrors is partially transparent. Additionally, the height of the peaks increases proportional to the quality factor of the cavities m^{th} mode [*Kleppner (1981)*]

$$Q = \frac{\omega_m}{\kappa}. \quad (1.22)$$

For large transparency of the mirror ($g \ll \kappa$), the loss of photons through the mirror is larger than the qubit's reabsorption of photons from the cavity mode and the photon is lost by leaving the cavity through the mirror (Purcell limit [*Purcell (1946); Kleppner (1981); Goy et al. (1983)*]). The Purcell decay rate of the atom into the cavity mode (and out of the cavity) can be related to Γ_0 by [*Haroche and Raymond (2006)*]

$$\Gamma_p \approx \frac{g^2}{\kappa} = \frac{2d^2}{\epsilon_0 \hbar} \frac{Q}{V_m} = \frac{3}{4\pi^2} \frac{Q\lambda^3}{V_m} \Gamma_0. \quad (1.23)$$

where the last expression is also correct in the limit of $g \gtrsim \kappa$.

For a good cavity $Q \gg 1$ (e.g. $Q \approx 10^8$ in [Thompson *et al.* (1992); Hood *et al.* (2000)]), and for a small cavity volume (in our example: $V_m \sim \lambda^3$) the Purcell rate Γ_p exceeds g (i.e. $\eta \ll 1$). To increase η for imperfect mirrors, one needs to increase the mode volume to reduce the Purcell rate, with the drawback of g being reduced also. The two parameters Γ_p and g scale differently with V_m [compare V_m^{-1} for Γ_p in Eq. (1.23) and $V_m^{-0.5}$ for g in Eq. (1.6)] and an optimum for η exists, see Buck (2003) for calculations of the cavity used in Thompson *et al.* (1992); Hood *et al.* (2000).

Since typical free-space decay rates of (alkali) atoms in states close to the ground state are on the order of several MHz [Steck (2010a,b,c, 2013)] optical Fabry-Perot cavities are also produced with $\kappa \approx 1$ MHz. As a consequence, maximal coupling ratios $\eta \approx 2000$ as achieved with a perfect cavity can not be exploited. For additional information in this direction, we refer to Alton (2013) and references therein. Alton (2013) discusses in detail the ratios between coupling into the cavity mode including reflectivity of mirrors ($g, \kappa > 0$) and spontaneous decay ($\sim \Gamma_0$) for the two specific examples of ground state atoms in Fabry-Perot cavities and close to photonic waveguide structures.

In systems with finite κ , the possibility to observe coherent dynamics is typically quantified by the cooperativity

$$C = \frac{g^2}{\kappa \Gamma_{ac,\perp}} > 1. \quad (1.24)$$

This is the product of the coupling ratios [Eq. (1.5)] for the two decay channels present in the system. This is a useful quantity to determine whether the system is in the strong coupling regime when κ and $\Gamma_{ac,\perp}$ are on the same order of magnitude. In a system for which $\Gamma_{ac,\perp} > g \gg \kappa$, $C > 1$ but $\eta = g/\Gamma(\Gamma_{ac,\perp}, \kappa) < 1$ [Eq. (1.5)], such that Jaynes-Cummings dynamics cannot be observed. However, as long as $g \gtrsim \Gamma_{ac,\perp}$, the cooperativity C can be used to determine the effect of a single atom onto the (lossy) cavity. The reason for C being quantified in general is that in an experiment, κ can be improved by technical development until $\Gamma_{ac,\perp} \approx \kappa$. This is sufficient, because for a cavity QED system

$$\Gamma \approx \begin{cases} \Gamma_{ac,\perp} & \kappa \ll \Gamma_{ac,\perp}, \\ \kappa & \kappa \gg \Gamma_{ac,\perp}, \end{cases} \quad (1.25)$$

A consequence of this behaviour is that the systems with small natural decay rates $\Gamma_0 \propto \Gamma_{ac,\perp}$ have the potential to perform best in terms of η .

In contrast to low lying atomic states, Rydberg states (principal quantum number $n \gg 15$) have increased lifetimes (i.e. smaller $\Gamma_{ac,\perp}$) which scale approximately

as n^3 for low angular momentum states and as n^5 for 'circular' states with maximal angular momentum. As discussed in the next section, circular states are particularly suited to couple to microwave (Fabry-Perot) cavities to achieve very large coupling ratios [Anderson *et al.* (1988); Bernardot *et al.* (1992); Hagley *et al.* (1997); Gleyzes *et al.* (2007); Guerlin *et al.* (2007); Haroche (2013)].

1.1.4 Coupling ratios for different excitation states and scaling laws

In this section we compare the coupling ratio η [Eq. (1.5)] of a single atom (qubit) coupled to a single photon in a perfectly reflecting $\lambda/2$ -Fabry-Perot cavity for different atomic excitation levels and, as consequence, identify the atomic states with the potential to achieve largest coupling ratios η .

Combination of the coupling rate g [Eq. (1.6)] with the mode volume [Eq. (1.18)], mirror separation $l = \lambda/2$, atom position $z_a = l/2$ ($f_c(\mathbf{r}) = 1$) and a diffraction-limited mode waist [Eq. (1.16)] results in a coupling ratio

$$\eta = \sqrt{\frac{d^2 \omega_m}{2\epsilon_0 \hbar} \frac{\pi \lambda^2}{2} \frac{1}{4} l \Gamma_{ac}(z_a)} \approx \sqrt{\frac{8d^2 \omega_m}{\epsilon_0 \hbar} \frac{1}{\pi \lambda^3} \Gamma_{ac}(\lambda/4)}. \quad (1.26)$$

For the chosen configuration of the cavity, η depends on atomic properties only, i.e. on the transition frequency $\omega_q = \omega_m = 2\pi c/\lambda$, the transition dipole moment d and the cavity-modified, inverse lifetime of the states Γ_{ac} [Eq. (1.19)].

Because the atomic properties scale with the principal quantum number n of the excited state, η is also n -dependent. To identify the states with the largest possible coupling ratio, we will *first* derive the scaling laws for the atomic properties ω_q , d , and Γ_{ac} . *Secondly*, we calculate η for different atomic species, for $\Delta m = 0$ transitions between low angular momentum states, and for $\Delta m = 1$ transitions between 'circular' states with maximal magnetic and angular quantum numbers. As species we choose atomic metastable singlet helium (the atom species used in this thesis), cesium (the atom species used in previous sections and other cavity QED experiments), and atomic hydrogen, respectively. The choice of presenting also calculations using hydrogen is motivated by its exactly known energies, dipole moments and lifetimes for all quantum numbers n .

The *transition frequencies* ω_q are calculated for the different atom species (s) from the energy difference between the initial state [quantum numbers (n, l, m)] and final state [quantum numbers (n', l', m')], i.e.

$$\omega_q = \omega_{n', l'}^{n, l} = \frac{\Delta E_{n, l}^{n', l'}}{\hbar} = \frac{E_{n', l'} - E_{n, l}}{\hbar}, \quad (1.27)$$

using the Rydberg equation [Gallagher (1994)]

$$\frac{E_{n,l}}{h} = \frac{cR_\infty \left(1 - \frac{m_e}{m_s + m_e}\right)}{(n - \delta_l^s(n))^2} = \frac{cR_\infty \left(1 - \frac{m_e}{m_s + m_e}\right)}{(n^*)^2} \quad (1.28)$$

with R_∞ the Rydberg constant, renormalized by the effective mass fraction of the electron (m_e) and the ion core (m_s), and the effective quantum number $n^* = n - \delta_l^s$. The quantum defect $\delta_l^H(n)$ of hydrogen is 0 for all states, because the electron is bound by a perfect Coulomb potential conserving the Runge-Lenz vector [Gallagher (1994)]. In helium and cesium, the core electrons modify the binding potential in the vicinity of the core and energies of eccentric, low-angular momentum states are shifted because of a large overlap of the electron wavefunction with the core region. Consequently, the quantum defects for helium $\delta_l^{\text{He}}(n)$ [Drake (1999)] and cesium $\delta_l^{\text{Cs}}(n)$ [Goy *et al.* (1982); Sassmannshausen *et al.* (2013)] are finite and energy-dependent, but tend to a constant value for $n \gtrsim 30$.

The transition frequencies between adjacent- n states, i.e. $(n, l, m) \rightarrow (n+1, l \pm 1, m')$ scale with the principal quantum number n as

$$\frac{d\omega_{n,l}^{n+1, l \pm 1}}{dn} = \frac{1}{\hbar} \frac{dE_{n,l}}{dn} = 4\pi c R_\infty (n^*)^{-3} + O(n^{-4}). \quad (1.29)$$

Hence, typical interband (adjacent n) transition frequencies of Rydberg states for $n \geq 30$ are in the microwave region. In contrast, typical intraband (same n) transitions of ground-state alkali-atoms lie in the optical and infrared regime³.

The *transition dipole moments* d between initial $(\Psi^{nlm}(\mathbf{r}) = R_{n,l}(r)Y_{l,m}(\theta, \phi))$ and final $(\Psi^{n'l'm'}(\mathbf{r}) = R_{n',l'}(r)Y_{l',m'}(\theta, \phi))$ states are calculated for different Δm transitions as

$$d = \langle R_{n',l'}(r) | r | R_{n,l}(r) \rangle_r \begin{cases} \langle Y_{l',m'}(\theta, \phi) | \cos(\theta) | Y_{l,m}(\theta, \phi) \rangle_{\theta, \phi} & \Delta m = 0 \\ \langle Y_{l',m'}(\theta, \phi) | \sin(\theta) \exp(\mp i\phi) | Y_{l,m}(\theta, \phi) \rangle_{\theta, \phi} & \Delta m = \pm 1 \end{cases} \quad (1.30)$$

by individual integration over the radial wavefunctions using the Numerov-algorithm [Zimmerman *et al.* (1979)] and the angular wavefunctions. For large quantum number n the electron is located far away from the core and the transition dipole moment scales as [Gallagher (1994)]

$$d = e \langle \Psi_{n',l',m'} | r | \Psi_{n,l,m} \rangle \propto \begin{cases} (n^*)^{-\frac{3}{2}}, & \text{for } n' \gg n \approx 1 \\ (n^*)^2, & \text{for } n' \approx n \gg 1 \end{cases} \quad (1.31)$$

³In this statement we exclude intraband, hyperfine transitions in alkali atoms that can lie in the microwave regime.

The different n -dependencies are determined by the wavefunction-overlap in the core and the scaling of the atom radius, respectively. From the exact diagonalisation of the single-particle hamiltonian we note that the scaling of the transition dipole moment between circular states ($m = l = n - 1$) is given by the scaling of the Bohr-radius a_n of the n^{th} state, i.e.

$$d = ea_n = n^2 ea_0. \quad (1.32)$$

The dipole moment is reduced by a factor of $\sqrt{2}$ when driven with linearly polarized light of a TEM_{kj}-mode of a Fabry-Perot cavity, because only the circular component of the field can drive the transition.

The *free-space decay rates* Γ_0 of low angular momentum states [e.g. $(n, l, m) = (n, p, 0)$] and circular states $[(n, n - 1, n - 1)]$ scale differently with the quantum number n .

Atoms in states with low angular momentum decay to all unoccupied states with $n' < n$, $|l - l'| = 1$ and $|m - m'| = 0, \pm 1$. Consequently, the decay rate $\Gamma_0^{n,l}$ of a low angular momentum state is given by the sum over all dipole-allowed decay channels, i.e.

$$\begin{aligned} \Gamma_0^{n,l} &= \sum_{n'=n_{\min}}^n \sum_{l'=0}^{n'-1} \Gamma_{n,l}^{n',l'} && \text{with} \\ \Gamma_{n,l}^{n',l'} &= \frac{8\pi^2 e^2}{3\epsilon_0 \hbar c^3} \left(\frac{\Delta E_{n,l}^{n',l'}}{h} \right)^3 \left(d_{n,l}^{n',l'} \right)^2 && \text{and} \\ d_{n,l}^{n',l'} &= \sqrt{\frac{\max(l, l')}{2l+1}} \langle R_{n',l'}(r) | r | R_{n,l}(r) \rangle_r \delta_{|l-l'|,1}. \end{aligned} \quad (1.33)$$

Here, n_{\min} is the principal quantum number of the ground state, $d_{n,l}^{n',l'}$ the transition dipole matrix element, averaged over all dipole orientations [Gallagher (1994)], and δ the Kronecker delta. The free-space decay rate $\Gamma_0^{n,l}$ is dominated by the radiative decay to the state with the lowest energy (n_0, l_0) because of the large energy difference $\Delta E_{n,l}^{n_0,l_0}$. For transitions between states with small angular momentum l , n_0 is on the order of the quantum number of the valence shell and $\Delta E_{n,l}^{n_0,l_0} \approx C$ is approximately constant for large quantum numbers n . Hence,

$$\Gamma_0^{n,l} \approx \Gamma_{n,l}^{n_0,l_0} \propto \left(\Delta E_{n,l}^{n_0,l_0} \right)^3 \left(d_{n,l}^{n_0,l_0} \right)^2 \propto C^3 \left((n^*)^{-3/2} \right)^2 \propto (n^*)^{-3}, \quad (1.34)$$

using the scaling law $d \propto (n^*)^{-3/2}$ for the dipole moment [Eq. (1.30)].

The decay rate $\Gamma_0^{n,n-1}$ of a circular state is described by the decay of a dipole [Eq. (1.13)], with d and ω_q being the parameters of the only allowed decay channel

$[(n+1, n, n) \rightarrow (n, n-1, n-1)]$. Both states have minimal overlap with the core (quantum defect $\delta_{n-1}^s(n) = 0$) and the electron is located far away from the core, so that [Gallagher (1994)]

$$\Gamma_0^{n,n-1} \propto d^2 \omega_q^3 \propto (n^*)^4 ((n^*)^{-3})^3 = (n^*)^{-5}. \quad (1.35)$$

As a result, decay rates of low angular momentum states are larger than the ones for circular states.

In fact, the scaling of the decay rates turns out to be crucial for the scaling of η with quantum number n . Since the coupling rate g [Eq. (1.6)] for a Rydberg-Rydberg transition and a cavity with minimal mode volume [Eq. (1.18)] scales as

$$g \propto \sqrt{\frac{d^2 \omega_q}{V_m}} \propto \sqrt{\frac{d^2 \omega_q}{\lambda^3}} \propto \sqrt{\frac{d^2 \omega_q}{\omega_q^{-3}}} \propto \sqrt{\frac{(n^*)^4 (n^*)^{-3}}{((n^*)^3)^3}} \propto (n^*)^{-4}, \quad (1.36)$$

the ratio between the coupling rate g and the free-space decay rate $\Gamma_0^{n,l}$ scales as

$$\eta \approx \frac{g}{\Gamma_0^{n,l}} \propto \begin{cases} \frac{(n^*)^{-4}}{(n^*)^{-3}} = (n^*)^{-1} & \text{for low } l \text{ states} \\ \frac{(n^*)^{-4}}{(n^*)^{-5}} = n^* & \text{for circular states.} \end{cases} \quad (1.37)$$

As a result, circular states with large quantum number n are ideal to couple to single photons in a cavity, because η increases with increasing quantum number whereas it decreases in the case of low- l states.

Indeed, the theoretically calculated coupling ratios for low l (dashed lines) and circular states (solid lines) approach the estimated scalings of n^{-1} and n (lines plotted brown in Figure 1.3) for large quantum numbers n . Deviations from this scaling at lower n -values result from the too simplistic assumption for the scalings of Γ_{ac} and d .

To calculate the coupling ratios, we assumed the fundamental Gaussian mode of an ideal Fabry-Perot cavity [mode waist w_0 , Eq. (1.16)] with mode volume V_m [Eq. (1.18)], that couples resonantly with coupling rate g [Eq. (1.6)] to an atom positioned in the mode center. The transition frequencies, ω_m , the dipole moments d , and the lifetimes $\Gamma_0^{n,l}$ of the transitions were calculated exactly using the equations discussed in this section. For this plot, Γ_{ac} for a specific transition is given by the sum of the root-mean squares of the Γ_{ac} of the contributing states. We used the energy dependence of the quantum defects of helium and cesium given in the references [Drake (1999); Goy *et al.* (1982)], which can deviate up to 20% for $n \lesssim 10$. The calculated lines for the circular states lie on top of each other, because of the negligible quantum defect for high l -states, independent of the atomic species. For

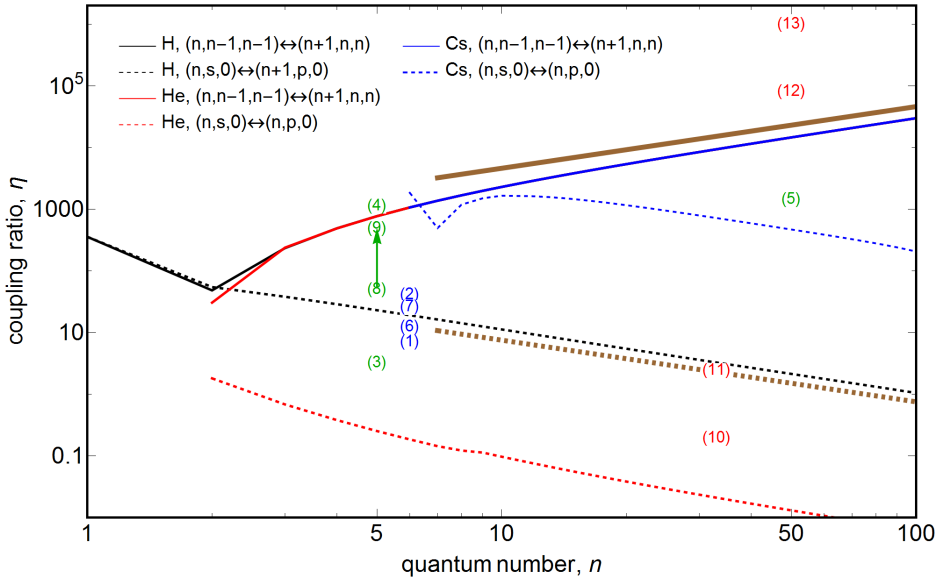


Figure 1.3: Coupling ratios η as a function of principal quantum number n for atomic hydrogen (black), metastable singlet helium (red) and cesium (blue) in low- l (dashed lines) and circular states (solid lines) positioned in the center of a perfectly reflecting $\lambda/2$ -Fabry-Perot cavity. Lines colored brown indicate expected scalings with n (solid) and n^{-1} (dashed), respectively. The labels (1 – 9) indicate experimentally achieved and predicted coupling ratios in different systems for atomic cesium (blue) and rubidium (green), for references see text. The coupling ratios labeled (10 – 13) indicate expected coupling ratios of the system discussed in this thesis and are calculated in Sec. 1.4. For details on the theoretical calculations leading to the lines in the figure, see text.

cesium at $n \lesssim 10$, the assumption that the quantum defect of the circular states, δ_{n-1}^{Cs} is zero is an approximation.

The coupling ratios η for low- l states of the atoms H, He and Cs differ significantly in magnitude. For example, the ground state of helium is bound more strongly than the ground state of hydrogen ($\lesssim -20$ eV in He vs. -13.6 eV in H), which results in a shorter lifetime of the np state in helium because of the larger energy difference $\Delta E_{1,p}^{n,l}$. Additionally, the frequency of the intraband transition between the ns and np ($\delta_s^{\text{He}}, \delta_p^{\text{He}} \approx 1.13, 0.98$) states is lower than that of the interband $ns \rightarrow (n+1)p$ transition of hydrogen. Both factors reduce η according to Eq (1.26). For cesium, the intraband transition frequencies and the lifetimes are larger because of its larger quantum defect ($\delta_s^{\text{Cs}}, \delta_p^{\text{Cs}} \approx 4, 3.5$) and because of $n_0 = 6$ being the quantum number of the valence electron of cesium.

In Fig. 1.3, the labels (1, 2, 3) correspond to values of η in experiments involving single cesium atoms in optical Fabry-Perot cavities. η was directly calculated

as g/Γ from the following parameters⁴: $(g, \kappa, \Gamma) = 2\pi \times (19, 4, 2.61)$ MHz [Kimble (1998); Buck (2003)], $2\pi \times (110, 14.2, 2.61)$ MHz [Hood et al. (2000)], and for a single ⁸⁵Rb atom $(2\pi \times (16, 1.5, 3))$ MHz [Sames et al. (2014)], respectively. As discussed in the previous section, the coupling ratios are reduced from the ideal value, because of the finite cavity decay $\kappa \neq 0$.

The observation of large coupling ratios $\eta \gg 100$ for atoms in ground states and single photons in Fabry-Perot cavities is only possible if g is enhanced by \sqrt{N} [Dicke (1954)], N being a large number of atoms, e.g. in a ⁸⁷Rb-Bose-Einstein condensate [label (4), parameters: $(g, \kappa, \Gamma) \approx 2\pi \times (10.6, 1.3, 3)$ MHz and $N \approx 2.2 \times 10^5$ in the experiments of Brennecke et al. (2007)]. Comparable coupling ratios for single atoms in Fabry-Perot cavities are only possible for circular Rydberg states [label (5), parameters for Rb: $(g, \kappa, \Gamma) = 2\pi \times (50 \times 10^3, 10, 33)$ Hz [Gleyzes et al. (2007); Guerlin et al. (2007); Haroche (2013)]]. In this experiment, because of the long wavelength of microwave radiation ($\omega_m = 2\pi \times 51$ GHz), the long lifetime of the Rydberg atoms and small $\kappa \approx \Gamma \ll g$, the mirror separation of ~ 27 mm is only 4.5 times larger than the wavelength of the radiation mode. This allows to achieve the highest coupling ratios $\eta \approx 1500$ for single-atom experiments so far.

For a fixed quantum number n , η can only be increased above the limit given by the solid lines in Fig. 1.3 by modification of the cavity design. Specifically, g can be increased by decreasing the mode volume V_m which is not minimal in Fabry-Perot cavities [Eq. (1.6)]. Current approaches use micro-fabricated devices to confine radiation to smaller mode volumes. Early experiments in this direction were performed for atoms in ground states in J. Kimbles group, where cesium atoms were coupled to the evanescent modes of micro-toroids with different diameters and a mode waist $w_0 \approx \lambda$ for all positions within the cavity. Corresponding coupling ratios are labeled (6, 7) in Fig. 1.3 calculated from parameters: $(g, \kappa, \Gamma) = 2\pi \times (50, 18, 3.91)$ MHz [Alton et al. (2011)] and $2\pi \times (105, 20, 3.91)$ MHz [Aoki et al. (2006)], respectively. Recent experiments involving atoms close to tapered fibers [Vetsch et al. (2010); Goban et al. (2012)] and photonic waveguides [Thompson et al. (2013); Tiecke et al. (2014); Goban et al. (2014)] may promise higher coupling ratios. Label (8) in Fig. 1.3 represents the coupling ratio of the experiment by Thompson et al. (2013) that couples a Rubidium atom to a photonic waveguide cavity with parameters: $(g, \kappa, \Gamma) = 2\pi \times (310, 840, 6)$ MHz, and the potential to increase g to $2\pi \times 3$ GHz [green, dashed arrow to label (9)].

So far, similar experiments with atoms coupled to chip-based microwave waveguides via hyperfine or Rydberg-Rydberg transitions [Petrosyan and Fleischhauer (2008)] have not been realized, which is attributed to technical difficulties [Kurizki et al. (2015)]. Typical limitations are inhomogeneous stray fields that

⁴For completeness, we also state κ .

lead to decoherence of the atoms or high-power photons that create losses in the waveguide. Comparison of coupling ratios η labeled (10, 11) with the red, dashed line in Fig. 1.3 indicates the expected increase that could be achieved for a low- l intraband Rydberg-Rydberg (helium) transition at $n = 33$ being coupled to a chip-based microwave waveguide with respect to a Fabry-Perot cavity. Here, label (10) indicates calculations for one atom, label (11) for 100 atoms. Similarly, labels (12, 13) indicate the increase for 1 and 100 atoms, respectively, and for transition between circular states at $n = 50$ coupled to a chip-based microwave waveguide with respect to a Fabry-Perot cavity. The calculated η of this hybrid system beats the fundamental limit of circular states coupled to microwave photons in a Fabry-Perot cavity by up to 2 orders of magnitude because it combines the best of two worlds, atoms and solid-state systems. Such a system has not been realized so far. The experiment which was setup in this thesis accomplishes the first, important step towards this goal. We discuss the concept of the hybrid system in detail in Sec. 1.4, together with the calculations of the points labeled (10 – 13, and after introducing into the 'world' of solid-state cavity QED.

1.2 Cavity QED systems in solid state devices

In the previous chapters we have discussed the 'world' of interfacing atoms and photons in free-space and cavities. Within the last decade, two breakthroughs in (the 'world' of) solid state physics have exploited the confinement of radiation in small mode volumes to create cavity QED systems with large coupling rates g in the microwave- and optical-frequency regime, respectively (for example, see [Wallraff *et al.* (2004); Hennessy *et al.* (2007)]). Instead of single atoms, both couple photons in micro or nano-fabricated waveguide cavities to meso- or nanoscopic structures that behave similar to atoms and are typically addressed as "artificial atoms". Both systems can be seen as solid-state counterparts to the atom experiments in Fabry-Perot cavities (Fig. 1.4). Despite their different physical nature, they all implement the Jaynes-Cummings Hamiltonian [Eq (1.3)] and can be characterized in terms of effective qubit parameters (\mathbf{d}, Γ_{ac}), cavity parameters ($\kappa, V_m, \mathbf{F}_m$) and a coupling rate g .

For example in the optical regime, excitons in a self-assembled quantum dot are coupled to a photonic-crystal nanocavity with parameters: $(g, \Gamma_{mode}, \Gamma_{exciton}) \approx 2\pi \times (20, 24.1, 8.5)$ GHz and $\eta \approx 2.35$ [Hennessy *et al.* (2007)]. Note that the coupling rate g is up to 1000 times bigger than for single atoms in ground states coupled to 3-dimensional Fabry-Perot cavities.

Wallraff *et al.* (2004) strongly coupled a superconducting artificial atom to a chip-based coplanar transmission line resonator (CPW-resonator) operating in

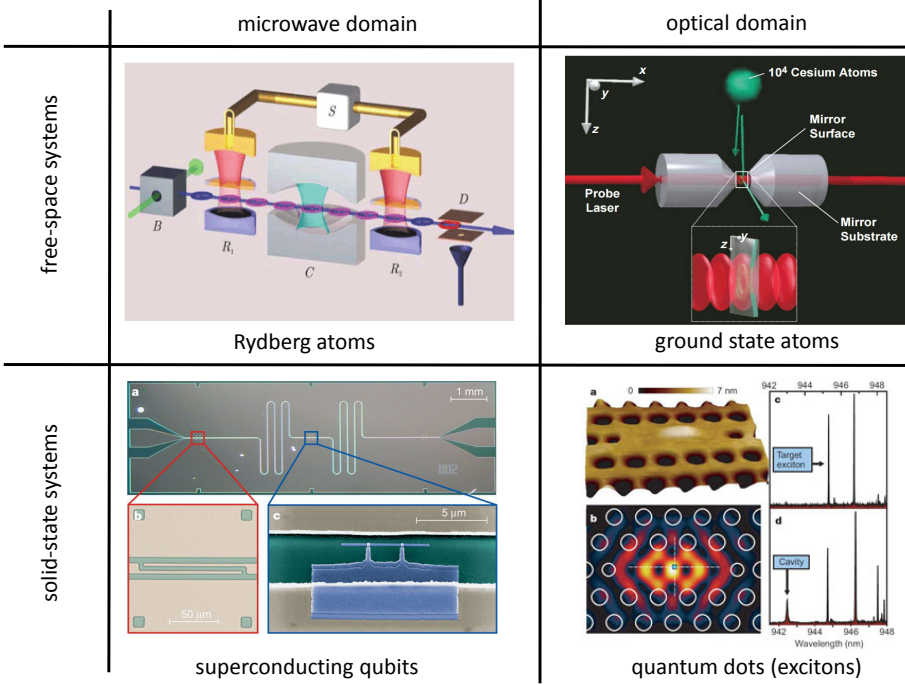


Figure 1.4: Prominent examples of physical systems that reached strong coupling between single photons and (artificial) atoms sorted by physical environment and radiation frequency. Pictures are taken from left to right, top to bottom from *Sayrin et al. (2012)*; *Hood et al. (2000)*; *Wallraff et al. (2004)*; *Hennessy et al. (2007)*.

the microwave regime at 6 GHz. This triggered the formation of a new field, called ‘circuit QED’, because the chips are designed as superconducting electric circuits.

In their initial system, *Wallraff et al. (2004)* realized the following cavity QED parameters: $(g, \kappa, \Gamma) = 2\pi \times (11.6, 0.8, 0.7)$ MHz, and hence $\eta = 16.5$. The effective dipole of a superconducting qubit (here: a cooper pair box) can be on the order of $d = 10^4 - 10^5 ea_0$ [*Blais et al. (2004)*]. It is comparable to the dipole moment of a circular state at $n = 100$ with similar transition frequency of ~ 6.5 GHz, and about 10 times larger than the dipole moment of the Rydberg-Rydberg transition at 51 GHz used in *Raimond et al. (2001)*. Albeit both dipole moments being of the same order of magnitude, typical coupling rates g can be $\gtrsim 2000$ times bigger in circuit QED experiments ($g \geq 2\pi \times 100$ MHz [*Blais et al. (2004)*]) than in a comparable experiment with a Rydberg atom in a microwave Fabry-Perot cavity. This is due to the very small mode volume of the chip-based, microwave cavities (here: coplanar transmission line resonators) which increases g [Eq. (1.6)]. Typical mode volumes in circuit QED experiments are on the order of $V_m \lesssim 10^{-6} \lambda^3$, to compare

with mode volumes of Fabry-Perot cavities $V_m \approx \lambda^3$. The small mode volumes of the chip-based CPW-resonators are a result of the quasi 1-dimensional geometry of the waveguides, see Sec. 1.4 for a calculation.

More recently, several groups were able to push coupling rates in solid-state systems to the ultra-strong coupling limit, where g approaches ω_m . The rotating wave approximation for the Jaynes-Cummings Hamiltonian [Eq. 1.3] is not justified anymore in this parameter regime. Prominent examples are circuit QED systems ($g \approx \omega_m/10 \approx 2\pi \times 1$ GHz) [Bourassa et al. (2009); Niemczyk et al. (2010); Forn-Díaz et al. (2010); Beaudoin et al. (2011)], polaritons in microcavities ($g \lesssim \omega_m/2 \approx 2\pi \times 1.4$ THz) [Gunter et al. (2009); Todorov et al. (2012)], and 2D electron gases in metamaterials ($g \approx \omega_m/2 \approx 2\pi \times 0.75$ THz) [Scalari et al. (2012)].

Albeit the large coupling rates g achieved in solid-state systems compared to atoms in free-space cavities, the final coupling ratio η does not increase as much because of larger decay rates in solid-state systems. For example, decay rates of superconducting charge qubits coupled to CPW-resonators in circuit QED systems are typically on the order of $\Gamma_{ac} = 2\pi \times 0.01$ MHz to $2\pi \times 0.1$ MHz [Devoret and Schoelkopf (2013)], compared to ~ 30 Hz of circular Rydberg states [Raimond et al. (2001)]. As a result, current typical coupling ratios $\eta \gtrsim 2000$ (for $\Gamma_{ac} \approx 2\pi \times 0.1$ MHz and $g \approx 2\pi \times 200$ MHz) in circuit QED setups are comparable to η of circular Rydberg states in Fabry-Perot cavities.

1.2.1 The role of cavity QED systems in applications of quantum information science

The parameters of the different cavity QED systems are spread over a wide range (Tab. 1.1). These parameter configurations make these systems particularly interesting for implementation in a variety of possible applications within the fields of quantum science and information technology. The system that we study in this thesis is a combination of two of these physical implementations of cavity QED, Rydberg atoms and circuit QED. Therefore, this section introduces the most promising future application of a circuit QED system with a hybrid interface to Rydberg atoms: *A quantum computer in a quantum network*.

Quantum computation is one of the "workhorse" developments in quantum information science. Simply spoken, in contrast to the bit-representation of a classical computer with a bit having two distinct states, a quantum computer processes quantum information using quantum bits (qubits) following the laws of quantum mechanics [Ladd et al. (2010)]. It was shown in many systems, that the additional resource of several entangled qubits [DiCarlo et al. (2010); Schindler et al. (2013); Barreiro et al. (2013); Bartkiewicz et al. (2015); Streltsov et al. (2015)] in superposition of their eigenstates ($|g\rangle$ and $|e\rangle$) allows an (exponential) speed-up of some algorithms [Gilowski et al. (2008); Berry et al. (2007); Kiktenko et al. (2015);

Table 1.1: Overview of typical parameter ranges of the different cavity QED systems discussed so far, that operate in the strong coupling regime. Coupling rate g indicates largest values, other values are typical. Systems chosen are: ground state (g.s.) atoms in 3D-cavities and microstructures, Rydberg atoms in circular states between $n = 30 \rightarrow 100$ in 3D cavities and a typical CPW-resonator (Fig. 1.7), the quantum-dot(QD)-nanocavity system of [Hennessy *et al.* (2007)], and superconducting charge qubits in coplanar waveguide (CPW) resonators. The collected parameter ranges are based on Kimble (1998); Buck (2003); Hood *et al.* (2000); Sames *et al.* (2014) (g.s. atoms in 3D-Fabry-Perot cavities), Aoki *et al.* (2006); Vetsch *et al.* (2010); Alton *et al.* (2011); Goban *et al.* (2012, 2014); Thompson *et al.* (2013); Tzeke *et al.* (2014) (g.s. atoms close to microstructures), Raimond *et al.* (2001); Gleyzes *et al.* (2007); Guerlin *et al.* (2007); Haroche (2013) (Rydberg atoms in 3D-Fabry-Perot cavities), Sec. 1.1.4 and Sec. 1.4 of this thesis (Rydberg atoms close to CPW-resonators), Hennessy *et al.* (2007) (quantum dots in nanocavities) and from Wallraff *et al.* (2004); Blais *et al.* (2004); Devoret and Schoelkopf (2013).

physical system	$\omega_m/(2\pi)$	λ_m	max. $g/(2\pi)$	$\kappa/(2\pi)$	$\Gamma/(2\pi)$
g.s. atoms/3D-cavities	300 – 800 THz	400 – 1000 nm	150 MHz	1 – 20 MHz	1 – 3 MHz
g.s. atoms/microstructures	300 – 800 THz	400 – 1000 nm	1 GHz	1 – 1000 MHz	1 – 10 MHz
Rydberg atoms/3D-cavities	6 – 250 GHz	1 – 50 mm	10 MHz	10 Hz	3 – 1500 Hz
Rydberg atoms/CPW-resonator	6 – 250 GHz	1 – 50 mm	300 MHz	1 MHz	1.5 – 750 Hz
QD/nanocavities	315 THz	950 nm	20 GHz	\sim 20 GHz	8 – 25 GHz
charge qubits/CPW resonator	1 – 15 GHz	20 – 300 mm	600 MHz	$>$ 1 MHz	0.01 – 0.1 MHz

Tame et al. (2014); Su and Yang (2014); Lloyd et al. (2014); Chuang et al. (1998)] such as the efficient search in a database [*Grover (1996); DiCarlo et al. (2009)*] or prime factorization [*Shor (1994, 1997); Vandersypen et al. (2001); Lanyon et al. (2007); Lu et al. (2007); Politi et al. (2009); Martin-Lopez et al. (2012)*]. Another application of a quantum computer is digital simulation of quantum systems, which gets exponentially hard on a classical computer with increasing number of particles [*Lanyon et al. (2011); Zhang et al. (2012); Mezzacapo et al. (2012, 2014); Las Heras et al. (2014); Barends et al. (2015); Chiesa et al. (2015); Lu et al. (2015); Salathé et al. (2015)*].

A physical system that aims at implementing an efficient quantum computer needs to fulfil the following set of 5 + 2 criteria [*DiVincenzo (2000)*]:

1. A scalable physical system with well characterized qubits.
2. The ability to initialize the state of the qubits to a simple fiducial state.
3. A qubit-specific measurement capability.
4. A universal set of quantum gates.
5. Long relevant decoherence times, much longer than the gate operation time.
6. The ability to interconvert stationary and flying qubits.
7. The ability to faithfully transmit flying qubits between specified locations.

The first three criteria define necessary properties of a qubit. Criterion 4 demands for a universal set of quantum gates that has functional completeness, similar to the NAND-gate for a classical computer. In quantum computing a universal set of quantum gates is typically a combination of single qubit gates and an entangling (2-qubit) gate [*Childs and Chuang (2000); Foletti et al. (2009); Mikelsons et al. (2014); Zu et al. (2014); De Michielis et al. (2014); Kapit (2015); Zhou et al. (2015); Hua et al. (2015)*]. Criterion 5 is possibly the most problematic demand on a physical system. It requires the control and isolation from the environment of the physical system on the single quantum information level for long (coherence) times. 'Long' means here, enough time to counteract or remove different sources of errors. For successful quantum computation, the chance of errors to occur needs to be less than 2%, depending on the number of involved qubits, operations and error-correction protocol [*Terhal (2015)*]. A large part of research in quantum computation is spent to develop and implement codes that correct for these errors [*Ahn et al. (2002); Aoki et al. (2009); Fedorov et al. (2012); Reed et al.*

(2012); Waldherr et al. (2013); Weinstein (2013); Ristè et al. (2015); Corcoles et al. (2015)].

For all physical implementations that fulfil the first 5 criteria, the important figure of merit is the number of gate operations and their fidelity within the systems coherence time. The two systems that currently perform best in terms of fulfilling the first 5 DiVicenco-criteria are ions in free-space, coupled by ion-lattice phonons, and circuit QED architectures with artificial atoms coupled by photons in microwave cavities. Ion experiments have typically very low errors and interface to optical photons, but are hard to scale up in number of qubits and have two-qubit gate times approaching MHz-regimes. In contrast, circuit QED architectures are, in principle, scalable in number of qubits and fast ($g \approx 200$ MHz). However, the gate errors were too large to scale the systems coherently until very recently, when first systems approached fault-tolerant error thresholds [Corcoles et al. (2015); Barends et al. (2014)] for an error-correction protocol called the 'surface code' [Bravyi and Kitaev (1998); Dennis et al. (2002); DiVincenzo (2009); Fowler et al. (2009, 2012); Fowler and Martinis (2014)].

The last two DiVicenco criteria demand for the transport of quantum information/entanglement between two separate nodes of a *quantum network* [Cirac et al. (1997); Kimble (2008); Northup and Blatt (2014)]. A quantum network consists of several, interconnected nodes that generate, store and process quantum information. A quantum computer could consist of one such node or even contain several nodes. The different nodes consist of stationary qubits [(artificial) atoms] and flying qubits (typically photons), which interconnect separate nodes by coherently transporting or teleporting quantum information to establish remote entanglement. Cavity QED systems which enhance the coupling between a single (artificial) atom and a single photon are ideal interfaces between flying and stationary qubits.

Suitable systems for quantum networks have large single-qubit-single-photon coupling rates that allow for large information transfer bandwidth and an interface to photons in the optical or telecom frequency range, which can be transported over long distances in optical fibers. Examples of successful interfaced nodes in simple quantum networks are atoms in Fabry-Perot cavities (Tab. 1.1) [Pellizzari (1997); Wilk et al. (2007); Kuhn et al. (2002); Ritter et al. (2012); Shomroni et al. (2014)], quantum dots or nitrogen-vacancy centers (in cavities), see Tab. 1.1 [Gao et al. (2015); Altaisky et al. (2015); Childress and Hanson (2013); Pfaff et al. (2014)], Rydberg atoms [Li and Lesanovsky (2013); Li et al. (2013)], and photons [Yin et al. (2012); Crisafulli et al. (2013)]. A public system has been tested, where users could send quantum encrypted information via photons in a quantum network consisting of 3 nodes separated by distances up to 18 km [Stucki et al. (2011)]. In future, the increase in bandwidth and the potentially large coupling ratios η make atoms

close to photonic waveguides [labels (8 – 9) in Fig. 1.3] one of the promising tools to be used as nodes in quantum networks. They could, for example, route single photons [Tiecke *et al.* (2014)] between nodes consisting of atom or solid-state based quantum memories [Wang *et al.* (2012); Harty *et al.* (2014); Bussi eres *et al.* (2014); Michelberger *et al.* (2014); Jobez *et al.* (2014, 2015)].

Although being a very promising candidate for quantum computers, circuit QED architectures have a clear disadvantage to establish a large-scale quantum network with respect to systems that interface qubits and optical photons in fibers: the large loss rate of microwave photons when the waveguides are not cryogenically cooled. A possibility to overcome this challenge is the coherent transfer of quantum information from the microwave domain to the optical domain in a *hybrid system* [Yin *et al.* (2015)], which could not be shown on a single photon level yet. Optical to microwave conversion has been investigated experimentally and theoretically via opto-mechanical transducers [Barzanjeh *et al.* (2011, 2012); Clader (2014); Andrews *et al.* (2014)] or ensembles of spins or rare-earth-doped crystals [Zhu *et al.* (2011); Staudt *et al.* (2012); O'Brien *et al.* (2014)]. Another approach could be the coupling of circuit QED systems to atoms which have transitions in both frequency domains and are therefore suitable for optical to microwave conversion, e.g. atoms in ground states with hyperfine transitions or Rydberg atoms [Petrosyan and Fleischhauer (2008); Hafezi *et al.* (2012); Maxwell *et al.* (2014)].

1.3 A potential quantum network of hybrid systems

The idea of interfacing systems of different physical character into hybrid systems to combine "the best of both worlds" has emerged within the last years (after ~ 2010) from the circuit QED community. Hybrid systems are expected to tackle systemic disadvantages in circuit QED systems such as the poor lifetime or the need for cryogenically cooling the communication channels used for large-scale quantum information transport. The review of Kurizki *et al.* (2015) summarizes the latest advances and possibilities for hybridization of different systems in the field of quantum information (Fig. 1.5). We will not discuss all (dis)advantages of these systems, but focus on a hypothetical setup of a future quantum network of hybrid systems.

Assume we have a working quantum computer at node 1 (Fig. 1.6), implemented in a large circuit QED system, that contains superconducting qubits coupled to chip-based resonators in the microwave regime (processor). Such a system has the advantage of large coupling rates $g \approx 2\pi \times 100$ MHz (compare Table 1.1 and Fig. 1.5). For long algorithms it is necessary to store quantum information for a

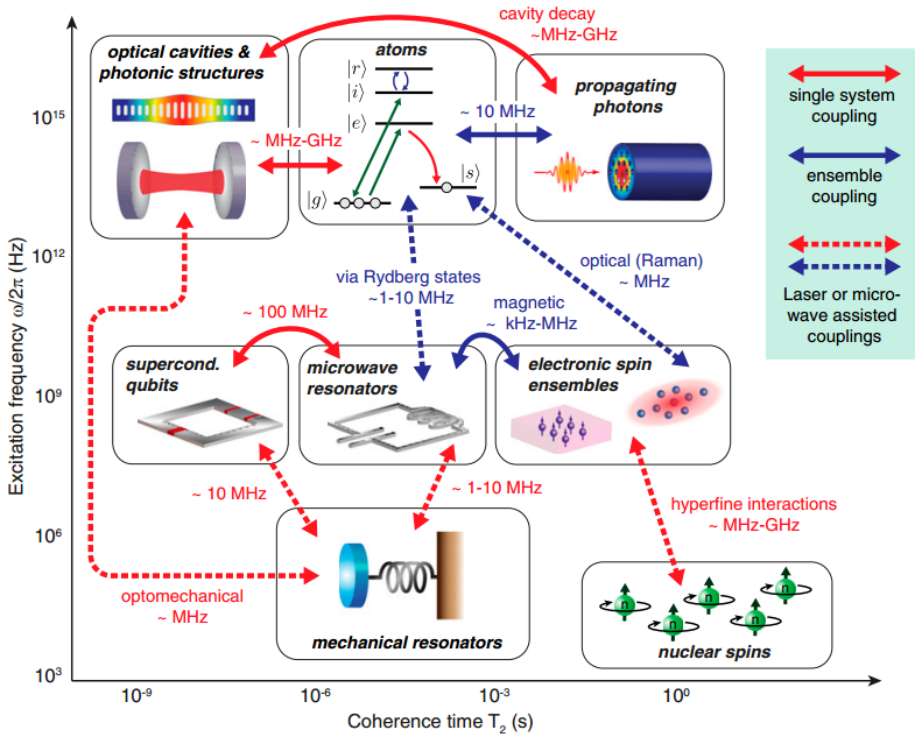


Figure 1.5: Overview of different physical systems, that reached strong coupling between photons, phonons and (artificial) atoms. Figure taken from *Kurizki et al. (2015)*.

time, that exceeds typical lifetimes of superconducting qubits. In the hypothetical setup presented here, this is done in a system of nuclear spins [quantum random access memory (qRAM)] with lifetimes on the order of seconds being interfaced to a superconducting resonator via electronic spins in a hybrid system. The write or read rate is ~ 1 MHz, compare Fig. 1.5, which is larger than typical decay rates of superconducting qubits.

To communicate or transfer the result of an algorithm to another quantum computer (node 2 in Fig. 1.6), e.g. via a quantum teleportation protocol [*Vaidman (1994)*; *Steffen et al. (2013)*; *Pirandola et al. (2015)*], one could use a Rydberg atom positioned close to a resonator of the superconducting circuit (processor) and a photonic waveguide. In this 'quantum router', the quantum information in the superconducting circuit is first coherently transferred to a Rydberg state ($|r\rangle$) with a transfer bandwidth that can exceed ~ 100 MHz (compare Tab. 1.1, Fig. 1.5 or Sec. 1.4). This system, highlighted by the red, dashed line, is studied in this thesis and is discussed in detail in Sec. 1.4.

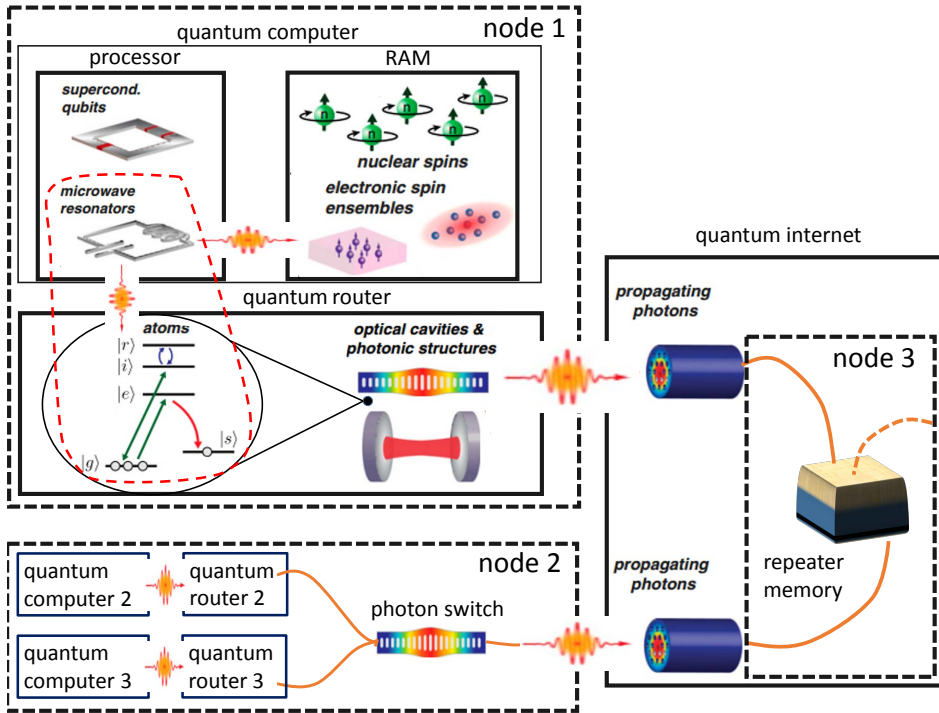


Figure 1.6: A possible quantum network consisting of 3 nodes (black, dashed lines) to entangle quantum computer 1 with quantum computer 2 or 3, see text for details. Thick lines indicate physical quantum systems that are interfaced via photonic interactions in hybrid interfaces. Orange lines indicate optical fibers and the orange dashed line a fiber connection to other nodes. The red, dashed line highlights the hybrid system of (Rydberg) atoms coupled to superconducting resonators. Small pictures taken from *Kurizki et al. (2015)*.

Subsequently, the population in the Rydberg state is imprinted onto the polarization states of an optical photon in the photonic structure, either directly [*Barrett et al. (2004)*; *Heidemann et al. (2007)*; *Kübler et al. (2010)*; *Wu et al. (2013)*] or in a stimulated Raman adiabatic passage similar to [*Ritter et al. (2012)*; *Reiserer et al. (2014)*] (green arrows), and emitted into a fiber at rates of $\kappa \gtrsim 100$ MHz (Tab. 1.1).

Optical photons are the best system for long distance quantum communication [*Ma et al. (2012)*; *Fuwa et al. (2014)*; *Graham et al. (2015)*; *Wang et al. (2015)*]. Entanglement between different nodes via optical photons may be achieved by quantum memories and quantum repeaters in solid-state [*Jin et al. (2015)*; *Jobez et al. (2015)*] or free-space atomic systems [*Julsgaard et al. (2004)*; *Yuan et al. (2008)*; *Brion et al. (2012)*; *Sangouard et al. (2011)*]. A photon switch, as realized

by [Tiecke *et al.* (2014)] could help to distribute photons (entanglement) within a node.

1.4 A hybrid system of Rydberg atoms coupled to a circuit QED architecture and an optical cavity

Hybrid systems aiming at coupling the internal state of atoms to solid-state devices have attracted significant interest in recent years. Realizations of such systems include neutral atoms close to atom chips [Fortagh *et al.* (1998); Vuletić *et al.* (1998); Drndić *et al.* (1998); Fortágh *et al.* (2002); Krüger *et al.* (2007); Böhi *et al.* (2010); Reichel and Vuletić (2011); Böhi and Treutlein (2012)], tapered fibers [Vetsch *et al.* (2010); Goban *et al.* (2012)] or photonic waveguides [Tiecke *et al.* (2014); Goban *et al.* (2014)], Rydberg atoms close to mesoscopic devices [Sørensen *et al.* (2004); Petrosyan and Fleischhauer (2008); Petrosyan *et al.* (2009)] and ions near surfaces [Seidelin *et al.* (2006); Ospelkaus *et al.* (2008)]. As also discussed in Sec. 1.3, an important motivation for the development of such a hybrid systems is the combination of the long coherence times characteristic of atomic ensembles and the strong interactions and fast processing capabilities of solid-state devices as a route towards scalable quantum computing [Petrosyan and Fleischhauer (2008); Petrosyan *et al.* (2009); Kurizki *et al.* (2015)]. Atomic and solid-state systems can be coupled by electromagnetic fields which have to be controlled with high accuracy.

In this section we consider a hybrid system combining a circuit QED system in which an artificial atom (named qubit hereafter) is coupled to a microwave resonator by a coupling rate g_t , and a cavity QED system, in which an atom is coupled to an optical cavity by g_p over a transition between, e.g., a Rydberg state and the ground state (Fig. 1.7). The hybrid link is achieved by coupling the systems via the coupling rate g_{Ry} between the chip-based microwave resonator and a Rydberg-Rydberg transition. In the course of this thesis a setup is described that is able to coherently manipulate Rydberg atoms close to patterned surfaces at cryogenic temperatures. Achieving coherent manipulation of Rydberg atoms with microwave radiation from chip-based microwave waveguides (also called 'transmission lines' hereafter) is a key step for realizing a working hybrid link.

In extension of Eq. (1.3) and in absence of decoherence (i.e. $\kappa = \Gamma_0 = 0$ for both cavities, the qubit and the atom), the Hamiltonian of the combined system can be written in the rotating wave approximation as:

$$\begin{aligned}
 H_{hy} &= H_q + H_{Ry} + H_o + H_\mu + H_p + H_{int,q\mu} + H_{int,Ry\mu} + H_{int,op} \\
 &= \frac{1}{2}\hbar\omega_q\sigma_q^z + \frac{1}{2}\hbar\omega_{Ry}\sigma_{Ry}^z + \frac{1}{2}\hbar\omega_o\sigma_o^z + \hbar\omega_\mu\left(a_\mu^\dagger a_\mu + \frac{1}{2}\right) + \hbar\omega_p\left(a_p^\dagger a_p + \frac{1}{2}\right) \\
 &\quad + \hbar g_t\left(a_\mu^\dagger\sigma_q^- + a_\mu\sigma_q^+\right) + \hbar g_{Ry}\left(a_\mu^\dagger\sigma_{Ry}^- + a_\mu\sigma_{Ry}^+\right) + \hbar g_p\left(a_p^\dagger\sigma_o^- + a_p\sigma_o^+\right),
 \end{aligned} \tag{1.38}$$

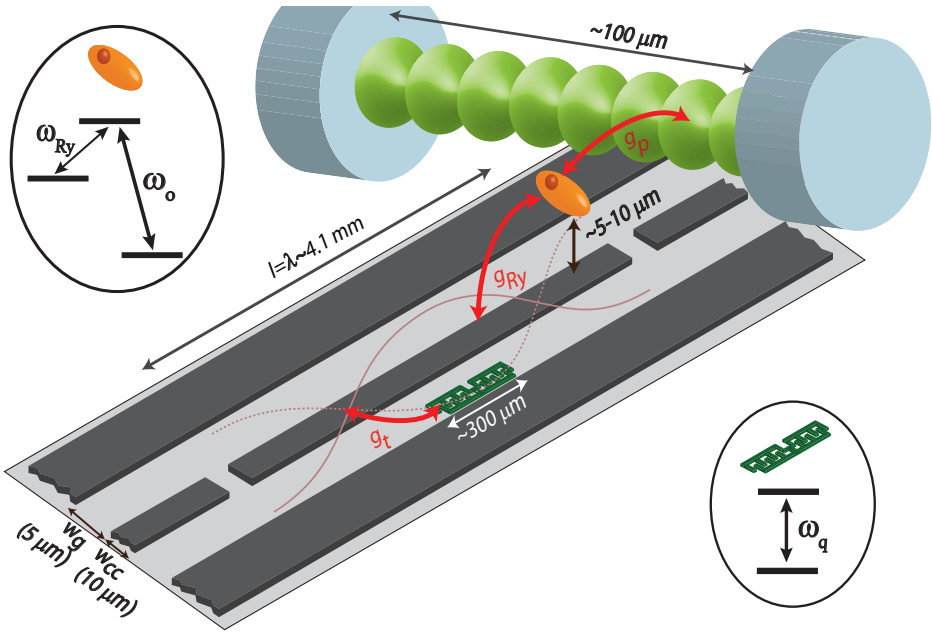


Figure 1.7: Sketch of a Rydberg-atom-circuit-QED hybrid setup. Microwave photons (brown) in a superconducting coplanar waveguide resonator (dark grey) on a dielectric substrate (grey) are coupled by g_{Ry} to a Rydberg atom (orange) and by g_t to a superconducting qubit (green). The Rydberg atom is coupled by g_p to an optical mode (light green) in an optical cavity (blue). Insets indicate the level schemes of the Rydberg atom and the superconducting qubit.

where the index 'q' denotes the qubit parameters, 'Ry' denotes the (microwave) Rydberg transition, 'o' denotes the optical Rydberg-groundstate transition, 'p' denotes the optical mode, and μ denotes the microwave mode. Note, that we simplified the three-level atomic Hamiltonian to be treated as two independent transitions (o,Ry), which is valid as long as the two transitions are not driven at the same time, i.e. at least one of both the microwave or the optical cavity is far off-resonant from the corresponding atomic transition at any time. As mentioned before, this system is the ideal candidate to coherently convert microwave photons to optical photons for quantum communication [Kurizki *et al.* (2015)] or to serve as a long-lived quantum memory for a circuit QED based quantum computer [Petrosyan and Fleischhauer (2008); Petrosyan *et al.* (2009); Kurizki *et al.* (2015)], as Tab. 1.1 indicates.

To elucidate the operation as a quantum memory, we consider the optical cavity (ω_p) to be detuned far enough from ω_o that it can be neglected. In this case

Eq. (1.38) simplifies to

$$H_{\text{hy}}^{\text{qm}} = \frac{1}{2} \hbar \omega_{\text{q}} \sigma_{\text{q}}^z + \frac{1}{2} \hbar \omega_{\text{Ry}} \sigma_{\text{Ry}}^z + \hbar \omega_{\mu} \left(a_{\mu}^{\dagger} a_{\mu} + \frac{1}{2} \right) + \hbar g_{\text{t}} \left(a_{\mu}^{\dagger} \sigma_{\text{q}}^{-} + a_{\mu} \sigma_{\text{q}}^{+} \right) + \hbar g_{\text{Ry}} \left(a_{\mu}^{\dagger} \sigma_{\text{Ry}}^{-} + a_{\mu} \sigma_{\text{Ry}}^{+} \right). \quad (1.39)$$

In the dispersive regime ($|\Delta_{\text{q},\mu}| = |\omega_{\text{q}} - \omega_{\mu}| \gg g_{\text{t}}$ and $|\Delta_{\text{Ry},\mu}| = |\omega_{\text{Ry}} - \omega_{\mu}| \gg g_{\text{Ry}}$) and by adiabatic elimination of the resonant Jaynes-Cummings interaction [Blais *et al.* (2007)], we get

$$\frac{H_{\text{hy}}^{\text{qm,d}}}{\hbar} = \frac{1}{2} \bar{\omega}_{\text{q}} \sigma_{\text{q}}^z + \frac{1}{2} \bar{\omega}_{\text{Ry}} \sigma_{\text{Ry}}^z + \omega_{\mu} \left(a_{\mu}^{\dagger} a_{\mu} + \frac{1}{2} \right) + \underbrace{\frac{g_{\text{t}} g_{\text{Ry}}}{2} \left(\frac{1}{\Delta_{\text{q},\mu}} + \frac{1}{\Delta_{\text{Ry},\mu}} \right)}_{g_{\text{eff}}} \left(\sigma_{\text{q}}^{-} \sigma_{\text{Ry}}^{+} + \sigma_{\text{q}}^{+} \sigma_{\text{Ry}}^{-} \right). \quad (1.40)$$

Here, $\bar{\omega}_{\text{q}} = \omega_{\text{q}} + g_{\text{t}}^2 / \Delta_{\text{q},\mu}$ and $\bar{\omega}_{\text{Ry}} = \omega_{\text{Ry}} + g_{\text{Ry}}^2 / \Delta_{\text{Ry},\mu}$ are the dispersively shifted transition frequencies of the qubit and the Rydberg atom, respectively. In Eq. (1.40) the last part indicates the swap interaction with rate g_{eff} between the two physically different systems that is representative for a hybrid system [Kurizki *et al.* (2015)]. Therefore, the processor (circuit QED system) can in principle perform quantum algorithms for extended periods of time when using the hybrid system as a quantum memory with the following protocol:

1. Initially $|\Delta_{\text{Ry},\mu}| \gg g_{\text{Ry}}$ and the Rydberg atom is prepared in the lower-energetic Rydberg state. In this case, the circuit QED processor can be operated in without interacting with the Rydberg atom.
2. After a certain processing time shorter than the coherence time of the circuit QED system (e.g. $\sim 10 \mu\text{s}$), $|\Delta_{\text{Ry},\mu}|$ and $|\Delta_{\text{q},\mu}|$ are changed to fulfill $|\Delta_{\text{Ry},\mu} - \Delta_{\text{q},\mu}| \approx 0$, while both, the Rydberg atom and the qubit are still dispersively coupled to the resonator [Eq. (1.40)]. Because the frequency-tuning of the Rydberg atom is typically done with electric fields via the Stark effect and the tuning of the qubit is achieved by (magnetic) flux pulses, the two systems can be tuned independently of each other (except via the interaction through the resonator g_{eff}).
3. After a time $t_{\text{swap}} = \pi / (2g_{\text{eff}})$ any superposition state of the qubit is mapped (iSWAP-gate) to a superposition of the Rydberg states (upon a phase ι for the excited state).

4. $|\Delta_{\text{Ry},\mu}| \gg g_{\text{Ry}}$. Because of the long lifetime of the Rydberg state, there is now enough time to prepare the circuit QED system in a defined state (initialization).
5. Repeating, in this sequence, steps 2 and 3 maps the state of the Rydberg atom back to the qubit with an opposite phase for the excited qubit state.
6. With a single qubit gate that compensates for this phaseshift and setting $|\Delta_{\text{Ry},\mu}| \gg g_{\text{Ry}}$, the circuit-QED-processor can continue to process the algorithm with the same state as initially in step 1.

As discussed below, g_{eff} can be on the order of tens of MHz (i.e. the swap time t_{swap} can be short) because the coupling rate g_{Ry} between a single or an ensemble of Rydberg atoms and a microwave photon can be increased to similar values as the typical coupling rate g_{t} between a microwave photon and a superconducting qubit, as we will see below. That the hybrid link between Rydberg atom and microwave resonator presents interesting perspectives in order to be operated as a quantum memory can also be seen from the large coupling ratio η which is maximized by maximizing g_{Ry} and minimizing radiative decay Γ_0 at the same time.

A possible conversion from a microwave excitation to an optical photon can be achieved by modification of the procedure discussed above. After step 4, the optical transition from the higher Rydberg state can be tuned in resonance with an optical cavity, while the microwave cavity is far-off resonant from the Rydberg transition, i.e. $\omega_0 = \omega_{\text{p}}$, and $|\Delta_{\text{Ry},\mu}| \gg g_{\text{Ry}}$. In this case, the hamiltonian of the system reduces to a Jaynes-Cummings type, i.e.

$$\begin{aligned}
 H'_{\text{hy}} &= H_0 + H_{\text{p}} + H_{\text{int,op}} \\
 &= \frac{1}{2} \hbar \omega_0 \sigma_0^z + \hbar \omega_{\text{p}} \left(a_{\text{p}}^\dagger a_{\text{p}} + \frac{1}{2} \right) + \hbar g_{\text{p}} \left(a_{\text{p}}^\dagger \sigma_0^- + a_{\text{p}} \sigma_0^+ \right).
 \end{aligned} \tag{1.41}$$

After a time $t'_{\text{swap}} = \pi/2g_{\text{p}}$, the state of the Rydberg atom is coherently mapped onto a Fock-state of the cavity via half a vacuum-Rabi oscillation. Alternatively, starting from a Fock-state of the microwave cavity, one can envision to transfer this state to a Fock state of the optical cavity by sequentially tuning ω_{Ryd} in resonance with ω_{μ} and then ω_0 in resonance with ω_{p} . This would take a time of $t''_{\text{swap}} = \pi/2(1/g_{\text{Ry}} + 1/g_{\text{p}})$ (neglecting the time to tune the atom and the qubit in resonance). Alternatively one can, in analogy to the protocol for a quantum memory, adiabatically eliminate the excited Rydberg state in the three-level hamiltonian of the atom by setting the frequencies of the resonators according to $|\Delta_{\text{Ry},\mu} - (\omega_0 - \omega_{\text{p}})| \approx 0$. In this case, we obtain the same interaction Hamiltonian between the two resonators as in Eq. (1.40), but g_{t} is replaced by g_{p} .

In the following we elucidate the different coupling strengths g , and we calculate the coupling ratio η for the hybrid link. Although the idea for the combination of the two physical implementation was presented more than 7 years ago [*Petrosyan et al. (2009)*], a working setup has not been shown until the present day [*Kurizki et al. (2015)*] and little calculations for g_{Ry} have been published. Therefore, the calculations of η and g_{Ry} here involve simulations of the coupling strength for the coplanar waveguide design we use, and for the design which is typically used in circuit QED experiments. The calculations of the other coupling strengths, g_{t} and g_{o} are in general well-known and not discussed. Specifically, I first present that the expression of g_{t} as used in circuit QED systems can be mapped onto the coupling rate (g_{Ry} or g_{p}) of a dipole coupled to a cavity mode. Second, this is combined with experimental constraints to derive an equation with which g_{Ry} can be estimated, and numerical calculations for g_{Ry} as a function of the atoms separation from the transmission line are presented.

A coplanar waveguide (CPW) consists of a center conductor (typical value for circuit QED experiments: $w_{\text{cc}} = 10 \mu\text{m}$) separated by isolating gaps ($w_{\text{g}} = 5 \mu\text{m}$) from two ground planes (compare dark grey structure in Fig. 1.7 without the intersections in the center conductor). This structure is patterned into a thin, superconducting film on a lossless substrate (gray) with dielectric constant ϵ_{r} , see Section 6 for more details. A voltage pulse with center frequency in the GHz-regime applied to the center conductor creates a propagating microwave electric field in the gaps. For voltages low enough (depending on the pulse length τ , see Section 1.1.1) individual photons are propagating along the central conductor. The geometry of the transmission line determines the propagation of the photon. Its propagation can be described by a medium with effective dielectric constant ϵ_{eff} and impedance Z_0 , which are given by the dielectric constant of the substrate and geometric parameters of the structure [*Simons (2001)*].

At an impedance mismatch, e.g. a gap in the center conductor, part of the voltage pulse is reflected (analogous to a mirror for optical photons). The larger the impedance mismatch, i.e. the width of the gap, the larger the fraction of reflected voltage (reflectivity of the mirror). Two impedance mismatches separated by a distance l form a microwave resonator (cavity) with an rms voltage given by [*Blais et al. (2004)*]

$$U_{\text{rms}} = \sqrt{\frac{\hbar\omega_{\text{m}}}{C_{\text{CPW}}l}} \quad (1.42)$$

with ω_{m} the resonance frequency of the resonator mode, C_{CPW} the capacity per unit length between center conductor and ground planes, and l the length of the resonator. U_{rms} is the voltage drop to which the superconducting qubit (green)

capacitively couples with a coupling strength

$$g_t = \frac{\beta e}{\hbar} U_{\text{rms}} \quad (1.43)$$

with β the ratio of the qubit-internal gate capacity and the sum of gate capacity and qubit-internal Josephson capacity [Blais *et al.* (2004)].

For simplicity, we can assume that all the electric field is contained in the plate capacitor defined by the center conductor and the ground planes we obtain the same expression for the field strength as for an atom coupling to a single photon in free space [Eq. (1.6)], i.e.

$$F_m \approx \frac{U_{\text{rms}}}{w_g} = \sqrt{\frac{\hbar\omega_m}{C_{\text{CPW}}l w_g^2}} = \sqrt{\frac{\hbar\omega_m}{\epsilon_0 t l w_g}} = \sqrt{\frac{\hbar\omega_m}{\epsilon_0 V_{\text{cap}}}} = \sqrt{\frac{\hbar\omega_m}{2\epsilon_0 V_m^{\text{CPW}}}} \quad (1.44)$$

with $C_{\text{CPW}}l = \epsilon_0 t l / w_g$ the capacity of the plate capacitor, t the thickness of the metallization and $V_{\text{cap}} = t l w_g$ the volume of the capacitor. In the last step we used that $V_{\text{cap}} = 2V_m^{\text{CPW}}$, the mode volume of the CPW, because of the standing wave of the electric field in the resonator.

For a specific estimation of F_m , the assumption that the electric field is constrained to a thickness t on the order of the film thickness is too simple. In fact, the electric field of the CPW has an evanescent mode structure from the chip surface that decays approximately as r^{-2} for distances $r > w_g$ from the center conductor, and with a decay to about half its value at $r \approx w_g$ [Fig. 1.8(a)]. The field is calculated using a finite element simulation for a transmission line (black) with the width of the center conductor w_{cc} twice the width of the gap⁵ w_g . The mode volume can therefore be approximated by replacing t with w_g , i.e.

$$V_m^{\text{CPW}} \approx \frac{l w_g^2}{2} \quad (1.45)$$

which is $\sim 2 \times 10^{-8} \lambda^3$, about 10^{-7} times smaller than comparable mode volumes of ideal Fabry-Perot cavities. This leads to the significant increase in coupling rate g of circuit QED systems with respect to 3-dimensional cavities (Sec. 1.2 and Sec. 1.1.4).

A Rydberg atom with dipole strength d (Fig. 1.7, orange) located above the gap couples to this evanescent field mode with coupling strength g_{Ry} given by Eq. (1.4). Because of the spatial inhomogeneity of the mode, the coupling strength depends

⁵This approximates an impedance of $\sim 50\Omega$ of the CPW better than 5% for typical CPW used in circuit QED experiments, i.e. superconductor on silicon/sapphire substrate with substrate-height ≥ 0.5 mm and $w_{\text{cc}} \leq 0.5$ mm.

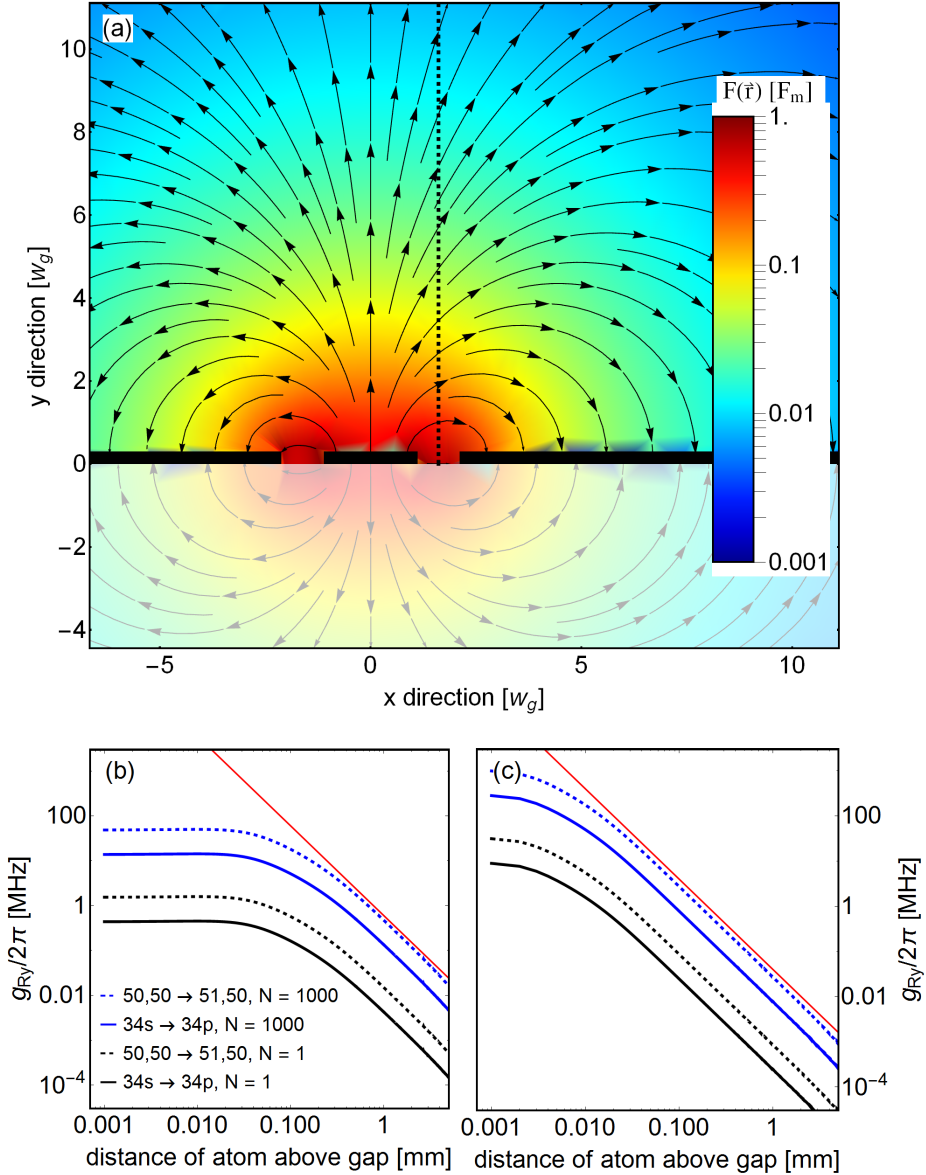


Figure 1.8: (a) Simulated electric field above coplanar transmission line when a potential difference is applied between the center conductor (middle black rectangle) and the two ground planes (left and right rectangles) with the shaded area denoting the substrate. Black arrows indicate electric field lines. The electric field strength is normalized to the electric field in the gap F_m [Eq. (1.44)] and indicated by the colors in a logarithmic scale. The dashed line indicates the horizontal axis of the panels (b) and (c). (b,c) Simulated coupling strength g_{Ry} of a single (black lines) or an ensemble of 1000 Rydberg atoms (blue lines) at varying heights above a transmission line with (b) $w_{cc} = 180 \mu\text{m}$ and $w_g = 80 \mu\text{m}$, and (c) $w_{cc} = 10 \mu\text{m}$ and $w_g = 4.5 \mu\text{m}$. The dashed of the curves differ between transitions between states labeled as (n, l) for low- l states (solid) and circular states as indicated in panel (b). Red lines approximate scalings of the field proportional to r^{-2} , see text.

on the distance of the atom to the transmission line. Fig. 1.8(b) and (c) indicate g_{Ry} for one (black lines) or an ensemble of 1000 helium atoms (blue lines) located at different positions above the gaps of two different resonator designs. The typical geometry used in this thesis has a gap width of $w_g = 80 \mu\text{m}$ and a width of the center conductor of $w_{\text{cc}} = 180 \mu\text{m}$ [panel (b)]. Panel (c) was calculated for a gap width of $w_g = 4.5 \mu\text{m}$ and a width of the center conductor of $w_{\text{cc}} = 10 \mu\text{m}$, a typical geometry used in circuit QED systems. The solid lines indicate the low- l transition used in this thesis and the dashed lines indicate the circular state of [Raimond *et al.* (2001)]. For the circular states we take into account that the dipole strength d is reduced by a factor $\sqrt{2}$ from the full dipole strength $d = n^2 e a_0$ with which they couple to circularly polarized light only (Sec. 1.1.4).

For the case that the atoms are positioned closer than w_g to the surface of the chip, we calculate the (maximal) coupling ratio η for these transitions. For the low- l states, Γ_{ac} is dominated by the transition to the ground state and hence given by its free-space value $\Gamma_0^{n,l}$. Specifically, for the $34\text{p} \rightarrow 34\text{s}$ transition Γ_{ac} is given by the short-lived 34p state, $\Gamma_{\text{ac}} = \Gamma_0^{34\text{p}} = \tau_{34\text{p}}^{-1} \approx 1/1.4 \mu\text{s} = 0.71 \text{ MHz}$ [Thiele *et al.* (2014)]. Therefore, $\eta \approx 0.3$ and $\eta \approx 3.7$, for the two CPW geometries, which are indicated by the labels (10) and (11) in Fig. 1.3, respectively. For a circular state the decay rate will be modified from the free-space decay rate by the presence of the chip surface [Arnoldus and George (1988)]. For an atom at a distance $z \ll \lambda$ from a perfectly conducting surface, the spontaneous decay of a dipole perpendicular to the surface is increased by a factor of 2, whereas the spontaneous decay of a dipole parallel to the surface is completely suppressed. Averaged over all possible directions of the dipole, the decay can be approximated by the free-space decay rate $\Gamma_0^{50\text{circ}} = \tau_{50\text{circ}}^{-1} \approx 1/30 \text{ ms} = 33 \text{ Hz}$. Therefore, $\eta \approx 6.6 \times 10^4$ and $\eta \approx 8.3 \times 10^5$, for the two CPW geometries [labels (12) and (13) in Fig. 1.3], respectively. These immense coupling ratios are possible, because the system maximizes the single-atom-single-photon coupling rate g (Eq. 1.6) and η (Eq. 1.5) for a fixed transition frequency. This, because it combines the large dipole moments and the long lifetimes of Rydberg states with the small mode volumes of coplanar transmission lines.

Up to now, such a system could not be implemented [Kurizki *et al.* (2015)], mainly because of difficulties that involve unwanted stray electric fields emanating from the surface. The large polarizability of the Rydberg atoms couples to these stray fields which leads to decoherence. The sources of these stray fields are manifold, with possible sources being patches of adsorbates or potential differences (charges) on the surface. The main part of this thesis focuses on the identification of these sources of stray fields. Furthermore, the setup of an experiment is discussed which combines fundamental Rydberg and solid-state physics to develop new techniques for characterization of static and time-varying electric fields close

to surfaces at cryogenic temperatures exploiting quantum-coherent effects. These techniques can also be used in other atomic systems to characterize and/or circumvent any decohering effects that involve (unwanted) stray electric fields. As will be shown, this allows to coherently manipulate Rydberg atoms in the vicinity of (patterned) surfaces.

1.5 Thesis contributions and outline

The main contributions of this thesis are:

1. We have set up a *novel atomic beam experiment* that allows to study coherent behaviour of Rydberg atoms at distances below 1 mm to *cryogenic surfaces*. Especially, it allows to minimize *impeding effects from surface adsorbates* during cooldown and operation.
2. We developed a *novel method to image DC and microwave electric field distributions* on a few-mm-scale and with a resolution of a $\lesssim 100 \mu\text{m}$. Calculations indicate, that the realistic resolution achievable could be as small as $4 \mu\text{m}$. We used this method to determine the vector field of unknown stray electric fields.
3. We have examined the *coherent population transfer* of Rydberg atoms close to plain and patterned chip surfaces at cryogenic temperatures. Specifically, the chip surface did not need to be specifically modified in order to observe long coherence times.
4. In a second setup, we developed and characterized a new atomic source optimized for Rydberg-surface experiments using metastable $(1s)^1(2s)^1\ ^3S_1$ helium. The supersonic atom beam is slow ($\sim 1000 \text{ m/s}$), transversally cooled close to the doppler cooling limit and works with repetition rates up to 1 kHz. The position and the angle of the atomic beam with respect to the surface can be precisely controlled and continuous-wave excitation to Rydberg states is possible.

In this document, we will focus on items 1, 2 and 3. Item 4 is shortly discussed in the outlook and explained in detail in numbers 10 – 16 of the following in the course of this thesis supervised theses (not in chronological order):

1. Barmettler R, 'Characterization of Overcoupled NbTiN Microwave Resonators up to 40 GHz' (master thesis) [*Barmettler (2012)*].

2. Waldburger D, 'Temperature Dependent Measurements of Undercoupled Coplanar NbTiN-Resonators' (semester thesis) [*Waldburger (2012)*].
3. Koenz M, 'Design, Build-up and Control of Electronic Equipment for the Hybrid Rydberg Experiment' (bachelor thesis) [*Könz (2014)*].
4. Seeman M, 'Evaluation Program for Rydberg Atom Spectra' (exchange student).
5. Ebert R, 'Temperature Feedback on Residual Gases using a Residual Gas Analyzer' (exchange student).
6. Mergenthaler M, 'Temperature Stabilization of a Cu-Sample-Holder on the 4 K-Stage of a Pulse Tube Cooler' (semester thesis, supervision taken over from Reim K.) [*Mergenthaler (2012)*].
7. Luethi F, 'Active Magnetic Field Compensation' (semester thesis) [*Lüthi (2013)*].
8. Goblot V, 'Realization of an Active Magnetic Field Compensation' (semester thesis) [*Goblot (2014)*].
9. Koepsell J, 'Up conversion board for amplitude and phase controlled microwave pulses on the 1.5-26.5 GHz scale' (semester thesis) [*Köpsell (2014)*].
10. Hambitzer A, 'Design of a Metastable Helium Source' (project) [*Hambitzer (2012)*].
11. Gerster L, 'Metastable Helium Source' (semester thesis) [*Gerster (2014)*].
12. Friese D, 'Deflection of Metastable Helium via Laser Light' (semester thesis) [*Friese (2014)*].
13. Melchner von Dydiowa M, 'Collimation of Metastable 2^3S_1 Helium Atoms Using Laser Cooling Techniques' (semester thesis) [*Melchner von Dydiowa (2014)*].
14. Friese D, 'Towards Continuous Wave Rydberg Excitation for 2^3S_1 Helium' (master thesis) [*Friese (2015)*].
15. Phillip M-T, 'Characterization of a cold metastable helium source with a dielectric barrier discharge'. [*Phillip (2015)*]
16. Moeller L, 'Isolating a cold beam of metastable triplet helium states'. [*Möller (2015)*]

This thesis is based on the following articles, with large fractions being modified and/or directly used from items (1), (2) and (3):

1. Hogan S. D., Agner J.-A., Merkt F., *Thiele T.*, Filipp S. and Wallraff A. ‘Driving Rydberg-Rydberg Transitions from a Coplanar Microwave Waveguide’. *Phys. Rev. Lett* **108**, 063004 (2012) [*Hogan et al. (2012a)*]
2. *Thiele T.*, Filipp S., Agner J.-A., Schmutz H., Deiglmayr J., Stammeier M., Allmendinger P., Merkt F. and Wallraff A. ‘Manipulating Rydberg atoms close to surfaces at cryogenic temperatures’. *Phys. Rev. A* **90**, 013414 (2014) [*Thiele et al. (2014)*]
3. *Thiele T.*, Deiglmayr J., Goblot V., Luethi F., Agner J.-A., Schmutz H., Merkt F. and Wallraff A. ‘Imaging electric field close to cryogenic surfaces using Rydberg atoms’. *Phys.Rev. A* **92**, 063425 (2015) [*Thiele et al. (2015)*]
4. Koepsell J. and *Thiele T.* ‘Determination of angle distribution between static and microwave electric field in a beam of Rydberg atoms’. in preparation [*Köpsell and Thiele (2016)*]

The thesis is organized in the following way. In part 1, we first give an overview of the experimental setup built in this thesis (Ch. 2). In this chapter, we introduce the main notation and nomenclature used throughout the rest of the thesis. Then we present characterization measurements of the atom source (Sec. 3.1), and the two main data acquisition techniques (Sec. 4.3.1 and 4.2), with which we characterized small and large electric fields efficiently. The most important characterizations of equipment (e.g. the Rydberg laser) that are needed to reliably reproduce and interpret data obtained when using the measurement techniques are presented in Sec. 4.3. The experimental setup is described in Ch. 5, where specific focus was put on the design of the cryostat (Sec. 5.2) and an active magnetic shielding of the experiment (Sec. 5.3). Part 1 is then concluded with a discussion and characterization of the different samples used in the experiments (Ch. 6).

In part 2, we present a set of three measurements where Rydberg atoms were coherently manipulated above surfaces at cryogenic temperatures. In a first experiment, Rydberg atoms were driven from microwave radiation from a printed-circuit-board based transmission line (Ch. 7). A set of challenges were identified that limited coherence of the Rydberg atom cloud. The limitations could be weakened in measurements above plain surfaces (Ch. 8) studying the different decoherence effects of static and microwave electric fields. We conclude the part with a chapter on coherent measurements above a patterned surface that allowed to measure static and microwave electric field distributions above the surface (Ch. 9).

In part 3, we first summarize the achievements of this thesis and present possible future applications of the different techniques developed. Then, in Ch. 10, we sketch the results of specific calculations for the next experiment in which we aim to dispersively couple a single or an ensemble of Rydberg atoms to a transmission line resonator. We also present the results of a second setup, that was built in parallel to the experiments presented in this thesis, but which is not described in the main part. This setup contributes a new source of helium Rydberg atoms that is expected to contribute to successfully carrying out the follow-up experiments.

PART I

**EXPERIMENTAL SETUP AND
MEASUREMENT PROCEDURE**

EXPERIMENTAL SETUP AND MEASUREMENT PROCEDURES

In this chapter an overview over the most important technical aspects of the experimental setup and the two main measurement procedures is given. The details are discussed in chapters 3, 2, 5, 6 and 6 of this part. This section is intended to serve as a introductory guide into the technical aspects of the experiment, sufficient to understand the experiments presented in part 2 of the thesis.

The experiment aims at coherently manipulating Rydberg atoms that pass within a distance of less than 2 mm over a patterned thin-film, normal metal or superconducting surface at cryogenic temperatures. The Rydberg atoms are created in a supersonic beam of metastable singlet $(1s)^1(2s)^1^1S_0$ helium atoms by a one-photon laser excitation (Secs. 3.2,4.3.1). Supersonic beams of Rydberg atoms offer several advantages to study interactions of strongly polarizable atoms with surfaces and for experiments aiming at coherent manipulation of (Rydberg) atoms and molecules near the surface of chips, a few of which are discussed in part 2. Most importantly, Rydberg atoms in supersonic beams can be deflected, decelerated and even trapped using printed circuits while still maintaining the flexibility of choosing the atomic species and a well-defined initial state [*Hogan et al. (2012b)*; *Allmendinger et al. (2013)*; *Lancuba and Hogan (2013)*]. In the case discussed here, the use of metastable states of (the inert and noble gas) helium allows us to mitigate the influence of stray fields caused by the adsorption of atoms onto the surface. Furthermore, we operate a specifically designed cryogenic experimental setup (Sec. 5.1) that minimizes adsorption of residual gases in the vacuum

chamber onto the chip surface (Sec. 5.2.4). Both approaches allow for coherent manipulation of the Rydberg atoms close to a patterned chip surface, see part 2.

The experimental setup consists of three differentially pumped vacuum chambers (Fig. 2.1): The source chamber in which the atomic beam is generated; the cryogenic chamber holding a pulse-tube cooler; and the ultra-high-vacuum-compatible experimental chamber. The pulse-tube cooler operating in a two-stage configuration provides the cooling power to reach cryogenic temperatures. The first stage is held at ~ 30 K and separates the cryogenic chamber from the experimental chamber, the inner part of which is held at 3 K by the second cooling stage.

In the source chamber, the supersonic beam of metastable $(1s)^1(2s)^11S_0$ He atoms, labeled as He* hereafter, is generated by combining a pulsed supersonic expansion (repetition rate: $R_{\text{Exp}} = 25$ Hz, pulse duration: $190 \mu\text{s}$), with a pulsed electric discharge seeded by electrons emitted from a hot tungsten filament, as described in *Halfmann et al. (2000)*. The source (black rectangle) used in this setup is discussed in detail in Sec. 3.1. In summary, each gas pulse contains about 10^{13} ground-state helium atoms (light blue) and propagates in positive z direction. The steady-state pressure in the source chamber rises from $p_c \approx 2 \times 10^{-7}$ mbar to about 10^{-5} mbar on average upon operation of the pulsed valve. To ignite the discharge, a 280-V potential-difference pulse is applied for $20 \mu\text{s}$ to a discharge electrode located 4 mm behind the nozzle orifice. This results in the production of about 9×10^7 He* atoms (green) assuming a conversion efficiency of $\sim 5 \times 10^{-5}$ and taking into account the different durations of the discharge and metastable-atom pulses.

The volumes of the source chamber and the experimental chamber are connected through a 1-mm-diameter hole of a skimmer (brown, dashed line) which allows for efficient differential pumping and selects the transversally coldest part (0.1% of all atoms) of the supersonic beam. The background pressure in the experimental chamber rises from $p_e \approx 10^{-8}$ mbar at room temperature and less than 5×10^{-9} mbar at 3 K (i.e. below the lower limit of the pressure gauge) to 5×10^{-8} mbar on average when the valve is pulsed. After the skimmer, the typical velocity of the He* beam is $v_0 \approx 1800$ m/s (Sec. 3.2). The supersonic beam is further collimated by another 1.5-mm-diameter skimmer and by two parallel razor blades (brown) in the y direction (Fig. 2.1) which are adjusted to the desired He* beam width and position in the experimental region (Sec. 4.3.3.3).

The experimental region consists of 4 distinct zones separated by 7 electrodes labeled $E1 - E4$ and $IL1 - IL3$, hereafter. In the first zone, roughly 1000 He* atoms are photoexcited to Rydberg states (blue) with a tunable, pulsed uv laser (Secs. 4.1, 4.3.1) applied between the two parallel disc-shaped metallic electrodes $E1$ and $E2$ (gray, labeled $E1$ and $E2$) separated by 10 mm (Sec. 5.2). Applying electric potentials, the electrodes can be used to generate a homogeneous electric field at

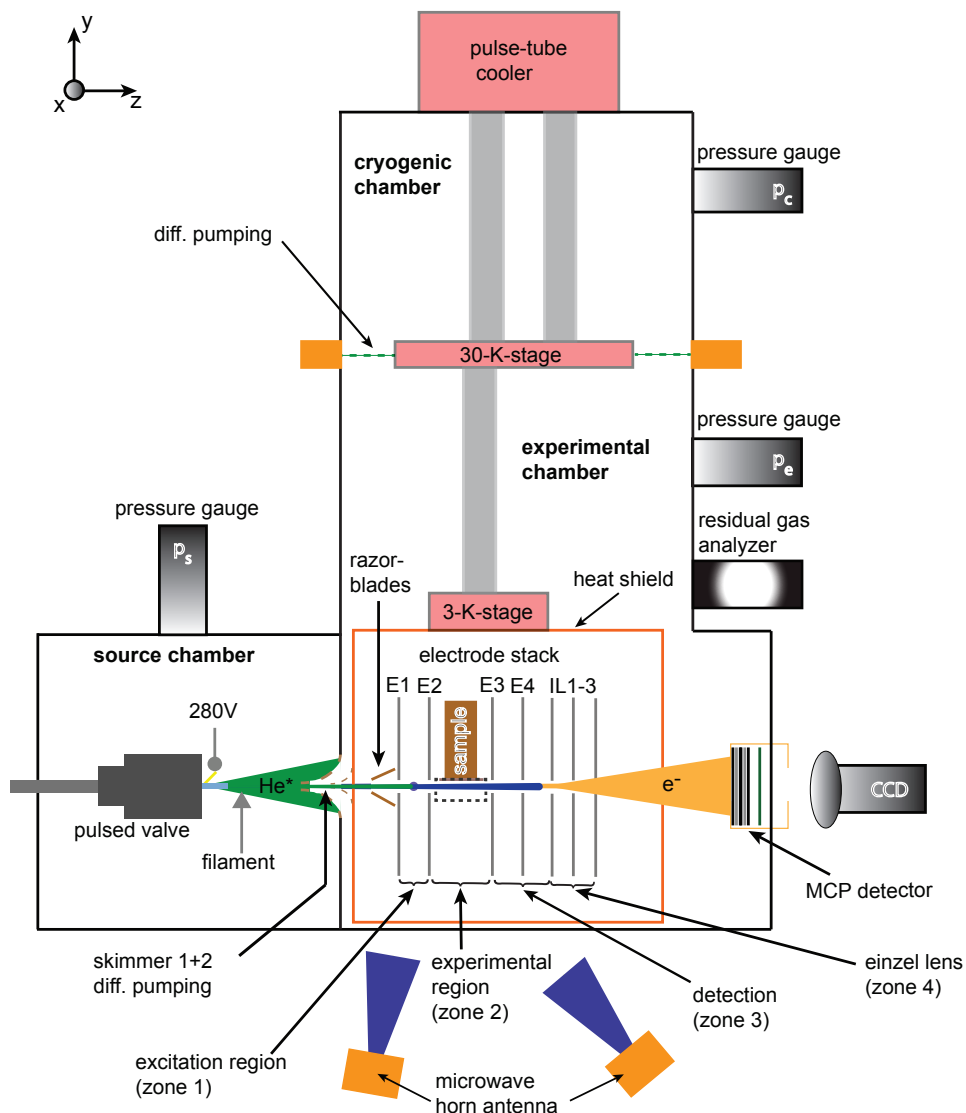


Figure 2.1: Sketch of the experimental setup, see text for details.

the position at which the atomic beam and the uv laser beam cross at right angles. Alternatively, $E2$ can be used to compensate stray fields in the experimental zone (zone 2) located between electrodes $E2$ and $E3$, separated by 15 mm. In this second zone, the Rydberg-atom beam may propagate at a well-defined distance from the surface of a sample (Ch. 6) at cryogenic temperatures. The third zone consists of another three, disc-shaped electrodes $E3$, $E4$ and $IL1$, separated each by 10 mm, which are identical to those located in the first zone. The Rydberg atoms are field ionized in this zone by applying a pulsed potential difference of 0.6 kV between either electrodes 3 and 4, or 4 and $IL1$ (Sec. 4.3.2). The resulting electrons (yellow region in Fig. 2.1) are accelerated toward a microchannel plate (MCP) detector in a chevron configuration connected to an oscilloscope for measuring time traces (Section 4.3.3.2) and a phosphor screen for imaging atom distributions (Section 4.3.3.3). To this end an einzel lens operated at field strengths up to ~ 1.5 kV/cm expands the electron cloud by a factor of 7 in x and y directions in a magnetic-field-free flight region of ~ 150 mm length.

Pulsed microwave radiation emitted from a horn antenna or sent along a chip-based transmission line is used to induce Rydberg-Rydberg transitions in zones 1, 2, and 3 by choosing an appropriate delay between the laser excitation pulse and the microwave pulse 4.2. The microwave radiation from the horn antenna penetrates into the setup through the apertures of 5 mm diameter in the heat shields, which also provide access for the Rydberg-excitation laser.

2.1 Internal state manipulations of atomic beam

In the following we provide an overview of the different sequential manipulations of the internal state of a pulse of helium atoms as it travels through the experimental apparatus. Because of the constant velocity of the atomic beam, manipulations of the atoms at specific locations in the experiment correspond to specific times in the duration of an experimental cycle. These times can be varied during an experiment. The notation that is introduced below is used throughout the remainder of the thesis.

The sequence of manipulations of the atom beam during an experiment is sketched in Fig. 2.2. The upper panel indicates a simplified level scheme of $(1s)^2\ ^1S_0$ helium with the excitation steps indicated by colored arrows. The lower panel sketches the temporal shape of the atomic beam as it would be measured by a detector at the location within the setup at which the manipulation takes place. The indicated times and positions are given with respect to the Rydberg laser excitation in zone 1 and can be converted into each other by multiplication of the beam velocity of $v_0 \approx 1800$ m/s.

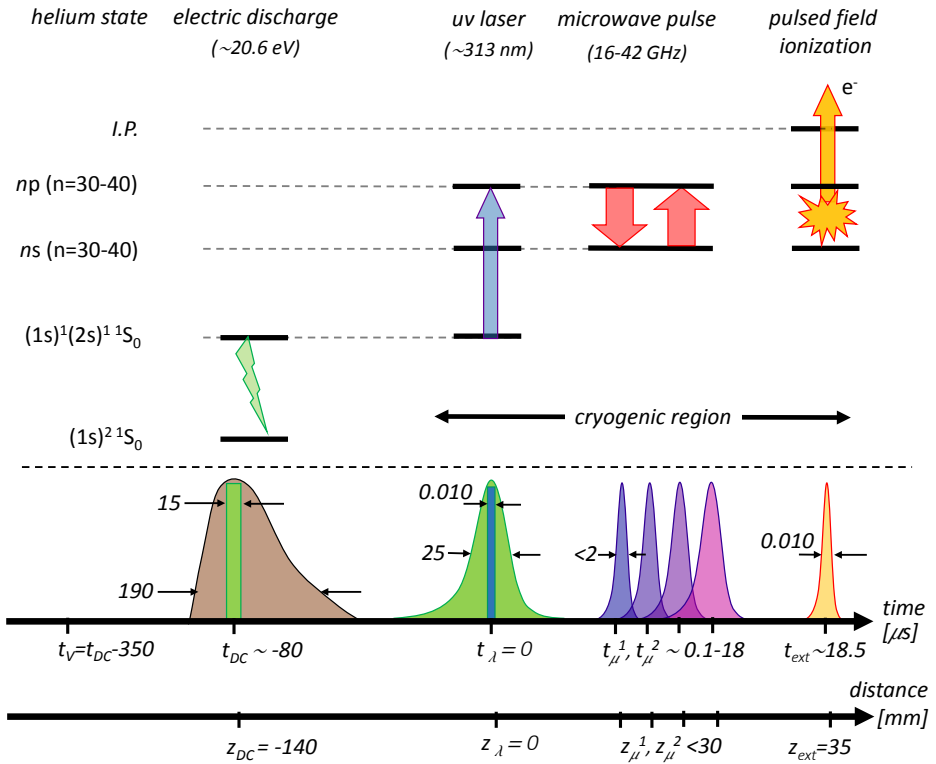


Figure 2.2: Sketch of the measurement procedure as a function of time, for details see text. (upper panel): simplified level scheme of $(1s)^2 \ ^1S_0$ helium. The discharge is indicated in green, the Rydberg excitation laser in blue, microwave pulses in red, and ionization of Rydberg atoms is indicated in yellow. (lower panel): schematic visualization of the corresponding particle pulses at each step. The pulses are colored according to the product of the corresponding excitation in (a), i.e. neutral atoms are indicated in brown, metastable atoms in green, Rydberg atoms in blue, and in red after microwave transfer, and Rydberg electrons are indicated in yellow.

An experiment begins with a control pulse at time t_V sent to a valve driver that triggers the opening of a valve $\sim 350 \mu\text{s}$ later. The valve is located 140 mm before the middle of zone 1 and opens for a duration of $\Delta t_V = 190 \mu\text{s}$. The supersonic pulse of ground state helium atoms $[(1s)^2 \ ^1S_0]$, brown is dense and cold in the beginning and warmer at the end (Sec. 3.2). In a region of 4 mm immediately after the nozzle the atoms are excited to the metastable $(1s)^1(2s)^1 \ ^1S_0$ singlet state (Sec. 3.1) by $\sim 20.6 \text{ eV}$ from a breakdown discharge [*Halfmann et al. (2000)*]. The discharge pulse is applied at $t_{DC} \approx -80 \mu\text{s}$ and lasts for durations varying between $\Delta t_{DC} \approx 10 - 30 \mu\text{s}$ ($15 \mu\text{s}$ in Fig. 2.2). For $\Delta t_{DC} \ll \Delta t_V$ only a few ground state atoms are excited to metastable states. The strongly varying electric field from the discharge and the seeded electrons heat and accelerate the atom beam from $\leq 1 \text{ K}$ to typical temperatures varying between 5 to $\lesssim 30 \text{ K}$ from the beginning to the end of the pulse, respectively (Sec. 3.2). Typically, t_{DC} is set such that helium atoms in the coldest and densest part in the beginning of the beam are excited.

After a flight distance of 140 mm the metastable atom beam has broadened to about $25 \mu\text{s}$ because of its temperature. A laser pulse ($\Delta t_\lambda = 10 \text{ ns}$) at $t_\lambda = 0$ of wavelength $\lambda \approx 313 \text{ nm}$ excites the atoms in zone 1 to the $(1s)^1(np)^1 \ ^1S_0$ Rydberg state. The fraction of atoms that are excited to Rydberg states depends on the laser wavelength, power and spot size in the atomic beam (Secs. 3.2,4.1,4.3.1). The typical Rydberg states used within this thesis lie in the range between $n = 30$ and 40.

Microwave pulses transfer population from the $(1s)^1(np)^1 \ ^1S_0$ state to the $(1s)^1(ns)^1 \ ^1S_0$ state when the atoms are in zone 2 or in the first part of zone 3, i.e. at times $t_\mu^{(i)} < 18 \mu\text{s}$, i being the i^{th} microwave pulse. For simplicity, we will denote the two states as np and ns hereafter. We typically use two microwave pulses with pulse lengths varying between $\Delta t_\mu^{(i)} = 20 \text{ ns}$ to $\Delta t_\mu^{(i)} = 2 \mu\text{s}$.

Finally, the atoms are pulsed-field ionized at the end of zone 3 at $t_{\text{ext}} \approx 18.5 \mu\text{s}$ with a short detection field pulse which also extracts the electrons toward the detector. Because of the instantaneous ionization of the Rydberg atoms and the small mass of the electrons, the width of the detected electron pulse in time is only a few tens of nanoseconds (Sec. 4.3.2). The smallest measured widths at the MCP at distances $z_{\text{MCP}} = 190 \text{ mm}$ are limited to $\sim 10 \text{ ns}$ by the time resolution of the MCP detector assembly.

DYNAMICS OF ATOMIC BEAM

In the experiments presented in this thesis, we choose to operate the atomic beam in the pulsed, supersonic regime because of the achievable large densities and low temperatures, for typical numbers see Morse (1996) and Halfmann et al. (2000). Being independent of the particle species, supersonic expansion for the creation of atomic or molecular beams is a well established technique since decades, with applications in many experiments [Van De Meerakker et al. (2008)]. Recent experiments with molecular beams can be divided into two main categories, molecular spectroscopy [Snels et al. (2011)] and manipulation of external degrees of atoms and molecules [Vliegen and Merkt (2005, 2006); Vliegen et al. (2007); Hogan and Merkt (2008); Hogan et al. (2008, 2009, 2011, 2012b); Seiler et al. (2011); Allmendinger et al. (2013, 2014)]. Generation of supersonic beams of metastable, noble gases (e.g. helium) has been intensively studied [Morse (1996)] and optimal sources for continuous [Rothe et al. (1965); Theuws et al. (1982); Woestenenk et al. (2001); Browaeys (2002); Kotyrba (2010)] and pulsed operation [Even et al. (2000); Even (2014); Luria et al. (2009, 2011)] have been developed.

In this chapter, setup and characterization measurements of the atomic beam source and the dynamics of the supersonic atom beam source used in this experiment are presented. The characterization measurements of the beam are independent of the source and can also be applied to other types of setups. Specifically, we discuss the generation of metastable atoms from the source, supersonic expansion and a second expansion at the first skimmer (Sec. 3.1). This includes determination of different beam dispersion angles at different locations in the ex-

perimental apparatus. Additionally, we determine temperature, length and velocity of the atomic beam in propagation direction at different locations in the setup (Sec. 3.2).

3.1 A source of a supersonic metastable helium beam

The commercially available, pulsed valve we use (*PARKER: general valve; 009 – 0442 – 900*) consists of a 316-stainless-steel body and a frontplate. The frontplate contains an orifice of diameter $d_0 = 0.51$ mm. A PTFE poppet, embedded into a magnetic cylinder, is pressed with a spring into the orifice which it closes with a leak rate of less than 10^{-7} mbar l/s. The pre-load of the spring can be adjusted by changing the distance of the frontplate with respect to the body. Under operation, the magnetic cylinder including the poppet is retracted, which causes gas at a reservoir-pressure of p_0 in the valve-body (reservoir) to exit the orifice in positive z direction. Before mounting, the pre-load is pre-adjusted by varying the distance between valve-body and frontplate while the valve is being operated and placed in ethanol. We found, that the optimal pre-load in terms of atomic beam parameters (e.g. temperature or density) is achieved when a bubble forms at a rate of ~ 1 Hz in front of the orifice¹, and when the pitch of the sound from the running valve increases. Additional fine-tuning of the pre-load when the valve is mounted in the experiment allows to operate the valve in two "modes". The strong- and weak-pre-load modes produce atom beams with different dynamics (Sec. 3.2).

The magnetic cylinder is retracted using the magnetic field produced by a current-pulse in a coil in the body of the valve. The current has a triangular profile as a function of time (measured by a pick-up coil inserted into the body) and is produced by an externally-triggered valve driver (*PARKER: Iota one pulse driver system*). The delay time of ~ 350 μ s between the valve trigger at t_V and the opening of the nozzle ($\sim t_{DC}$) is attributed to the drivers generation of the current-pulse, and an additional time (~ 30 μ s) that depends on the pre-load of the spring. The dissipated power causes the temperature of the valve to increase to more than $\sim 90^\circ$ C without external cooling. The water-cooling we use to cool the (aluminium) valve holder reduces the temperature increase to $\sim 20^\circ$ C at the frontplate. The use of a valve holder allows the transversal displacement of the entire valve (x - y plane) over a total range of ~ 10 mm.

The valve is operated with helium gas at a reservoir backing-pressure between 6 and 8 bar. The helium gas in the reservoir can be described as an ideal gas with its

¹This value depends on different valve parameters, in the presented case here, a repetition rate of the experiment $R_{\text{Exp}} = 25$ Hz, $d_0 = 0.51$ mm and $p_0 \sim 6$ bar.

velocity distribution given by the Maxwell-Boltzmann distribution. Upon the sudden opening of the valve, the gas undergoes an isenthalpic, supersonic expansion into the vacuum of the source chamber ($p_s = 2 \times 10^{-7}$ mbar), because the mean free path of the helium in the valve being $\lambda_0 \approx 33 \mu\text{m} \ll d_0$ [Morse (1996); Kotyrba (2010)], see Fig. 3.1(a). λ_0 was estimated from Eq. (1.4) and Tab. (1.3) in Kotyrba (2010). During the supersonic expansion, the gas can be described by a hydrodynamic model in which the stagnation enthalpy in the reservoir is converted into forward velocity, and the atoms thermalize because of many collisions in the orifice.

Every pulse contains about $N_0 \approx 1.8 \pm 1 \times 10^{13}$ ground state helium atoms as calculated using the ideal gas law with a temperature of $T = 290$ K and the additional pressure by which the source chamber increases at every opening of the valve²

$$p_p = \epsilon_p^{\text{He}} p_s^{\text{op}} \left(\frac{1}{1 - \exp\left(-\frac{R_{\text{TP}}}{V_s} R_{\text{Exp}}^{-1}\right)} - 1 \right)^{-1} \approx 7.8 \times 10^{-3} \text{ mbar}. \quad (3.1)$$

Here, $R_{\text{Exp}} = 25$ Hz is the repetition rate of the experiment, $V_s \approx 7.8$ l the volume of the source chamber, $R_{\text{TP}} = 655$ l/s the pump speed of the turbopump, and $p_s^{\text{op}} \approx 5 \times 10^{-5}$ mbar the measured pressure in the source chamber when the valve is operated. The factor $\epsilon_p^{\text{He}} = 6$ takes into account the sensitivity of the cold-cathode pressure gauge of helium (Sec. 5.1).

In the 'zone of silence' (area enclosed by brown contour in Fig. 3.1), the mean velocity of the gas pulse is supersonic and given for a circular nozzle at $T_0 = 300$ K by [Morse (1996); Kotyrba (2010)]:

$$v_0 = \sqrt{\frac{2C_p T_0}{\mu}} = \sqrt{\frac{5RT_0}{\bar{m}_{\text{He}}}} \approx 1756 \text{ m/s} = M c_{\text{He}}. \quad (3.2)$$

In the second step we have used that for helium the characteristic heat capacity $C_p = \frac{5}{2}R$, R being the ideal gas constant. For a pure helium beam, the effective molecular mass μ is given by the molar mass of helium \bar{m}_{He} . In the zone of silence, the velocity of $v_0 = 1756$ m/s is larger (mach number $M \gg 1$) than the speed of sound in the medium

$$c_{\text{He}} = \sqrt{\frac{\gamma k_B T}{m_{\text{He}}}} = 58.8 \sqrt{T}, \quad (3.3)$$

which depends on the current temperature T of the beam and the heat capacity ratio $\gamma = 5/3$ of helium³. Because of the supersonic velocity, the dynamics of the

²This pressure can be calculated by taking the limit of $n \rightarrow \infty$ of the pressure before the n^{th} gas pulse, given by $P_{n-1} = (P_{n-2} + p_p) \exp\left(-\frac{R_{\text{TP}}}{V_s} R_{\text{Exp}}^{-1}\right)$.

³For a beam at $T = 290$ K, $c_{\text{He}} = 1002$ m/s, and for $T = 10$ K, $c_{\text{He}} = 186$ m/s.

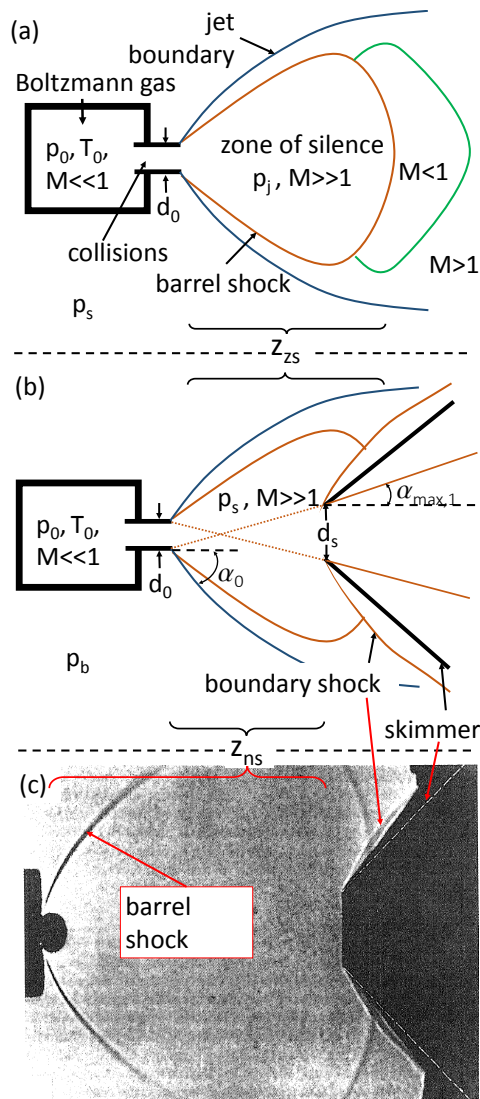


Figure 3.1: (a) Supersonic beam expansion from a (pulsed) valve without skimmer. A Boltzmann gas (Mach number $M \ll 1$) in a reservoir (p_0 , T_0) expands through a nozzle with diameter d_0 into vacuum at pressure p_s and accelerates. The supersonic region (brown, $M \gg 1$) extends to z_{zs} and is separated by the barrel shock from the subsonic regions (green) and the turbulent regime (blue). (b) A skimmer (black, thick cone) with diameter d_s is placed at distance $z_{ns} < z_{zs}$ in the supersonic region. The collision of the atoms with the surface leads to a boundary shockwave. For low enough beam densities p_s , the initial beam divergence α_0 reduces in the skimmer to $\alpha_{max,1}$, given by the maximal solid angle between the nozzle and the skimmer (brown, dashed line). (c) Shadow photograph of a supersonic beam expansion into a skimmer at high pressures. Sketches in (a,b) adapted from *Kotyrba (2010)*, photograph taken from *Bier and Hagen (1966)*.

atoms is given purely by the expansion process and is independent from external influences, e.g. pressure in the source chamber p_s . The zone of silence is therefore separated by a barrel shock from a turbulent, less dense region in which $M \gtrsim 1$, that extends to the jet boundary (area enclosed by blue contour). The distance to which the zone of silence extends depends on the pressure in the valve p_0 , the current pressure in the source chamber p_s and the orifice diameter d_0 , i.e. [Morse (1996); Kotyrba (2010)]

$$z_{zs} = 0.67 d_0 \sqrt{\frac{p_0}{p_s}} = \begin{cases} 58 \text{ m} & p_s = 2 \times 10^{-7} \text{ mbar} \\ 1.5 \text{ m} & c_p^{\text{He}} p_s^{\text{op}} = 3 \times 10^{-4} \text{ mbar} \end{cases} \quad (3.4)$$

The two cases indicate the best and worst case for our experiment. The first case is calculated for the average pressure when the valve is not in operation, i.e. the minimum pressure reached in the first chamber. The second case is calculated for the average pressure when the valve is operated.

Atoms are best extracted from within the zone of silence, which is achieved using a skimmer [Fig. 3.1(b,c)]. Skimmers are pinholes on a trumpet-formed cone, which minimizes turbulences in the beam, i.e. minimizing the area between the boundary shock and the skimmer. In our case, we position a skimmer (*BEAM DYNAMICS*) with diameter $d_s = 1$ mm at a distance of $z_{ns} = 60$ mm from the nozzle, such that $z_{ns} \ll z_{zs}$ for the worst case pressure.

The atomic beam is transversally colder after the skimmer because only atoms with a small transverse velocity pass the pinhole. The maximal dispersion angle $\alpha_{\max,1}$ of the atom beam after the skimmer is given by geometrical considerations, i.e.

$$\alpha_{\max,1} = \frac{d_s + d_0}{2 z_{ns}} = 12 \text{ mrad} = 0.7^\circ. \quad (3.5)$$

Hence, larger z_{ns} lead to colder transversal temperatures, but also to less atoms in the beam. We measured $\alpha_{\max,1}$ in a separate experiment (Ch. 10.1) where the atoms can expand freely after the skimmer [Gerster (2014)]. Specifically, we positioned an imaging microchannel plate detector (Sec. 4.3.3.1) at a distance of 900 mm after the skimmer and detected atoms in metastable states of the beam. Given α_{\max} and the geometry of the setup, we expect a maximal beam diameter of 22 mm at the position of the MCP. However, an atom beam diameter of $\gtrsim 65(5)$ mm is observed, which is larger than the MCP's diameter of 43 mm [Gerster (2014)]. This corresponds to a measured dispersion angle of $\alpha'_{\max,1} \approx 0.035 \text{ mrad} = 2^\circ \geq \alpha_{\max,1}$. We attribute this to a second expansion of the beam at the skimmer. A second expansion is likely to occur because of the small mean free path ($\ll 0.3$ mm) of the atoms in the dense beam, and the large pressure difference from within the beam to the pressure in the experimental chamber, i.e. $\sim 1.1 \times 10^{-5}$ mbar, calculated using Eq. (2.7) in Morse (1996) with respect to $p_e \approx 10^{-8}$ mbar, respectively.

We strengthen the assumption of a second expansion in a second measurement where the source is moved in the (x, y) plane over a distance of ± 5 mm (Fig. 3.2). Given the geometry of the experiment and $\alpha_{\max,1}$, a displacement of 5 mm of the source with respect to the skimmer would result in the atom beam missing the detector, as indicated by the pink, dashed lines in the right, lower sketch of panel (a). However, we observe the same spatial atom distributions on the MCP for all displacements, i.e. the expansion of the beam after the skimmer does not depend on the position of the valve, as indicated by the green areas, and as expected from a second expansion.

This setup is well suited to determine the angle α_0 [Fig. 3.1(b)] with which the atomic beam exits the valve. The integrated metastable atom intensity over the MCP is proportional to the intensity of atoms at the skimmer. Hence, monitoring the integrated MCP signal while varying the valve's position over the maximal possible range in the (x, y) samples the atom number distribution of the beam at the position of the skimmer [Fig. 3.2(a)]. The maximal signal is observed when the valve is on-axis with the skimmer. The normalized atom number distribution is fitted by a Gaussian function in 2 dimensions. The black data in Fig. 3.2(b) presents a cut along the dashed, green line in Fig. 3.2(a), the red line indicates the Gaussian fit. The fitted full width at half maximum of the atom number distribution at the skimmer is 30.6 mm, corresponding to an angle of $\alpha_0 = 0.25$ rad $\approx 15^\circ$. The measured full angle $2 \times \alpha_0 = 0.5$ rad $\approx 29^\circ$ corresponds well to the simulated beam spread in *Luria et al. (2011)*.

To obtain a transversally cold beam in the experimental chamber, a second skimmer with diameter 1.5 mm is placed at a distance of 62 mm after the first skimmer (Fig. 3.3). At the position of the second skimmer, the pressure in the gas beam is small enough that the atoms do not undergo a third expansion. Consequently, the maximal dispersion angle of the atoms is given by the geometry of the two skimmers, i.e.

$$\alpha_{\max,2} = \frac{d_1 + d_2}{2 \times 62} = 20.1 \text{ mrad} = 1.15^\circ, \quad (3.6)$$

which corresponds to the maximal observed angle in the experiment [*Gerster (2014)*].

We produce metastable singlet ($1s^1 2s^1 \ ^1S_0$) and triplet ($1s^1 2s^1 \ ^3S_1$) states of helium with an electric discharge [*Halfmann et al. (2000)*]. A stainless-steel tip (red, dashed line) is positioned at a distance of 4 mm from the nozzle and pulsed with $V_{\text{DC}} \approx 280$ V with respect to the potential of the valve (photograph and sketch in Fig. 3.3). A filament (*PLANO: A054C*) is positioned at a distance of ~ 10 mm (red contour) from the frontplate and points toward the nozzle. The applied AC-current of $I_{\text{DC}} \approx 5.25$ A at 50 Hz emits electrons which start an electric discharge between the tip and the nozzle, ionizing the helium atoms. The fraction of atoms

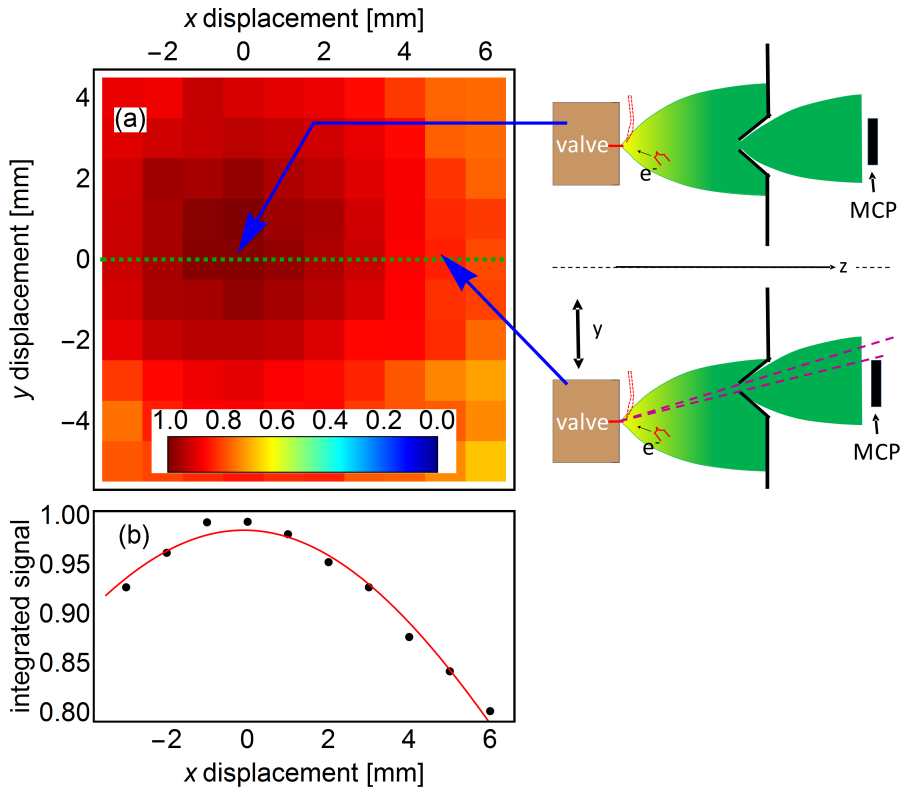


Figure 3.2: Measurement of the angle of expansion of the gas jet from the nozzle [Gerster (2014)]. (a) (left panel): Normalized integrated metastable signal at MCP for different valve positions relative to the symmetry axis of the first skimmer. (right panels): sketch of metastable beam (green) expansion for different valve positions (brown) with respect to the skimmer (black). Because of the second expansion at the skimmer, the expansion of the atom beam points in z direction only and is not given by the relative position of skimmer and valve (pink, dashed lines). (b) Cut along the green dashed line (black data points) in (a) and Gaussian fit (red line).

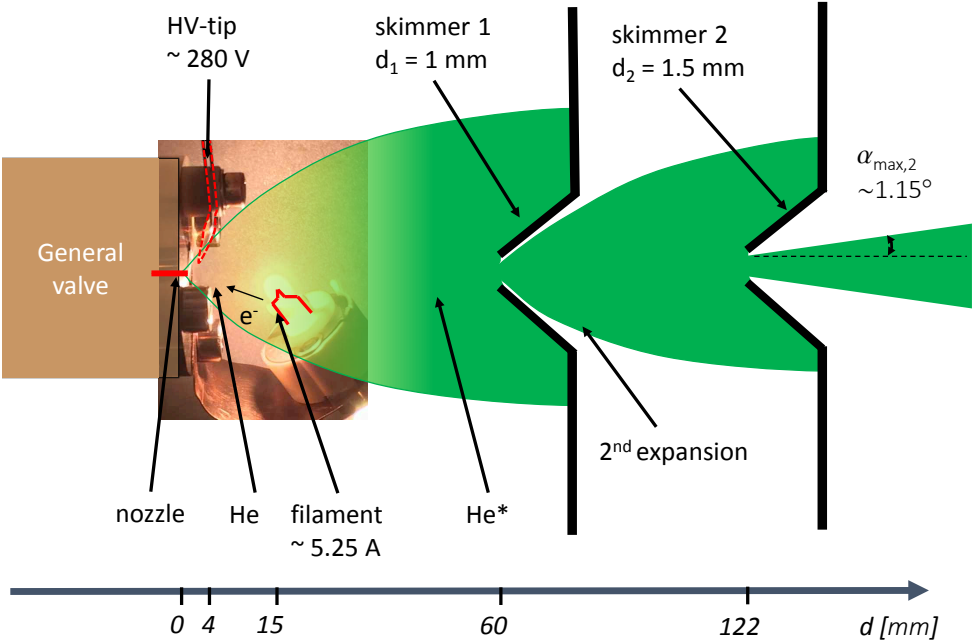


Figure 3.3: Photograph and sketch of the metastable helium source with electric discharge, second expansion and 2 skimmers, details see text.

that recombines to the metastable singlet or triplet He^* state, F_{He^*} , is according to *Halfmann et al. (2000)* $\sim 10^{-7}$ and 10^{-6} , respectively. However, in this experiment we estimate a larger fraction of $F_{\text{He}^*} \approx 1.0(3) \times 10^{-4}$ for singlet state atoms. This value is comparable to efficiencies of experiments with electron impact [*Brutschy and Haberland (1977)*] and might be because of the larger current $I_{\text{DC}} \approx 5.25$ A and higher backing pressures ($p_s \approx 6$ bar) in the valve we use compared to the values of *Halfmann et al. (2000)* ($I_{\text{DC}} \approx 3$ A, $p_s \approx 0.8 - 2$ bar).

F_{He^*} is estimated from the propagation of the reduction of the number of atoms from the valve to the first and from the first skimmer to the second skimmer (Tab. 3.1). For simplicity, we assume that $\Delta t_{\text{DC}} = \infty$, i.e. that all ground state atoms are excited to metastable states with probability F_{He^*} . The geometric reduction factor from the valve to skimmer 1 is given by the fraction of the skimmer area with respect to the beam diameter of the metastable beam at the skimmer 1, i.e.

$$\text{Red}_{v,s,1} = \frac{\pi d_0^2}{\pi (2\alpha_0 z_{\text{ns}})^2} = 1.7 \times 10^{-3}. \quad (3.7)$$

Table 3.1: Atom numbers per pulse for He, He* and Rydberg atoms for positions after the valve, after the first and after the second skimmer, respectively. Numbers inferred from measured quantities are indicated green, black numbers are estimates as explained in the text.

position	reduction	N_{He}	$N_{\text{He}^*} = F_{\text{He}^*} N_{\text{He}}$	$N_{\text{Ryd.}} = F_{\text{Ry}} N_{\text{He}^*}$
valve	-	1.8×10^{13}	1.8×10^9	-
skimmer 1	1.7×10^{-3}	3.1×10^{10}	3.2×10^6	-
skimmer 2	0.12	3.7×10^9	3.8×10^5	~ 1000

The reduction from the expansion at the first skimmer to the second skimmer ($\text{Red}_{v,s,2} = 0.12$) was estimated using the measured expansion angle $\alpha'_{\text{max},1}$ and the distance between the two skimmers. With these factors, the number of ground state atoms (N_{He}) in the pulse can be estimated at every position. However, we cannot measure the number of metastable atoms at this positions but we can measure the number of Rydberg atoms that are excited by the laser, i.e. $N_{\text{Ryd.}} \approx 1000$ (Sec. 4.3.3.2). Under the assumption that the focus size of the laser beam is transversally larger than the atomic beam, and that we saturate the Rydberg transition (i.e. 50% of the metastable atoms in the focus of the laser beam are excited to Rydberg states), the overlap of the laser focus and the volume of the atom beam in zone 1 determines the fraction of all metastable atoms that are excited to Rydberg states, i.e.

$$F_{\text{Ry}} = \frac{d_{\lambda}^z}{\nu_0 \Delta t'_{\text{He}}} = 5.2 \times 10^{-3}, \quad (3.8)$$

with $d_{\lambda}^z \approx 2$ mm the excitation laser beam diameter along z direction, $\nu_0 \approx 1800$ m/s the velocity of the atoms, and the duration of the ground state atom pulse $\Delta t'_{\text{He}} = \Delta t_{\text{He}} + 15 \mu\text{s} = 205 \mu\text{s}$ in the first zone⁴. The number of singlet He* atoms N_{He^*} in the atomic beam after skimmer 2 is calculated from F_{Ry} and the measured number of Rydberg atoms per pulse $N_{\text{Ryd.}}$. Comparison of N_{He^*} and N_{He} after skimmer 2 results in F_{He^*} .

3.2 Longitudinal dynamics of metastable and Rydberg atom pulse

We characterize the metastable and Rydberg atom beams in our experiment with a set of three parameters, N is the number of (metastable or Rydberg) atoms in the pulse, ν_0 its mean velocity in the propagation (z) direction, and $\delta t(t)$ its time-dependent spread in z direction, which can be converted into a time-independent longitudinal beam temperature T . We find that these parameters vary strongly

⁴The 15 μs take into account the typical expansion of the atom beam in z direction because of its finite temperature (Sec. 3.2).

within the groundstate gas pulse that exits the valve. Hence, the parameters (N_{He^*} , ν_0 , $\delta t_{\text{He}^*(0)}$) of the metastable atom pulse depend strongly on the time when the discharge pulse at t_{DC} is applied with respect to t_V . Additionally, they depend on the pre-load configurations of the valve-poppet. In this section we present the parameter characterizations of two valve configurations; configuration 1 can produce larger densities of metastable atoms, but the atom beam is faster and warmer than in configuration 2, which produces smaller densities (Tab. 3.2)⁵.

The full dynamics of the He^* beam (Fig. 3.4) can be determined either for configuration 1 [panels (a-c)] or configuration 2 [panels (d-f)] in a single experiment where $\Delta t_{\text{DC-V}}$ and $-t_{\text{DC}}$ are varied while recording the integrated electron signal on the MCP and normalizing it to the maximal measured value (Sec. 4.3.3.2). Large signal (red colours) indicate settings, where a large number of atoms is excited to the (here: 47p) Rydberg state. In the dark blue regions no Rydberg atoms were excited. A larger $\Delta t_{\text{DC-V}}$ corresponds to the excitation of helium atoms, leaving the valve at later times, to metastable states. Variation of $-t_{\text{DC}}$ while keeping $\Delta t_{\text{DC-V}}$ fixed, moves the metastable atoms pulse in zone 1 with respect to t_λ . Hence a larger $-t_{\text{DC}}$ corresponds to the excitation of He^* atoms, arriving in zone 1 at later times, to Rydberg states. For the same laser energy, the number of Rydberg atoms detected at the MCP is proportional to the number of atoms in the metastable atom beam in zone 1. Cuts along the vertical direction in Fig. 3.4 (i.e. varying t_λ) reveal the temporal shape of the metastable pulse in zone 1 for a given $\Delta t_{\text{DC-V}}$. The data from each cut is fitted well by a Gaussian function, albeit in some cases fits with a distribution based on a Boltzmann velocity distribution could improve fitting errors marginally. From the fit, the center (arrival) time and the full-width-at-half-maximum (FWHM) are extracted. Fig. 3.4(b,c) and (e,f) present these numbers as a function of $\Delta t_{\text{DC-V}}$.

For both valve configurations it is observed that the metastable atoms arrive later in zone 1 if they are excited earlier from the groundstate atom pulse [Fig. 3.4(b,e)]. Given the fixed distance $z_{\text{DC}} = 140$ mm this indicates smaller

⁵It depends on the type of the experiment which configuration to choose, i.e. whether a large signal but slightly warmer beam (configuration 1) or a cold beam and less signal (configuration 2) is more preferable.

Table 3.2: Different operating regimes of the valve.

configuration	pre-load	N_{He^*}	ν_0 [mm/ μ s]	$\delta t_{\text{He}^*(0)}$ [μ s]	T [K]
1	weak	$\gtrsim 3 \times 10^4$	1.8 – 2.1	15 – 25	$\gtrsim 7$
2	strong	$\lesssim 10^4$	1.7 – 2.0	20 – 30	$\gtrsim 3$

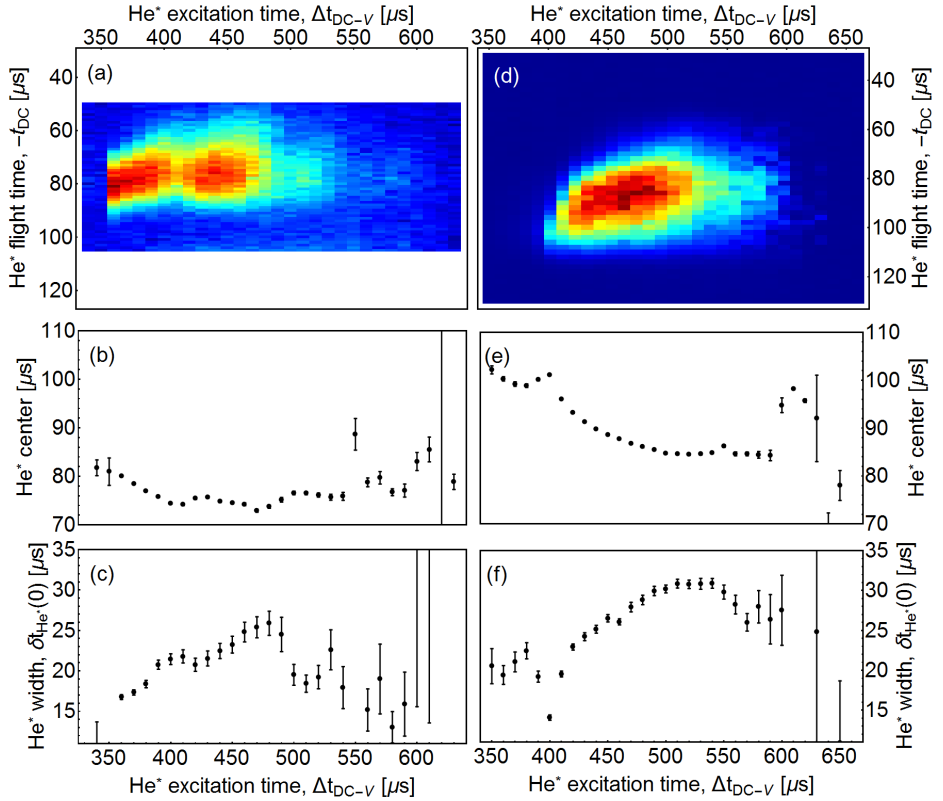


Figure 3.4: Helium beam characteristics for weak (a-c) and strong (d-f) valve pre-load. (a,d) Integrated electron signal as a function of delay of HV_{DC} -pulse with respect to valve trigger and delay of laser pulse with respect to the HV_{DC} trigger, see text for details. The colorscale ranges from no signal (dark blue) to maximum signal (dark red). (b,e) Full width at half maximum and (c,f) extracted centers of He^* -beam determined from Gaussian fits along the vertical axis in (a,d) for different HV_{DC} -pulse delays.

longitudinal velocities relative to atoms that are excited later. To calculate the mean velocities v_0 , one needs to take into account that the mean of the He* pulse is generated $t_{\text{del}} \approx 5 \mu\text{s}$ and $12 \mu\text{s}$ later than t_{DC} in the two measurements (compare Fig. 3.6), a time that needs to be subtracted from the measured arrival times. The mean velocities for the presented measurements lie in the range of $\sim [1800, 2100]$ m/s for configuration 1 and $\sim [1700, 2000]$ m/s for configuration 2, respectively.

Similarly, the FWHM of the metastable atom pulses increases when the atoms are excited later in the pulse [Fig. 3.4(c,f)]. A larger FWHM indicates a larger velocity spread, i.e. a larger longitudinal temperature. In analogy to a cold, expanding gas [Lett *et al.* (1988); Thiele (2010); Palittapongarnpim (2012)], we relate the FWHM $\delta t_{\text{He}^*}(0)$ of the pulse at time $t_\lambda = 0$ to the longitudinal temperature by

$$\delta t_{\text{He}^*}(0) = \sqrt{\delta t_{\text{He}^*}(t_{\text{DC}} - t_{\text{del}})^2 + 8 \log(2) \frac{2k_b T}{v_0^2 m} (t_{\text{DC}} - t_{\text{del}})^2}. \quad (3.9)$$

The mean temperatures for the presented cases lie in the range of $\sim [7.1, 24.6]$ K for configuration 1, i.e. panel (c) and $\sim [3.5, 26.3]$ K for configuration 2, i.e. panel (f), respectively.

The FWHM of the measured metastable atom pulse can be underestimated up to $\sim 25\%$ if detected by pulsed field ionization because of an effect that is strongly linked to the detection process. In Sec. 4.3.2 it is discussed in detail, how only a certain volume in zone 3 is efficient in detecting Rydberg atoms. For a fixed extraction time t_{ext} , and for varying velocities of the Rydberg atom packet excited from the metastable beam in zone 1, the overlap with this detection region in zone 3 [Fig. 4.12(d)] varies. Hence, the detection efficiency is reduced for early and late $-t_{\text{DC}}$ and the FWHM of the metastable atom beam is underestimated. As also explained in Sec. 4.3.2 the spatial extension of the detection region can be increased when the einzel lens is used [compare Fig. 4.12(d) and Fig. 4.18(a)]. Hence, the error in determining the FWHM of the atom cloud can be reduced to a minimum.

The parameters (N_{Ry} , $v_{0,\text{Ry}}$, δt_{Ry}) of the Rydberg atom pulse depend strongly on the value of t_λ , i.e. which part of the metastable atom pulse is excited to Rydberg states in zone 1. To measure the parameters it is necessary to develop a technique with which the atom distribution in z direction of the Rydberg atom beam can be measured. Pulsed field ionization (PFI) is not a suitable technique because almost all atoms of the Rydberg atom beam are ionized by the same pulse, and the width of the detected electron packet at the MCP is below the temporal resolution of the detector. Also, stepwise changing t_{ext} with respect to t_λ is not suitable, because the number of detected atoms is a convolution of the atom beam distribution and the region in which the Rydberg atoms are being ionized. Both can not be easily deconvolved.

Therefore, we use a different technique with which we acquire $(N_{\text{Ry}}, \nu_{0,\text{Ry}}, \delta t_{\text{Ry}})$ simultaneously to the measurements of valve-configuration 1 presented in Fig. 3.4(a-c). We exploit adiabatic ionization of Rydberg atoms (here: in the state 47p) with static electric fields that we apply to IL1 (-20 V) and IL3 (164 V). As a consequence, the Rydberg atom pulse, which is excited for a specific $\Delta t_{\text{DC-V}}$ and t_{DC} , enters the field region with a speed $\nu_{0,\text{Ryd}}$, and the Rydberg atoms adiabatically ionize at the same field line. Finite-element simulations of the applied potentials indicate that the electric field at $z_1 \approx 50$ mm from the middle of zone 1 is large enough to ionize the Rydberg atoms. Because of the large electric fields, the charged particles arrive almost instantaneously at the MCP. Hence, the signal we observe at the MCP corresponds to the number of Rydberg atoms that arrive at z_1 as a function of time.

The signal fits well to a Gaussian function and the center time and FWHM can be converted to the mean velocity and the temperature of the Rydberg atom beam. Determination of the velocity $\nu_{0,\text{Ry}}$ is not straight-forward. Because the fields are not pulsed, the Rydberg atoms do not move in a field-free environment prior to ionization. As shown in Fig. 4.5, p -type Stark states increase their potential energy and simultaneously reduce their kinetic energy when moving into an electric field. The additional travel time can be accounted for by estimating an effective distance of $z_1^{\text{eff}} = 63$ mm the atoms would travel at constant speed. $\nu_{0,\text{Ry}}$ is then determined by z_1^{eff} and the center time of the MCP signal.

To determine the temperature we use Eq. (3.9), the measured δt_{Ry} in the detection region and a laser spot of 1 ± 0.1 mm width, which determines the initial ensemble-width in zone 1. The temperature distribution of the Rydberg atom ensembles that can be excited for valve-configuration 1 [Fig. 3.5(a)] indicate that we can excite cold packets of Rydberg atoms ($T_{\text{Ry}} \lesssim 1$ K) if we excite metastable atoms shortly after the valve opened ($\Delta t_{\text{DC-V}} = 360 \mu\text{s}$). These temperatures are significantly lower than the average temperatures of the He* beam [compare Fig. 3.4(c)], because at the position of the laser excitation the fast and slow atoms have been separated by temperature.

This separation is also observed in the velocity distribution of the Rydberg ensembles. For example, the velocity distribution at $\Delta t_{\text{DC-V}} = 360 \mu\text{s}$ [Fig. 3.5(b)] indicates a monotonous increase in $\nu_{0,\text{Ry}}$ from ~ 1.7 mm/ μs for $-t_{\text{DC}} = 95 \mu\text{s}$ to ~ 2.25 mm/ μs for $-t_{\text{DC}} = 65 \mu\text{s}$, and with small temperatures $T_{\text{Ry}} \lesssim 1$ K. For $\Delta t_{\text{DC-V}} \geq 360 \mu\text{s}$ we observe a larger variation of beam temperatures T_{Ry} , i.e. a less clean separation of the fast and slow atoms.

In summary, the combination of Fig. 3.4(a) (for N_{Ry}) and 3.5(a,b) (for $\nu_{0,\text{Ry}}, T_{\text{Ry}}$) allows to determine optimized parameter configurations $(N_{\text{Ry}}, \nu_{0,\text{Ry}}, T_{\text{Ry}})$ for a given valve configuration by choosing $-t_{\text{DC}}$ and $t_{\text{DC-V}}$.

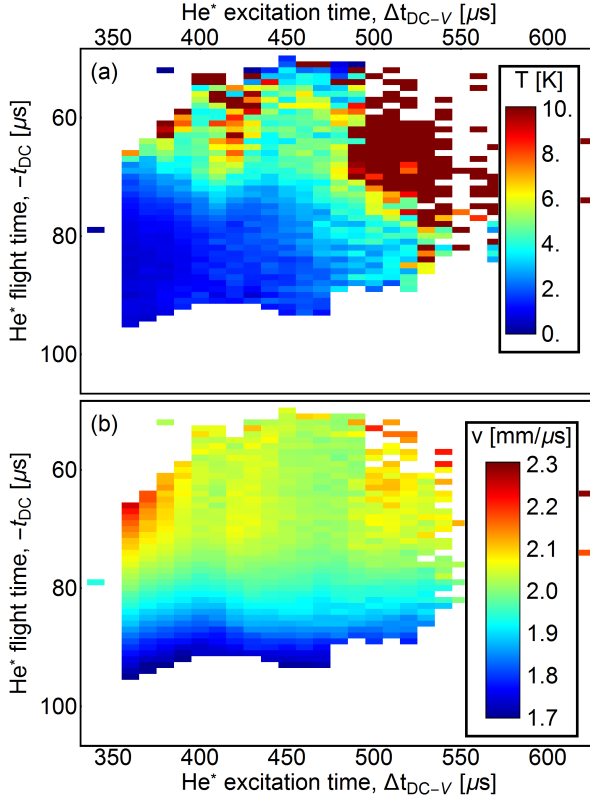


Figure 3.5: (a) Temperature and (b) velocity of the Rydberg atom beam as a function of delay of HV_{DC} -pulse with respect to valve trigger and delay of laser pulse with respect to the HV_{DC} trigger. The data was extracted from Gaussian fits to the continuous ionization TOF-measurements of the Rydberg atom beam for the low-tension valve configuration from Figure 3.4(a-c), details see text. White areas indicate measurements, in which the detected electron number was below $\sim 10\%$ of the maximal detected value.

The time evolution of the metastable and Rydberg atom packet can be calculated and compared with the measured atom distributions (Fig. 3.6). As an example, we compare for valve-configuration 1 two measurements of a He^* pulse that was excited at $t_{DC-V} = 360 \mu s$, and the measurement of a Rydberg atom pulse that was generated from the He^* pulse (prepared at $t_{DC} = -82 \mu s$) with the predictions of a calculation.

Specifically, the data indicated blue in Fig. 3.6 belongs to a vertical cut of the data at $t_{DC-V} = 360 \mu s$ presented in Fig. 3.4(a), i.e. it indicates the time-of-flight distribution of the He^* atom beam in the center of zone 1. In this plot, zero delay corresponds to the time when the metastable helium atom pulse is created at the valve at $-t_{DC} \approx 80 \mu s$ [i.e. it is shifted by $\sim 80 \mu s$ with respect to Fig. 3.4(a)].

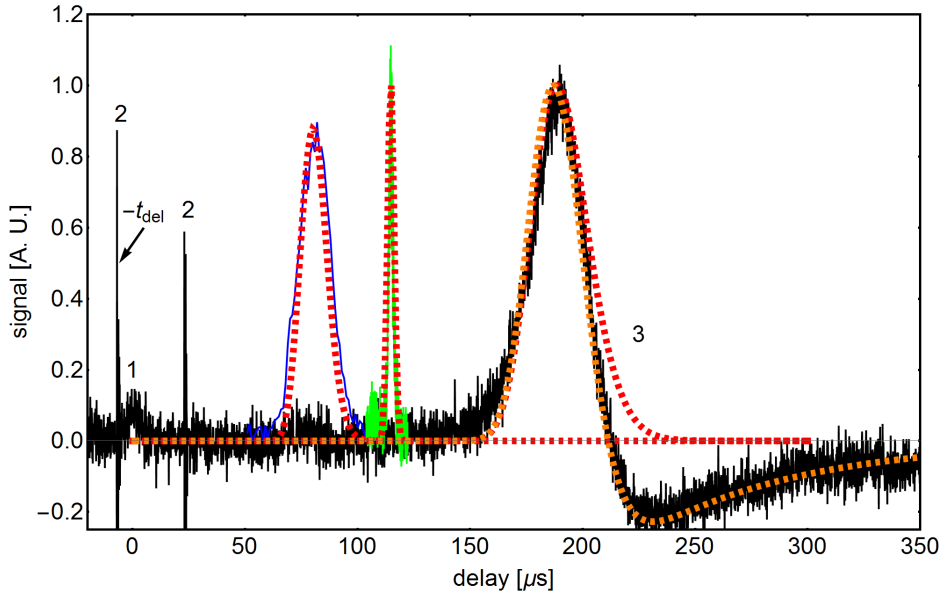


Figure 3.6: Normalized metastable (data indicated blue and black) and Rydberg atom pulse intensities (data indicated green) for different delays/positions in the experimental apparatus and corresponding fits to a simple model (red, dashed lines), see text. The black curve presents a time-dependent signal of the MCP showing light generated by the discharge at $0 \mu\text{s}$ [label (1)] for a HV_{DC} -pulse delay of $360 \mu\text{s}$ and peaks labeled (2) indicate (spurious) capacitive couplings from the discharge high-voltage pulse. The signal at $180 \mu\text{s}$ corresponds to the measured metastable pulse arriving at the position of the MCP. The deviation from the prediction [label (3)] can be taken into account, see text (orange, dashed line). The data in blue colour shows the arrival time of the metastable atom beam in the middle of the Rydberg excitation zone (162 mm after the nozzle). The green line shows the arrival times of Rydberg atoms at the position of the continuous field ionization in the detection zone (207 mm after the nozzle).

The data indicated green is the Rydberg-electron signal as measured by the MCP in the static-field detection. This corresponds to the time-of-flight signal of the Rydberg-atom pulse at the end of zone 3. The data indicated black is a time trace measured by the MCP, when only the metastable source is switched on. The signal labeled (1) is uv-light emitted during the discharge and indicates that a $5\text{-}\mu\text{s}$ -long He^* pulse is generated at the source. The maximal intensity of the discharge is reached $t_{\text{del}} = 5 \mu\text{s}$ after the discharge high-voltage has been switched on at t_{DC} and off at $t_{\text{DC}} + \Delta t_{\text{DC}}$. These times are precisely indicated by spurious electrical signals [labeled (2)] that couple into the (high-impedance) detector. The signal at $180 \mu\text{s}$ is the He^* atom pulse which is detected at the MCP. The negative signal [label (3)] is attributed to a combination of two effects, i.e. a space-charge that builds up inside the MCP detector or saturation of the preamplifier after the MCP detector (Sec. 4.3.3.1).

In the calculations we assume a 5- μ s-long metastable atom pulse at the excitation with a velocity distribution given by

$$P_v(v) = Av^3 \exp\left(-m_{\text{He}} \frac{(v - v_0)^2}{2k_b T}\right), \quad (3.10)$$

with $v_0 = 1910\text{m/s}$ and a temperature $T = 8\text{ K}$ as determined from the measurement presented in Fig. 3.4(a-c). To predict the different traces (red dashed lines) indicating the metastable atom signals, this atom pulse is mathematically convolved to later times and plotted versus arrival time at the specified locations (i.e. in the center of zone 1 and at the MCP, respectively). We find, that the predicted evolution of the atom packet with time agrees well with the measured metastable atom distribution.

We simulate the effect of the detector response (orange dashed line) by folding the calculated metastable signal with the expected detector response modeled as a delta-peak of finite height 1 followed by a negative, exponential function with amplitude $1/85$ and decay time of $\sim 70\ \mu\text{s}$.

The prediction for the time-of-flight signal of the Rydberg atoms is obtained in a similar way than for the metastable atoms, i.e. by preparation of a Rydberg atom pulse of 1-mm width in zone 1 with the measured velocity of 1950m/s and the measured temperature of $\sim 0.5\text{ K}$. Comparison of the simulation with the measured data (green trace) results in the fitted effective distance of $z_1^{\text{eff}} = 63\text{ mm}$.

SPECTROSCOPY OF RYDBERG ATOMS

The following chapter introduces the two main types of data acquisition used for the measurements presented in this thesis, laser and microwave spectroscopy. Specifically, I focus on interpretation of laser Rydberg spectra of atoms in free-space experiments and compare the detection of ions and electrons, generated from Rydberg atoms by field ionization (Sec. 4.1). The laser spectra are used to quantify the effects of large (> 1 V/cm) electric fields on the Rydberg atoms, and also to characterize these fields. The microwave spectra, in contrast, are well suited to study the effects of small electric fields and to characterize such fields (Sec. 4.2). The last section (Sec. 4.3) presents characteristic features of the different Rydberg excitation and detection procedures used in this thesis.

4.1 Laser spectroscopy

Rydberg states are produced by laser excitation of the $(1s)^1(2s)^1S_0$ metastable state of helium in zone 1 (Fig. 4.1). The pulsed, Nd:YAG-pumped-dye excitation laser [labeled (1)] is operated at a uv-wavelength of $\lambda \approx 313$ nm and excites the atoms in a one-photon transition (Sec. 4.3.1). Optical selection rules restrict transitions to the singlet np Rydberg series that converges to the $(1s)^1 2S_{1/2}$ ground state of He^+ .

We routinely record laser excitation spectra of this Rydberg series by monitoring the electron signal produced on a microchannel plate detector (MCP,

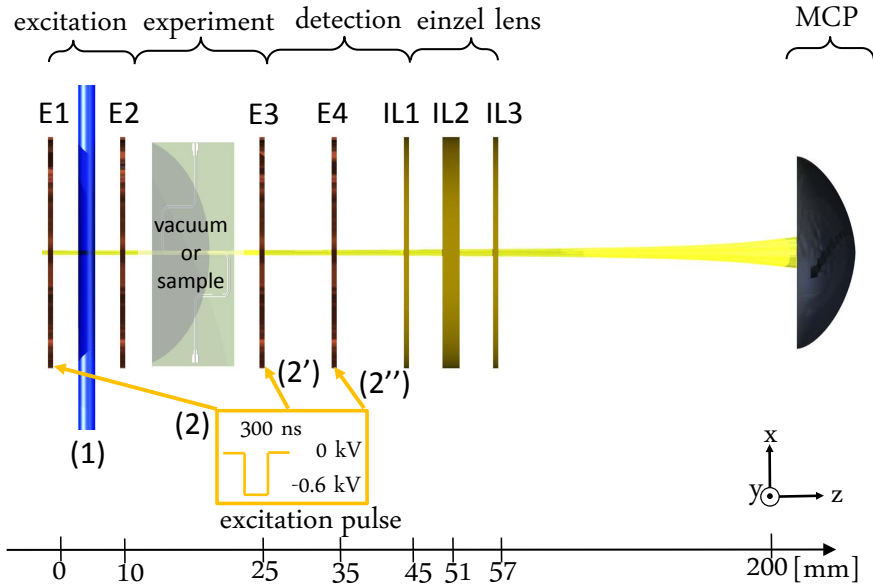


Figure 4.1: Measurement procedure for laser spectroscopy indicated by labels (1 and 2). The metastable atom beam (yellow) is excited to np -Rydberg states in the middle of the excitation zone [label (1)]. The Rydberg atoms may be pulsed field ionized immediately after excitation by applying a -0.6 -kV-ionization pulse of 50 ns length to electrode 1 [label (2), electrodes indicated brown] or to electrode 4 [label (2')] after passing the experimental zone. The resulting electrons are detected at the MCP (black).

Sec. 4.3.3.1) by delayed pulsed field ionization (Sec. 4.3.2) of the Rydberg atoms as a function of the frequency of the uv laser. The Rydberg states are detected by field ionization either in the first zone [label (2)] after 100 ns of flight time, or in the third zone [labels (2'), (2'')] after a time of flight of $14.1 \mu\text{s}$ and $19.5 \mu\text{s}$, respectively. At a beam velocity of 1770 m/s , the atoms have traveled distances of $\sim 0.2 \text{ mm}$, 25 mm and 35 mm from excitation to detection, respectively. The potential pulse (-0.6 kV) applied to the electrodes has a rise time of $\sim 50 \text{ ns}$ and a duration of $\sim 300 \text{ ns}$.

4.1.1 Spectroscopy of Rydberg atoms in a field-free environment

The measured spectra displayed in Fig. 4.2(a-c) are different when the atoms are detected in different zones. In this figure, we compare the normalized electron (data indicated red) or ion (data indicated black) MCP signal with simulations (green data trace). For all spectra, the excitation laser wavelength is converted into a frequency detuning (E_1) from the well-known, field-free ionization energy

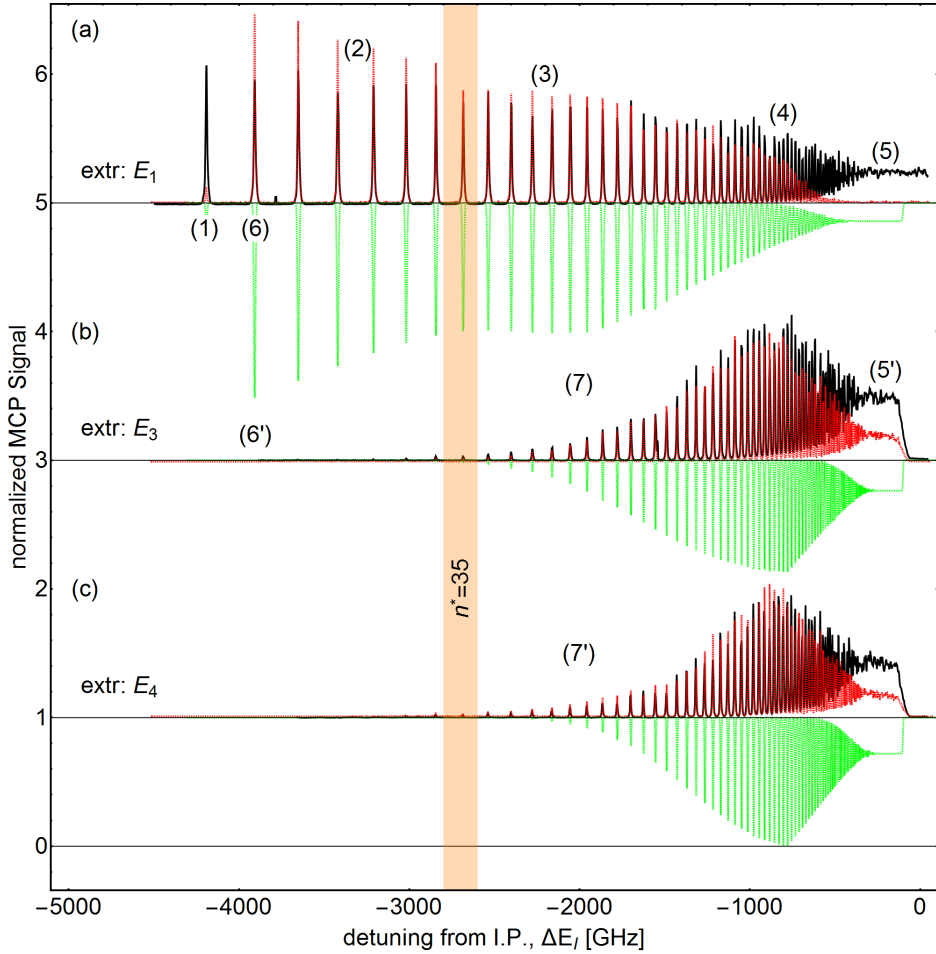


Figure 4.2: Normalized laser spectra of metastable $(1s)^1 (2s)^1 1 S_0$ helium as function of detuning from the ionization limit for pulsed field detection at (a) electrode E_1 , (b) electrode E_3 and (c) electrode E_4 , respectively. For reference, the state $n^* = 35$ is highlighted. Data in black indicate detection of ions, data in red indicate detection of electrons and the green trace indicates the corresponding simulations (parameters given in the text). The features labeled 1 – 7 are also described in the text.

($E_1 = 24.587$ eV) of helium [NIST (2015)]. The spectra are normalized, because we are interested in the relative change of the transition-strength as a function of the atom state only. Using the characterization measurements of the MCP (Sec. 4.3.3.2), the observed strengths of the resonances can be converted into a total number of detected atoms; and if the extensions of the laserfocus and the density of atoms are known, also to a (relative) population of the Rydberg state.

The six spectra were recorded for 'standard' conditions (Tab. 4.1) up to the exceptions listed below.

1. For the spectra in panel (a), the extraction pulse was applied to electrode 1, in panel (b) to electrode 3, and in panel (c) to electrode 4.
2. To detect *ions* the field-ionization pulse is generated using a commercial switch (BEHLKE: GHTS 60A), which has slightly different performance than the homebuild high-voltage pulser we use for *electron* detection (Sec. 4.3.2).
3. The spectra for which electrons are detected (red spectra) were acquired with smaller stepzise (0.001 nm).

Each spectrum exhibits a set of resonances that correspond to the different excited (np)-Rydberg states of He¹. As a reference, we indicate the state with $n^* = 35$. The resonances have a Gaussian shape and are characterized by their center frequency, amplitude and full width at half maximum (FWHM). The Gaussian line shape is a consequence of either the Gaussian-shaped linewidth of the excitation laser that dominates the natural linewidth of the transition, or it is a consequence

¹Because the quantum defect of the p-state of singlet helium is $\delta_p^{\text{He}} = 0.98 \approx 1$, the peak labeled n^* corresponds to the excitation of $(n + 1)p$.

Table 4.1: Standard settings for laser spectrum acquisition

experimental setting	number
number of averages	25
laser energy	$P_\lambda \approx 400 \mu\text{J/pp}$
laser stepwidth	0.002 nm
MCP sensitivity	$V_b = 1.6$ kV
MCP integration window	(-5, 10) ns to maximum of MCP time signal
extraction pulse	applied to electrode 4
extraction potential	$V_{\text{ext}} = -0.6$ kV
detected particles	electrons

of electric field inhomogeneities or power broadening of the lines. Therefore, the calculated spectra (green data traces) assume gaussian-shaped resonances with a FWHM corresponding to the laser-linewidth and with center frequencies and amplitudes as discussed in the following.

The observed *transitions frequencies* up to $n^* \approx 93$ ($\Delta E_1 = -380$ GHz) coincide with the predicted field-free transition frequencies as calculated by Eq. (1.28) better than the resolution of the acquired spectra, i.e. ~ 1.5 GHz. The frequency separation of the $n^* \approx 93$ and $n^* \approx 94$ states is ~ 8 GHz. For larger excitations, the differences between the calculated and measured transition frequencies increase with increasing n^* -value. This is a consequence of small electric fields in the excitation region that shift the transitions because of the larger polarizability $\alpha \propto n^{*7}$. The highest states that are fully separable, i.e. for which the transitions do not overlap, are $n^* = 74$ and $n^* = 75$ ($\Delta E_1 = -600$ GHz). The frequency separation of these two states is 15 GHz. The highest state that can be resolved spectrally is $n^* = 100$ ($\Delta E_1 = -328$ GHz) which has a frequency separation to $n^* = 101$ of 6.1 GHz.

The *strengths* of the different transitions contain information on atomic properties and experimental parameters, such as the strength of electric stray-fields in the experiment, the lifetime of the different np states or the adiabaticity of the field ionization process. In the following we discuss a number of important effects labeled (1 – 7) in Fig. 4.2. All these effects are caused by properties of Rydberg atoms that were taken into account to calculate the green data traces and which are also discussed in the following.

- (1) No transitions are observed below $n^* = 28$ because the applied electric ionization field is not strong enough to ionize lower Rydberg states. A potential of 600 V applied to electrode 1 generates an electric field in zone 1 of ~ 520 V/cm, which is close to the adiabatic ionization limit of $n^* = 28$ (522 V/cm). The adiabatic ionization field for a state n^* is given by [Galagher (1994)]

$$F_{\text{ad}}(n^*) = \frac{1}{16n^{*4}} F_0, \quad (4.1)$$

where $F_0 = 5.14 \times 10^9$ V/cm is the atomic unit of the electric field. In the simulations we use a simple model to determine the fraction of atoms that are ionized by the electric field pulse below $n^* = 35$. Because of the ionization process in the limited detection region where the atoms are efficiently ionized (Sec. 4.3.2), the fraction of the detected atoms tends to a constant value. This value can be determined by comparing the relative strength of the calculated and measured electron data and may change with the applied ionization field strength. In the calculation a fraction of $\sim 50\%$ describes the data presented in Fig. 4.2 well.

- (2) As discussed in Sec. 1.1.4 [Eq. (1.31)] and as detailed in Sec. 4.3.1 [Eq. (4.13)], the strength of the transition drops with increasing Rydberg states as n^{*-3} if the transition is not saturated.
- (3) The observed plateau in the strength of the transitions between $n^* = 36$ and $n^* = 44$ can be explained by adding to the (adiabatic) ionization model described in item 1 an n^* -dependent increase in the number of atoms that are ionized. This is because the p-state of helium with quantum number n^* can ionize diabatically at an electric field of [Gallagher (1994)]

$$F_{\text{dia}}(n^*) \approx 2 \frac{1}{9n^{*4}} F_0. \quad (4.2)$$

Therefore, we expect all atoms above the state $n^* = 39$ [labeled (3)] to be ionized by the pulsed field. However, the diabatic ionization as a function of n^* is not sharp, but calculated in the approximation for purely diabatic ionization by Eqs. (1) and (6) in *Damburg and Kolosov (1979)*. For states $n^* \gtrsim 48$, the strength of the transition decreases as $(n^*)^{-3}$.

For states $n^* \gtrsim 48$, the detected electron signal (red) is smaller than the ion signal (black). This is attributed to be a secondary effect from detection. As will also be discussed in Sec. 4.3.2, the atoms are ionized instantaneously and the electrons and ions are accelerated by the electric ionization field. Because the ionization field decreases with increasing quantum number n^* , the electrons are slower, which makes them more susceptible to stray electric and magnetic fields. Therefore, the electrons deviate from their trajectories and, as a result, can miss the MCP detector (Sec. 5.3).

- (4) The transitions to different n^* states start to overlap. Because the energy difference between two adjacent states decreases with n^{*-3} [Eq. (1.29)] the density of states per frequency interval increases with n^{*3} .
- (5,5') This label indicates the state-resolution limit of the experimental setup, i.e. the FWHM of the transition exceeds the frequency separation of two adjacent states. Two experimental parameters determine this width. On the one hand, the FWHM of the observed transition is always limited by the width of the laser (~ 1 GHz, Sec. 4.3.1). On the other hand, the transitions can be broadened additionally by stray electric fields, as discussed below.

For the spectra depicted in panel (a) we observe a Rydberg signal for laser frequencies above the ionization limit. However, this is not observed for the spectra in panel (b) and (c), where the signal drops to 0 below the ionization limit. In panel (a), ions that are generated in zone 1 by photoionization with

the excitation laser or by stray field ionization, are immediately (after 0.1 μs) accelerated toward the MCP by the detection pulse. For the panels (b) and (c), the electric stray fields in the experiment are large enough to deflect the ions out of the extraction region, such that they are not accelerated toward the MCP when the ionization pulse is applied after 14.1 and 19.5 μs .

The maximal stray field encountered by the Rydberg atoms as they fly through the apparatus, can be estimated by the well-known classical expression derived from Eqs. (4.1,1.28),

$$\Delta E_1/(hc \text{ cm}^{-1}) = -6.12\sqrt{F/(\text{V/cm})} \quad (4.3)$$

which relates ΔE_1 to the maximal field strength F . In this case, this is $\sim 0.3 \text{ V/cm}$ ($\equiv -90 \text{ GHz}$).

- (6,6') The difference between the spectra presented in panels (a) and (b) is the time of flight of the Rydberg atoms (0.1 μs versus 14.1 μs). The difference in the strength of the transitions is because of the radiative decay of the n^*p states, which have lifetimes $\tau_{n^*}^p \leq 2.5 \mu\text{s}$ for $n^* \leq 40$. The lifetime τ_n^p of the np series is estimated from the dependence of the lifetime on the effective quantum number $n^* = n - \delta_l$ as [Gallagher (1994)]

$$\tau_n^p = \tau_1^p n^{*3} = \tau_1^p (n - \delta_p)^3 \quad (4.4)$$

with $\tau_1^p \cong 3.8 \times 10^{-11} \text{ s}$ determined from the measured lifetime of $\sim 1.4 \mu\text{s}$ of the 34p state [Thiele *et al.* (2014)] and the quantum defect $\delta_p = 0.98787$ of the p series [Drake (1999)]. This lifetime scaling law, when combined with the $(n^*)^{-3}$ dependence of the photo-excitation cross section, implies that the detection of Rydberg states below $n \approx 40$ in the third zone is inefficient in the absence of stray electric fields.

- (7,7') The detected signal for states between $n^* \approx 40$ and $n^* \approx 50$ is enhanced, because of small stray electric fields ($\leq 50 \text{ mV/cm}$) in the excitation region. The l -mixing [Chupka (1993)] and m_l -mixing [Merkt and Zare (1994)] of the initially prepared short-lived p Rydberg states induced by the stray electric fields additionally increases the lifetimes by a factor of n or n^2 .

4.1.2 Spectroscopy of Rydberg atoms in an electric field

We study the effect of electric fields on the singlet helium Rydberg atoms in an experiment where we excite the state $n^* = 29$ in an electric field F (Fig. 4.3). The electric field F is produced in zone 1 by applying specific potential differences up to $\sim 80 \text{ V}$ between electrode 1 and electrode 2. For each applied electric field, the

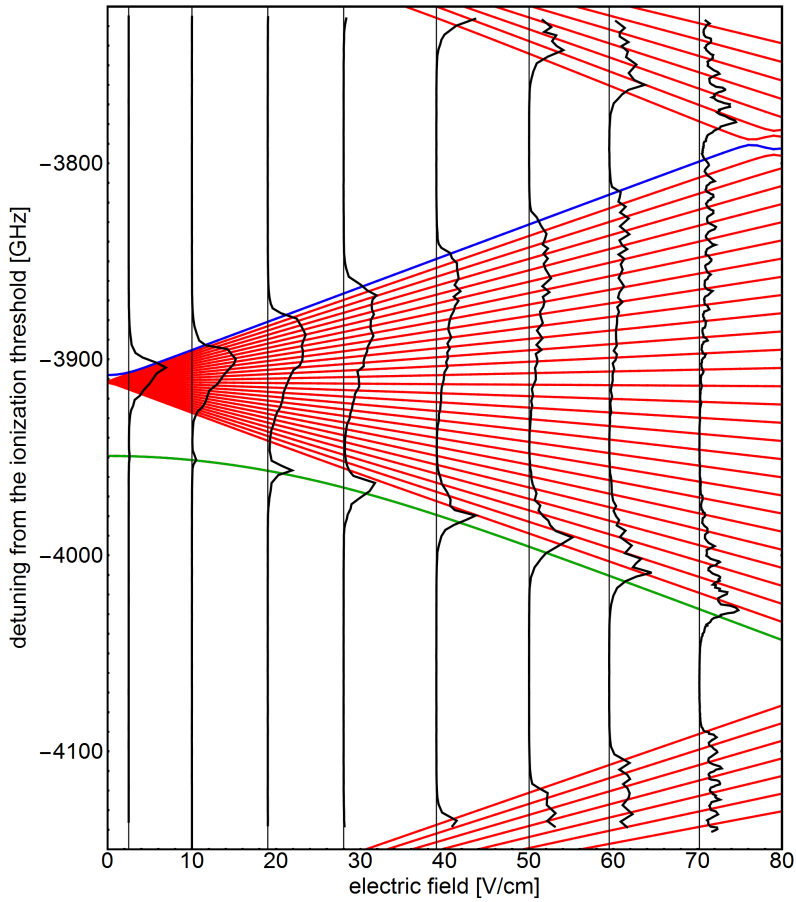


Figure 4.3: Measured (black traces) Stark spectra and calculated (red lines) center frequencies of the state $n = 29$ without free parameters. The states indicated blue and green correspond to the p- and s-type Stark states of the $n^* = 29$ manifold, respectively.

laser frequency is scanned between -3700 GHz and -4150 GHz with respect to the ionization limit of singlet helium and the MCP electron signal is recorded (black data). We compare the measured spectra with eigenstates obtained by direct diagonalization of the single-particle Stark Hamiltonian (red lines) for $m = 0$ in the vicinity of $n^* = 29$, and using the energy-dependent quantum defects of the helium atom [Zimmerman *et al.* (1979); Drake (1999)].

Diagonalization of the Stark Hamiltonian indicates that the states of the n^{th} manifold split into $n - |m|$ separate states for finite F . This is a consequence of the atomic system being only rotational (not spherically) symmetric if an electric field F is applied, such that the quantum numbers (n, l, m) are not 'good' anymore [Gallagher (1994)]. In an electric field, new quantum numbers (n_1, n_2, m) are given to the energy states. Using the relation

$$n = n_1 + n_2 + |m| + 1 \quad (4.5)$$

and

$$k = n_1 - n_2 \quad (4.6)$$

we can relabel the Stark states of the n^{th} -manifold with the quantum numbers (n, k, m) , with k ranging from $n - |m| - 1$ to $-n + |m| + 1$ in steps of 2 for increasing binding energy. The Stark states can be described as superpositions of the field-free states. Note that because of its large quantum defect, the $(n, p, 0)$ is converted adiabatically into the $(n - 1, n - 2, 0)$ Stark state as soon as it joins the manifold (blue line for $n = 30$). Similarly, the $(n, s, 0)$ is adiabatically converted into the $(n - 1, -n + 2, 0)$ Stark state as soon as it joins the manifold (green line for $n = 30$). From now on, for simplicity, we will label these two l -type Stark states according to their l -character for $F = 0$.

The electric fields that we apply are too small to shift the metastable singlet 1S_0 state of helium. Because of the selection rules, the only state that can be excited for $F = 0$ by a one-photon transition is therefore the 30p-state (blue), i.e. the p-type Stark state of the $n = 29$ manifold. In the measurement, we observe that for fields $F \geq 2$ V/cm the states of the manifold acquire p-character, and therefore can be excited by the laser. For electric fields $F \lesssim 30$ V/cm, only the states in the manifold which are close in energy to the p-type Stark state acquire significant p-character, i.e. are more probable to be excited. This effect leads to an effective blue-shift of the resonance. For very large electric fields ($F \gtrsim 60$ V/cm), the probability to excite the states equilibrates. We cannot resolve the separate states because of the large linewidth of the excitation laser. The p-type Stark state joins with the s-type Stark state of the next higher manifold ($n^* = 30$) at the Inglis-Teller field given by (here $n^* = 29.5$) [Gallagher (1994)]:

$$F_{\text{IT}}(n^*) = \frac{1}{3n^{*5}} F_0 \approx 76 \text{ V/cm}. \quad (4.7)$$

Because of the selection rules, the s-state cannot be excited by a one-photon transition for $F = 0$. However, for electric fields $F \geq 20$ V/cm, the s-type Stark state (green) acquires significant p-character. Because of the large quantum defect of the s-state of helium the Stark state does not mix into the manifold for electric fields $F \lesssim 40$ V/cm and can therefore be observed as a narrow, separate transition in the spectra. For fields large enough ($F \geq F_{\text{IT}}/2 \approx 35$ V/cm), the s-type Stark state has more p-character than the p-type Stark state.

We observe the transitions to the s-type Stark states as 'satellite' peaks in Rydberg spectra, taken under the same conditions as the spectra presented in Fig. 4.2(a), with an additional potential of 5 V ($\equiv 4.3$ V/cm) applied to electrode 2 during Rydberg excitation [Fig. 4.4(a), label (1)]. The green lines indicate the calculated positions for the s-type Stark states, the blue lines indicate the calculated positions for the p-type Stark states.

We observe a broadening of the p-type Stark transitions for increasing n^* . This is expected, because for larger n^* the p-type Stark state mixes into the manifold at smaller electric fields. As a consequence, for fixed electric field and increasing n^* , the states of the manifold acquire an increasing fraction of p-character.

For $n^* \geq 45$ the s-type Stark state has more p-character than the combined p-type and the manifold Stark states. From the measured transition strengths in Fig. 4.3, we can expect that to happen when the applied electric field $F = 4.3$ V/cm $\approx F_{\text{IT}}/2$. From Eq. (4.7) we expect this at $n^* = 45.5$, which is in agreement with the observed value of $F_{\text{IT}}(45.5) = 8.78$ V/cm.

The applied electric field exceeds the Inglis-Teller field at state $n^* \geq 53$ [label (2)], which is calculated using Eq. (4.7). Alternatively, the quantum number of this state can be determined from Fig. 4.4(a) from the transition for which the calculated position of the p-type Stark state (blue lines) overlaps with the next higher calculated s-type Stark state (green line), i.e. at ~ -1100 GHz.

For quantum numbers $n^* \approx 60$ a set of 3 clear resonances lies between the calculated positions of the s- and p-type Stark states. For these states, $F > F_{\text{IT}}$ and the inner states of the manifold acquire a significant p-character.

In Fig. 4.4(b), the Rydberg atoms are excited in the same electric field $F \approx 4.3$ V/cm and detected at the end of zone 3 after a flight time of $19.5 \mu\text{s}$ of which $\sim 16.5 \mu\text{s}$ are in a field-free environment.

Similar to panel (a), we observe the 'satellite' peak which indicates that population is initially transferred to the s-type Stark state [label (1')]. Also in comparison with panel (a), we observe, that the p-type Stark state radiatively decays much faster for states $n^* \leq 40$ than the s-type Stark state or the manifold states. This is expected for the long field-free flight time of the atoms. For example, in an electric field the s-type Stark state can be acquire significant population because of

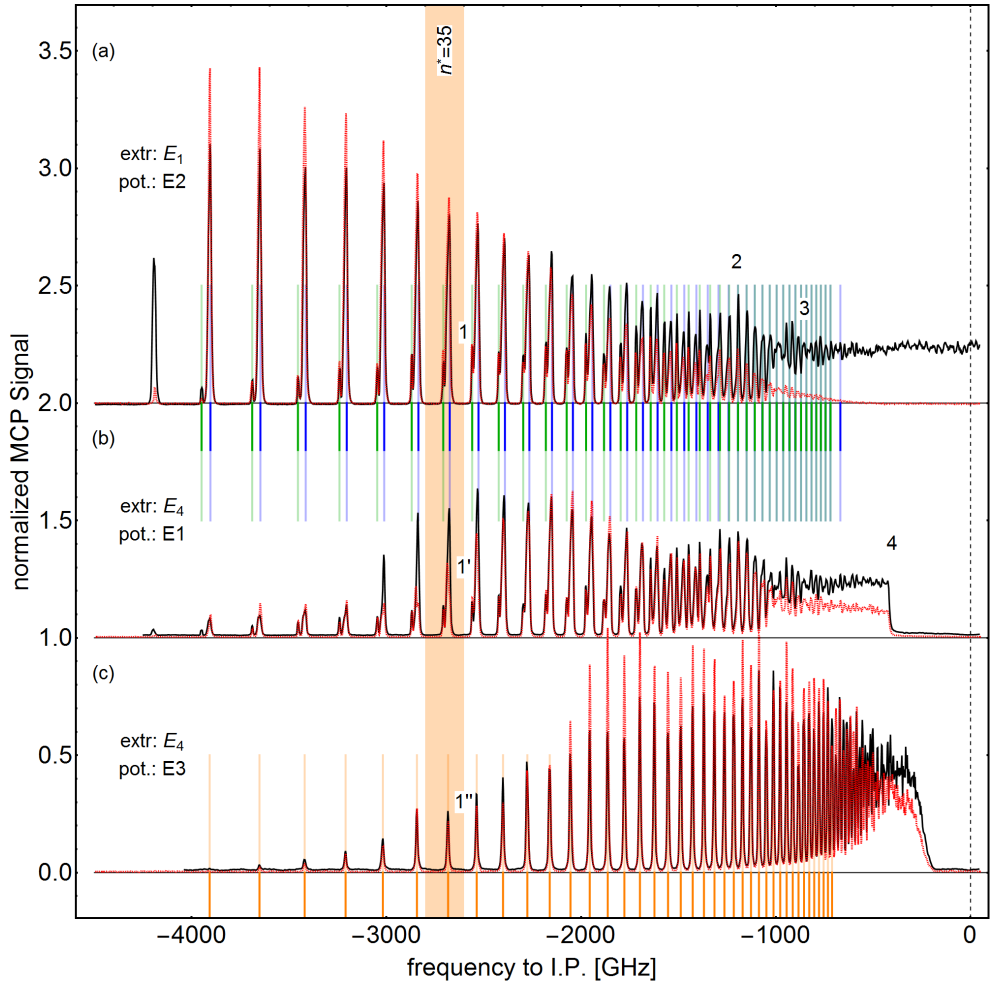


Figure 4.4: Normalized laser spectra of metastable $(1s)^1(2s)^1\ ^1S_0$ helium as function of the detuning from the ionization limit and a potential of 5 V applied to (a) electrode E_2 and detection at electrode E_1 , (b) electrode E_1 and detection at electrode E_4 , and (c) electrode E_3 and detection at electrode E_4 . For reference, the state $n = 35$ is highlighted. Black data indicate detection of ions, red data indicate detection of electrons. The green and blue lines indicate the theoretical positions of the np and ns -series for an electric field of 4.5 V/cm, respectively. The orange lines indicate the theoretical positions of the np -series for $F = 0$. The effects labeled (1 – 4) are explained in the text.

the large p-character that is excited by the laser. The Stark state is then adiabatically converted to the corresponding field-free state, the s-state, if the atom enters a field-free space. The decay of the s-state to the ground state of helium is dipole forbidden and therefore it has a longer lifetime ($\tau_{n^*}^s \in [65, 165] \mu\text{s}$ for $n^* \in [30, 40]$) than the p-state ($\tau_{n^*}^p \leq 2.5 \mu\text{s}$ for $n^* \leq 40$). The same argument is true for states in the manifold. As a result, the radiative decay of the population that is transferred to the s-type Stark state or the manifold is strongly suppressed with respect to the radiative decay of the p-type Stark state.

The sharp ionization limit [label (4)] can be approximately calculated by Eq. (4.3), i.e. -385 GHz ($n^* = 93$). States above $n^* = 93$ are photo-ionized by the excitation laser, and the electrons or ions deflected such that they are not accelerated toward the MCP by the ionization pulse.

The spectrum for which a potential of 5 V was applied to electrode 3 [Fig. 4.4(c)] differs from the spectra discussed in panels (a) and (b). In this case, no potential is applied in zone 1, i.e. the Rydberg atoms are excited in a field-free environment. From the $19.5 \mu\text{s}$ that the atoms travel until detection at the end of zone 3 (extraction pulse applied to electrode 4), only $5.5 \mu\text{s}$ are in a field-free environment. The field-free excitation and detection in zone 4 allows direct comparison of the positions and strengths of the transitions observed in Fig. 4.2(c).

In both spectra, the positions of the transitions coincide at the theoretical field-free positions (orange lines). Because the atoms are excited in a field-free environment, all population is transferred to the p-state, i.e. no satellite peak is observed [label (1'')].

However, the observed number of atoms for $n^* \leq 60$ is enhanced when an electric field is applied to electrode 3. This is a result of the longer lifetime of the n^* p-like Stark states with respect to the field-free n^* p states. For $n^* < 50$ only the lifetime of the p-state is short enough to decay effectively during the $19.5\text{-}\mu\text{s}$ -long time of flight. If the Rydberg atom is in a Stark state, the Stark state decays with a probability that is proportional to the fraction of the p-character. The larger the electric field for a specific state is compared to the Inglis-Teller field, the smaller is its p-type character is and the longer it lives.

4.2 Microwave spectroscopy - A sensitive way of measuring electric fields

In this thesis I performed sensitive measurements of stray electric fields close to surfaces exploiting microwave transitions between Rydberg-Rydberg states. In this section I introduce the microwave measurement techniques for characterizing stray fields in a free-space environment. Specifically, we study $np \leftrightarrow ns$ intraband

transitions for electric fields $F \lesssim 1$ V/cm and in the range $30 < n^* < 40$. These transition frequencies are in the convenient microwave range between 15 – 42 GHz, and the p and s states can be field-ionized state selectively.

4.2.1 Coherent microwave spectroscopy

The electric field dependence of the states in the $n^* = 33$ manifold [(Fig. 4.5(a))] is obtained by diagonalization of the single-particle Stark Hamiltonian using the energy-dependent quantum defects of the helium atom [Zimmerman *et al.* (1979); Drake (1999)]. The two states between which population is transferred are indicated blue (34p) and red (34s). For fields $F \lesssim 1$ V/cm, both states are well separated from the manifold states and are dominated by their field-free character, i.e. can be treated as field-free states with a (quadratic, see below) energy dependence on the electric field.

A microwave Rydberg experiments starts with excitation of Rydberg atoms to np states using the dye laser in zone 1 [label (1) in Fig. 4.6(a)]. These states decay before reaching zone 2 because of the small lifetime of the np states, i.e. $\tau_n^p \lesssim 2 \mu\text{s}$ [Eq. (4.4)]. We coherently transfer the Rydberg-state population from the np states to the ns states to overcome the life-time induced decay of Rydberg states. The 160-ns-long microwave pulse is generated using a horn antenna, positioned outside the vacuum chamber, and applied shortly after laser excitation [label (2)]

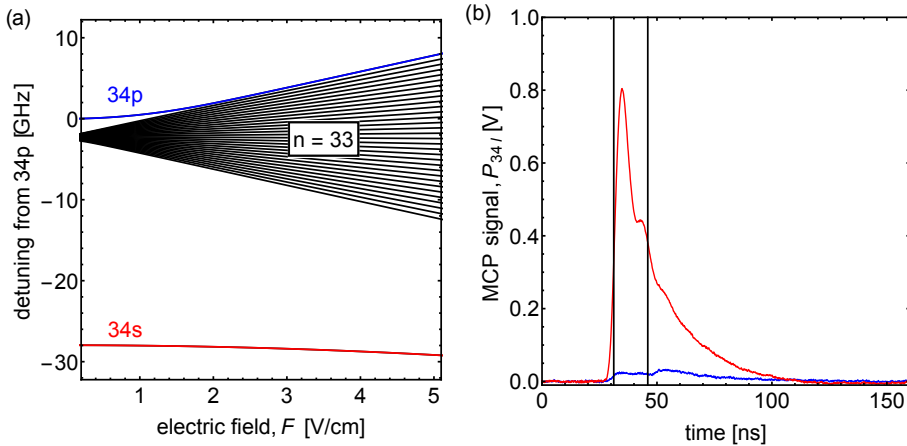


Figure 4.5: (a) Calculated Stark spectrum of the $n^* = 33$ manifold as a function of detuning from the 34p state (blue). For electric fields $F \leq 5$ V/cm the transition to the 34s state (red) changes quadratically with F . (b) Typical MCP electron signal of detected 34p-state population (blue) and 34s-state population (red). Vertical black lines indicate a typical integration window.

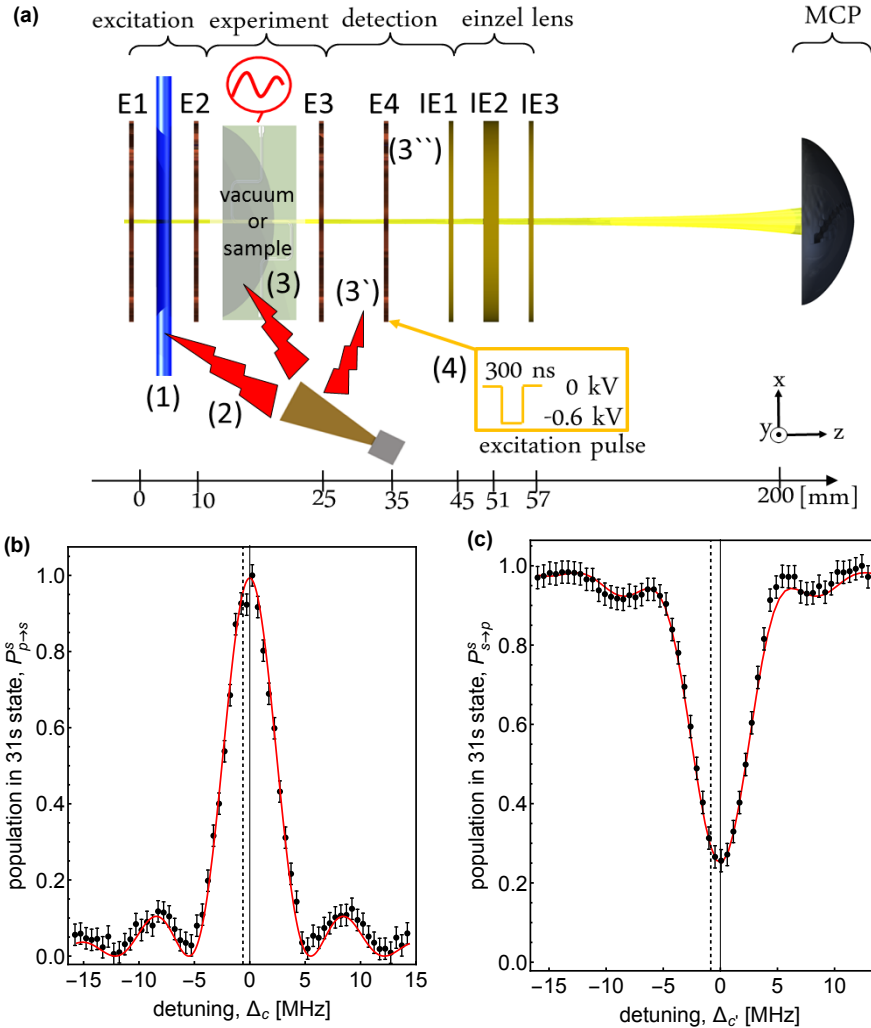


Figure 4.6: (a) Measurement procedure for microwave spectroscopy indicated by labels (1,2,3 and 4), see text. The metastable atom beam is indicated yellow. The electrodes are shown in brown and golden colour. The microwave and the laser pulses are indicated blue and red, respectively. The detection field pulse is indicated yellow. The MCP is indicated black. (b) Measured spectrum of the $31p \rightarrow 31s$ transition of singlet helium recorded with a 160-ns-long microwave pulse. The red line is a fit of $P_{p \rightarrow s}^s$ [Eq. (4.8)]. (c) Measured spectrum of the $31s \rightarrow 31p$ transition recorded with a second 160-ns-long microwave pulse at a delay of $t_{\mu}^{(2)} = 8.26 \mu\text{s}$. The red line is a fit of the expected s-state population $P_{s \rightarrow p}^s$ [Eq. (4.9)]. The dashed vertical lines correspond to the calculated field-free frequency. Detunings are specified relative to the fitted line center.

at time $t_\mu^{(1)} \approx 0.1 \mu\text{s}$. The ns states have lifetimes² in the range of $65 \mu\text{s}$ to $165 \mu\text{s}$ for n between 30 and 40, which is long enough to retain more than 80% of the atoms in their excited state during their time of flight from zone 1 to the detection zone 3.

In our experiments, the population in the long-lived ns state can be transferred back to the short-lived np state by means of a second microwave pulse [labels (3,3',3'') in Fig. 4.6(a)] at a variable time delay $t_\mu^{(2)}$ ranging from $3 \mu\text{s}$ (start of zone 2) to $17 \mu\text{s}$ (center of zone 3) with respect to the uv laser pulse at t_λ . As indicated by label (4) the Rydberg atoms are pulsed field ionized at the end of zone 3 (t_{ext} , Fig. 2.2) with a 300-ns-long pulsed electric field (Sec. 4.3.2). The radiative decay of the np states during the remaining time of flight between $t_\mu^{(2)}$ and t_{ext} leads to a depletion of the pulsed field ionization signal.

The difference in the detected amplitude of the MCP electron signals of the np (blue) and ns (red) states is more than an order of magnitude [Fig. 4.5(b)] after pulsed field ionization. The traces are acquired with a bias of 1500 V applied to the MCP and the black lines define a typical integration window (Sec. 4.3.3.1). Using the MCP signal calibration (Fig. 4.15) the number of atoms detected within the time window are ~ 30 and 830 , for the $34p$ and $34s$ state, respectively. The number of detected atoms can be maximized, e.g. by increasing the laser power. In this case, detected atom numbers exceeding 1500 per pulse can be reached.

Typical microwave spectra with a single and with two microwave pulses, respectively, are presented in Fig. 4.6(b,c) for $n = 31$. They are recorded by detecting the pulsed field ionization signal as a function of the microwave frequency. For these measurements neither sample nor sample holder were inserted in region 2. The data shown in both panels is obtained by normalizing the signal to the (same) maximum value obtained when the amplitude and frequency are varied and by subtracting a constant background signal, which never exceeds 5% of the total signal. The signal after the first pulse [Fig. 4.6(b)] is therefore approximately equal to the population of the s state, $P_{p \rightarrow s}^s$, at the time of field ionization. This population, assuming that all atoms are initially in the p state, is described by the excitation probability³

$$p(\Delta_c, \Omega, \delta t) = \frac{\Omega^2}{\Delta_c^2 + \Omega^2} \sin \left[\frac{\delta t}{2} \sqrt{\Delta_c^2 + \Omega^2} \right]^2 \approx P_{p \rightarrow s}^s, \quad (4.8)$$

with the detuning $\Delta_c = \nu - \nu_c$ of the microwave pulse at frequency ν from the atomic transition at frequency ν_c , and the Rabi frequency Ω . For a microwave

²The lifetimes were calculated using Eq. (1.33) and agree well with lifetimes calculated by [Theodosiou (1984)].

³This equation describes the coherent evolution of a qubit in a resonant field. For a coherent state (α), it can be deduced from the Jaynes-Cummings model [Eq. (1.3)] with $\Omega \approx 2g|\alpha|$.

pulse of duration $\delta t = \Delta t_{\mu}^{(1)} = 160$ ns and $n = 31$, a fit to Eq. (4.8) results in the Rabi frequency $\Omega/2\pi = 2.958(84)$ MHz and a center frequency $\nu_c = 37\,245.775(28)$ MHz. The value ν_c is shifted by 614 kHz from the field-free transition frequency ν_0 between the 31s and 31p states of 37 245.161 MHz. This shift results from the Stark effect induced by homogeneous (because no dephasing is observed) stray electric fields present in zone 1.

Using the horn antenna, application of a second microwave pulse with variable frequency ν at $t_{\mu}^{(2)} = 8.26$ μ s transfers parts of the population back to the p state. The remaining population, $P_{s \rightarrow p}^s$, in the s state is modeled by the excitation probability p [Eq. (4.8)], averaged over a Gaussian distribution of transition frequencies $\rho(\Delta_{c'}) = (\sqrt{2\pi}\sigma_{\text{stray}})^{-1} \exp[-\Delta_{c'}^2/(2\sigma_{\text{stray}}^2)]$ caused by the slightly inhomogeneous stray electric field present at the time of the second microwave pulse,

$$P_{s \rightarrow p}^s(\Delta_{c'}) = 1 - \xi \int \rho(\Delta_{c'} - \delta) p(\delta, \Omega, \delta t) d\delta. \quad (4.9)$$

For a $\delta t = \Delta t_{\mu}^{(2)} = 160$ ns long pulse we obtain the Rabi frequency $\Omega/2\pi = 3.18(23)$ MHz and a center frequency $\nu_{c'} = 37\,246.000(54)$ MHz for the data shown in Fig. 4.6(c). The center frequency $\nu_{c'}$ is shifted by 840 kHz from the field-free frequency ν_0 , indicating that the stray field is larger at this position than at the positions where the atoms are interacting with the first microwave pulse. We also find an incomplete population transfer probability of the second pulse, $\xi = 90\%$, which can be attributed to a non-uniform microwave excitation field across the atomic ensemble. The signal is also not zero on resonance because of the inhomogeneous broadening taken into account by the fit parameter $\sigma_{\text{stray}} = 1.4(1)$ MHz.

The resonance frequencies ν_c and $\nu_{c'}$ provide information on the magnitude of the stray electric fields. At an electric field strength F of less than 1 V/cm, the Stark shift

$$\Delta\nu_{\text{Stark}} = \frac{1}{2}\Delta\alpha F^2, \quad (4.10)$$

of the $np \leftrightarrow ns$ transition frequency is purely quadratic for $n < 40$ [Fig. 4.5(a)]. For example, for the $34p \leftrightarrow 34s$ transition used in the next section and for the field measurements in Sec. 9, the diagonalization of the Hamiltonian including the Stark shift [Zimmerman *et al.* (1979)] leads to a value of $1078.03 \text{ MHz}(\text{V}/\text{cm})^{-2}$ for the polarizability $\Delta\alpha$. Because of the small quantum defect of the np state, $\Delta\alpha$ is larger by 2 to 3 orders of magnitude compared to the polarizability between low- l states of alkali atoms [Pritchard (2011)]. This transition therefore provides a sensitive tool to measure electric fields.

4.2.2 Spatially resolved measurement of electric fields

To measure and compensate stray electric fields, the method described in [Osterwalder and Merkt (1999)] is used. The line shifts $\Delta\nu_{\text{Stark}}$ of the $34p \leftrightarrow 34s$ transition

are measured for several intentionally applied potential differences between electrodes 1 and 2 (zone 1), 2 and 3 (zone 2), or 3 and 4 (zone 3). In zone 1, the field was estimated from spectra recorded with one microwave pulse, as illustrated in Fig. 4.6(b), whereas in zones 2 and 3, spectra are obtained after applying two microwave pulses using the procedure described in the previous section.

A typical stray-field measurement carried out 10 μs after the laser excitation in zone 2 (without sample and sample holder) is displayed in Fig. 4.7(a). In this figure, $\Delta\nu_{\text{Stark}}$ is plotted against the applied potential difference V (bottom horizontal scale). The solid line represents a fit to the measured central frequencies using Eq. (4.10). The electric field \mathbf{F} was decomposed into its components perpendicular (F_{\perp}) and parallel (F_{\parallel}) to the propagation direction (z direction) of the atomic beam,

$$F^2 = F_{\perp}^2 + F_{\parallel}^2 = F_{\perp,\text{stray}}^2 + (F_{\parallel,\text{stray}} - cV)^2. \quad (4.11)$$

The factor c relates the potential difference V between electrodes 2 and 3 to the parallel electric field component at the position of the atoms. The position of the apex of the parabola given by Eq. (4.10) and (4.11), and measured in Fig. 4.7(a) represents the potential difference for which the component of the stray field parallel to the beam-propagation axis is compensated, i.e., $F_{\parallel} = 0$. A remaining shift at this position originates from a perpendicular component of the stray electric field and potentially further systematic shifts such as pressure shifts and ac Stark shifts. With the value of $\Delta\alpha$ given above, one obtains stray-field components $F_{\parallel,\text{stray}} = 65(1)$ mV/cm and $F_{\perp,\text{stray}} = 27(5)$ mV/cm. The extracted value of c ($0.601(6)$ cm $^{-1}$) corresponds closely to the value of 0.615 cm $^{-1}$ obtained from a two-dimensional finite-element calculation of the electric-field strength in zone 2 for our electrode configuration. The 2% discrepancy may originate from the uncertainty of the position of the atom cloud. Because both the pressure shifts and the ac Stark shifts are negligible under our experimental conditions, we consider the perpendicular component of the stray field to be the dominant contribution to the shift of 414(160) kHz of the zero-field resonance frequency. Given the sensitivity of the Rydberg transition, the typical duration of a microwave pulse (~ 200 ns), and the absolute maximal travel time of the atoms through the zone (≤ 5 μs) these fields are small enough to not be a limiting factor for coherent population transfers in the Rydberg cloud.

By carrying out similar measurements for different delays $t_{\mu}^{(2)}$ between laser excitation and the second microwave pulse and as a function of the detuning $\Delta_0 = \nu - \nu_0$ of the microwave frequency with respect to the field-free transition ν_0 , we determine the local stray-electric-field strength along the propagation axis for a known beam velocity. Such a measurement, carried out between electrodes 2 and 3 in zone 2 (without sample and sample holder), is depicted in Fig. 4.7(b).

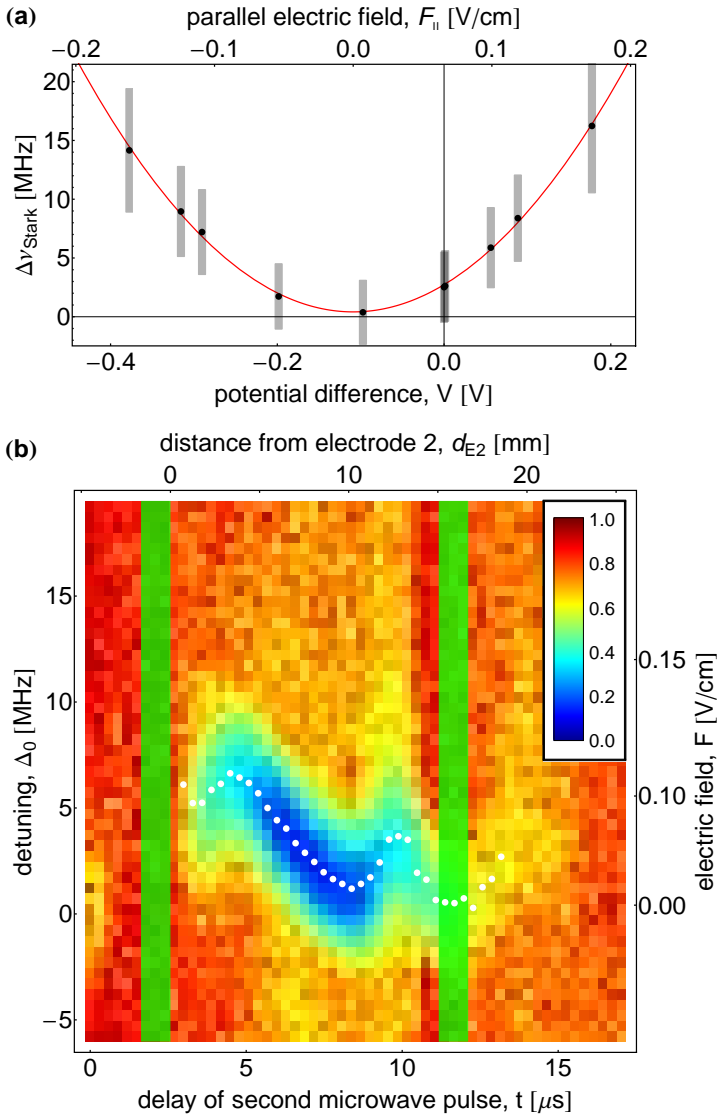


Figure 4.7: (a) Measured transition frequency as a function of the applied electric potential difference V to electrode 3 (bottom axis) and the corresponding parallel electric field $F_{||}$ (top axis). The uncertainties of the transition frequencies are of the order of the size of the dots. The vertical bars correspond to the widths (FWHM) of the lines in MHz and the red line is a quadratic fit of the Stark shift. (b) Population in the $34s$ state as a function of the time delay t (bottom axis) and the detuning Δ_0 of the microwave frequency from the field-free (atom) transition frequency (left axis). The blue areas indicate low $34s$ state population and the green areas show the positions of the electrodes 2 and 3. This provides a map of the stray electric field strength along the propagation axis (top axis) in the sample region with the right axis indicating the electric field F , determined from the fitted transition frequencies (white dots).

In this region, the stray field does not exceed 110 mV/cm. Also, the finite size of the atom cloud which could average over different electric field strengths is negligible, because the observed linewidths are all close to the transform limit of the microwave pulse.

The different strengths of the observed transitions are because of a position-dependent microwave field amplitude. In Sec. 8.1 we present a method to simultaneously determine the microwave field strength and the electric field strength above a gold surface. Using amplitude and phase-controlled microwave pulses we also pursued coherent measurements in free-space from which we were able to determine the relative angle between electric and microwave fields [Köpsell and Thiele (2016)]. The microwave field distribution is determined by the geometry of the setup and the position of the horn antenna and cannot be determined a priori. We consistently observe the formation of standing waves between the electrodes in zone 2.

4.3 Important experimental methods and characterizations

In this section we discuss important technical characterizations of the Rydberg excitation laser (Sec. 4.3.1), the pulsed field ionization (Sec. 4.3.2), and the microchannel plate detector (Sec. 4.3.3.1).

4.3.1 Rydberg state excitation laser

The simplest excitation of the helium atoms from the metastable 1S_0 singlet state to the np Rydberg states is achieved with a one-photon transition by means of a high power laser pulse, the wavelength of which can be tuned over a range of several nanometers, and which has a fixed duration T_λ and intensity I_λ . The excitation rate (Rabi rate) decreases with n as [Eq. (1.4) and (1.30)]

$$\Omega = \frac{\langle \Psi_{n,p} | \mathbf{d} | \Psi_{2,s} \rangle}{\hbar} \sqrt{\frac{2I_\lambda}{\epsilon_0 c}} \propto n^{-\frac{3}{2}}. \quad (4.12)$$

As consequence, a threshold state n_{th} exists, above which $\Omega T_\lambda < 2\pi$. For $n \leq n_{\text{th}}$, the resonant excitation probability $p(0, \Omega, T_\lambda) \approx 0.5$ [Eq. (4.8)] if the excitation is incoherent. For coherent excitation $p \leq 1$ depending on the pulse length and intensity. For $n \gg n_{\text{th}}$, $p(0, \Omega, T_\lambda)$ decreases with n as

$$p(0, \Omega, T_\lambda) = \sin \left[\frac{T_\lambda}{2} \Omega \right]^2 \approx \left(\frac{T_\lambda \Omega}{2} \right)^2 \propto n^{-3}. \quad (4.13)$$

Larger laser intensities I_λ increase n_{th} such that Rydberg states with larger principal quantum number n are efficiently excited.

In this subsection we present the important characterizations of the Nd:YAG-pumped dye laser system we use in the experiments. The system consists of a combined pump (Nd:YAG) and dye laser system. The Nd:YAG laser (interchangeably used with pump laser hereafter) creates population inversion in a dye that decays. These systems are a good choice as a Rydberg excitation laser with the following strengths and challenges:

Strengths

- a) large-range wavelength *tunability* over several 100 nanometers by using different dyes.
- b) short-range wavelength *tunability* over ranges exceeding tens of nanometers, depending on the fluorescence bandwidth of the dye.
- c) *large peak intensities*: For example, for dyes lasing in the visible red, energies exceeding 80 mJ per pulse length of $T_\lambda \approx 10$ ns are possible. The corresponding peak powers are in the range of tens of megawatt and can be focused to areas well below 1 mm^2 .
- d) efficient *frequency doubling*; because of the large peak intensities conversion efficiencies of $\gtrsim 20\%$ can be achieved in a single pass of the doubling crystal.

Challenges

- a) *repetition rates* are limited to ~ 25 Hz for large pulse energies, because of the Nd:YAG pump laser⁴.
- b) large *linewidth* ($\gtrsim 0.1$ GHz), limited by the oscillator design or, fundamentally, by the short pulse length.
- c) large ($> 5\%$) *power fluctuations* from shot to shot.

The *pump laser* (INNOLAS: SpitLight 600-25) is operated at the repetition rate of $R_{\text{Exp}} = 25$ Hz. It is optimized to produce an optimal pump power of 90 mJ per pulse with minimal power fluctuations. Inversion population in the Nd:YAG crystal is achieved by pumping with an externally triggered flashlamp pulse of $200 \mu\text{s}$ length. The 10-ns-long laser pulse at 1064 nm is produced at t_λ by Q-switching a cavity using an externally triggered Pockels cell. The radiation is amplified in a second crystal and then frequency doubled ($\lambda = 532$ nm) within a LiB_3O_5 (LBO) crystal. The orientation of the crystal with respect to the beam axis is adjustable from

⁴There exist also Nd:YAG laser systems that operate in the kHz regime (or continuous mode), but with smaller pulse energies.

outside the laser head and should be checked bimonthly. We have the possibility to add an additional BaB_2O_4 (BBO) crystal for frequency tripling to 355 nm. For definition of the laser mode and production of fourier-transform limited pulses, the laser features a seed-laser, the use of which is specifically important when pulse-amplifying cw-lasers in dye solutions.

To minimize power fluctuations in the Nd:YAG laser, the energy per pulse is measured as a function of the delay of the Pockels-cell with respect to the flash-lamp trigger [black, solid line in Fig. 4.8(a)]. The pulse-energy is measured using a pyro-electric head (*OPHIR:PE50BF-DIF*) after a $f = -100$ mm diverging lens positioned after the laser output to reduce peak intensities. The values are obtained by calculating the mean and standard deviation of the measured pulse energies during a time of 1 min. Maximal energy per pulse is produced when the Pockels cell switches $215 \mu\text{s}$ after the flashlamps is being triggered. Because the energy fluctuations are almost independent of the Pockels cell delay (dashed line, scaled by 10), minimal relative fluctuations (red trace) are obtained for maximal pump-laser output power.

To adjust the maximal output power of the Nd:YAG laser [Fig. 4.8(b)] to the optimal pump value of ~ 90 mJ/pp a Pockels cell delay of $150 \mu\text{s}$ (green trace) is therefore not ideal. Operation of the laser at the optimal point and reduction

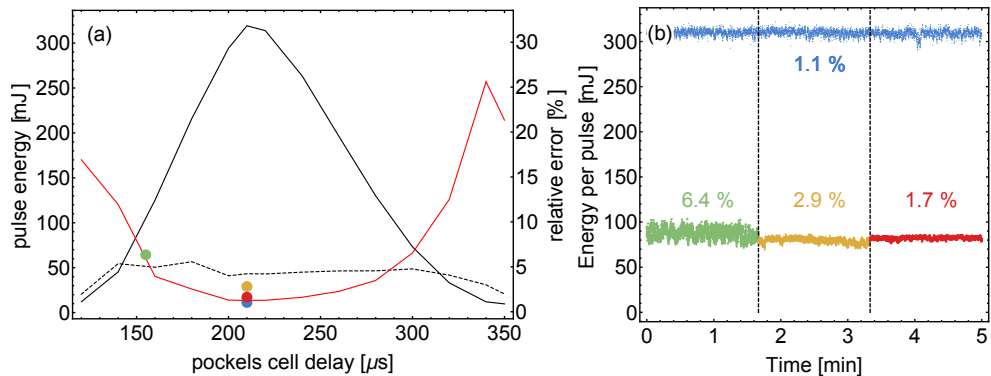


Figure 4.8: (a) Nd:YAG pulse energy (black curve) as function of Pockels cell delay with respect to flashlamp trigger and absolute fluctuations (black dashed line, scaled by factor of 10) are given by the left axis. Relative fluctuation levels (red line) are given by the right axis. The colored dots indicate settings and fluctuation levels for the measurements in (b). (b) Nd:YAG laser pulse energy measured as function of time. The blue and green trace show measured pulse energies for Pockels cell delays of $215 \mu\text{s}$ and $155 \mu\text{s}$, respectively. The yellow measurement shows pulse energies at optimal laser conditions after a $\lambda/2$ -plate and Glan-Thompson polarizer and the red curve after a motorized attenuator consisting of 2 polarizers. Numbers correspond to fluctuation levels (standard deviation). Because of an uncoated, diverging lens in front of the power meter, all measured energy levels are reduced by $\sim 10\%$ from the true values.

of the power at the output of the laser head using a Glan-Thompson polarizer in combination with a $\lambda/2$ -waveplate, reduces power fluctuations to 3 % (yellow). The increased fluctuations with respect to the optimal point are attributed to additional polarization changes in the waveplate. The best fluctuations levels of 1.7% (red trace) are achieved with a motorized attenuator before frequency doubling, i.e. in the laser head. The attenuator consists of a waveplate and a polarizer, the rotation of which varies the output energy with a visibility between $\sim [12.5, 87]\%$. Large visibilities approaching $[0, 100]\%$ cannot be reached because of temperature-induced rotations of the polarization in the waveplate, caused by the 25-Hz-repetition rate. In summary, we present the most important settings for the Nd:YAG laser in Tab. 4.2.

The dye laser we use (*FINE ADJUSTMENT: Pulsare-S*) fluoresces between 595 nm and 665 nm (FWHM) using a DCM dye (*SIRAH*) diluted in ethanol. The concentration in the first (rectangular) cuvette is 0.34 mg/l, positioned in a resonator made of an output coupler and a double grating with 2400 l/mm. The oscillator beam is pre-amplified in the same cuvette and then amplified in a bethune cell (DCM concentration: 0.06 mg/l). A rough procedure to align the dye laser can be found in the manual and should be checked and re-optimized on a biweekly basis. The optimal energy parameters can be found in Tab. 4.3.

We extract 1% of the laser output power after the dye laser for additional beam characterization. About 10% of this light enters a hollow-core helium-neon discharge lamp for absolute calibration of the laser wavelength. A small fraction ($< 1\%$) is coupled into an optical multimode fiber and sent to a wavemeter (*HIGH FINESSE:WS/6-200-UV*) with a measurement range from 248 nm to 1100 nm and an absolute accuracy of ≤ 200 MHz. The remaining light is sent through an etalon, whose transmission is monitored by a photodiode.

Table 4.2: Operation settings of Nd:YAG laser.

oscillator		Pockels cell	
amplitude	560 μ s (typ.)	high voltage	90%
pulse width	200 μ s	high voltage	enable
trigger	extern	delay	215 μ s (extern)
delay	0 μ s	stepper	
shot mode	normal	set value	40% (typ.)
available elem		interlock 2	
shutter	OK	shut. closed, sim. off	OK
single pulse	OK	energy control	no regulation
one stepper	OK	admin password	Dieter

Table 4.3: Optimal operation values of dye laser. Values are measured after indicated position.

position	wavelength [nm]	energy [mJ/pp]	power fluctuations [%]
Nd:YAG	532 nm	90	1.7
bethune	625 nm	21	< 5%
output	312.5 nm	2.8	< 8%

The spectral linewidth of the dye laser is specified to $< 0.04 \text{ cm}^{-1} = 1.2 \text{ GHz}$. However, a well-aligned dye-laser can exhibit smaller linewidths of $\sim 0.5 \text{ GHz}$ [Fig. 4.9(a)]. The data was acquired by the wavemeter over a time of 1 h, and fitted by a Gaussian distribution.

The main laser light from the dye laser is frequency doubled in an LBO crystal with an efficiency exceeding 10% (Tab. 4.3). Because the conversion efficiency being very sensitive to the orientation of the crystal with respect to the beam propagation axis, the crystal needs to be rotated if the wavelength is varied. We calibrated the rotation of the doubling crystal such that the output power of the frequency-doubled dye laser is approximately constant over the relevant range between 312 nm and 317 nm [Fig. 4.9(b)].

For the standard settings (Tab. 4.2 and Tab. 4.3), the output power of the dye laser can be tuned with the variable attenuator in the Nd:YAG laser between 0.2 and 9 mJ/pp at 312.5 nm [Fig. 4.9(c)]. The red line is a fit to the expected sinusoidal behaviour of the polarizer and the waveplate:

$$P_{\lambda} = 4.6 - 4.4 \sin(1.3 + 3.6 \frac{x}{100}). \quad (4.14)$$

The combined Nd:YAG-dye-laser system needs about 1.5 h to warm up and stabilize its output pulse energy [Fig. 4.9(d)]. For this plot, 9 different warm up curves with final values randomly distributed between 0.5 and 2.8 mJ have been normalized and overlayed. The black line indicates a running average over 2000 measurement points.

After the dye laser, the laser beam is spatially filtered with a telescope [focal lengths $L1 = 50 \text{ mm}$, $L2 = 75 \text{ mm}$] and a pinhole (not shown) in the focus [ABCD-matrix calculations in Fig. 4.10(a,c)]. The second lens is mounted on a translation stage and can be moved. Two pinholes ($PH1$, $PH2$), opened to a diameter of 4 mm, are positioned at a fixed distance of 403 mm and 708 mm to $L1$, respectively. A collimating lens ($L3 = 1000 \text{ mm}$) is positioned after $PH2$ at a distance of 55 mm. The last pinhole is positioned after a distance of 865.0 mm, and opened to 3 mm. The final cylindrical lens ($L4 = 200 \text{ mm}$) at a distance of 50 mm from $PH3$ focuses the laser beam along the x direction into the experiment. It is oriented such that

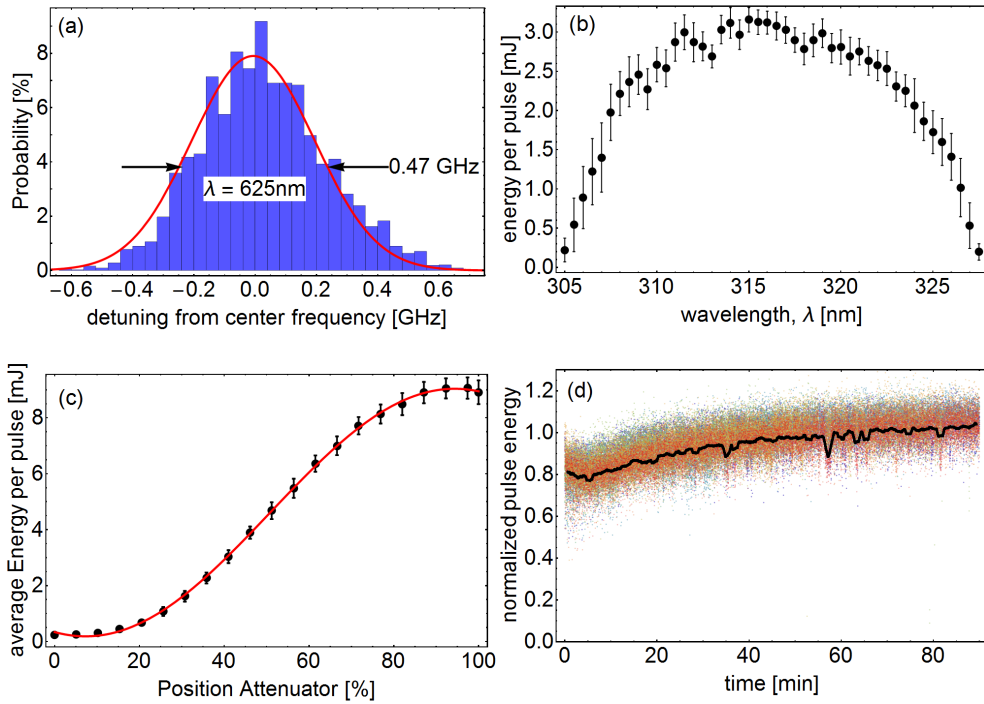


Figure 4.9: Dye-laser properties when pumped with Nd:YAG laser in configuration corresponding to the red trace in Fig. 4.8(b). (a) Histogram of 625-nm-radiation from the Dye laser as function of detuning from center frequency (blue data). The red curve indicates a Gaussian fit with a FWHM of 0.47 GHz. (b) Average dye-laser pulse energy as function wavelength. (c) Average dye-laser pulse energy when the power of the pump laser is varied using the adjustable attenuator (black dots). The red line is a fit to a sinusoid. (d) Normalized dye-laser pulse energies for 9 different measurements as function of time during laser warm-up. The black line indicates a running average over 2000 measurement points taken at a rate of 25 Hz.

in the focus, the width of the laser beam is smallest in z direction, i.e. atom beam propagation direction.

The spatial overlap of the laser beam and the atomic beam can be changed in a specific way by varying the position of $L2$ with respect to $L1$ to either 121 mm or 133 mm. Relevant beam paths (indicated in caption) for the two configurations are shown in Fig. 4.10(a,c), respectively. In Fig. 4.10(b,d) corresponding simulations show the possible beam radii for the z (red) and y direction (blue) at the position of the atoms, and for all possible laser divergences after the dye laser.

Configuration 1 (distance $L1$ to $L2$ is 121 mm) creates a focus in z direction and has a width of ~ 2 mm in the y direction. This is a configuration that is suited to excite Rydberg atom packets that are optimized for imaging electric fields above

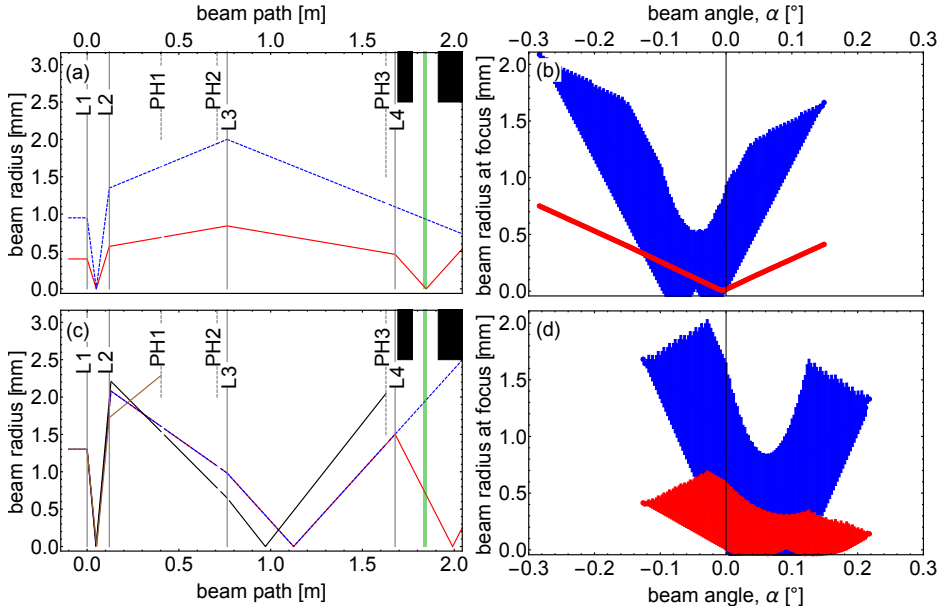


Figure 4.10: (a,c) Laser beamwidth calculations for two different lens configurations L2. Black lines indicate positions of lenses (L1-L4) and black dashed lines indicate positions and diameter of diaphragms (PH1-PH3), values given in the text. The black areas indicate the dimensions of the entrance holes in the heat shield. (a) Laser path for configuration 1, see text, to get a small beam in z (red) direction and a wide beam in y direction (dashed, blue). (b) Possible laser-radii as a function of initial dispersion angle of laser beam at position of atoms [green line in (a)] for z direction (red area) and y direction (blue area), and for lens configuration 1. (c) Laser path for configuration 2, see text, to get a beam width in z (red) direction of ~ 1.5 mm and a beamwidth in y direction (dashed, blue) of less than ~ 4 mm. The black and brown traces indicate blocked beams with an initial dispersion angle of 1 and -1 mrad, respectively. (d) All possible radii as a function of initial dispersion angle of laser beam at position of atoms [green line in (c)] for z direction (red area) and y direction (blue area), and for lens configuration 2.

chip surfaces because they are small in z direction and extended in y direction (Sec. 9).

Configuration 2 (distance $L1$ to $L2$ is 133 mm) maximizes the beam in y direction (maximal width ≤ 4 mm) such that it never clips at the exit laser hole of the cryostat [second black rectangle in panel (c)]. In the z direction the length of the excited atom packet extends up to 1 mm. Because of the temperature in the longitudinal direction of the atom beam (Sec. 3.2) this length grows until $\lesssim 4$ mm, which is on the order of extensions of the region out of which Rydberg electrons can be efficiently extracted during ionization (Sec. 4.3.2). This configuration is best suited for measurements where the number of atom is to be maximized.

4.3.2 Pulsed field ionization

Rydberg atoms are typically detected in zone 4 between electrode 4 and 5 using pulsed field ionization. To pulse the high voltage (HV) electric field we use two different HV-switches the difference of which we highlight in the following. Specific focus is put on the characterization of the custom-built switch used for detection of electrons.

For detecting *ions* we use a commercial switch (*BEHLKE: GHTS 60A*). This push-pull switching unit can switch up to ± 6 kV between two high-voltage-(HV) levels and within tens of nanoseconds. However, the trigger signal is transformer-coupled to the high voltage output switch and needs to be refreshed in order to overcome the low-frequency characteristics of the transformer. This refresh pulses couple as 3-V-noise spikes of ~ 100 ns duration to the output. The charging rate ~ 5715 Hz is incommensurate with the 25-Hz-repetition rate of the experiment. The spikes lead to measured potential differences > 100 mV between electrode 3 and the ground of the sample holder, a potential difference corresponding to additional stray fields > 200 mV/cm in the center of the experimental region.

To detect *electrons*, we use a custom-built, simplified push-pull pulser which does not recharge the capacitors. A TTL-pulse of 100 ns length controls a driving section that switches a high-voltage MOSFET between ground (0 V) and an applied high voltage V_{app} . For $V_{\text{app}} = -1.2$ kV, the voltage at the output reaches the same value within 70 ns when measured with a high-voltage probe [blue trace in Fig. 4.11(a)]. The measured voltage overshoots to -1.4 kV and oscillates because of poor impedance matching at the probe. The signal exhibits an exponential decay back to 0 V (fit indicated brown) at the end of the trigger pulse. The decay time (215 ns) is explained by the RC-time of the capacitance of the probe cable and the 1 k Ω resistance to ground at the output of the pulser.

If the pulser is connected to the experiment, the potential pulse at electrode 4 (solid, black trace) exhibits a longer decay time of 802 ns (exponential fit indicated red). The pulse form was measured with the same HV-probe and with respect to the ground potential of the experimental setup and differs less than 5% when measured with respect to the potential on the close-lying electrode 5 (dashed data). The potential difference between electrodes 4 and 5 is relevant, because it produces the electric field for ionization. The RC-time is given by the same 1k Ω resistance to ground at the output of the pulser and the combined 217 pF capacitance of the electrode to ground and the high voltage cable in the cryostat (Fig. 5.5).

The measured maximal potential (~ 600 V) at electrode 4 does not correspond to the applied potential of $V_{\text{app}} = -1.2$ kV. In fact, the pulser exhibits a linear correspondence between applied and measured, maximal output voltage up to $V_{\text{app}} \approx -.75$ kV, only [black data in Fig. 4.11(b)]. A linear fit results in a pitch of 1.06 (solid, red line). For larger applied potentials, the energy provided by the device is

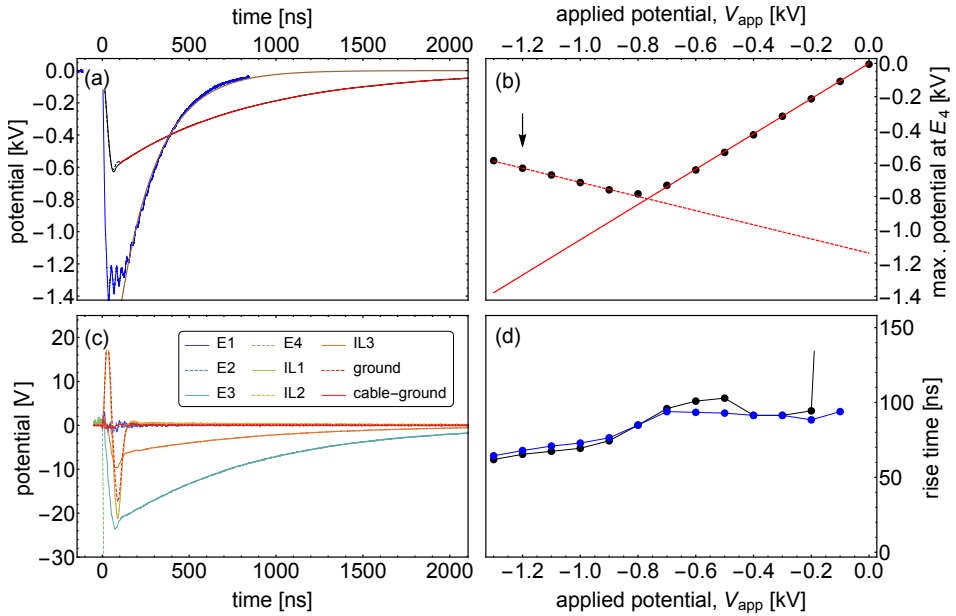


Figure 4.11: HV-switch characterization. (a) Measured high-voltage pulses at output of HV-switch (blue data) and at electrode 4 with respect to experiment ground (solid black data) and with respect to electrode 5 (black dashed data). Red and brown lines indicate exponential fits with best fit values given in the text. (b) Maximal electric potential at electrode 4 as function of applied electric potential. Measured data is indicated black, red lines indicate linear fits. In the experiments we use the configuration indicated by black arrow. (c) Capacitive couplings from electrode 4 to other electrodes and ground as function of time. (d) Rise time of HV-pulse at electrode 4 (black data) and for potential difference between electrode 4 and 5 (blue data) as function of the applied potential to the HV-switch V_{app} .

not enough to charge the electrodes because of the large resistance (88Ω) of the high voltage cable in the cryostat. As a result, the maximal potential difference between electrode 4 and experiment ground decreases for $V_{app} \leq -0.75$ kV with a fitted pitch of -0.425 (dashed, red line). In the experiments we apply a potential of $V_{app} = -1.2$ kV to produce a potential difference of 600 V with respect to experiment ground and electrode 5, respectively (black arrow). This, because the rise times of ~ 65 ns are smaller than the 100 ns for $V_{app} = -0.6$ kV [Fig. 4.11(d)].

The fast potential change on electrode 4 for $V_{app} = -1.2$ kV couples capacitively to the nearby electrodes [Fig. 4.11(c)]. Because of different capacitances, different electrodes exhibit different potential changes as a function of time. The nearest electrodes *E3*, *IL1* and the experimental ground exhibit maximal potential

changes between 3% and 4.1% of the total potential change at electrode 4. This indicates that the capacitive coupling is dominated by the Al_2O_3 plates by which the electrodes are isolated from experimental ground (Sec. 5.2.1).

In Fig. 4.12(a) 2-dimensional finite element simulations of electric fields in the rotationally symmetric ionization region are presented. For a potential on electrode 4 (green rectangles at 0 mm) of $V_4 = -0.6$ kV, the fields range from 0 V/cm (blue) to more than 650 V/cm (dark red). The black arrows indicate the direction of the electric field and the opaque blue area indicates the typical position and dimensions of a Rydberg atom beam at ionization. Panels (b) and (c) show cuts along the white, dashed lines, i.e. through the saddle point of the field in the center between electrodes 4 and 5.

For a Rydberg beam with velocity of $v_0 \approx 1800$ m/s, $t_{\text{ext}} = 18.5$ μs is the extraction time for which a maximum number of atoms is detected for $n^* \geq 30$. For this extraction time the center of the Rydberg atom beam is positioned 1.5 mm before the center of E_4 and $IL1$. Monte-Carlo simulations of electron trajectories reveal, that extraction from positions at distances ≥ 5 mm from electrode 4 is inefficient, because the electrons do not arrive at the MCP [Fig. 4.12(d)]. The black trajectories correspond to initial positions (black dots) from which the electrons arrive at the MCP, located at a distance of 150 mm in z direction. Red dots correspond to initial positions from which electron trajectories end on metallic surfaces before the MCP [compare e.g. Fig. 4.18(b)].

The trajectories are almost independent of the applied electric field for two reasons. *First*, the electrons are insensitive to the temporal change of the electric field. Because of their small mass the electrons are accelerated to $\sim 0.1c$ and travel through the ionization region (i.e. ≤ 5 mm) within < 1 ns, a time during which the electric field can be considered stationary. *Second*, the applied electric field strength at all positions scale linearly with V_4 (the only applied potential), but the local electric field direction is independent of V_4 (up to a sign). As a result, also the electron trajectory is independent of V_4 as long as the polarity does not change. Larger V_4 contribute only to larger velocities of the electron along their trajectory.

From the simulations we can explain why the state $n^* = 28$ in the spectra presented in Fig. 4.2 and Fig. 4.4 is only partially ionized. The adiabatic ionization field of this state is 522 V/cm. Since we expect only a few diabatic crossings between adjacent states in the ionization process [Gallagher (1994)], the atoms ionize at the same adiabatic electric field value. The area enclosed by the thick black lines in Fig. 4.12(a) and (d) [dashed lines in Fig. 4.12(b,c)] indicate the region, for which the electric field varies between ± 5 V/cm from this value. The poor detection efficiency of the state $n^* = 28$ is therefore because of the small overlap of the Rydberg beam at its ionization position and the region in which the state can be ionized. Additionally, the push-pull pulser provides potential differences $\gtrsim -600$ V

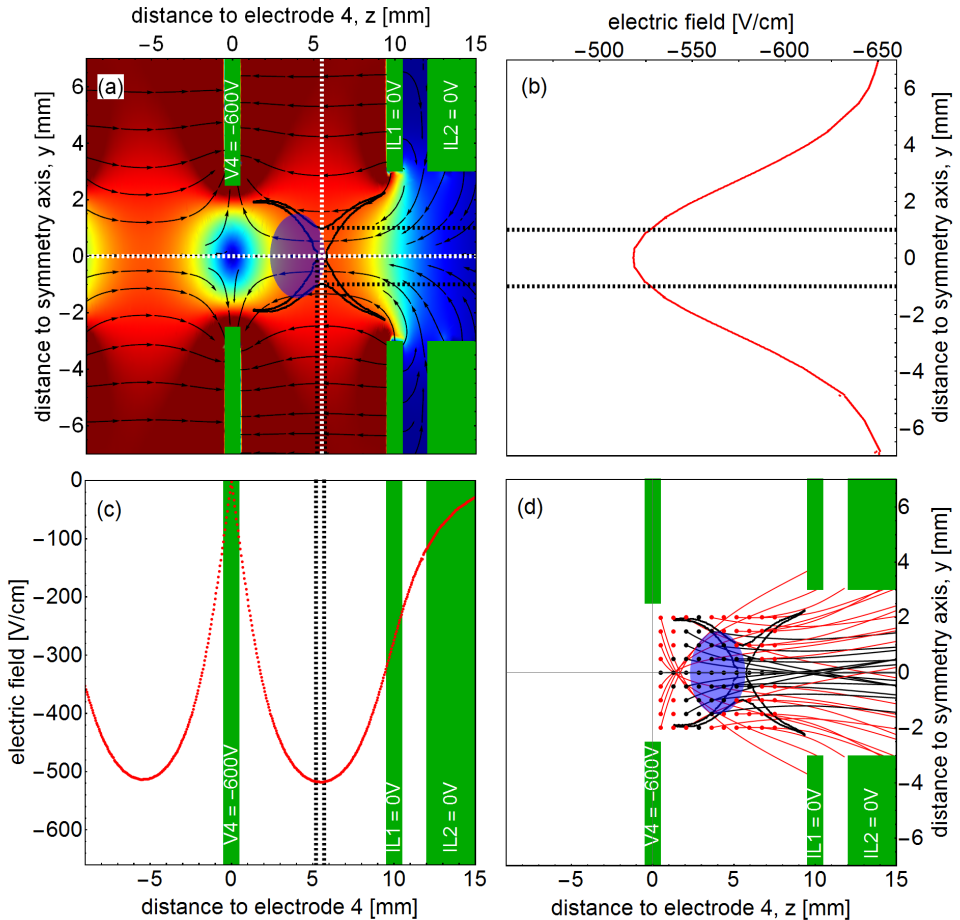


Figure 4.12: (a) Simulated electric field strength (colored data) and direction (black arrows) in ionization region for a potential of -600 V applied to electrode 4. The green areas indicate the positions of electrode 4 and einzel lens electrodes IL1 and IL2. The black contour indicates the region where the electric field does not deviate by more than 10% from its value in the center. The colorscale goes from -650 V/cm (dark red) to 0 V/cm (dark blue). (b,c) Crosssections along the white, dashed lines in (a). The black dashed lines indicate the region where the electric field does not deviate by more than 10% from its value in the center. (d) Simulated trajectories of electrons when accelerated by the electric field. Black trajectories correspond to electrons that reach the MCP, electrons following red trajectories do not.

only for a few nanoseconds [Fig. 4.11(a)] in which the Rydberg atoms can be considered stationary, i.e. do not move into the ionization region during the extraction pulse.

4.3.3 Atom beam detection techniques

For the detection of Rydberg electrons/ions we use an imaging microchannel plate detector assembly (MCP) in a chevron configuration (*PHOTONIS: APD 2 PS 40/12/10/8 I 60:1 P47*). Because of their large internal energies, detection of the He^* atom pulse with maximal MCP-amplification decreases the lifetime of the detector. Therefore, we operate it in pulsed mode, as highlighted in Sec. 4.3.3.1. We apply two different read-out techniques, i.e. read out of detector time traces for Rydberg atom detection, and measurements of atom distributions within the beam. We discuss acquired time traces of the microchannel plate detector in Sec. 4.3.3.2. Additionally, we convert the detected MCP signal to an equivalent number of Rydberg atoms in the pulse. Although we use the imaging option of the detector to characterize He^* and Rydberg atom distributions, the detected signal depends also on other aspects, e.g. the performance of the einzel lens, which will be discussed in a separate section (Sec. 4.3.3.3).

4.3.3.1 The microchannel plate detector

The detector consists of two microchannel plates (front- and backplates indicated black in Fig. 4.13). Each plate contains microchannels of diameter $10\ \mu\text{m}$ distributed over a circular area with diameter $40\ \text{mm}$ and which are spaced by $12\ \mu\text{m}$. A single particle that enters one of these channels collides with the walls because of the channels aspect ratio of $60:1$ and the angle of 8° with respect to the surface. For large enough energies, the particle creates secondary electrons out of a dielectric coating. Because of the large potential difference $\gtrsim 1.8\ \text{kV}$ between the first (biased with $V_f = 0\ \text{V}$) and the second plate (biased with $V_b = 1.8\ \text{kV}$), the electrons are accelerated and multiplied in an avalanche effect⁵. The avalanche effect continues in the channels of the second microchannel plate [potential difference to phosphor screen (blue) $\sim 3.2\ \text{kV}$]. As a result, a single particle is converted to more than $\gtrsim 5 \times 10^6$ electrons [Wiza (1979)], the charge signal of which can be extracted from the output face of the second plate to obtain time-resolved measurements of the arriving particles. Because amplification happens only if the particle enters a channel, the active area of the MCP is given by the combined diameters of all channels, which cover about 55% of the plate area (OAR: Opening aspect ratio).

The final electron avalanche excites the phosphor screen (P47) displaying phosphorescence at a wavelength of $400\ \text{nm}$, and with a decay time of $\sim 60\ \text{ns}$.

⁵The presented applied potentials are optimized for detection of neutral and negatively charged particles.

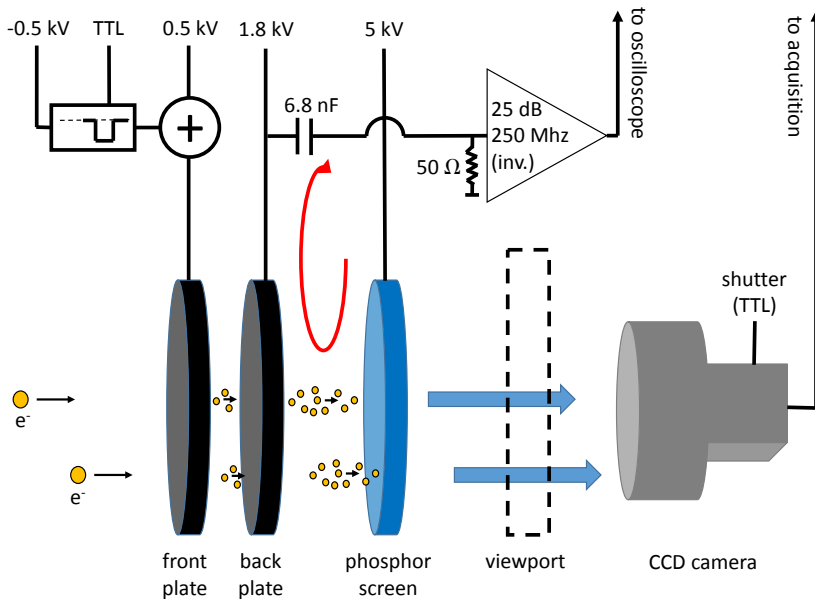


Figure 4.13: Sketch of typical working principle of the imaging, chevron-type microchannel plate detector assembly we use. The presented applied potentials are optimized for detection of neutral and negatively charged particles. The front microchannel plate (black disk) is constantly biased with 0.5 kV and can be reduced to 0 kV upon a TTL-trigger. Primary electrons (yellow) are avalanche-multiplied within the potential difference to the back plate (black disk), typically biased at 1.8 kV and again within the potential difference to the phosphor screen (blue disk), typically biased at 5 kV. The voltage drop because of the compensating current (red line) between front and back plate is capacitively monitored by an oscilloscope via an inverting amplifier of ~ 250 MHz bandwidth. The light from the phosphor screen is imaged using a CCD camera outside the vacuum chamber.

The light is collected with an objective (*FUJINON: 16mm HF16HA-1B*) and a CCD camera (*SONY: XCD-V60*) outside of the vacuum chamber. A fast acquisition system (*I/O PCIe-8255R* with FireWire interface) allows for read out of the camera images with the repetition rate of the experiment (25 Hz) and are post-processed in the control program (Sec. 5.4). The camera images reveal spatial information of the arriving particle distributions in the $x - y$ plane.

Microchannel plates have finite lifetime because of a maximum cumulated charge that can be processed by the dielectric coating [*Authinarayanant and Dudding (1976); Kishimoto et al. (2006)*]. *Kishimoto et al. (2006)* quote a processed charge density of $\sigma_{\text{tot}} \approx 10^{19} e^- / \text{cm}^2$ ($\sim 600 \text{ mC/cm}^2$) until the gain drops by 5–20%. Similar values are quoted by the manufacturer of our detector. As a result,

in our experiment, we expect the lifetime of the detector to be reached after a few days, i.e. heavily exposed areas of the detector are getting dark (no amplification).

Indeed, only the uv-photons generated in the discharge, the metastable, and the Rydberg atoms have enough internal energy to create secondary electrons. The total charge transferred in an experiment is dominated by the number of metastable atoms $N_{\text{He}^*} \sim 2 \times 10^5$ (Sec. 3.1). In a series of experiments where all the metastable atoms are detected, the maximal transferred charge is reached after a time of $t_{\text{life}} \approx 60$ h as estimated from

$$t_{\text{life}} = \frac{\sigma_{\text{tot}} A_{\text{He}^*}}{GN_{\text{He}^*} R}, \quad (4.15)$$

with the metastable atom beam diameter at the MCP of $A_{\text{He}^*} \approx 1\text{cm}^2$, the gain $G \approx 5 \times 10^6$ [Wiza (1979)] for $V_b = 1800$ V and the repetition rate of the Experiment $R_{\text{Exp}} = 25$ Hz.

The best way to increase t_{life} is to reduce G when the metastable pulse arrives at the MCP. The gain depends exponentially on the applied potential difference between front and back plate [Wiza (1979)] as characterized in Fig. 4.15(b). For example, a moderate reduction of 200 V is enough to change the gain by 1 – 2 orders of magnitude. Consequently, we bias the frontplate at a constant potential of $V_f = 500$ V ('MCP front') and the back plate at $V_b = 1.8$ kV ('MCP back', Fig. 4.13) decreasing the gain by more than 3 orders of magnitude. For efficient detection of Rydberg electrons the potential at the frontplate is lowered to 0 V by adding -500 V ('MCP switch') to the frontplate potential for the time window at which electrons arrive at the MCP. The window is controlled by an external TTL-trigger. Therefore, the potential difference relevant for the amplification of the MCP detector is given by the potential applied at the back electrode V_b .

The large applied potentials and the fast switching rates require the microchannel plates to be operated at pressures well below 10^{-6} mbar. Additionally, the MCP assembly needs to be conditioned before the first use and after being exposed to air. The start-up procedure [Photonis (2009)] takes about a day and requires to increase the potentials at the different plates in specific voltage and time steps.

4.3.3.2 Detection of time traces of Rydberg atoms

The electron pulse that leaves the backplate of the MCP develops a voltage across the path of lowest impedance in the MCP-readout-electronics circuit, which includes the $50\text{-}\Omega$ input resistor of the preamplifier (red arrow in Fig. 4.13). This drop is amplified by 25 dB using the inverting amplifier with a bandwidth of ~ 250 MHz [Friese (2015)], and detected using an oscilloscope.

Fig. 4.14(a-g) presents preamplified MCP signals as acquired with the oscilloscope for decreasing time intervals. The green area in every picture indicates the time interval shown in the next panel. We present measurements of three different configurations. Red traces indicate typical measurements, when Rydberg atoms are detected, black traces indicate measurements when the Rydberg excitation laser is blocked, and for blue traces the high voltage of the MCP's frontplate is kept at the constant potential of 0.5 kV, i.e. is not pulsed. All traces are averaged over 25 instances. Because the MCP being triggered by the falling edge of the extraction pulse, 0 s in the presented time traces corresponds to $t_\lambda + 18.5 \mu\text{s}$. Because of the high impedance of the MCP, the detection is sensitive to small potential changes caused by capacitive coupling to other potentials that are switched fast. In the following, we explain the different events we observe in our experiment (labeled 1 – 9) in each panel.

- (a) The events indicated (1) and (2) show two consecutive repetitions of the experiment, separated by the repetition time, i.e. $\tau_{\text{Exp}} = 1/R_{\text{Exp}} = 40 \text{ ms}$. A single repetition of the experiment does not last longer than one millisecond. The baseline fluctuations between two consecutive events are ground fluctuations caused by the 50 Hz of the mains. The noise in the mains signal causes a temporal jitter of $\sim 20 \mu\text{s}$ between two experiments. Hence, fast oscillations [compare event labeled (5) panel (c)] are averaged out in the second experiment at 40 ms with respect to the acquisition trigger at 0 ms.
- (b) Label (3) indicates a capacitive coupling from the valve driver at t_V , i.e. when the valve opens. In this realization of the experiment, $t_{V\text{-DC}} = 480 \mu\text{s}$ for valve configuration 2 [Fig. 3.4(d-f)].
- (c) The two spurious signals separated by $30 \mu\text{s}$ [label (4)] are caused by switching the high-voltage discharge pulse V_{DC} on and off. The transient oscillations [label (5)] in the black trace decay on a timescale of $\sim 150 \mu\text{s}$. They are produced in the amplifier and arise from switching the 500-V-potential on the frontplate of the MCP.
- (d) The two events labeled 6, separated by $1 \mu\text{s}$, are spurious signals due to the from switching the high voltage of the Pockels cell in the Nd:YAG laser head (Sec. 4.3.1). Label 7 indicates the spurious signals from the trigger of the camera taking images of the phosphorscreen (Sec. 4.3.3.3).
- (e) Events indicated (8) are oversteering of the amplifier to its saturation level of $\pm 4 \text{ V}$ because of the large potential difference (500 V) being switched on

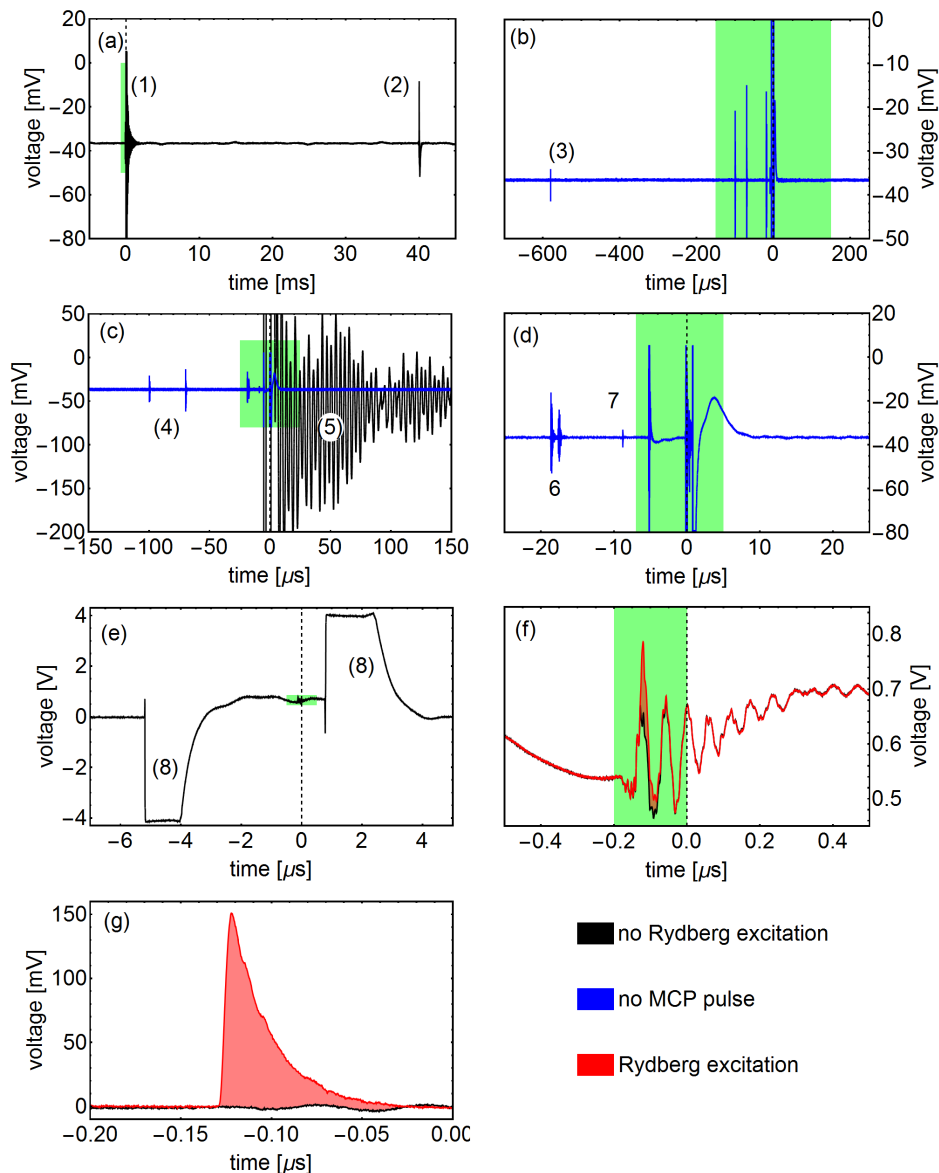


Figure 4.14: Sequential zoom into the MCP timetrace starting from timespans ranging (a) between two subsequent pulses to (g) time trace of Rydberg signal, see text for details. The pulsing of the MCP is switched off for blue data and black data are acquired with a blocked laser as compared to the typical measurement situation (red data). Green areas indicate region of the next plot. Labels are explained in the text.

the frontplate within a microsecond. The transient oscillations also dominate the variation of the ground level between the switching pulses [compare event labeled (5) in (c)].

- (f) Typical time window as acquired by the oscilloscope during an experiment. The slow oscillations in the black and red trace are remaining transient oscillations from switching the MCP amplification [compare label (8)]. The fast oscillations in the traces are capacitively coupled signals from the extraction pulse of 600 V at time t_{ext} (Sec. 4.3.2).
- (g) Similar traces as in panel (f), but after electronic subtraction of the black trace using the oscilloscope. The red signal indicates the measured Rydberg-electron signal (compare Fig. 4.5) that is acquired by the measurement computer. The small oscillations in the black trace never increase to more than 20 mV peak-to-peak. They arise if the extraction time t_{ext} jitters because of ground fluctuations.

To interpret the measured signal in panel (g) with an experimental quantity, we estimate the number of detected electrons in the pulse by division of the signal of a single Rydberg electron [Fig. 4.15(a)].

The histogram indicates the probability of integrated MCP signals (pulse-height-distribution) for a back voltage $V_b = 2.05$ kV, and when a single Rydberg electron is detected. To detect only single atoms, $\Delta t_{V\text{-DC}} = 310$ μs (valve configuration 1) and the laser energy $E_\lambda \approx 80$ $\mu\text{J/pp}$. Only MCP traces were considered, in which the measured MCP voltage signal surmounts a threshold twice above the noise level of the acquired traces (i.e. 0.15 mV), far below the typical measured maximum voltages of 250 mV. From all acquired 2101 traces only 20% (387) contained a signal. The mean of all measured integrated MCP signals (20.3 nVs) agrees with the most probable signal (red line) which we define as the integrated signal of a single Rydberg electron⁶. The large spread of the probability distribution is typical for microchannel plate detectors, which rely on the avalanche effect.

We determine the amplification of the MCP as a function of the voltage applied to the back electrode by two different measurements [Fig. 4.15(b)]. The black datapoints correspond to fitted amplitudes of the spectra of the $(1s)^1(2s)^1\ ^1S_0 \rightarrow 47p$ transition. The blue data points correspond to integrated MCP traces. For both measured datasets, the linearity of the amplification process was assured by delaying $\Delta t_{\text{DC-V}}$ and therefore reducing the signal strength if the maximal measured

⁶It is safe to identify this signal with a single Rydberg atom because of the suppressed peak at $\gtrsim 30$ nVs, and because only 80% of the traces showed no detected peak.

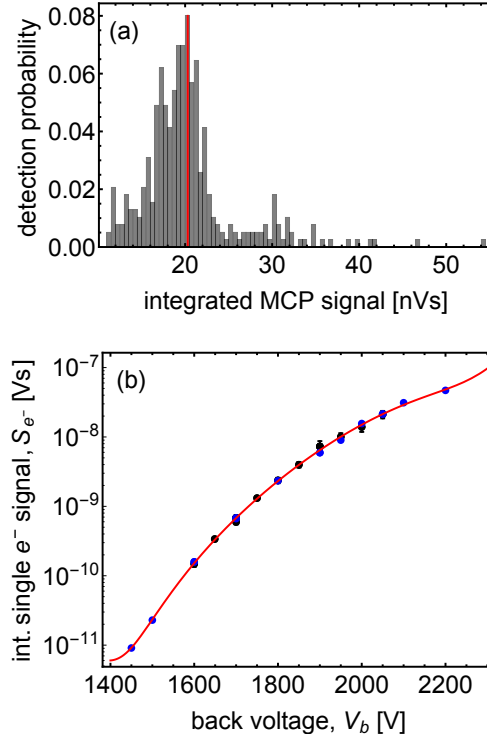


Figure 4.15: (a) Histogram of integrated MCP signals for amplification potential of 2.05 kV and single atom detection. The red line indicates the typical single atom signal of 19 nVs. (b) Amplification of MCP normalized to single atom signal as a function of the MCP backplate voltage for two different measurements (blue and black points), see text. The red line is a fit to a Eq. (4.16).

voltage exceeded 500 mV. Nonlinearities may arise if the MCP amplifier is operated above its saturation point (~ 4 V), or the electron avalanche in the microchannels saturate. Saturation of the microchannels is more likely for larger amplification, when more than one particles enter the same channel within its recovery time.

The measured data was normalized to the single atom value determined in Fig. 4.15(a). The red line describes the integrated signal strength S_{e^-} of a single Rydberg electron for the MCP's relevant bias range between 1500 – 2100 V and can be fitted by a modified exponential:

$$S_{e^-} = 5.09 \times 10^{-18} e^{0.01097V_b} \left(1004.113 - 2.65643 V_b + 2.763421 \times 10^{-3} V_b^2 - 1.4129849 \times 10^{-6} V_b^3 + 3.554940 \times 10^{-10} V_b^4 - 3.5253 \times 10^{-14} V_b^5 \right) \quad (4.16)$$

Other MCPs with similar fabrication parameters are expected to exhibit a similar gain function, but can have an additional offset in V_b because of a different resistance between front and back plate.

4.3.3.3 Detection of spatial atom distributions

In our experiments, we detect the spatial distributions of metastable and Rydberg atom distributions arriving in the x - y -plane at the MCP. Helium atoms in metastable states have enough internal energy to create secondary electrons that multiply and can be detected using the phosphor screen. Direct detection of Rydberg atoms is inefficient, because the number of co-propagating metastable atoms dominates the number of Rydberg atoms (Tab. 3.1). Therefore, the Rydberg atoms are pulsed field ionized and the electrons accelerated such that they arrive at the MCP before the metastable pulse (Fig. 3.6). In this subsection we first explain the detection of metastable atom beam distributions and then concentrate on the imaging of Rydberg-electron distributions using the MCP combined with an einzel lens.

Images of the *metastable atom* distribution in the beam are useful to determine the size and position of the atom beam relative to the sample. The MCP frontplate is located ~ 150 mm downstream from electrode 4. To convert the image size and position measured at the detector into the size and position of the beam above the sample surface, a slit aperture of 0.8 mm width is placed immediately after the sample, with its lower edge at the sample surface. The beam image [Fig. 4.16(a)] is limited in its upper (lower) part by the upper (lower) edge of the aperture and on the sides by the circular hole of 6 mm diameter through which the beam passes when it exits the cryostat. The shape of the image and the knowledge of the geometric constraints provide a one-to-one correspondence between image pixels and small tubular volumes above the sample surface.

A pair of razor blades (Fig. 2.1) aligned parallel to the surface of the samples (x direction) is used to collimate the beam just before zone 1. For instance, in the coherent experiments above plain surfaces (Sec. 8.1), the distance between the blades is reduced to ~ 500 μm , i. e., less than the laser-beam width. The position of the blades is individually adjustable in the direction orthogonal to the surface so that they form an adjustable slit aperture. The cross-section of the beam, see Fig. 4.16(c), is then constrained in its lower and upper parts by the razor blades. The absolute position of the beam center at 250 μm above the surface is derived from the image pixels and the previously determined one-to-one correspondence to the tubular volumes. The beam width (full width at half maximum) in the direction normal to the surface (y direction) can be directly estimated from the detected intensity of the images along the yellow lines in Fig. 4.16(a) and (c). These are 0.8(1) mm and 0.50(6) mm, respectively, in the presented example.

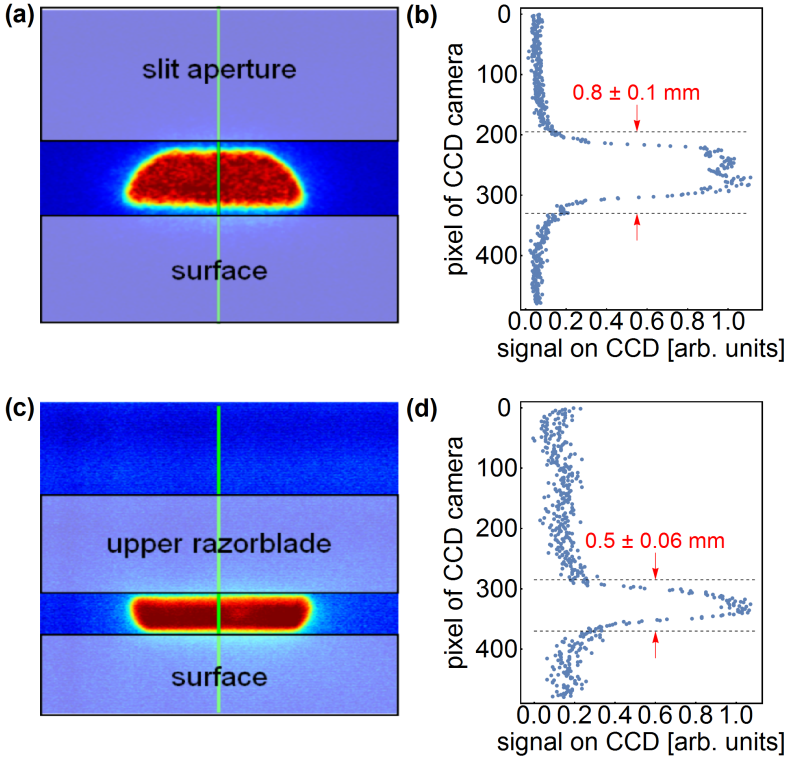


Figure 4.16: Measurement of the position and width of the He* beam above the chip surface with an imaging MCP. Image obtained without (a) and with (c) collimating adjustable aperture. The intensity profiles along the vertical lines in panels (a) and (c) are displayed in panels (b) and (d), respectively (see text for details). The color scale in (a) and (c) corresponds to the minimal (blue) and maximal (red) value of each measurement and can be deduced from the cuts along the green lines.

To detect *Rydberg atoms*, the camera shutter is triggered open for $10 \mu\text{s}$ when Rydberg electrons arrive at the MCP and closed before the arrival of the metastable atoms [compare label (7) in Fig. 4.14(d)]. If the einzel lens is inactive, the Rydberg electrons arrive at the same spot at the MCP, given a magnetic-field-free flight region between zone 4 and MCP (Sec. 5.3).

The detection of Rydberg atoms with images is expected to be equivalent to a detection of Rydberg atoms with integrated time traces of the MCP. To verify this, laser spectra were taken by integration of camera images over the same spatial filter (e.g. a square of 50×50 camera pixels for red trace in Fig. 4.17), and they were compared with spectra acquired by integration over a time window of the MCPs time trace [Fig. 4.14(g)]. Both traces exhibit similar noise values and show simi-

lar relative strengths of the spectroscopic lines. The difference in signal strength for $n \gtrsim 80$ ($\Delta E_{\text{I}} \gtrsim -500$ GHz) is attributed to both, the non-ideal magnetic field compensation and to a spread observed in the arrival position of the electrons at the MCP which is larger than the spatial integration window. For these large values, the observed crosssection of the Rydberg electrons has a rectangular shape, is aligned to the magnetic compensation coils and most of the signal is concentrated on two adjacent corners.

Application of a suitably chosen, constant potential V_{IL2} to the center electrode of the *einzel lens* (IL2) allows to image distributions of Rydberg atoms at the position of ionization (i.e. between electrode 4 and IL1 in zone 3). The electrostatic lens expands the electron cloud by a factor more than 6 in the x and y direction while it travels in a magnetic-field-free region of ~ 150 mm length (Sec. 5.3). The ideal potential that is applied to obtain undistorted⁷ images of Rydberg atom distributions depends on the ionization potential of the examined Rydberg state. We have performed characterization measurements of the performance of the einzel lens with atoms in state $n^* = 47$ and simulations for both, atoms in state $n^* = 47$ and $n^* = 33$. The motivation to also simulate detection of Rydberg atoms in state

⁷As characterized from simulations and by comparison of acquired images of a Rydberg beam (not interacting with a chip surface) with the expected shape from the excitation of the Rydberg laser.

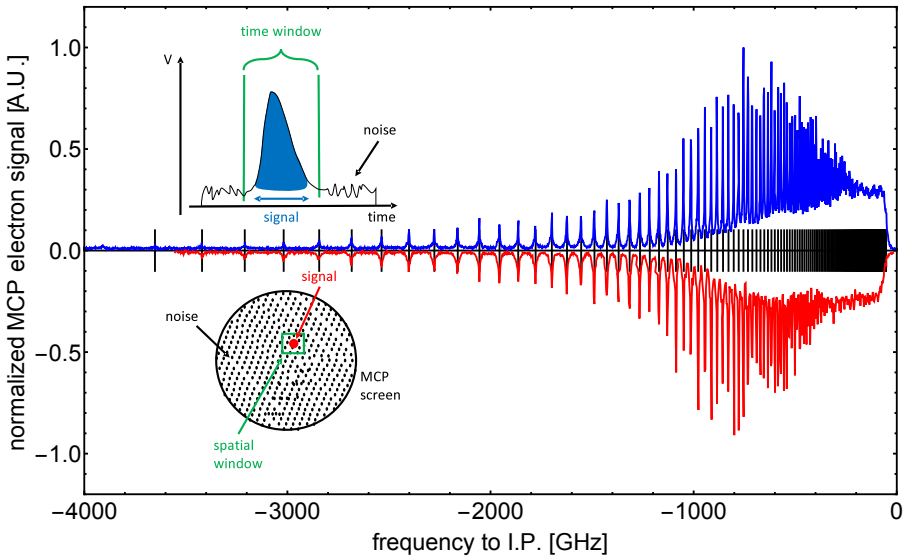


Figure 4.17: Comparison of two similar spectra acquired by integration over a window of the MCP time trace (blue data, upper panel) and by integration over a spatial window in the MCP images acquired by the CCD camera (red data, lower panel). Black lines indicate theoretical positions of the Rydberg states. Data and sketches modified from *Goblot (2014)*.

$n^* = 33$ is given by our atom distribution measurements above patterned surfaces (Ch. 9). In the following, we therefore discuss the performance of the einzel lens on the basis of these two states.

As discussed before, the region between electrode 4 and *IL1* where ionization takes place is rotationally symmetric, and separated by 22 mm from the experimental region (zone 2), including a 9 mm-long, sample-free space between electrode 3 and 4 (Sec. 5.2.1). Electrode 4 (green rectangle indicated 'E4' in Fig. 4.18) is separated by 10 mm from the einzel lens, a set of 3 electrodes with centers separated by 6 mm. All electrodes are circular, disk-shaped with outer diameter of 80 mm and have a hole of diameter 5 and 6 mm for the ionization electrode and the einzel lens, respectively.

The optimal applied potential to image Rydberg atoms in state $n^* = 33$ with minimal distortion in the images is $V_{IL2} = 600\text{V/cm}$ (determined below), which creates electric field strengths up to $\sim 1.5\text{ kV/cm}$ [Fig. 4.18(a)]. Our extraction pulse (Sec. 4.3.2) ionizes the state $n^* = 33$ purely adiabatically [Fig. 4.2(a)] at electric field strengths $F_I \approx 480\text{ V/cm}$. As soon as the ionization pulse exceeds values of -425 V at electrode 4, the field in the center of the ionization exceeds F_I . All other metallic surfaces (indicated green) are at 0 V.

We performed Monte-Carlo simulations of trajectories of electrons that are generated by ionization from ensembles of Rydberg atoms located between E4 and *IL1*. For the simulation we consider all applied electric fields, including electric fields generated from the potentials applied to the MCP, as obtained from finite element simulations. The electric fields from the ionization pulse are considered static. The calculation with static electric fields is justified, because in the experiment ionization of the Rydberg atoms is achieved by pulsing a potential on E4 that falls linearly from 0 to -600 V within $\sim 60\text{ ns}$ (Sec. 4.3.2). Within this short time, the position of the Rydberg atoms is not changed but the atoms are ionized as soon as the electric field strength exceeds the characteristic ionization field strength at their position. Because of their small mass, the electrons leave the ionization region within $\lesssim 1\text{ ns}$, a time, during which the ionization field has not changed. From the simulations we observe that the presence of the additional electric field from the einzel lens results in a larger range of positions in the ionization region from which electrons hit the MCP (black dots) as compared for $V_{IL2} = 0$ [Fig. 4.12(d)].

We characterize the performance of the einzel lens with Monte-Carlo simulations of 13 different ensembles of Rydberg electrons equally distributed between -3 and 3 mm in the y direction [Fig. 4.18(b)⁸]. Each ensemble contains 3000 particles the initial positions of which are normally distributed with a full width at

⁸For better comparison with measurements presented in Ch. 9, the y direction is given relative to the sample surface, positioned 0.5 mm below the symmetry axis of the experiment.

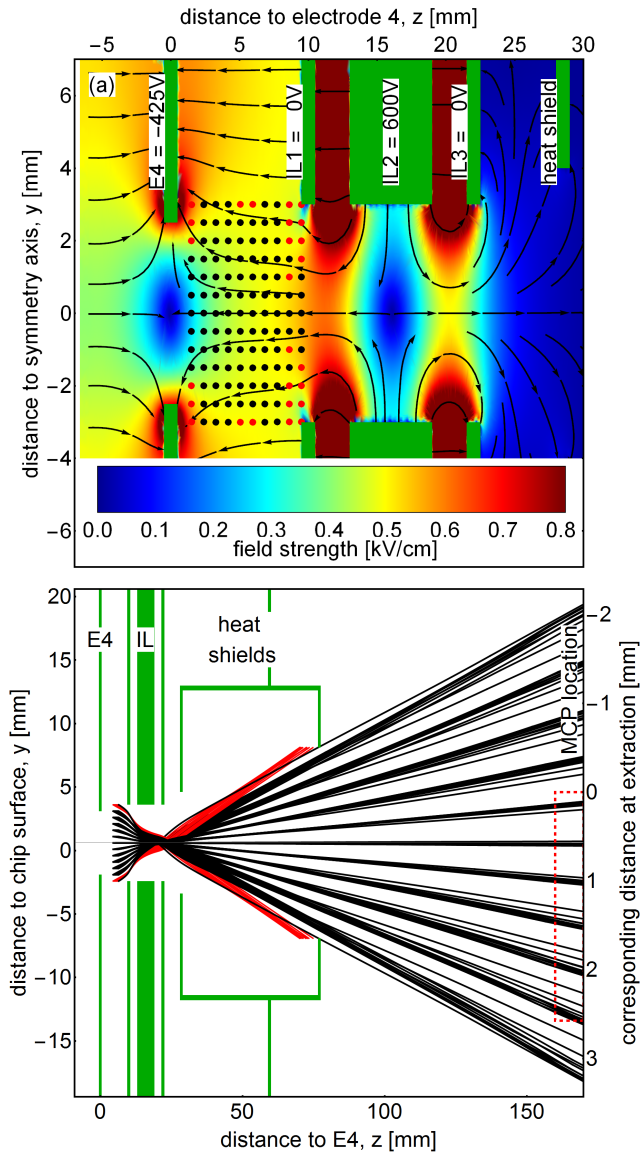


Figure 4.18: (a) Electric field strength and direction for pulsed field ionization of state $n^* = 33$. Green areas indicate positions (from left to right) of electrode 4, einzel lens electrode IL1, IL2 and IL3 and the grounded 3-K-heat-shield. The black dots correspond to locations that are imaged onto the MCP, locations indicated red are not. (b) Corresponding simulation of electron trajectories imaged onto the microchannel plate detector (MCP). Initial positions of the electrons beam are in the ionization region between the ionization lens (green rectangles labeled 'E4') and the einzel lens assembly (3 electrodes indicated by green rectangles and labeled 'IL'). The vertical distance from the position of the chip surface is given by the left axis. The corresponding position at the MCP is given on the right axis. Typical detection region on the MCP of atom beam in Ch. 9 is indicated by red, dashed line. Trajectories of electrons detected by MCP are indicated black, others are indicated red. Vertical and horizontal distances are scaled differently with the y direction given relative to the sample surface (positioned 0.5 mm below the symmetry axis of the experimental apparatus).

half maximum (FWHM) of 2.35 mm in the z direction, corresponding to the length of the Rydberg atom pulse at ionization. For the optimal value of V_{IL2} , we plot in Fig. 4.18(b) trajectories of only 10 particles per ensemble that are equally spaced within a distance of ± 1 mm from the central position in z direction. The trajectories of electrons which are detected by the microchannel plate detector (MCP), located at a distance of ~ 150 mm in z direction are indicated black, others are indicated red. We observe from the simulations that all electrons of one ensemble are mapped onto similar lateral (y -)positions of the MCP as expected for a faithful image, i.e. for well chosen V_{IL2} .

To determine the optimal value for V_{IL2} , we repeat the simulations for V_{IL2} varying between 0 and 800 V [Fig. 4.19(a)]. Here, we present histograms of electron distributions at the position of the MCP as a function of V_{IL2} , normalized to their maximal value. We observe, that faithful imaging is possible between 550 and 700 V, where 11 of the 13 considered electron ensembles are mapped onto similar y positions on the MCP. From their initial separations of 0.5 mm in y direction we conclude that the magnification of the electron beam varies between 5.8 and 7.6. For $V_{IL2} < 550$ V, imaging is not possible as the absence of the well-defined peaks in the histogram shows. A focusing of the electron beam onto the MCP is observable at $V_{IL2} \approx 220$ V. The white, dashed line in Fig. 4.19(a) and the red, dashed line in Fig. 4.18(b) indicate the typical part of the atom beam detected by the MCP for the field measurements presented in Ch. 9.

Further evaluation of the normalized simulated electron distributions at the position of the MCP provides details about the point-spread function of the electron beam imaging at the position of the MCP. Specifically, we observe that for a fixed einzel lens voltage of $V_{IL2} = 600$ V/cm the FWHM of a Gaussian fit to the electron distributions at the position of the MCP [red lines in right panel in Fig. 4.19(b)] varies between 0.21 mm in the center to 0.53 mm at the edge of the MCP, corresponding to distances above the surface of $\sim 25 \mu\text{m}$ and $\sim 66 \mu\text{m}$, respectively. This minimal feature size at the MCP corresponds approximately to the smallest feature size observed in our camera images. The fitted widths are almost independent of V_{IL} for values between $V_{IL} \approx 550 - 700$ V. Because the einzel lens produces an almost perfect quadrupole field at the locations through which the electrons pass, the point-spread function is determined by the varying directions of the electric field for every atom ensemble at ionization. In fact, these inhomogeneous electric fields in the ionization region limit the resolution fundamentally for this setup. In order to study the effects of fluctuating or wrongly applied potentials (e.g. due to wrongly determined ionization fields) on the point-spread function, we can average over the simulated electron distributions of V_{IL2} because of the linearity in the problem. The trace in the left panel of Fig. 4.19(b) presents the averaged electron distributions for V_{IL2} between 570 and 630 V/cm, i.e. $\pm 5\%$ of V_{IL2} . In this case, the

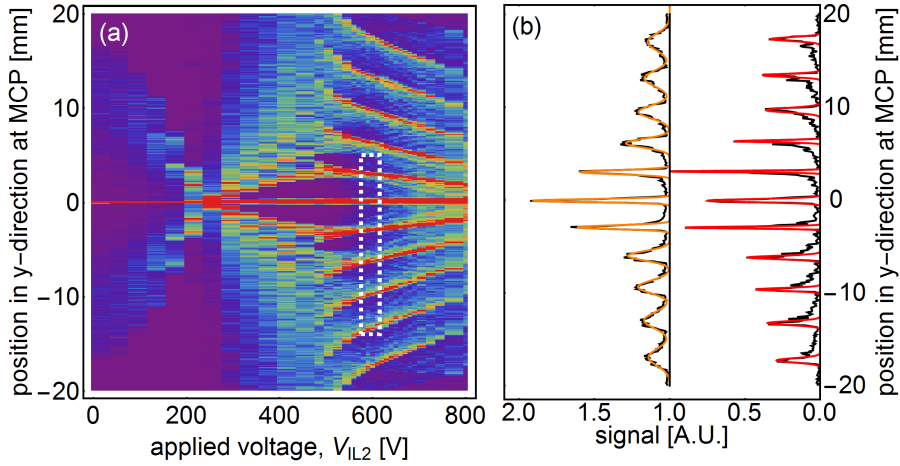


Figure 4.19: (a) Normalized spatial distribution of electrons at the position of the MCP as a function of V_{IL2} . The white, dashed line indicates the positions for which Rydberg electrons are detected in Ch. 9. The colorscale ranges from 0 (blue) to 1 (red) and can be deduced from the cuts in panel (b). (b) Normalized spatial distribution for $V_{IL2} = 600$ V (right panel) and averaged spatial distributions for V_{IL2} between 570 V and 630 V (left panel). The colored lines indicate Gaussian fits.

point-spread function broadens for atom positions that are ≥ 1 mm from the symmetry axis of the experiment. Fitted Gaussian functions (orange trace) reveal the FWHM varying between 0.39 mm and 2.1 mm at the position of the MCP or $48 \mu\text{m}$ and $260 \mu\text{m}$ for the corresponding positions above the surface.

In our experiments, the resolution of the images is not limited by the resolution of the electron-beam, but by the transversal velocity distribution of the Rydberg atoms in the beam. In a separate measurement, the shape of the Rydberg atom beam was manipulated at locations of 22 mm and 47 mm before the ionization by skimming the atomic beam using the razorblades and by strongly localized transfer of atom population, respectively. The smallest possible features observed were $\sim 130(10)$ and $\sim 250(20) \mu\text{m}$, respectively. A linear fit through the two points $(-47 \text{ mm}, 250 \mu\text{m})$ and $(-22 \text{ mm}, 130 \mu\text{m})$, reveals a beam spread of $\sim 0.48(14)^\circ$ and an offset of $24(36) \mu\text{m}$. The fitted beam spread of $0.48(7)^\circ$ corresponds to a maximal spread of $2 \times 0.48^\circ = 0.96(28)^\circ$, which agrees with the calculated maximal beam spread $\alpha_{\text{max},2}$ [Eq. (3.6)].

In an experiment that is designed for the best resolution of the fields, a laser-cooled beam of metastable $1s^1 2s^1 \ ^3S_1$ helium could reduce this spread to $\sim 0.01^\circ$ [Melchner von Dydiowa (2014)], given the doppler temperature $T = 29 \mu\text{K}$ of the $1s^1 2s^1 \ ^3S_1 \rightarrow \ ^3P_2$ transition, corresponding to a transversal velocity of 0.28 m/s,

and the velocity of the atom beam of ~ 1700 m/s. As a result, every point above the surface would expand to a disk with diameter of $4 \mu\text{m}$ after a flight distance of 22 mm, i.e. at the position of ionization. This is the fundamental limit of the resolution of the imaging system, because all subsequent spreading can, in principle, be overcome by designing homogeneous ionization fields and creating larger magnification by a long electron beam expansion or additional einzel lenses.

The results of the trajectory simulations have been compared with an experiment where Rydberg atoms have been excited to the $n^* = 47$ state (Fig. 4.20). The diabatic ionization field for the $n^* = 47$ state is 117 V/cm which is 24% of the ionization field of $n^* = 33$. The trajectories for electrons are determined by the relative strengths of the electric fields only, which is why we expect to observe the same performance of the einzel lens if we scale $V_{\text{IL}2}$ by 24%.

In fact, in the simulations [Fig. 4.20(a)] we observe the same electron distributions at the MCP as for the state $n^* = 33$ [Fig. 4.19(a)] when we simulate a potential at $E4$ of -105 V and vary $V_{\text{IL}2}$ between 0 and 200 V. Here, we present simulations of a single ensemble of 10000 Rydberg electrons that are normally distributed along the z direction with a FWHM of 2.3 mm and along the y direction with a FWHM of 4.5 mm.

In the experiment, Rydberg atoms were excited to $n^* = 47$ and the beam was restricted by the two razorblades to a FWHM of ~ 1.5 mm with its center at ~ 0.5 mm offset from the symmetry axis of the experiment. Similar to the simulation, $V_{\text{IL}2}$ was varied between 0 and 200 V. For every applied potential an image of the MCP was recorded and normalized to the maximal measured value. The line along the y direction containing the maximal measured signal in the picture was extracted, normalized and plotted for every applied $V_{\text{IL}2}$ [Fig. 4.20(b)]. The white dots in panel (a) correspond to the fitted FWHM of the measured atom distributions in panel (b).

The measured widths of the electron distributions agree well with the simulations. The slightly smaller observed width is because of the discrepancy between the simulated width in y direction (4.5 mm) and the width of the atom beam in the experiment (1.5 mm). The variation of the position of the maximal detected signal for small ($V_{\text{IL}2} < 50$ V) and large ($V_{\text{IL}2} > 170$ V) applied potentials is partially because of the offset of the atom beam from the symmetry axis, and a small misalignment between the symmetry axis of the electrode stack and the MCP.

Finally, we present in Fig. 4.19 (a-l) the trajectory simulations of Rydberg electrons produced from ionization of atoms in state $n^* = 47$. To observe the effect of faithful imaging, we simulate again the 13 ensembles separated by 0.5 mm along the y direction. The potential on electrode 4 is -105 V and $V_{\text{IL}2}$ was varied between 0 and 200 V with an additional simulation for $V_{\text{IL}2} = 600$ V as comparison to the optimal $V_{\text{IL}2}$ for detection of Rydberg atoms in state $n^* = 33$.

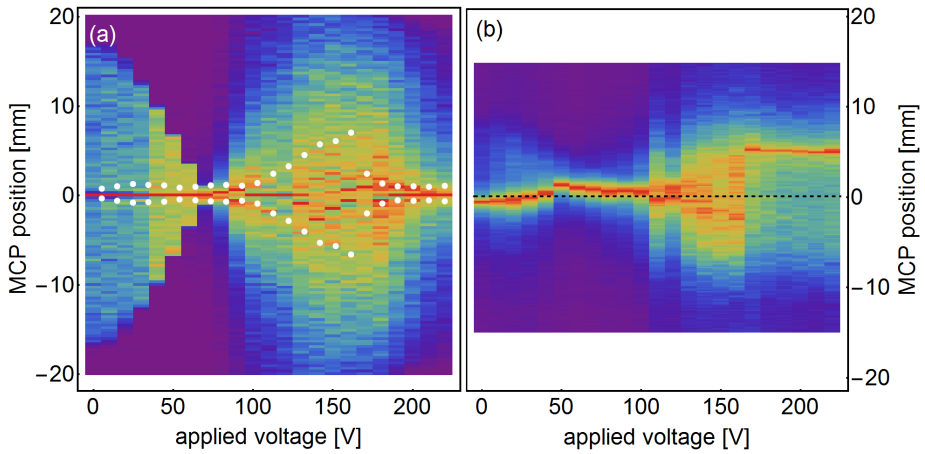
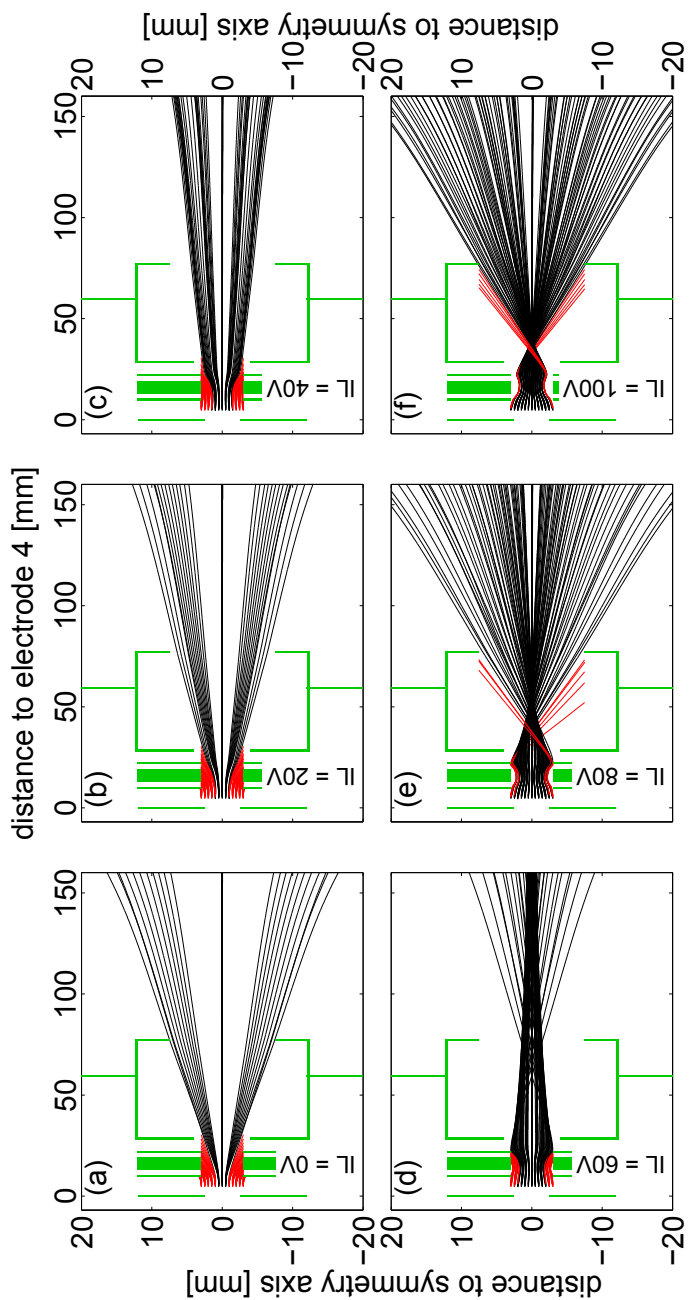


Figure 4.20: (a) Normalized simulated cuts through an image of a Gaussian distributed atom beam, see text, for einzel lens configurations as presented in Fig. 4.19(a-k). The black dashed lines indicated locations of focused electrons onto the MCP. White dots correspond to fitted FWHM of measurements in (b). (b) Corresponding measurements and cuts through the images containing the highest signal. Deviations of the focused electron beam to the center position of the MCP can be attributed to a rotation of the electrode stack and the atom beam not being centered with respect to the symmetry axis of the experiment. In both panels, the colorbar ranges from 0 (violet) over 0.5 (green) to 1 (red).

As also discussed for Fig. 4.12(d) in Sec. 4.3.2, only atoms close to the symmetry axis, i.e. ± 0.5 mm are detected if $V_{IL2} = 0$ and the atoms are detected from the middle between electrode 4 and $IL1$ [panel (a)]. With increasing V_{IL2} , positions at larger y -separations can reach the MCP until for $V_{IL2} = 60$ V [panel (d)] the electrons are focused onto the MCP. For higher V_{IL2} , the focus approaches the einzel lens until for $V_{IL2} \approx 140 \pm 10$ V, we observe faithful imaging onto the MCP. For this optimal einzel lens potential, the focus of the electron beam lies at about 5 mm after $IL3$. In a future setup, a pinhole could be installed at this position, such that the electrons can still be extracted and imaged on the MCP, but the solid angle for room temperature radiation to the sample is reduced (compare Sec. 5.2). Additional increase of V_{IL2} moves the focus into the einzel lens from which point faithful imaging is not possible anymore [panel (i-k)]. For excessive potentials ($V_{IL2} \approx 600$ V) applied to the einzel lens [panel (k)] the electrons are accelerated toward the metallic surfaces and only electrons which are extracted from the symmetry axis of the experiment reach the MCP.



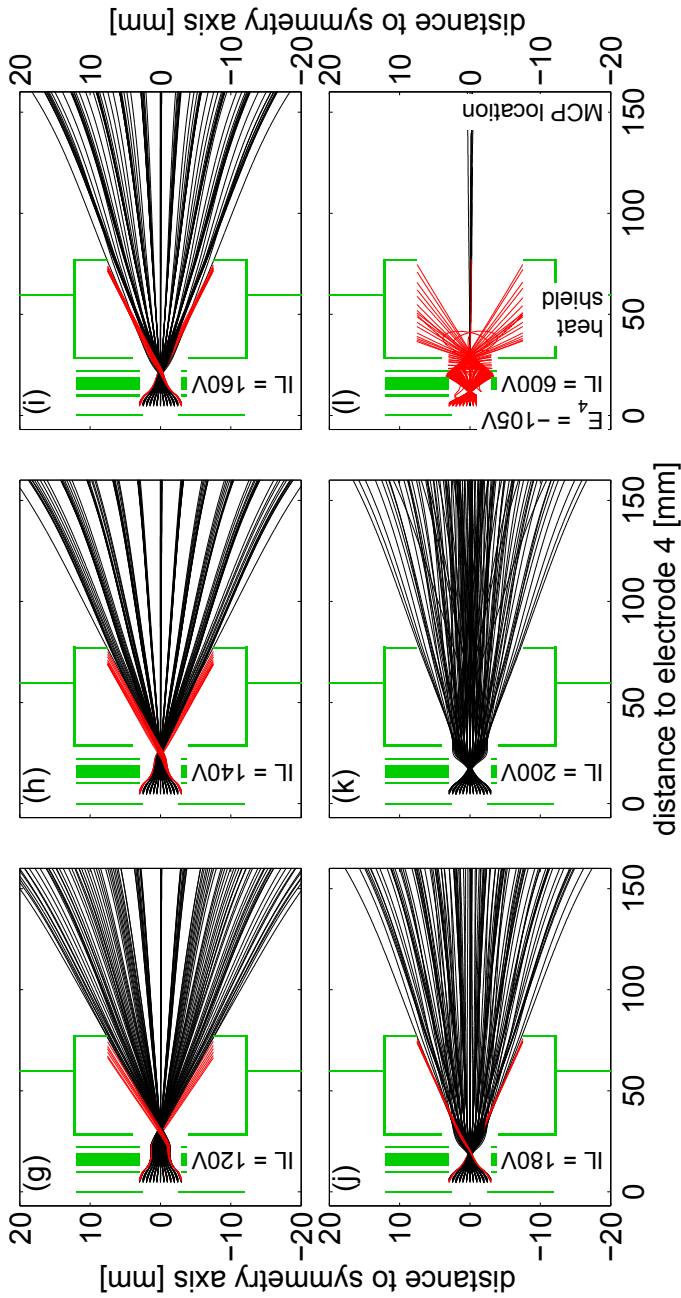


Figure 4.19: (a-l) Electron trajectories for 11 different atompackets in state 47, see text, and varying einzel lens potential, value given in panel. Faithful imaging of the initial atom distribution is observed for a potential of $IL \sim 140$ V [panel (h)].

DESIGN OF VACUUM CHAMBER AND CRYOSTAT

The adsorption of residual gas onto the sample surface leads to the build up of charges in the matrix of adsorbed material which causes rapidly increasing inhomogeneous stray electric fields leading to line shifts and line broadenings. These were the most important sources of decoherence in initial measurements [*Hogan et al. (2012a)*] (Sec. II). We avoided these effects by limiting the operating temperature to $T > 100$ K in these experiments.

To minimize the adsorption onto the sample surface and to reach workable temperatures below 4 K, we built a new vacuum chamber, a new cryostat, and developed a new cooling procedure to avoid residual gas adsorbing onto the sample holder or the sample surfaces. The setup is a key ingredient to do experiments of Rydberg atoms close to surfaces and fostered all the experiments presented in part 3 [*Thiele et al. (2014, 2015)*].

In this chapter we focus on the technical design of the experimental setup. Specifically, the vacuum setup is explained in Sec. 5.1 and the technical implementation of the cryostat and the design of the experimental region in Sec. 5.2. In Sec. 5.2.4 we present the design and measurement results of the specialized cooldown procedure which allows to minimize adsorption of residual gas onto the cold samples. Magnetic field compensation of the flight region of the Rydberg electrons, crucial for imaging atom distributions, is explained in Sec. 5.3. We conclude the chapter with a section on experimental control including a circuit

diagram of the different components and an overview of the control programs (Sec. 5.4).

5.1 Design of vacuum chamber

The experiment consists of three differentially pumped vacuum chambers, the source, the cryogenic, and the experimental chamber [schematics: Fig. 5.1(a), photograph: panel (b)]. The metastable atom beam is generated in the source chamber (green). Excitation, interaction with the surfaces, and detection of atoms in Rydberg states takes place in the cryostat (brown) and in the experimental chamber (black). The cryostat is supported by the cryogenic chamber (red), which contains the vacuum feedthroughs for the experimental control. Using a crane (magenta), the cryostat and the cryogenic chamber can be separated from the other chambers for maintenance. All chambers are supported by a light aluminum profile (*KANYA*) which forms a rigid connection between laser table and chamber for maximum stability. Depending on their functionality, the design of the vacuum chambers had to fulfill different constraints which will be discussed separately in the following for each chamber.

The high-vacuum-compatible *source chamber* (indicated green) consists of a stainless-steel ISO K-160 crosspiece with its four arms aligned along the z and y direction. The chamber is large enough to contain the atomic source (Sec. 3.1) which is inserted into the arm pointing in negative z direction. The source is attached to a specially designed source flange that consists of a metallic plate positioned on a dynamic seal which allows movement of the source in the x - y plane. A homebuild, 55-mm-thick adapter port of 220-mm diameter with 8 additional KF-25 ports is attached to the arm pointing in positive y direction. A vacuum gauge and the pre-vacuum side of the turbo pumps (blue) pumping the other chambers are attached to these ports. The chamber arm in positive z direction is elongated and reduced in diameter, such that it inserts into the arm of the experimental chamber to which it is connected by a 1-mm-sized skimmer. The chamber is pumped through the arm in negative y direction by a turbo molecular drag pump [Turbo pump, *PFEIFFER: HiPace 700*, indicated blue in Fig. 5.1(b)] with a pump rate of 685 l/s and a compression of 3×10^7 for helium.

The turbo pump provides high-vacuum conditions in the source chamber by maintaining a pressure difference of 5 orders of magnitude to the pre-vacuum ($\sim 5.2 \times 10^{-2}$ mbar). The pre-vacuum is created by a multistage roughing pump (*ADIXEN: ACP 15 Dry Pump*) that is connected with a 15-m-long vacuum hose to the gas outlet of the turbo pump. We measure pressures in the source chamber with a combined Pirani/cold-cathode vacuum gauge (*PFEIFFER: PKR 261*), which

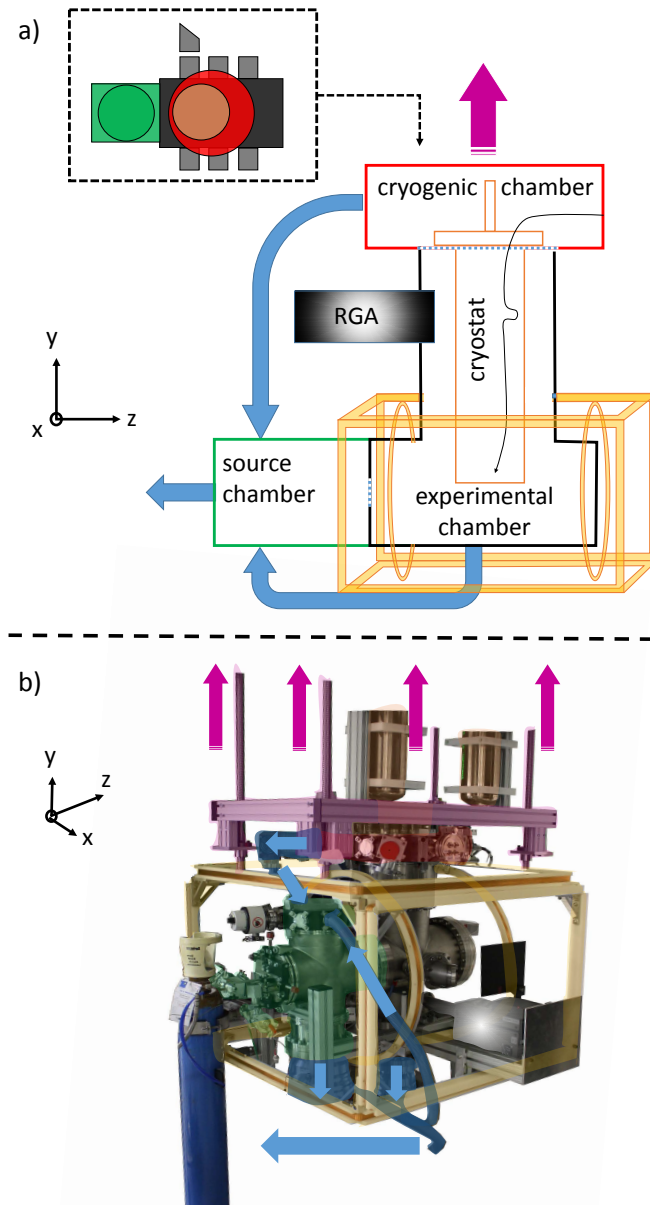


Figure 5.1: a) Schematic overview of the experimental setup. The cryogenic chamber (red) holding the cryostat, can be lifted off (magenta arrow) the experimental chamber (black) containing the experimental part of the cryostat and a residual gas analyzer. The experimental chamber is differentially pumped (blue dashed line) to the cryogenic chamber and the source chamber (green), respectively. Blue arrows indicate pressure gradients enforced by turbomolecular pumps. Magnetic coils (yellow) compensate the earth magnetic field and are explained in Sec. 5.3. The inset shows a top-view of the experiment. b) Corresponding colored photograph of the experiment.

determines the pressure below 100 mbar with a precision of 30% for air. For helium, the pressure is underestimated by a factor 6. The typical base pressure of the source chamber is $p_s \lesssim 5 \times 10^{-7}$ mbar when the valve is not operated. On the one hand, this pressure is dominated by the additional gas load that originates from using the source chamber as pre-vacuum to the cryogenic and experimental chamber [compare blue arrows in Fig. 5.1(a)]. On the other hand additional gas load is introduced through particle diffusion through the viton o-rings. Viton has typical permeation rates of 10^{-8} mbar l/sec cm^2 and outgassing rates of $\sim 10^{-7}$ mbar l/sec cm^2 . Upon operation of the valve, the measured pressure rises to a pressure of $\sim 5 \times 10^{-5}$ mbar or 1×10^{-4} mbar for the valve configurations 1 or 2, respectively (Sec. 3.2). Because the increase in pressure being caused by the helium gas of the atom beam that exits the valve, the partial pressure of helium in the chamber is $\sim 3 \times 10^{-4}$ mbar or $\sim 6 \times 10^{-4}$ mbar, respectively.

The *experimental chamber* (black) consists of a modified stainless-steel, ISO CF-200 cross which is large enough to contain the cryostat, and the imaging microchannel plate detector (Sec. 4.3.3.1). The arms of the cross are aligned to the z and y direction. The chamber is pumped by a turbomolecular pump through the arm pointing in negative y direction. The arm that connects to the source chamber (negative z direction) is shortened by 60 mm to minimize the travel time of the metastable atom pulse between pulse generation and excitation to Rydberg states. The microchannel plate detector (MCP) is mounted on a blind flange in the arm pointing towards positive z direction. The flange contains a high voltage feedthrough (*MDC vacuum*) which is specified for potentials up to 10 kV), and a DIN CF-63 viewport to take camera images of the MCP (Sec. 4.3.3.1). The cryostat containing the experimental region is inserted through the arm pointing in positive y direction. 6 additional CF-40 ports facing in positive and negative x direction [inset Fig. 5.1(a)], are attached at the sides of the chamber that have no arms (3 per side). A residual gas analyzer (RGA, *SRS: TGA-300*) and a vacuum gauge (*PFEIFFER:PKR 261*) are connected to two of these ports. To minimize deviations of the Rydberg-electron beam propagation direction (z direction) because of the remaining magnetic field strength of the μ -metal-shielded vacuum gauge, it is aligned parallel to the z direction using a vacuum elbow. Uncoated fused silica viewports are attached to two of the remaining CF-40 ports allowing the Rydberg excitation laser to pass through the chamber. The viewport by which the laser exits the experimental chamber is mounted at an angle of 45° with respect to the z direction and is electrically isolated with an ultra-high-vacuum compatible ceramic piece from the rest of the chamber. Additional baffles inserted before the viewport minimize laser light being reflected from the facet of the viewport into the excitation region (zone 1). The electric isolation allows to apply potentials (~ 10 V) to the exit

viewport to remove secondary electrons that are produced by radiation impact of the laser on the metallic surfaces of the chamber.

The experimental chamber is optimized to reach high vacuum levels and to minimize potential channels through which gases can enter into the experimental region (gas load). This is necessary, because it was found that adsorption of residual gases onto the cryogenic chip surface, as caused by insufficient vacuum conditions, is detrimental to the coherence of the Rydberg atoms close to the surface (Sec. 5.2.4). Therefore, all the components of the experimental chamber are metal(copper)-sealed because copper seals have negligible permeation and outgassing rates. The number of direct electric feedthroughs between the outside and the inside of the experimental chamber is reduced to the high voltage feedthrough for the MCP and the RGA-internal feedthroughs. All other electric control lines (black arrow) pass a specially designed differential pumping stage that connects the experimental chamber to the cryogenic chamber (red). The dominating source of gas load in the experimental chamber beside outgassing of the chamber walls is given by the skimmer of 1 mm diameter through which the atom beam enters the chamber from the source chamber (green). Additional gas loads that originate from cryostat-internal cavities that release trapped gas (virtual leak) contribute to the final pressure at room temperature but freeze out when the cryostat is cooled to cryogenic temperatures. To minimize direct outgassing of the chamber walls, the experimental chamber was baked at temperatures $\leq 100^\circ\text{C}$ for 5 days and exposition to air afterwards was minimized.

The final pressure of the experimental chamber at room temperature ($p_e \approx 1.6 \times 10^{-8}$ mbar) is limited by the pump speed of the turbo molecular drag pump (PFEIFFER: HiPace 300) with a pump rate of 260 l/s for helium and a compression of 10^8 (blue). To minimize back-diffusion through the pump, its pre-vacuum outlet is connected by a 1.5-m-long vacuum bellows to the high-vacuum of the source chamber ($p_s \lesssim 10^{-4}$ mbar). When the cryostat is cooled to cryogenic temperatures, cryogenic pumping causes the pressure to drop below the range of the vacuum gauge (i.e. $< 5 \times 10^{-9}$ mbar). In this case, the only observed partial pressure in the chamber is H_2 ($\lesssim 6 \times 10^{-10}$ mbar) as measured with the RGA. H_2 is well known to outgas from stainless steel (i.e. the chamber walls) and does not adsorb to the outer heat shield of the cryostat. Because the sensor of the RGA being positioned close to the (warm) chamber walls, the measured partial pressure of H_2 gives therefore an upper limit for the effective pressure in the experimental region (zone 2) in the heart of the cryostat. Upon operation of the valve the partial pressure of helium in the experimental chamber rises to $\sim 3 \times 10^{-7}$ mbar as measured consistently by the RGA and the pressure gauge.

The *cryogenic chamber* is designed for two main purposes. On the one hand it provides enough vacuum ports for all electronic control connections of the ex-

periment and it supports the cryostat (orange) we use to cool the experiment. On the other hand it contains a specially designed adapter with a differential pumping section, minimizing gas diffusion through the electric feedthroughs into the experimental chamber.

The top part of the cryogenic chamber (Fig. 5.2, red) is circular with a diameter of 330 mm and a height of 75 mm. The pulse-tube cooler (*CRYOMECH: PT415*) used to cool the experimental region to 3 K is inserted into the cryogenic chamber from the top (positive y direction) at a distance of 15 mm to the chambers symmetry axis in y direction. The flange through which the cooler is inserted, also contains three KF-25 ports, one of which is holding a drag-pull to control the razor-blades for atom-beam alignment. Along its circumference, the cryogenic chamber features 10 KF-40 ports which provide enough space to feedthrough all electric connections to control the experiment. Also attached to these ports are a right-angle valve for venting and a μ -metal-shielded pressure sensor (*PFEIFFER:PKR 261*).

The lower part of the cryogenic chamber consists of a stainless-steel-adapter (green) that reduces the inner diameter of the cryogenic chamber from 250 mm to 200 mm. The top part of the adapter is connected to the rest of the cryogenic chamber (red) with a viton-o-ring sealed ISO-K connection. The bottom part connects to the experimental chamber (blue) with a copper-ring based CF seal. Dif-

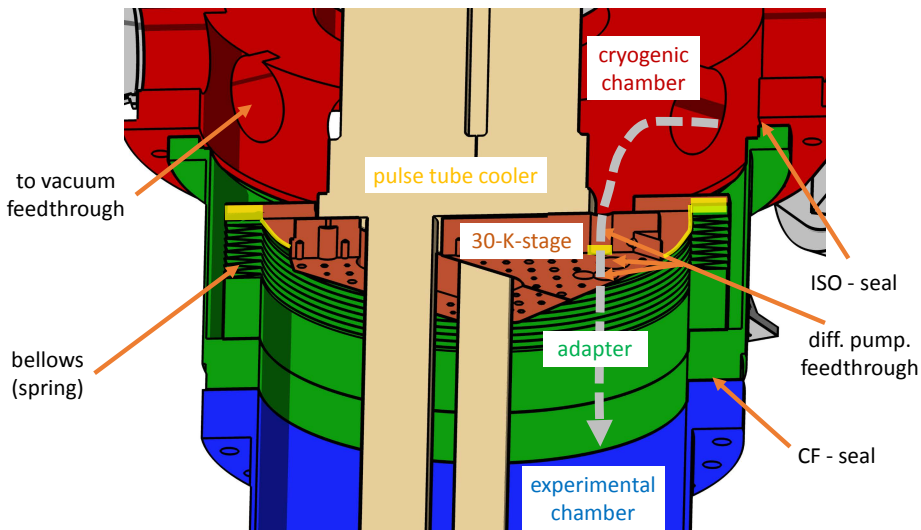


Figure 5.2: Cut through a colored CAD-illustration of the cryogenic (red) and the top part of the experimental chamber (blue), KF- and CF-sealed to the vacuum adapter (green), respectively. The 30 K-stage (dark brown) of the pulse-tube cooler (brown) closes the differential pumping line (yellow) toward the bellows. Cables (gray) are fed through holes in the 30 K-stage.

ferential pumping between the cryogenic chamber and the experimental chamber is achieved by a bellow that is integrated into the adapter pressing against the copper 30-K stage (brown) of the pulse-tube cooler (light brown). The contact surfaces (yellow) are polished such that the number of (microscopic-sized) channels is minimized through which gas can leak from the cryogenic chamber into the experimental chamber. The control cables (gray) are fed through holes in the copper plate. For a summary of all electronic control cables see next section Fig. 5.5 and Fig. 5.6. Cables that carry small potentials (< 50 V) are clamped between two copper bars which are fixed to the 30-K stage such that the holes are closed. High-voltage cables are fed through alumina (Al_2O_3) plates to minimize electric coupling between the cables and experimental ground because of large capacity.

At room temperature, the base pressure in the cryogenic chamber is $p_c \approx 5 \times 10^7$ mbar and limited by the pump rate of 67 l/s of the turbo molecular drag pump (PFEIFFER: HiPace 80) with compression of 1.3×10^7 for helium (Fig. 5.1, blue). The pump is attached to one of the KF-40 flanges with the pre-vacuum outlet connected by a ~ 200 mm-long vacuum-line to the high-vacuum part of the source chamber. The base pressure lies above the pumps specified level of 10^{-7} mbar because of the additional gas load from diffusion and outgassing of the numerous viton seals in the cryogenic chamber. Given the base pressures p_e and p_c of the experimental and cryogenic chamber, respectively, the ratio between between the pressure in the cryogenic chamber and the experimental chamber is ~ 30 .

When the experiment is cooled to cryogenic temperatures, p_c drops below the sensitivity of the vacuum gauge $< 5 \times 10^{-9}$ mbar because of additional cryogenic pumping of the 30-K stage. In this case, it is impossible to determine the relative pressure difference of the differential pumping. However, small virtual leaks in the cryogenic chamber may limit p_c to values $\lesssim 5 \times 10^{-8}$ mbar. In this case, a lower threshold of the relative pressure gradient between the two chambers (ratio ~ 300) can be determined by comparing p_c with the partial pressures of air (N_2 , O_2 , CO_2) measured by the RGA. These pressures are typically below the detection limit of the RGA (10^{-10} mbar).

The top part of the cryogenic chamber and the cryostat can be lifted out of the experiment and moved to the side by opening the ISO-K seal connecting the top part of the cryogenic chamber to the adapter. The crane used for moving the cryostat was designed by J. Luetolf and consists of four threaded bars that are connected to a light aluminum profile (KANYA) by roller bearings (Fig. 5.1, magenta). The top part of the cryogenic chamber is fixed to the aluminum profile, such that simultaneous screwing of the threaded bars into the roller bearings, lifts the chamber up. The threaded bars are supported by two movable rails which allow to move the chamber to the side.

5.2 Design of cryostat

In this chapter the design and setup of the cryostat will be discussed. The cryostat is designed to:

1. skim metastable atom beam transversal to its beam propagation direction (z direction) and control its size and position along the y direction,
2. have a small solid angle of the chip surface at cryogenic temperatures in the experimental region open to surfaces at room temperature,
3. manipulate and detect Rydberg atoms using electric fields,
4. apply microwave radiation to the sample,
5. provide optimal cooling to cryogenic temperatures of the Rydberg-atom-beam environment and the chip surface (sample).

The cryostat is build around a pulse-tube cooler (*CRYOMECH: PT415*) consisting of two cooling stages, which are cooled to 30 K and 3 K, respectively. The design of the 30 K stage is part of the differential pumping stage between the cryogenic and the experimental chamber, and was explained in the last section. In the following we will first discuss the (mechanical) design of the 3-K stage (items 1,2,3) and then we discuss the electric cabling (items 3,4). At the end of the chapter, we focus on the combined heat load from the mechanical parts and the cabling onto the different stages (item 5).

5.2.1 Mechanical design of the 3-K stage

The 3-K stage is connected to the 30-K stage by the two thin stainless steel pulse and regenerator tubes and positioned in the center of the experimental chamber (Fig. 5.3, dark blue). Two copper plates (green) are attached to the 3-K stage of the pulse-tube cooler (light brown). The upper plate is used to thermalize cable connections and mount electronic (microwave) devices such as cold amplifiers or circulators. A 3-K heat shield (green) is connected to the lower plate, enclosing the electrode stack (brown) that consists of the sample holder (red) and 7 copper electrodes (yellow). The 3-K stage is enclosed by a heat shield cooled to 30 K (dark brown) which connects to the extended arm of the source chamber (light blue) with a dovetail construction. The dovetail construction defines the position of the cryostat within the experimental chamber and ensures reproducible positioning of the cryostat when inserted back into the experimental chamber after sample exchange.

The metastable atom beam (travelling in positive z direction) passes 3 skimmers (magenta) out of which the first and third one skim the atoms in transversal

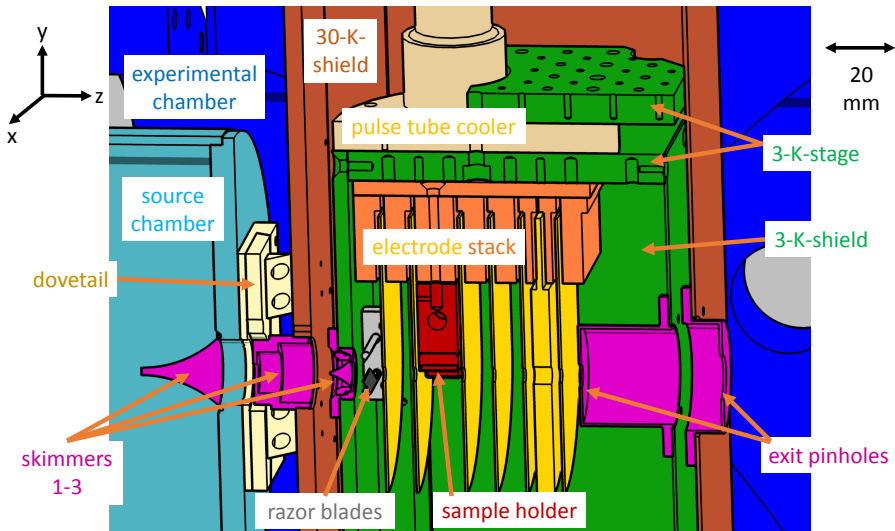


Figure 5.3: Coloured CAD-illustration of the experimental region. Atoms coming from the source chamber (light blue) enter the experimental region in the experimental chamber (blue) via a set of 3 skimmers (magenta) and leave it via two exit pinholes (magenta). The experimental region contains two adjustable razorblades (gray) and the electrode stack (electrodes are yellow, stack is orange) with the sample holder (red). Everything contained and attached to the 3-K stage (green) is cooled by the pulse-tube cooler (light brown). A dovetail-system (light brown) attached to the 30-K-shield (dark brown) guarantees reproducible repositioning of the experiment with respect to the atomic beam.

direction (x - y direction), as discussed in Sec. 3.2. The second and third skimmer are mounted on the heat shields and are cooled to 30 K and 3 K, respectively. Before the electrode stack, the metastable atoms are skimmed in y direction with a movable slit aperture, consisting of two individually movable razor blades (gray). After passing the electrode stack, the atoms and electrons (generated during the experiment) leave the cryostat by two exit pinholes (magenta).

The electrode stack (photograph Fig. 5.4) is directly mounted onto the copper plate that connects to the 3-K stage for optimal thermalization. It contains 7 gold coated plate electrodes named electrode 1 – 4 and $IL1$ – $IL3$ (einzel lens). The electrodes are coated with gold to increase reflectivity and minimize absorption of room temperature radiation that enters through the skimmers and exit pinholes. All electrodes except $IL2$ have a diameter of 80 mm and a thickness of 1 mm. $IL2$ has a diameter of 80 mm and a thickness of 6 mm. Electrodes 1 – 4 have a hole of 5 mm in the center through which the atom beam can pass. The ion lens electrodes ($IL1$ – $IL3$) have holes of diameter 6 mm. All electrodes are clamped between grounded copper bars from which they are separated by isolating ceramic plates made of alumina (Al_2O_3). Large potentials up to 1.2 kV can be applied to

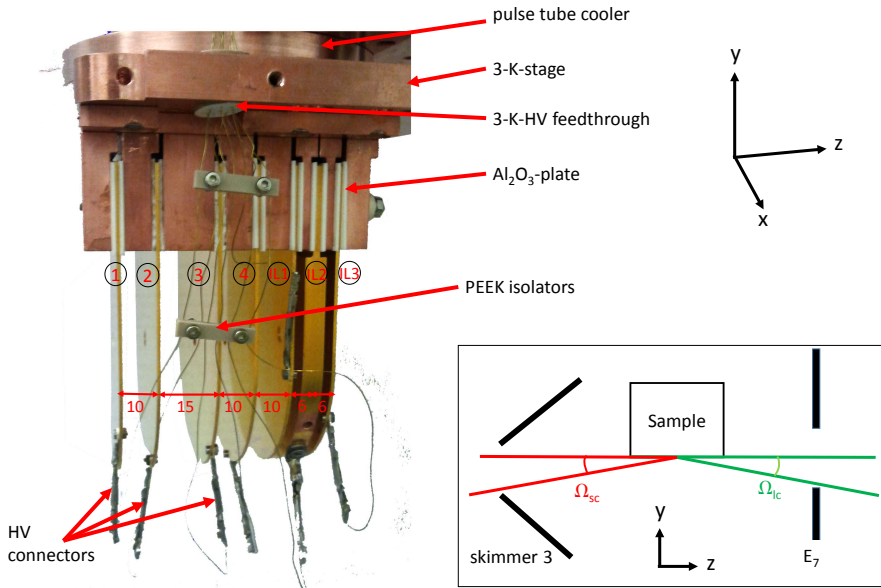


Figure 5.4: Photograph of the electrode stack without sample holder with gold-coated electrodes 1 – 4 and einzel lens, separated by Al_2O_3 -plates from the copper holders attached to the pulse-tuber cooler. Distances between electrodes given in mm. Lasered PEEK isolators and feedthroughs guarantee that the HV-cables are well isolated from the surrounding parts. The inset sketches the largest possible solid angles (values given in text) of the sample surface with respect to the 300 K environment.

each electrode individually by high voltage connections that are fed through the 3-K stage through holes in an alumina plate. The large diameters of the electrodes with respect to the diameters of the holes ensure that the electric field in the experimental regions is defined from potentials applied to the electrodes and not from, e.g., connecting cables.

The separation of each pair of electrodes (given in picture) is determined by the task of the region defined by the two electrodes within an experiment. All separations between electrode 1 and IL1 are kept as short as possible such that radiative decay of Rydberg states is minimized when the atoms travel between the different electrodes during an experiment. The separation between electrode 1 and 2 (excitation, zone 1) is 10 mm, long enough to produce homogeneous electric fields over a distance of ~ 1 mm if a potential difference between the electrodes is applied [compare Fig. 4.12(c)]. It is important to have homogeneous fields over a distance of 1 mm, because this is the typical diameter of the excitation laser [compare Fig. 4.10(d)]. The space between electrode 2 and 3 is 15 mm and called experimental region (zone 2). It contains the sample holder with the chip surface

and the separation is large enough to produce homogeneous electric fields of up to 5 mm along the beam propagation (z) direction. The region between electrode 3 and $IL1$ is called detection region (zone 3). The separation of 10 mm between electrode 3 and 4 is long enough that the travel time for Rydberg atoms ($\gtrsim 5.5 \mu\text{s}$) between the two electrodes is longer than the typical lifetime of np states ($\lesssim 2 \mu\text{s}$). The separation between electrode 4 and $IL1$ (10 mm) is chosen larger than the typical length of the Rydberg atom pulse along z direction ($\lesssim 3$ mm, Sec. 3.2) at this position, but short enough that potential differences of several hundreds of Volt lead to electric fields of hundreds of V/cm (Fig. 4.12). The separations of $IL1$ and $IL3$ with respect to the center of $IL2$ are designed to be 6 mm. Given the thickness of $IL2$ and the diameter of the holes in the electrodes, the separations of the einzel lens electrodes are optimized to produce the quadrupole field needed for imaging Rydberg atom distributions (Sec. 4.3.3.3).

Samples (chips) are placed upside down in zone 2, 0.5 mm above the symmetry axis of the experiment and aligned within the x - z -plane using a specially designed sample holder which will be explained in detail in Sec. 6.1.1. This position within the electrode stack is optimal to reduce direct line of sight from the chip surface to chamber walls at room temperature, characterized by the two effective solid angles Ω_{sc} and Ω_{lc} towards positive and negative z direction, respectively (inset Fig. 5.4). Ω_{sc} is approximately given by the area of skimmer 3, A_{s} , with radius 0.75 mm, the distance between the skimmer and the center of the chip surface ($d_{\text{sc}} = 36$ mm), the exposed chip surface ($A_{\text{c}} \approx 12 \times 5 \text{ mm}^2$), and the angle $\alpha_{\text{sc}} \approx 0.5 \text{ mm}/d_{\text{sc}}$ under which the chip surface sees the skimmer surface, i.e.

$$\Omega_{\text{sc}} = \frac{A_{\text{s}}A_{\text{c}}}{4\pi d_{\text{sc}}^2} \sin(\alpha_{\text{sc}}) \approx 9 \times 10^{-5}. \quad (5.1)$$

Similarly, Ω_{lc} is approximately given by half the area of the hole in $IL3$, $A_{\text{IL3}}/2$, i.e. the fraction which lies below the symmetry axis of the experiment, the distance between $IL3$ and the center of chip surface ($d_{\text{lc}} = 30$ mm) and the angle $\alpha_{\text{lc}} \approx 0.5 \text{ mm}/d_{\text{lc}}$ under which the chip surface sees the skimmer surface, i.e.

$$\Omega_{\text{lc}} = \frac{A_{\text{IL3}}}{2} \frac{A_{\text{c}}}{4\pi d_{\text{lc}}^2} \sin(\alpha_{\text{lc}}) \approx 1.2 \times 10^{-3}. \quad (5.2)$$

5.2.2 Wires and connections

For an experiment, different potentials need to be applied to the electrodes or the sample. Also, the temperature has to be controlled constantly. Specifically, to operate the experiment, we need to

1. measure and control the temperature of the cryostat (thermometry),

2. apply large potentials to the electrodes 1 – 4 and to the einzel lens (*IL1* – 3),
3. apply small potentials to the sample holder,
4. apply microwave signals to the sample holder.

For each of these items, cable bundles connect vacuum feedthroughs in the cryogenic chamber (red dashed) with connectors at the 30-K (green dashed) and 3-K stage (blue dashed) (Fig. 5.5 and Fig. 5.6). For all cables an optimal resistance exists for which heat transfer between the stages is minimal (large resistance) but the signal loss in the cable is still suited for the application (small resistance). We will first discuss the cabling setup for low-frequency signals (≤ 100 MHz) and then for microwave signals.

The number, length, type, and total resistance of all fixed cable bundles for low frequency applications are grouped in Fig. 5.5 according to the application of elements to which they are connected, i.e. as thermometry, high voltage and DC-cabling. All parts below the dashed lines are fully enclosed by the heat shields of the corresponding stage. The boxes indicate the type of the cable bundles, the vacuum-feedthrough, and the number of cables in brackets. Circles containing a *T* denote strong thermalizations of the cables with rectangular pillars of copper that are tightly fixed to the 30-K stage, and to which the cable bundles are clamped. Open rectangles denote connectors between lines which are weakly thermalized to the corresponding stage by Al_2O_3 -plates, indicated by the dotted lines.

For *thermometry*, 2 cable bundles (12 twisted pairs of constantan) are designed to connect 4 temperature sensors (16 cables in total) at either the 30-K stage (dark blue line) or the 3-K stage (violet line). Because the sensors (*LAKESHORE:DT601*) are diodes that use four-point measurements, we need 4 cables per temperature sensor. The performance of the sensors is not affected by the resistance of the cables such that small diameter cables can be used. To control the temperature of the cryostat on both stages (blue and green lines, respectively) we use cartridge heaters (*LAKESHORE:HTR-25-100*) that are operated by sending a current through 2 copper cables per heater. The cables are made of copper with a diameter of 0.3 mm such that the resistivity is small enough that only a fraction of $\lesssim 0.8\%$ of the maximally applied power (≤ 50 W) is dissipated in the cables. Because the cables are in vacuum and can thus dissipate little heat, a smaller diameter would result in the evaporation of the isolation and melting of the cables when maximal power is applied. The *high voltage* cables (manganin) connect the vacuum feedthrough (*MDC:K150-HV5-30C-8*), safe up to specified for 5 kV, directly with all electrodes of the electrode stack. The resistance of the cables (88Ω) and the reduced capacity because of weak thermal connections by the alumina plates is good enough to pulse electric potentials up to 600 V in 60 ns (Sec. 4.3.2). A set of 22 (11 twisted pairs

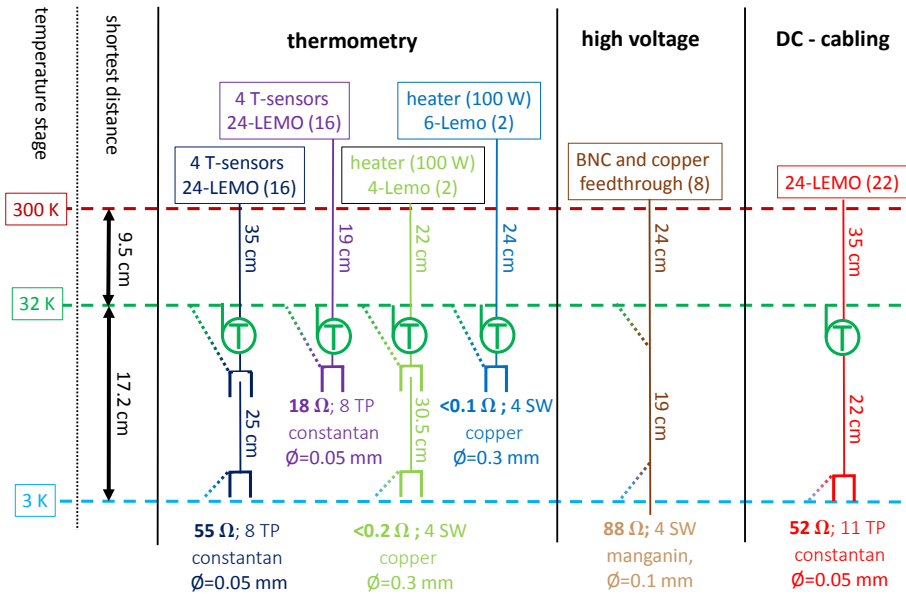


Figure 5.5: Thermometry, high voltage and DC-cabling scheme between the room temperature part (300 K, red), the 32-K-stage (green) and the 3-K stage (blue). Parts below a dashed line are fully enclosed by the corresponding heat-shield. For each line the connector-type and number (in brackets), the cable length and diameter, material and room-temperature resistance is annotated. Two-colored dashed lines indicate weak thermalizations, labels "T" denote clamped thermalizations and open rectangles indicate connectors.

of constantan) cables with a resistance of 52 Ω allow to apply potentials ≤ 100 V to additional, optional devices such as chip-based electrodes or bias-tees.

Microwave signals are transferred to the sample using semi-rigid coaxial cables. The number, length, and type of all microwave cables are presented in Fig. 5.6. The three different types of coaxial cables we use (cu, ss, ss-ss) have a diameter of the outer conductor of 2.2 mm with thickness of 0.3 mm, and a diameter of the inner conductor of 0.5 mm. They differ in the different materials used for the center conductor and the outer conductor, but they all use PTFE as dielectric and exhibit the same signal propagation velocity of 70% of the speed of light. The outer conductor of cables indicated 'cu' (*UT-085-TP-M17/133-0007*) consists of copper, the inner conductor consists of silver-plated copperweld (SCPW) and they are specified for frequencies below 20 GHz with insertion losses up to 4.3 dB/m at 20 GHz. The outer conductor of cables indicated 'ss' (*UT-085-SS*) consists of 304-stainless-steel, the inner conductor consists of silver-plated copperweld (SCPW) and they are specified for frequencies below 61 GHz with insertion losses up to 7 dB/m at 20 GHz. The outer and inner conductor of cables indicated 'ss-ss' (*UT-*

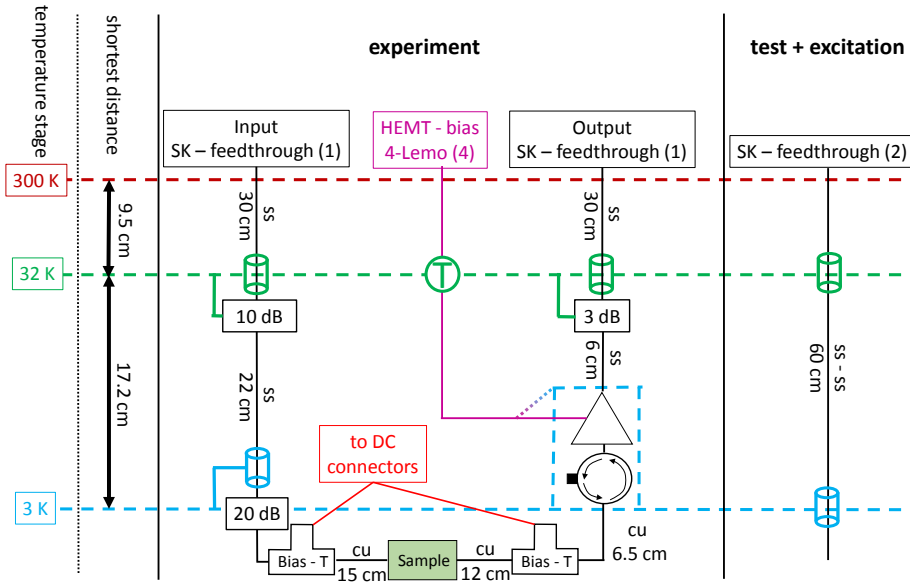


Figure 5.6: Experimental and test-microwave cabling scheme between the room temperature part (300 K, red), the 30-K-stage (green) and the 3-K stage (blue). Parts below a dashed line are fully enclosed by the corresponding heat-shield. For each section the cable length and material is annotated. Cylinders indicate solid clamp-thermalizations of outer conductor, boxes indicate attenuators to thermalize center conductors, two-colored dashed lines indicate weak thermalizations and labels "T" denote clamped thermalizations.

085-SS-SS) consists of 304-stainless-steel and they are specified for frequencies below 61 GHz with insertion losses up to 18.9 dB/m at 20 GHz.

For the experiment, we apply microwave radiation to the sample with two coaxial 'ss'-cables and a copper cable. The outer conductors of the 'ss'-cables are thermalized to the 30-K and the 3-K stage by clamping (green and blue cylinders). The black boxes indicate attenuators that thermalize the center conductor with the temperature of the stage. Bias-tees are inserted before and after the sample to apply dc-bias to the center conductor of the sample. A signal that leaves the sample by the output port is first sent through an isolator (*PAMTECH:PTH1827KI*) with a backwards isolation of ~ 20 dB, and then amplified in a cold high-electron-mobility transistor (HEMT) amplifier (*CALTECH:CRYO1126*, noise temperature ~ 15 K) by ~ 30 dB. The HEMT amplifier is biased via 2 twisted copper pairs that are weakly thermalized to the 3-K-stage. After amplification, the microwave signal leaves the cryostat with minimal attenuation of $\lesssim 6$ dB from the attenuator and the 'ss'-coaxial cable losses. To test noise spectra of the electrode and ground

of the sample, two additional microwave 'ss-ss' cables reach directly from the 3-K stage to the room temperature vacuum feedthroughs.

The microwave cabling is designed to minimize both thermal-room-temperature radiation impinging onto the sample (thermalization), and to minimize signal loss from the sample. Attenuation of thermal radiation is particularly important in the frequency range of the experiment. From the overlap of the bandwidths of the isolator (18 – 26.5 GHz), and of the HEMT-amplifier (11 – 26 GHz) we obtain the bandwidth of the microwave setup, i.e. the *K*-band (18 – 26.5 GHz). On the input line, we thermalize noise from the room-temperature and 30-K stage to the temperature of the 30-K stage and 3-K stage, respectively, using the attenuators. For each stage, the value of attenuation is chosen such that the noise power spectral density (given by the 1-dimensional Planck law) of the warmer stage is reduced to below 10% of the noise power spectral density of the colder stage. On the output line, the combined isolation of the amplifier (~ 15 dB), the isolator and the attenuation of the 3-dB-attenuator in the direction from the output port to the sample is large enough to reduce room temperature radiation to a negligible level while minimizing signal loss from the sample in the other direction.

5.2.3 Heat loads

For a successful hybrid interface between Rydberg atoms and chip-based, superconducting microwave resonators it is essential, that the sample reaches temperatures ≤ 3 K. This is only possible, if the cooling stages of the cryostat reach their base temperatures of 32.5 K and $\lesssim 3$ K. The equilibrium temperature of a cooling stage is determined by the cooling power P_s^c at this stage ($s = 3$ or 30, respectively) of the pulse-tube cooler we use (Fig. 3.16 in [Marx (2010)]), and the summed heating power $P_{\text{tot},s}^h$ of all sources at this stage. Both powers depend monotonically on temperature such that larger cooling power is available for larger equilibrium temperatures. The equilibrium temperature for a stage is reached if $P_s^c = P_{\text{tot},s}^h$. Therefore, $P_{\text{tot},s}^h$ needs to be as small as possible. $P_{\text{tot},s}^h$ is the sum of pulse-tube internal heating rates ($P_{\text{int},s}^h$) and external heating rates ($P_{\text{ext},s}^h$), e.g. thermal radiation. The internal heating rates of the pulse tube cooler limit the base temperatures of the two stages to 31.9 K and 2.8 K, respectively. Therefore, to reach base temperatures of similar level, $P_{\text{ext},s}^h \ll P_{\text{int},s}^h$.

$P_{\text{ext},s}^h$ is the sum of heat power impinging on the stage s by radiation $P_{\text{rad},s}^h$, and by heat transport $P_{\text{tr},s}^h$ through mechanical connections, e.g. cables. The radiative heat load between two parallel planes one of which belongs to a reservoir with temperature T_1 and surface A_1 , and the other to a reservoir of temperature T_2 , is approximately given by [White and Meeson (2002)]

$$P_{\text{rad},s}^h \approx \sigma A_1 (T_1^4 - T_2^4) \frac{\epsilon_1 \epsilon_2}{\epsilon_1 + \epsilon_2 - \epsilon_1 \epsilon_2}, \quad (5.3)$$

with $\sigma = 5.67 \times 10^{-8} \text{ W/m}^2\text{K}$ the Boltzmann factor, and ϵ_1 and ϵ_2 the reflectivities of the surfaces of the two reservoirs, respectively. The transport heat through a material of crosssection A and length d between two reservoirs of temperature T_1 and T_2 , respectively, is approximately given by [White and Meeson (2002)]

$$P_{\text{tr},s}^{\text{h}} \approx \kappa \frac{A}{d} (T_1 - T_2), \quad (5.4)$$

with κ being the heat conductivity of the material.

The radiative heat load onto the 30-K stage $P_{\text{rad},30}^{\text{h}} \approx 2.5 \text{ W}$ is given by the sum of the radiative heat loads from the stainless steel walls ($\epsilon \approx 0.074$) at room temperature onto the gold-coated heat shield ($\epsilon \approx 0.023$) and the copper plate of the differential pumping stage ($\epsilon \approx 0.02$) at approximately 32 K. The reflectivities are taken from White and Meeson (2002). Heat is transported by all control cables ($\sim 0.41 \text{ W}$), the microwave coaxial cables ($\sim 0.43 \text{ W}$), and (the negligible contribution from) the bellows of the adapter between the cryogenic and the experimental chamber ($\sim 0.002 \text{ W}$). All heat conductivities (κ) were calculated as temperature averages from NIST-conductivity integrals [Marquardt et al. (2000)]. To calculate the heat loads for all cables, we assumed $d = 95 \text{ mm}$, i.e. the shortest distance between the chamber walls and the 30-K stage, and neglected heat transport through the dielectric of the coaxial cables. The dominating contribution ($\sim 0.37 \text{ W}$) of the transport heat load comes from the copper cables of the heater. The total heat load of $P_{\text{tot},30}^{\text{h}} \approx 3.4 \text{ W}$ agrees exactly with the heat load that the calibration measurement in Fig. 3.16 of [Marx (2010)] predicts to obtain the measured base temperature of the 30-K stage of $T_{30} \approx 32.4 \text{ K}$.

Equivalently, the radiative heat load onto the 3-K stage $P_{\text{rad},3}^{\text{h}} \approx 4.6 \times 10^{-4} \text{ W}$ is given by the sum of the radiative heat loads from the 30-K heat shield ($\epsilon \approx 0.023$) at 32.5 K and the crosssection of the skimmer 3 and the exit pinhole at room temperature (292 K) onto the surfaces of the 3-K stage at approximately 2.8 K. The combined surfaces of the 3-K stage are from the gold-coated heat shield ($\epsilon \approx 0.03$), the copper plate of the 3-K stage ($\epsilon \approx 0.015$), and additional copper elements used to thermalize the control and microwave cables. The largest contribution of radiative heat load comes from the large (diameter 8 mm) exit pinhole, i.e. $\sim 3.1 \times 10^{-4} \text{ W}$. Heat is transported by all control cables ($\sim 0.015 \text{ W}$) and the microwave coaxial cables ($\sim 0.011 \text{ W}$). To calculate the heat loads for all cables, we assumed $d = 172 \text{ mm}$. The dominating contribution ($\sim 0.013 \text{ W}$) of the transport heat load comes from the copper cables of the heater. The total heat load of $P_{\text{tot},3}^{\text{h}} \approx 0.026 \text{ W}$ is expected (Fig. 3.16 of [Marx (2010)]) to cause no temperature increase of the specified base temperature. This is in agreement with the measured base temperature of the 3-K stage of $T_3 \approx 2.8 \text{ K}$.

Finally, we can estimate the radiative heat that impinges directly on the sample surface through holes in the 3-K stage through which the atoms enter and exit

the electrode stack. The maximal heat load directly impinging onto the sample from skimmer 3 is given by the total heat power radiated from the skimmer ($P_s^h \approx 4.3 \times 10^{-5}$ W) times the crosssection $\Omega_{sc} \approx 10^{-4}$, i.e.

$$P_{sc}^h = P_s^h \Omega_{sc} \approx 4.3 \times 10^{-9} \text{ W.} \quad (5.5)$$

Similarly, the radiation from the exit pinhole through *IL3* is

$$P_{lc}^h = P_1^h \Omega_{lc} = 3.1 \times 10^{-4} \times 1.2 \times 10^{-3} \approx 3.7 \times 10^{-7} \text{ W.} \quad (5.6)$$

5.2.4 Adsorption-free cooldown of samples

The sequence in which the different elements of the cryostat are cooled is optimized to avoid adsorption of gas onto the sample holder and the chip surface [Thiele *et al.* (2014)]. The actual cooling process is monitored by measuring the temperature of the sample holder and the partial pressures of the relevant gaseous species (H_2O , CO_2 , N_2 and O_2) in the chamber with the residual gas analyzer (RGA).

The key to avoid adsorption on the sample holder is to keep its temperature above the adsorption temperature of the different gaseous components as long as these have measurable partial pressures (i.e., $> 5 \times 10^{-10}$ mbar) in the experimental chamber. This approach leads to the gas adsorbing predominantly onto the 30-K stage.

Before starting the cooling procedure (Fig. 5.8), pairs of reference partial-pressure and temperature values (p_i^{ref} , T_i^{ref}) are defined for all relevant gaseous species ($i = 1 - 4$ for H_2O , CO_2 , N_2 and O_2) as indicated in Table Tab. 5.1. While continuously monitoring the partial pressures, the temperature of the sample is maintained with a cartridge heater at the maximal T_i^{ref} value for which the condition $p_i^{\text{measured}} > p_i^{\text{ref}}$ is fulfilled, i.e., $T = 278$ K in the initial phase (Fig. 5.7). The cartridge heater is biased from a voltage-controlled-current-source (VCCS), the control voltage of which is generated by a computer.

Because H_2O and N_2 are by far the most abundant components of the residual gas which adsorbs, an additional reference pair of partial-pressure and temperature values is defined to decrease the temperature gradient between the two temperature stages, so that, for instance, the maximal temperature is maintained at 200 K as long as p_3^{ref} is in the range between 5×10^{-10} and 5×10^{-9} mbar.

When all partial pressures are below their reference values, the temperature feedback is stopped and the system cooled to base temperature. The final temperature is then determined by the cooling power of the pulse-tube cooler, which is < 3 K at the sample in our system. At this point, the partial pressures are below the detection limit of the RGA.

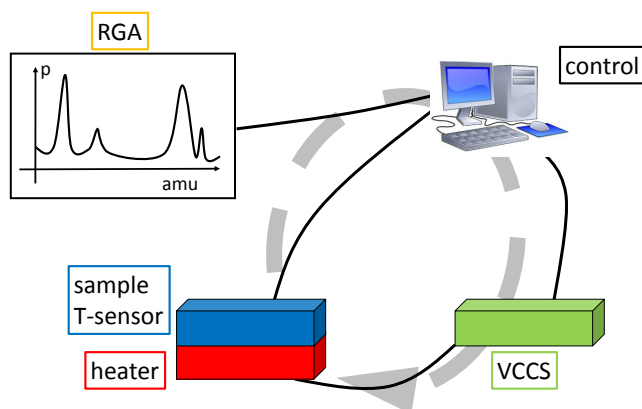


Figure 5.7: Sketch of cooldown feedback (gray arrow). The control unit (computer) takes information on the current residual gas pressures and temperature sensor and controls a heater using a voltage-controlled-current source (VCCS).

Table 5.1: Adsorption temperatures $T_{\text{adsor.}}$ and reference temperatures T^{ref} and pressures p^{ref} of residual gases in the vacuum chamber.

species	$T_{\text{adsor.}}$ [K]	p^{ref} [mbar]	T^{ref} [K]
H ₂ O	160	5×10^{-9}	278
		5×10^{-10}	200
CO ₂	125	5×10^{-10}	200
N ₂	55	5×10^{-9}	150
		5×10^{-10}	90
O ₂	60	5×10^{-10}	90

Figure 5.8 illustrates this procedure by showing in panel (a) the temperatures of the sample holder (dark red trace) and the 30-K stage (red), in panel (b) the total pressure of the experimental chamber (dark blue) and the cryogenic chamber (blue), and in panel (c) the partial pressures of H₂O (black), H₂ (blue trace), CO₂ (brown), and N₂ (red).

The green lines indicate the position of the adsorption temperatures estimated from the sublimation points observed by an increase in partial pressure of the respective residual gas when letting the system warm up (Sec. 5.2.4.1). Panel (c) shows that the partial pressure of each residual gas decreases as soon as the adsorption point is reached. It also shows that, initially, the residual gas in the experimental chamber is dominated by water vapor. Also the initial pressure in the cryogenic chamber is dominated by water, as can be observed from the drop in

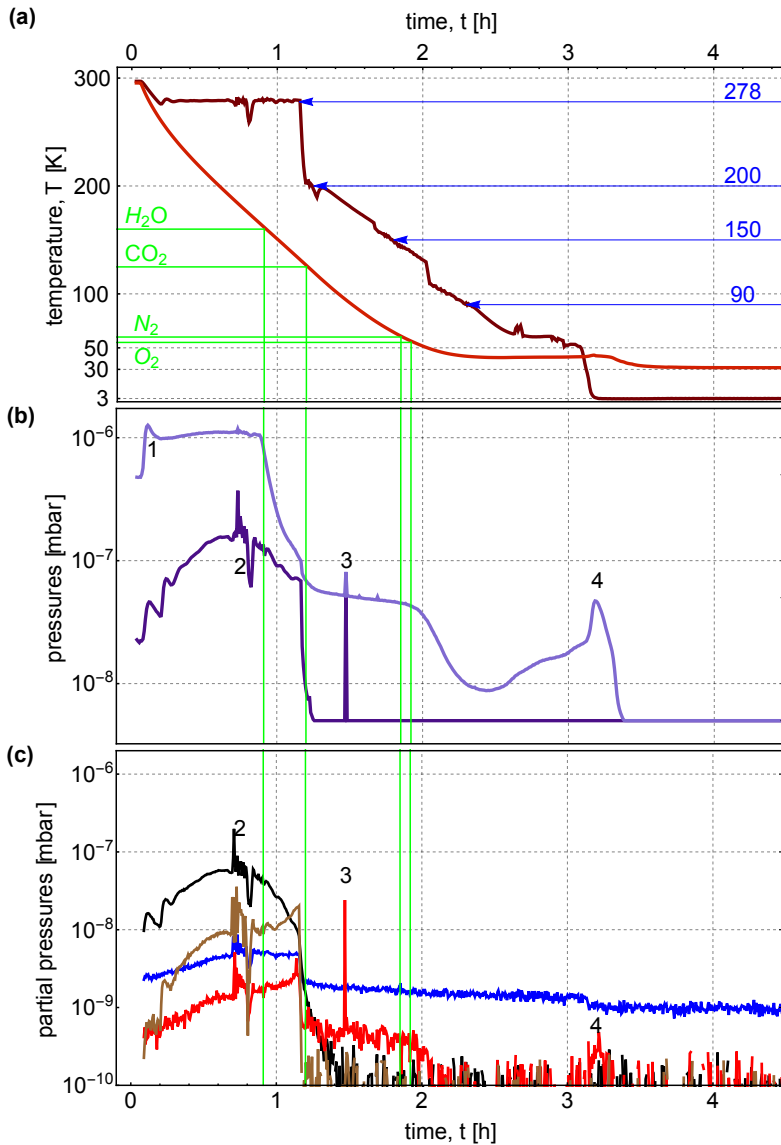


Figure 5.8: (a) Temperatures of the sample holder (dark red line) and 30-K stage (red line) during the cooling procedure. The green lines indicate the temperatures at which critical gases freeze out. The blue lines show temperatures at which the sample holder is stabilized. (b) Typical pressures measured in the cryogenic chamber (light blue line) and the experimental chamber (dark blue line). The features at positions labeled 1-4 are discussed in the text. (c) Partial pressures of H_2O (black line), CO_2 (brown line), H_2 (blue line) and N_2 (red line) measured in the experimental chamber.

pressure of the cryogenic chamber in panel (b) when the adsorption temperature of water is reached.

We interpret four irregularities indicated by the labels 1, 2, 3 and 4 in panel (b) and (c) of Fig. 5.8 as follows: Soon after the cooling procedure is started, the residual pressure in the cryogenic chamber rises (irregularity 1) because of the temperature increase of the high-temperature reservoir of the pulse-tube cooler. The increase in partial pressure of H₂O and N₂ between irregularities 1 and 2 results from outgassing of the heater, which is reduced as the set-point temperature is lowered from 278 K to 200 K after ~ 1.2 h. At this time, ~ 50 W are dissipated by the heater and the temperature of the sample holder is above all adsorption temperatures such that it is unlikely to be contaminated by adsorption. Irregularity 2 is an artefact of the feedback procedure because of a temporary failure caused by an inadequate time constant, which was then adapted manually¹.

The sudden spike in the nitrogen partial pressure (irregularity 3) is likely caused by a sudden release of trapped gas (virtual leak). Finally, irregularity 4 is the result of the last rapid phase of cooling which leads to a temperature increase in a restricted area of the cryogenic chamber only (presumably at the bellows of the adapter between cryogenic and experimental chamber) that exceeds the adsorption temperature of nitrogen for a short time. One sees from the temperature evolution of the sample holder that the main motivation to set the reference points (p^{ref} , T^{ref}) for CO₂ and O₂ in Tab. 5.1 is to slow down the cooling process and to prevent the residual gas from adsorbing at the sample holder. After the two stages of the cryostat reached their base temperature, the main and only measurable residual gas in the experimental chamber is H₂ which does not adsorb at surfaces of temperature ≥ 3 K with unit probability [Baglin (2001)] and equilibrates at a pressure of $\sim 6 \times 10^{-10}$ mbar after a day.

We have used the spectrum of the $[\text{He}^+]np \leftarrow (1s)^1(2s)^1 \ ^1S_0$ Rydberg series in the vicinity of the ionization threshold to monitor the build up of stray fields near the sample surface after the system has been cooled down. For the presented measurements, a cloud of Rydberg atoms was excited in zone 1 and passed within 1 mm of a gold surface. After 10.5 hours of experiments under conditions where charges could accumulate in the matrix of frozen material at the gold sample surface, the spectrum of this series [Fig. 5.9(a)] differs markedly from the spectrum obtained under conditions where the adsorption of residual gas onto the sample surface was suppressed [Fig. 5.9(b)] by means of the temperature-feedback procedure.

In Fig. 5.9(a), the transitions to np Rydberg states below $n = 50$ are strongly enhanced and the ionization limit (green line) is reduced because of stray fields

¹This irregularity does not appear when the T_1^{ref} is reduced from 278 K to 250 K.

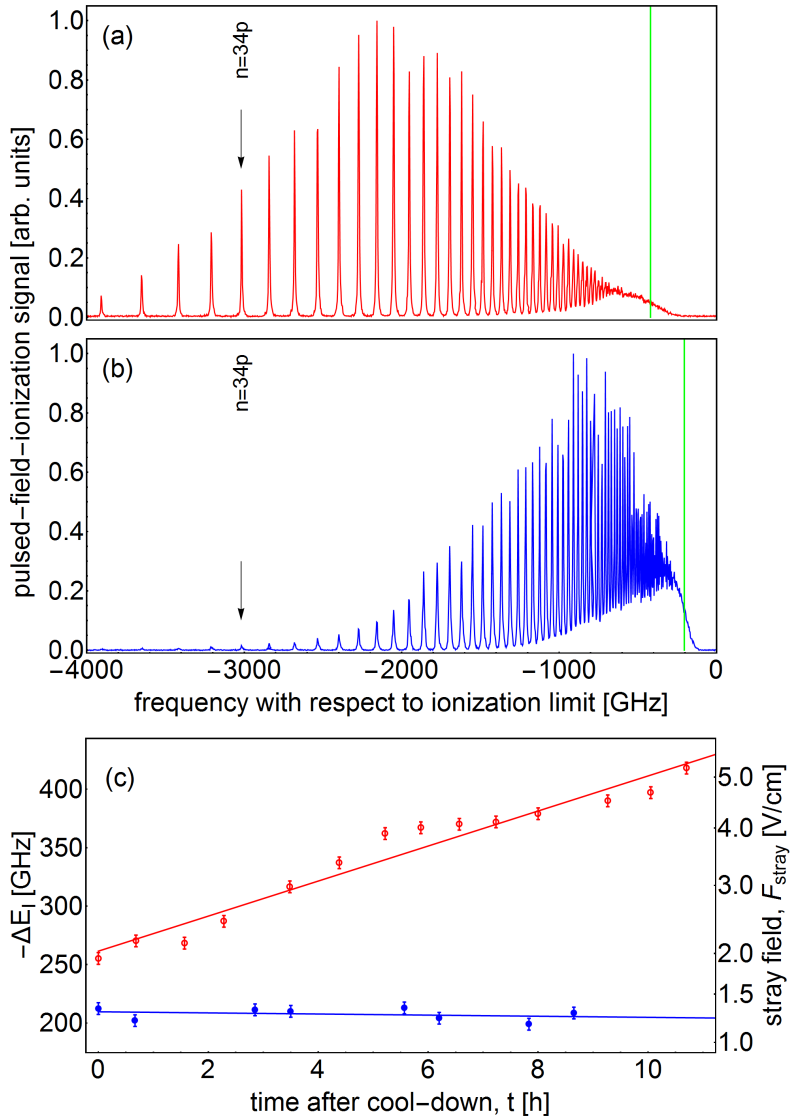


Figure 5.9: Spectra of the $[\text{He}^+]np \leftarrow (1s)^1(2s)^1\ ^1S_0$ Rydberg series of He recorded when (a) the residual gas adsorbed and charges build up in the matrix of frozen material, and when (b) the adsorption process onto the sample surface was suppressed. (c) Evolution of the field-induced shift of the ionization threshold ($-\Delta E_i$) versus time, with (full blue circles) and without (open red circles) suppression of adsorption of residual gas onto the sample surface.

(Sec. 4.1). The field-induced shift of the ionization threshold ΔE_I is determined by fitting an error-function to the field-ionization signal and taking its inflection point. Based on Eq. (4.3), this observation indicates that the stray field along the beam-propagation axis reaches values up to 5 V/cm above the sample surface. In Fig. 5.9(b), the weakness of the lines corresponding to transitions to $n \leq 40$ Rydberg states and the observation of a field-ionization signal up to -200 GHz with respect to the field-free ionization threshold indicate that the maximum stray field between laser excitation and pulsed field ionization along the beam-propagation axis does not exceed values of 1.5 V/cm.

By repeatedly recording spectra such as the one displayed in Fig. 5.9(a) and determining from each spectrum the shift of the ionization threshold ΔE_I , we have determined the gradual build-up of stray fields above the surface as the experiment progresses. The results are depicted in Fig. 5.9(c) as red open circles. Immediately after cooling the sample surface to 3 K, the field-induced shift of the ionization threshold (ΔE_I) is -250 GHz. It decreases to -450 GHz at a rate of 15(1) GHz/hour, revealing that the maximal value of the stray field along the beam-propagation axis has increased to more than 5 V/cm after 11 hours of continuous measurements.

Using the cooling procedure described above, the field-induced shift of the ionization threshold remains constant ($-0.5(6)$ GHz/hour) after cooling the sample surface to 3 K, as shown by the full blue circles in Fig. 5.9(c) and by the spectrum depicted in 5.9(b), which was recorded after a continuous experimental run of 8.5 hours.

The constant stray field after cooldown indicates that a negligible amount of gas adsorbed at the sample surface during cooldown. Hence, after cooldown, the only gas that can adsorb at the surface is gas that enters the cryostat through the skimmer and the exit pinhole and hits the sample surface.

The most abundant residual gas in the experimental chamber after cooldown is H_2 which outgasses from the warm chamber walls with a rate of 6.6×10^7 /s/cm² [Chiggiato (2006)]. It is very unlikely that a H_2 molecule that enters the experimental region and does not hit the sample holder in the first place will adsorb at the sample later. Because the number of collisions an atom has to undergo before returning to the sample surface with 3-K-cold surfaces other than the sample is so large ($\gg 10$ assuming elastic collisions) that it will adsorb at these surfaces with nearly unit probability.

An upper threshold of particle flux that impinges directly onto the chip surface can be estimated by assuming unit adsorption probability and the holes in the 3-K stage to consist of warm chamber walls. Taking into account the combined solid angles Ω_{lc} and Ω_{sc} [Eq. (5.2) and 5.1] under which the chip surface is accessible through the holes by direct line-of-sight, we obtain a maximal particle flux of \sim

20000/s H₂ molecules that adsorb at the surface. Given the average diameter of an H₂ molecule being 0.74Å [DeKock and Gray (1989)], we obtain a maximal fraction of $\sim 3.5 \times 10^{-6}$ of the chip surface A_c being covered with atoms after seven days after cooldown of the experiment.

5.2.4.1 Warmup of the cryostat

When the experiment is warmed up, the temperatures of the 30-K stage and the 3-K stage increase monotonically with time. The total pressure in the cryogenic and the total and partial pressures in the experimental chamber we observe as a function of time can therefore uniquely be linked to the temperatures of the different stages (Fig. 5.10).

In Fig. 5.10, we link the typical total pressures of the cryogenic (red) and experimental chamber (violet) in panel (a), and the partial pressures of the most abundant gases measured by the RGA in the experimental chamber in panels (b) and (c) (colors indicated in the panel) to the temperatures of the 30-K stage (top axis) and the 3-K stage (bottom axis) during warm up. If a stage reaches a temperature in which gas desorbs from cold surfaces, the total pressure and partial pressure of this gas increases. Studying the shape and position of the different peaks observed in the traces, it is possible to carefully interpret at which stage residual gases freeze out during and after cooldown.

The following assumptions (rules) are made to interpret the data:

1. If the total pressure of the experimental chamber reaches the same pressure as the pressure in the cryogenic chamber, gas desorbed only in the experimental chamber.
2. If several partial pressures exhibit peaks of the same shape and at the same temperatures, the desorption temperature corresponds to the gas with the strongest peak, and the other gases were trapped earlier in its matrix of frozen gas.
3. Desorption starts as soon as the stage has reached the adsorption temperature. The maximum of the detected desorption may be at higher temperatures because the ice has to warm up, i.e. because of finite sublimation energy.
4. If gas desorbs only once, it only adsorbs to the 3-K stage, if it desorbs twice, it first desorbs from the 30-K stage and then from the 3-K stage.
5. H₂O and CO₂ are trapped more efficiently to cold surfaces than N₂ and O₂ [DeKock and Gray (1989)].

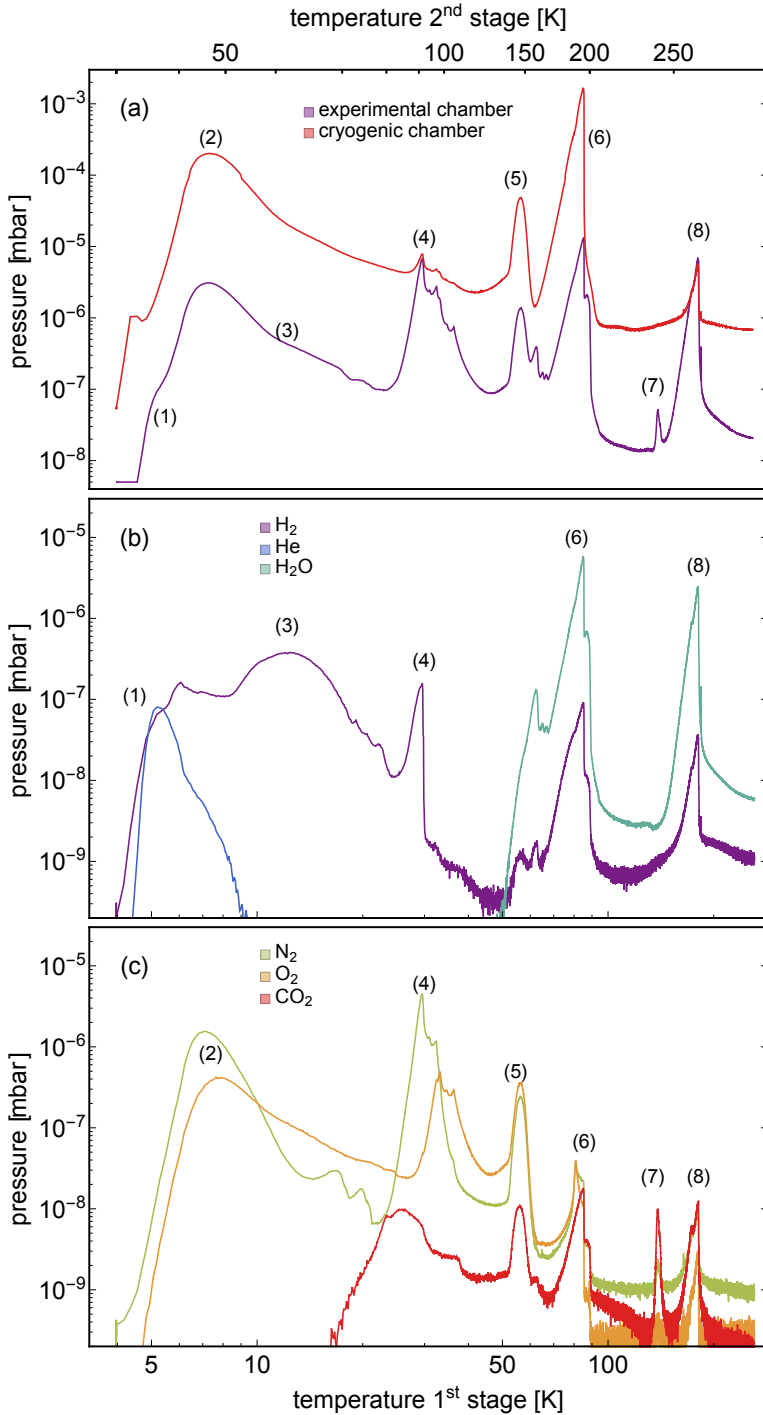


Figure 5.10: (a) Total pressures and (b,c) partial pressures as function of temperature of the pulse-tube stages during warm up. The features at positions labeled 1-8 are discussed in the text.

In the following we will follow the graph (Fig. 5.10) from left to right as warm-up time increases, because of the monotonical increase of the stage's temperatures. The different peaks labeled (1 – 8) will be discussed separately in the following:

1. After switching off the pulse-tube cooler, liquified helium starts to desorb from the 3-K stage as soon as it has reached a temperature of ~ 4 K.
2. Gas desorbs in the cryogenic chamber (maximal total pressure $> 10^{-4}$ mbar). It diffuses through the differential pumping into the experimental chamber where it is detected by the RGA. Rule 2 identifies the gas as N_2 , which desorbs at slightly lower temperatures than O_2 . The measured desorption temperature of the 30-K stage is ~ 40 K, i.e. ~ 20 K before the expected desorption temperature of N_2 and O_2 (compare Tab. 5.1). Therefore, we attribute this desorption of gas being localized to the edge of the copper plate of the 30-K stage that is metallically connected with the bellows of the differential pumping section. This region is expected to warm up faster than the part of the 30-K stage which is in the experimental chamber, within the 30-K heat shield, and to which the temperature sensor for the 30-K stage is attached, because it is directly exposed to the radiation heat from the warm chamber walls.
3. H_2 gas desorbs at temperatures ~ 10 K from the 3-K stage (see rule 4).
4. N_2 gas (rule 2) desorbs starting from temperatures ~ 60 K from the 30-K stage (rule 3) in the experimental chamber (rule 1). The outer layers (that desorb first) are formed by gas that adsorbed to the stage during event labeled (2), and include additional adsorbed H_2 gas [item (3)] that adsorbed also during the period in which the experiment was cooled. This can be concluded from the sharp edge of the peak in the H_2 line [panel (b)], when the peak in the N_2 line [panel (c)] is not sharp, i.e. lower layers of N_2 -ice desorb. Again, O_2 starts to desorb at higher temperatures [panel (c)].
5. H_2O desorbs from the copper ring at a temperature of ~ 20 K before the expected desorption temperature (compare event 2). Trapped N_2 and O_2 gas that diffused into the experimental chamber is detected by the RGA. H_2O is not efficiently detected (rule 5).
6. Starting from temperatures of ~ 160 K of the 30-K stage, H_2O desorbs in both chambers from the main part of the 30-K stage, releasing H_2 , N_2 and O_2 gas that was trapped during events (2), (4), and (5). Simultaneously, the 3-K stage reaches desorption temperatures of O_2 and N_2 .

7. At about 125 K, CO₂ gas desorbs from the 3-K stage that adsorbed during the initial phase of the cooldown. A similar peak is not observed for the 30-K stage because of rule 5.
8. H₂O desorbs from the 3-K stage, that adsorbed efficiently during events (5) and (6), releasing remaining trapped gases of CO₂, N₂ and O₂.

5.2.5 Fast temperature stabilization of the sample holder

The temperature of the 3-K stage oscillates with approximately 200 mK about its base temperature of 2.8 K at a well-defined frequency of 1.41 Hz, because of the compression of the helium gas in the pulse-tube cooler. Due to the good thermalization of the sample holder to the 3-K stage, also the temperature of the sample holder oscillates with the same amplitude and frequency. Temperature fluctuations of 0.2 K cause shifts of the resonance frequency of superconducting resonators of ~ 120 kHz at $\nu_0 \approx 5$ GHz (Sec. 6.2). This impedes sensitive measurements of resonator shifts and broadenings and hence need to be minimized.

We have reduced the temperature fluctuations on a test sample holder from 200 mK to 8 mK at an increase of the sample holders mean temperature of ~ 0.77 K [Mergenthaler (2012)]. The sample holder was positioned at the top plate of the 3-K stage and contained a heating wire and a temperature sensor. Temperature fluctuations were reduced by a combination of a (passive) thermal decoupling of the sample holder from the 3-K stage and an (active) thermal compensation of the temperature fluctuations using a computer-controlled heater [Fig. 5.11(a)].

Passive compensation is achieved by isolation of the sample holder from the 3-K stage using a 0.8-mm-thick layer of fiber-reinforced plastic (FRP) [Hasegawa *et al.* (2010); Nakamura *et al.* (2011)] with a thermal diffusivity of $\sim 2.47 \times 10^{-6}$ m²/s. This measure reduced the 200-mK-strong temperature fluctuations [Fig. 5.11(b), green] to temperature fluctuations with amplitude ~ 65 mK (red).

Reduction of the temperature oscillations from ~ 65 mK to ~ 8 mK (black) is achieved by applying a time-dependent current to the heating wire on the sample holder [Mergenthaler (2012)]. The current is generated by a voltage-controlled-current-source (VCCS) to which a sinusoidal waveform is applied by a controller (signal generator). The waveform has the same frequency as the oscillation of the pulse-tube cooler (1.41 Hz) and has a fixed phase slightly below π with respect to the temperature fluctuations, such that the maximal current is applied to the heater if the temperature is lowest. The feedback loop can be closed by phase locking the two oscillations [dashed line in panel (a)], i.e. adjust the phase of the heater signal, such that the oscillation amplitude is minimal. We have observed that adjusting the phase of the two signals as described above performs better than using a PID-control to adjust the current in the heater, which increases the base-temperature [Mergenthaler (2012)].

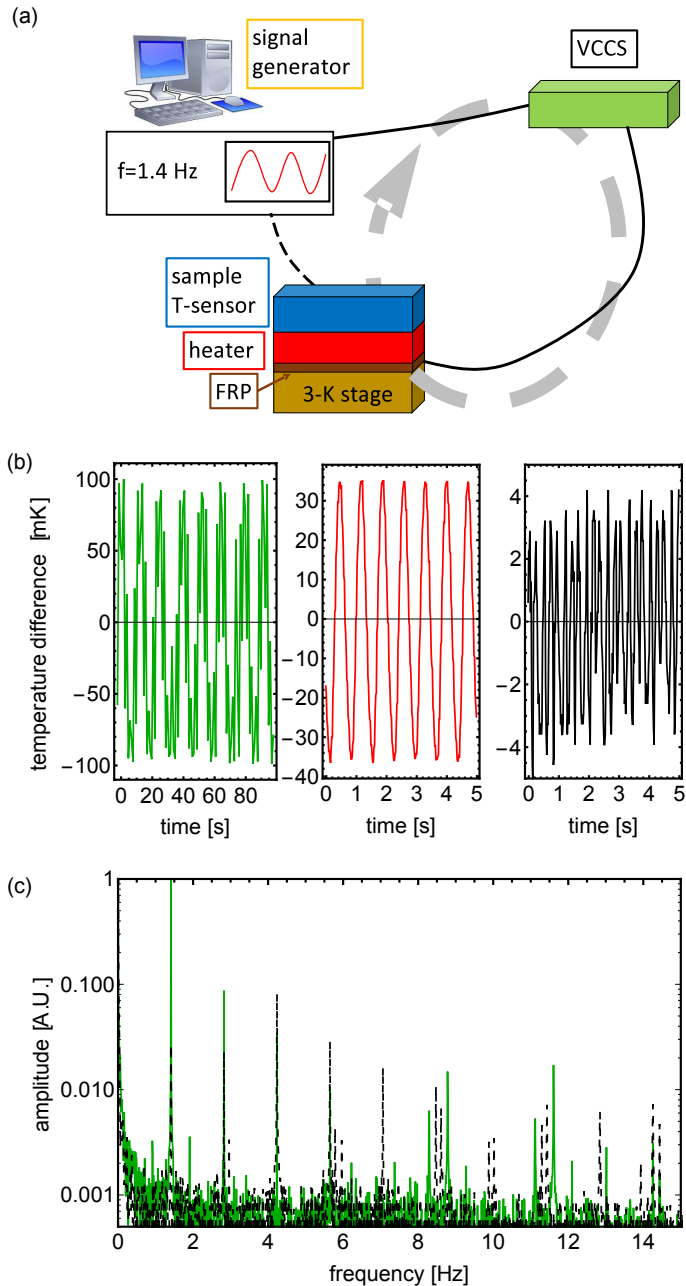


Figure 5.11: (a) Principle of temperature feedback (gray arrow). The voltage-controlled-current source (VCCS) is indicated in green. The temperature sensor (blue), the heater (red) and the fiber-reinforced plastic (FRP, brown) at the sample, and the computer are also shown. (b) Measured temperature fluctuations from mean temperature over time. Green data shows initial temperature fluctuations, red data shows temperature fluctuations after passive decoupling and black data shows temperature fluctuations after active compensation. (c) Fourier transform of measured temperature oscillations for the uncompensated (green) and the compensated (black dashed) case. Data in second and third panel in (b) and in (c) also presented in *Mergenthaler (2012)*.

In Fig. 5.11(c) we observe from the Fourier-transform of the uncompensated (green) and the compensated (black) temperature signal, that the dominant peak at ~ 1.41 Hz is reduced by a factor of 50. However the second harmonic at 4.24 Hz is increased by a factor of 2. An improved temperature controller could further reduce the temperature oscillations by generating an optimized waveform that is applied to the heating wire, and that consists of the fundamental 1.41 Hz and of higher harmonics.

5.3 Magnetic field compensation for optimal detection of atom distributions

The trajectories of the Rydberg electrons that are generated from ionization of Rydberg atoms in zone 3 and which are detected at the microchannel plate (MCP) are very sensitive to external magnetic fields because of their small mass². We observe that the electron beam is deflected away from the symmetry axis in z direction of the experiment in the presence of magnetic fields. This distorts images taken from the Rydberg atom distributions. As a consequence an active magnetic-field feedback has been developed that compensates the magnetic fields in the electrode stack and the flight region of the electron beam. In this section, we present a simple model that calculates the deviation of the electron beam, created from ionization of $n^* = 33$ and $n^* = 47$ Rydberg states in a magnetic field, and we present the effect of the compensation of magnetic fields onto Rydberg spectra. The magnetic field control is presented in Sec. 5.3.1 and the compensation procedure and results on electron beam deviations are presented in Sec. 5.3.2.

The deviation in x direction, $\Delta x(t)$, due to a homogeneous (stray) magnetic field $\mathbf{B} = (0, B, 0)$ from the trajectory of an electron propagating along the z direction with velocity v_e (Fig. 5.12) can be approximated as [Lüthi (2013)]:

$$\Delta x(t) = \frac{-e}{2m} v_e B t^2 \approx \frac{-e}{2m} B \frac{z_{I,MCP}^2}{v_e}. \quad (5.7)$$

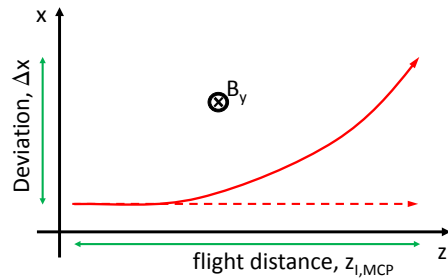


Figure 5.12: Sketch of electron beam trajectory (red line) deviating from the ideal trajectory (dashed line) during a flight in finite magnetic field.

²Imaging electrons is more sensitive than imaging ions. However, we perform electron imaging because of the clean detection procedure in well-defined electric fields (Sec. 4.3.2 and 4.3.3.3).

Here, m_e is the electron mass, $t = z_{I,\text{MCP}}/v_e$ the electron travel time, $z_{I,\text{MCP}} = 150$ mm the distance between ionization region and MCP, and we assumed that $\Delta x(t)/t \ll v_0$. Assuming the Rydberg atoms are ionized between E_4 and $IL1$, the velocity of the electrons v_e depends on half the value of the potential U_4 applied to electrode 4. If all potential energy is converted to kinetic energy

$$v_e = \sqrt{\frac{eU_4}{m_e}}. \quad (5.8)$$

U_4 differs from one Rydberg states n to the other, because of the difference in ionization potentials.

For the state $n^* = 33$ ($n^* = 47$), the relevant ionization potential at the ionization electrode 4 (Sec. 4.3.3.3) is $U_4 = -425$ V ($U_4 = -105$ V) and therefore $v_e = 8.6 \times 10^6$ m/s ($v_e = 4.3 \times 10^6$ m/s). The earth magnetic field ($B \approx 30$ μT) causes deviations of $\Delta x \approx 7.8$ mm and $\Delta x \approx 15$ mm for the $n^* = 33$ and $n^* = 47$ state, respectively. For stray magnetic fields up to $B \approx 60$ μT (measured at positions close to the experiment) the deviations are $\Delta x \approx 15$ mm and $\Delta x \approx 31$ mm for the $n^* = 33$ and $n^* = 47$ state, respectively³. We expect the detection of Rydberg states with quantum numbers $n \geq 50$ to be inefficient (for $B = 30$ μT) because the deflection $\Delta x(t)$ becomes larger than the radius of the MCP-detector (20 mm). However, a compensated magnetic field, i.e. $B = 0$ μT , should result in a deviation $\Delta x(t) = 0$ mm, independent of the Rydberg state [Eq. (5.7)].

Comparison of two spectra with and without magnetic field compensation under otherwise identical measurement conditions (Fig. 5.13) shows that states above $n \approx 50$ (≤ 1000 GHz) are detected less efficiently for the uncompensated case (red data) with respect to the compensated case (violet data). In both cases we detected Rydberg electrons from electrode 4 (zone 3), when no sample was inserted into zone 2, and stray fields were compensated at the excitation position.

5.3.1 Magnetic field controller

We compensate the magnetic field along the symmetry axis of the experiment with 4 cylindrical and 2 circular compensation (shim) coils (yellow structure in Fig. 5.1 and Fig. 5.14). The coils have 200 copper windings on Polyoxymethylene (POM) profiles with U-shaped crosssection [Goblot (2014)]. The two circular coils of 300 mm radius are oriented in z direction with 400 mm separation. The rectangular coils that are oriented along the y direction have dimensions in the (z - x)-plane of (800,800) mm. The coils that are oriented along the x direction have dimensions in the (z - y)-plane of (800,500) mm. The magnetic field

³For these deviations, the initial assumption ($\Delta x(t)/t \ll v_e$) starts to break down.

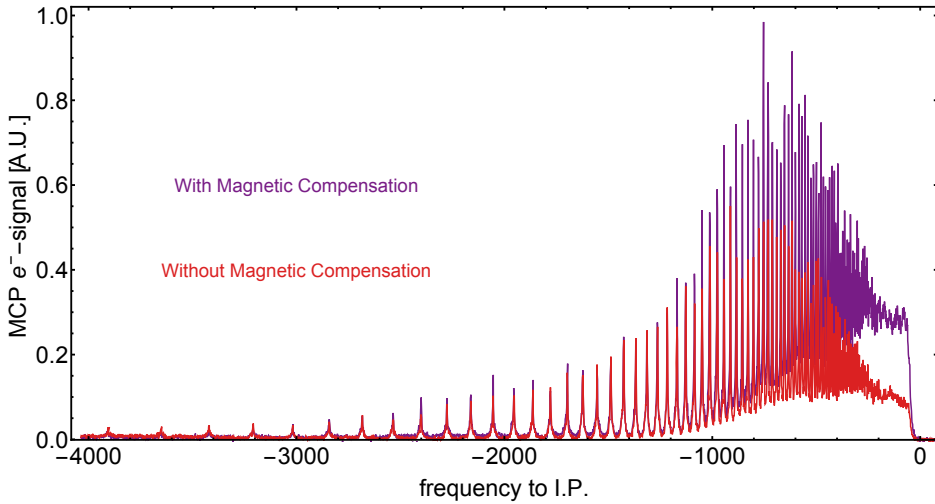


Figure 5.13: Comparison of two spectra with (violet) and without (red) magnetic field compensation, acquired with identical settings and without a sample holder inserted into the experimental region. Data presented also in *Goblot (2014)*.

produced by each shim coil can be individually controlled and the combination of all coils allows compensation of external magnetic field gradients in a region of $(x, y, z) = (\pm 0.1, \pm 0.1, \pm 0.18)$ m, centered around the extraction region (zone 3) [*Goblot (2014)*]. We measure the total magnetic field, i.e. the sum of the stray magnetic fields and the compensation field produced by the coils, with two three-axial sensors (*Stefan-Mayer Instruments:FLC3-70*), that produce a total of 6 magnetic field values (channels). The sensors are aligned along the x , y and z direction of the experiment and positioned relative to zone 3 at $(x, y, z) = (0.1, 0.1, -0.15)$ m and $(-0.1, -0.1, 0.05)$ m, i.e. close to the diagonal of the box defined by the rectangular coils. The positions of the magnetic field sensors with respect to the coils are chosen such that the field produced by each coil is closely aligned with one measurement axis of the sensor.

The shim coils are individually controlled with a stand-alone feedback system [Fig. 5.14(a)] which reacts automatically to changes in the stray magnetic field strength [*Lüthi (2013)*]. The magnetic field is measured along the three directions at the position of the sensors. The analog measurement signal of all 6 channels ('measured output') from the sensors is converted to a digital signal in an analog-to-digital converter (ADC) card (*National Instruments: NI-9205*). In the control unit, first the difference between the measured field and a reference signal is calculated. Then, an integral controller implemented in a LabView program calculates a control output which is converted to an analog signal in a digital-to-analog converter (DAC) card (*National Instruments: NI-9264*). The analog signal controls a

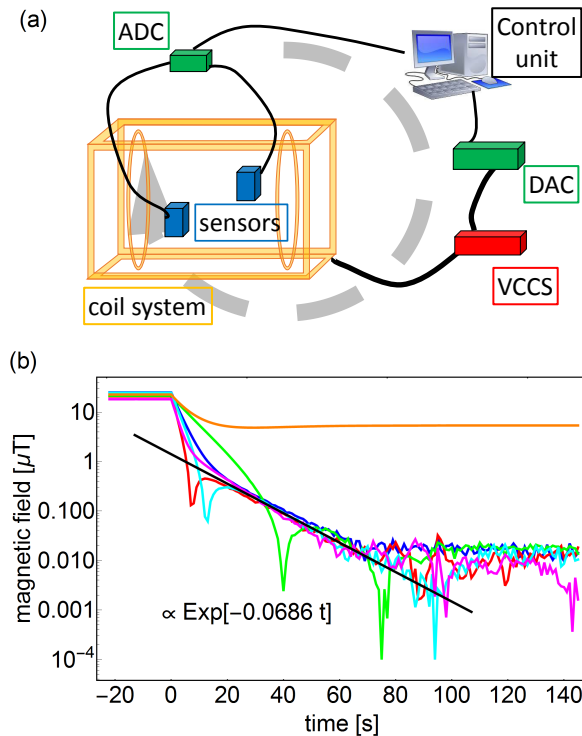


Figure 5.14: (a) Sketch of magnetic feedback (gray arrow). Analog data from two three-axial magnetic field sensors (blue) is digitized using a DAC (green) and read by the control (computer). The error signal controls the current in the coils (yellow) via a voltage-controlled-current source (red) and a DAC (green). (b) Measured magnetic field in all directions as a function of time after the control was activated. The circular coil close to one sensor was not controlled (orange curve denotes z -component of that sensor). The black line is an exponential fit with a decay constant of ~ 15 s. Picture (b) taken from *Lüthi (2013)*.

home-built voltage-controlled-current-source (VCCS) that produces the currents to operate the coils. The maximal magnetic field strengths that can be compensated by this system are $\sim 300 \mu\text{T}$, limited by the VCCS [*Goblot (2014)*].

The integral controller is designed as 6 parallel single-input-single-output (SISO) controllers [*Lüthi (2013)*]. The input to one SISO-controller corresponds to the measurement signal of one axis of one sensor. The output signal of the same SISO-controller produces a current in the coil that dominantly affects the magnetic field in the same direction at the position of the sensor. Because a current in a specific coil produces a change of the magnetic field in all channels, the controllers are not independent. The controllers become active if the measured magnetic field deviates by 25 nT from the reference value which is defined for ev-

ery controller separately. A similar feedback system has also been implemented recently for magnetic-resonance-imaging systems [Dürst *et al.* (2015)].

In a characterization measurement [Fig. 5.14(b)] we set the reference magnetic fields for all controllers to zero and observe the measured magnetic field strengths along all three directions (x, y, z) at the positions of the sensors (colored traces) [Lüthi (2013)]. In this measurement, we switched off the SISO control for the circular coil positioned close to the source chamber such that the current in this coil is always 0. This coil affects the magnetic field in z direction at the position of sensor 1 at (0.1, 0.1, -0.15) m strongest (orange trace). *First*, we observe that the controlled field directions reach their reference values after $t_c \approx 60$ s after switching on the feedback at time $t = 0$ s. The control time of the feedback system is ~ 15 s as obtained from an exponential fit (black line). On the one hand, this time constant is determined by the tuning parameters of the SISO controllers and can be made shorter if the controllers were tuned more aggressively. On the other hand it is determined by the crosstalk between the different control channels which lead to the zero-field crossings in the measured signals (indicated by peaks in the colored traces). *Second*, the z direction of the magnetic field at sensor 1, which is not controlled, remains at high field values but is reduced to 25% with respect to its uncontrolled value because of the crosstalk of the different coils (control channels).

We have developed and tested an improved version of the controller during the work of Goblot (2014), i.e. a multiple-input-multiple-output (MIMO) controller, which has not been installed permanently. The basis in which the MIMO-controller was implemented is determined by the 6 measured magnetic field channels of the sensors. Therefore, the measurement of the magnetic field can be represented as a vector in a 6-dimensional space. The magnetic field generated by a single shim coil is then given by a 6-dimensional vector, the entries of which are dominated by the component of the magnetic field channel that is affected most strongly by this coil. The other entries of the vector characterize the crosstalk between this coil and the other channels. In the MIMO-controller, we compensate for this crosstalk by first inverting the matrix that is given by the combination of all measurement vectors that are produced when the same current is applied to each shim coil separately. The inverted matrix reveals the relative currents that need to be applied to all coils simultaneously to change the value of a single magnetic field channel. This information is then used in an additional processing step after the 6 SISO controllers described above to decouple the different control channels, such that the output of one SISO controller controls one magnetic field channel only. First measurements (not shown) indicate that this MIMO controller can reach control rates $\gtrsim 1$ Hz.

5.3.2 Measured deflections of an electron beam for different Rydberg atom states

The control system described in the last section allows to control the position at which the Rydberg-electron beam hits the microchannel plate (MCP) detector [Fig. 5.12(a)]. Rydberg electrons were generated by ionization of $n = 34s$ Rydberg states. The position of the electron beam at the MCP (black dots) was adjusted along the x and y direction, by changing the setpoint of the SISO controller that operates on the channel corresponding to the coil pointing in positive y and x direction. The measured positions were determined from fits to the detected electron distribution in CCD-camera images taken from the phosphor screen of the MCP (Sec. 4.3.3.3). The green circle corresponds to the position at which the electrons are detected if they move in a magnetic-field-free region, i.e. $B = 0 \mu\text{T}$ over the entire volume V_{ep} through which the electrons travel.

The field-free configuration is reached if $\Delta x = 0$ mm, independent of the Rydberg state from which the electron beam was generated by ionization, as motivated in the following. Given the $(n^*)^{-4}$ -dependence of the ionization field (Eqs. 4.1 and 4.2), the $(n^*)^{-2}$ -dependence of the binding energy of a Rydberg state [Eq. (1.28)], and Eq. (5.7), we expect that for a Rydberg state excited from the metastable singlet state [Goblot (2014)]

$$\Delta x = A \left(\frac{1}{\lambda} - \frac{1}{\lambda_{\text{IP}}} \right) \quad (5.9)$$

with λ the laser excitation wavelength, $\lambda_{\text{IP}} = 312.176$ nm the excitation wavelength to the ionization limit and A a proportionality constant. A is proportional to the modulus of the total magnetic field integrated over V_{ep} .

To determine the reference values of the magnetic-field-compensation system for which $A = 0$ (i.e. $B = 0 \mu\text{T}$ for V_{ep}), we choose two Rydberg states with large n and small n , respectively, typically $n = 47p$ and $n = 34s$. Then, we iteratively adjust the reference values of the SISO-controllers until the detected positions of the corresponding electron beams at the MCP overlap [Goblot (2014)].

For an uncompensated stray magnetic field (A large), the expected dependence of Δx as a function of Rydberg state excitation wavelength λ agrees with measurements [black dots Fig. 5.15(b)], as shown by a fit (green trace, $A = 0.00101(2)$ nm px). The dashed line indicates the edge of the detection region (camera images). Electrons generated from ionization of Rydberg states $n \gtrsim 50$ (excitation wavelengths $\lambda \leq 312.45$ nm) are deflected by more than 20 mm (corresponding to ~ 350 px on the camera) and are detected inefficiently. The only magnetic-field-strength distribution for which $\Delta x = 0$ mm, independent of the Rydberg state is $B = 0$ for all positions within the volume in which the electrons

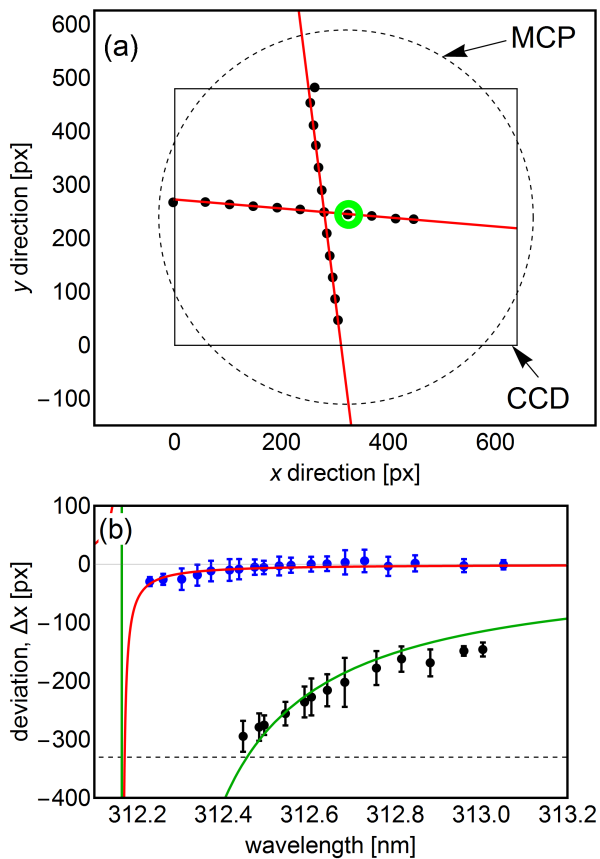


Figure 5.15: (a) Fitted positions (black data) of the electron beam at the MCP for different currents through the rectangular coils in x and y direction. Red lines are linear fits and the green circle denotes the magnetic-field-free position. (b) Vertical deviations from field free position of electron beam as a function of excitation laser wavelength. Blue and black dots correspond to fitted center positions (error bars indicate full-width-at-half maximum) when the magnetic field was and was not compensated. The green and red lines are fits to a simple model, see text. Pictures modified from *Goblot (2014)*.

travel. A measurement of Δx as a function of λ for a (compensated) B -field distribution for which $B \approx 0 \mu\text{T}$ is shown by the blue data points, with the fit to Eq. (5.9) indicated by the red trace ($A = 2.2(2) \times 10^{-5} \text{ nm px}$). The comparison between the two fitted proportionality factors A indicates that the total modulus of the stray magnetic field in the flight region of the electrons (V_{ep}) was reduced by a factor 45.

5.4 Electronic control of the experiment and data acquisition programs

To operate the experiment, various equipment operating at different voltage and frequency regimes, has to be combined with minimal interplay. We present in Fig. 5.16 an interconnectivity diagram of the different devices in the experiment. We have not included other, stand-alone systems, such as the magnetic-field feedback (Sec. 5.3), the pulse-tube control and the equipment needed to do the adsorption-free cooldown (Sec. 5.2.4). At the end of the section we discuss the structure of the two control programs we use to operate the system.

The different devices can be sorted in roughly 6 different groups according to their operation regimes: timing control (black), high-voltage (HV) (green), microwave (red) and low-voltage (orange) devices, laser operation and the digital data acquisition (blue). In the experiment, the digital, microwave, signal, and trigger cables are spatially separated to reduce cross-coupling.

All apparatuses are synchronised to two different clocking domains we generate in the *timing control group*, the 25-Hz-repetition rate of the experiment and a 10-MHz-frequency standard. On the one hand, the trigger signal for the repetition rate of the experiment is generated in a home-built trigger box ('line trigger') which is locked to the mains of 'phase 1'. On the other hand a rubidium clock provides a 10 MHz frequency standard. Because of the large jitter in the mains frequency ($\lesssim 0.5 \text{ Hz}$), the mains-trigger signal can be considered asynchronous to the 10 MHz signal. The mains-trigger is locked to the 10-MHz-frequency standard using an arbitrary waveform generator (AWG) with a bandwidth of 80 MHz (*Agilent:33250A*), i.e. the experiment-trigger pulse is produced only if the input signal from the 'line trigger' and the rubidium clock both passed a certain threshold.

The experiment-trigger is distributed to the different equipments by three delay generators (*Stanford Research Systems:DG645*), connected in series. Each of the delay generators ('DG1-DG3') has an external trigger input and 5 output channels, of which the first (t_0) replicates the external trigger and the rise and fall times of the other four 4 channels [(rise, fall) = (A,B); (C,D); (E,F); (G,H)] can be controlled individually [*Könz (2014)*]. DG1 triggers the opening of the valve ('valve trigger', $t_0 = t_V$), the high voltage of the electric discharge ('DC pulser', A), the high-voltage pulse for the Nd:YAG laser flashlamps ('FL Nd:YAG', C), the Pockels

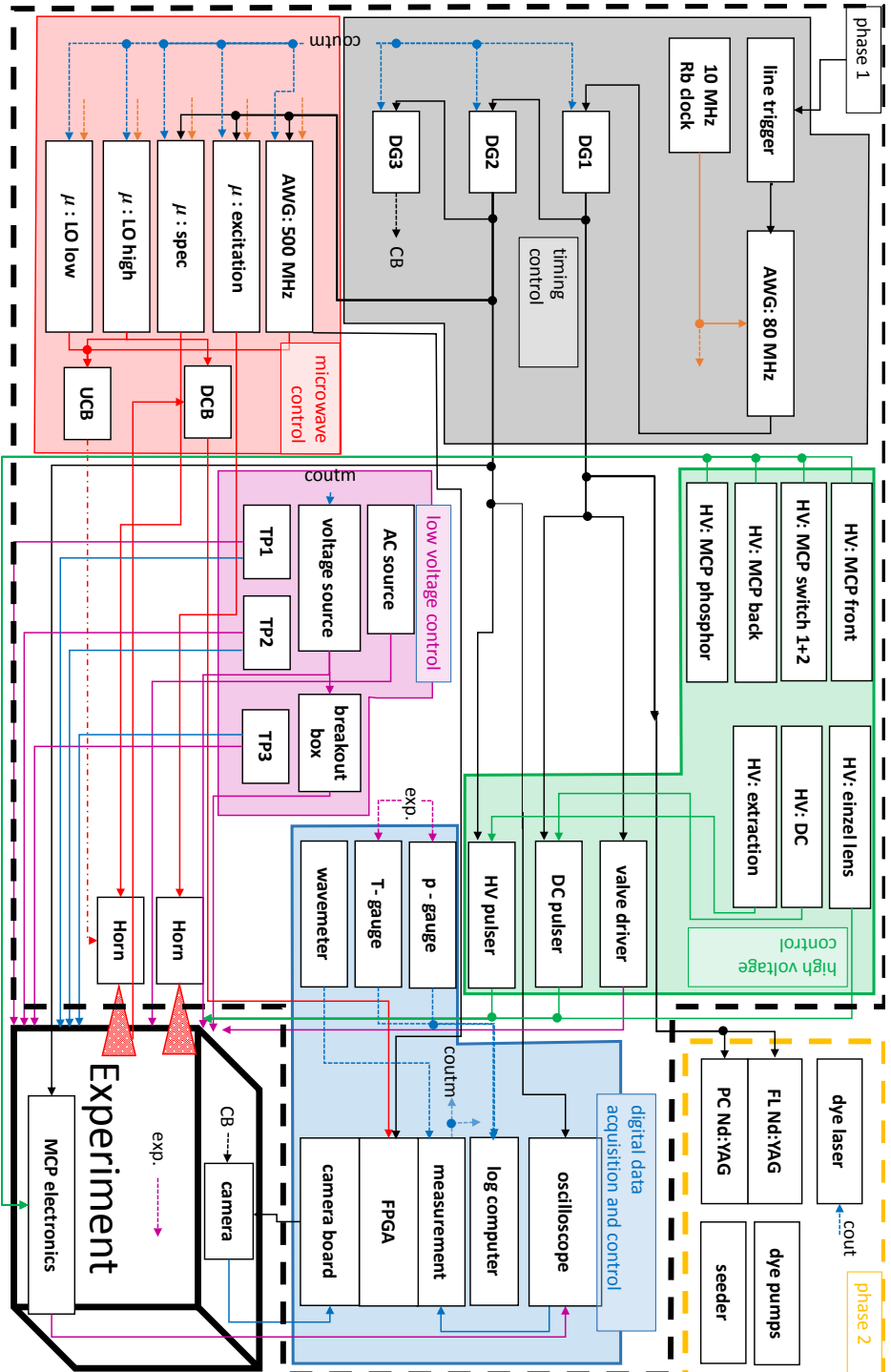


Figure 5.16: Electric connection scheme of the experimental setup organized by signal properties corresponding to type of signal line. Digital lines are indicated blue, analog lines magenta, trigger lines black, high voltage lines green and microwave lines are red. Thick dashed lines indicate which systems are connected to line phase 1 (black) or 2 (yellow).

cell ('PC Nd:YAG', E), and it triggers DG2 (G). Channel t_0 of DG2 triggers DG3, and the remaining channel define the detection window of the MCP (A, B), the extraction pulse and the oscilloscope trigger (C, D), and the two microwave pulses [(E, F) and (G, H)]. For experiments involving the up-conversion-board ('UCB'), channel G triggers the '500-MHz-AWG'. DG3 includes a high-power output at the rear-panel of the instrument, that generates the short 10-V signal used to trigger the CCD-camera that takes images of the phosphor screen.

From the 8 high-voltage sources of the *high voltage (HV) group*, 5 generate the potentials needed to operate the microchannel plate detector. The HV-sources are labeled 'MCP front, MCP switch 1 and 2, MCP back' and 'MCP phosphor'(Sec. 4.3.3.1), and are all connected to the MCP electronics, located close to the experiment. The 'extraction'-HV-source biases the 'HV-pulser' that creates the extraction pulse (Sec. 4.3.2). The remaining sources provide high voltage for the einzel lens (Sec. 4.3.3.3) and the electric discharge (DC).

For experiments involving *microwave radiation* we generate microwave tones using 4 microwave sources ('excitation': AGILENT: E8257D-550, 'spec': AGILENT: E8257D-540, 'LO high': AGILENT: E8257D-540 and 'LO low': AGILENT: E8257D-520). 'Excitation' and 'spec' are typically operated in pulsed mode and produce the microwave square pulses used to transfer Rydberg population in the experiments presented in part 2. The microwave pulses are inserted into the experiment using two microwave-horn antenna. The up-conversion board ('UCB') [Köpsell (2014)] produces the amplitude- and phase-controlled microwave pulses from two local oscillators ('LO low' and 'LO high') we used to conduct high-resolution experiments of atoms in free-space [Köpsell and Thiele (2016)]. The down-conversion-board ('DCB') [Reim (2011); Ruffieux (2014)] first amplifies the small microwave signals from the experiment, and then coherently down-converts the signal to 25 MHz.

The *low-voltage group* contains the current source ('AC source') for the filament (Sec. 3.1), and 8 low-voltage sources (Stanford Research Systems: SIM928) that operate up to ± 20 V. One source is used to apply a potential to the output-viewport of the laser (Sec. 5.1), three are used to apply potentials to electrodes 1, 2 and 3. The remaining 4 sources are combined in a breakout box that connects to the DC-wires leading to the 3-K stage of the cryostat (Sec. 5.16). The controls of the turbo-molecular pumps ('TP1'-'TP3') provide power to the pumps via low-voltage cables and communicate by digital signals.

Data acquisition is done by means of two computers ('log computer' and 'measurement computer') and an oscilloscope. The 'log computer' is used, on the one hand, to log the temperature (LakeShore:Model 350) and pressure data (Pfeiffer:TP 256 A, MaxiGauge) of the cryostat and the three vacuum chambers. On the other hand (not shown in the diagram) it controls the pulse-tube cooler, the

adsorption-free-cooldown procedure (i.e. the cartridge heaters and the residual gas analyzer), and the magnetic-field feedback. The measurement computer reads the 'wavemeter', controls 'DG1', 'DG2' and 'DG3', the 500-MHz-AWG and the microwave sources, the 8 low-voltage sources and the 'dye laser'.

The measurement computer may acquire data through one of the following interfaces. Data acquisition of the MCP time traces is realised by controlling an oscilloscope (*LeCroy: waverunner 610ZI*) that measures the amplified microchannel plate detector signal (Sec. 4.3.3.1) and transfers the measured data digitally to the measurement computer. The images from the MCP phosphor screen acquired by the camera are processed in a PCI-card (*QMT:PCle-8255R*) directly inserted into the measurement computer. Microwave signals at 25 MHz from the DCB are first digitally down-converted in an FPGA-board (*Xilinx:Virtex 4*) and then further processed (e.g. averaged).

The *laser equipment group* consists of the flashlamp ('FL Nd:YAG') and the Pockels cell ('PC Nd:YAG') in the laser head of the pump laser, its 'seeder'-laser, and the 'dye laser' and the 'dye pumps' (Sec. 4.3.1).

The laser equipment is connected to a separate mains-phase (2, yellow, dashed line), because it has the largest power consumption. All other equipment are connected to mains-phase 1 (black dashed line) and the same ground potential. The motivation to bias all equipment except the laser instruments with one phase of the mains comes from the electromagnetic influence (EMI) of the mains phases. If all voltage sources are biased by the same phase, all potentials in the setup are defined relative to the same mains potential at one instant in time. In this case, time-jitters in triggered elements and stray electric fields between electrodes are minimized that would otherwise arise from the electric noise between the two mains-phases.

As indicated in Fig. 5.17(a), the custom-made *National Instruments:LabView*-code that runs on the 'log computer' reads (inputs) the information on the temperature from the temperature controller, the pressure data from the MaxiGauge, the measured magnetic field data from the two sensors (Sec. 5.3), the partial gas pressures in the experimental chamber as acquired by the RGA, and the wavelength of the wavemeter (channeled from the measurement computer). The output of the program can control a heater connected to the temperature controller from *Lakeshore*, the VCCS we use to produce the currents for the magnetic field coils and the heater for the adsorption-free cooldown.

The program is designed as 6 parallel control loops [Fig. 5.17(b)]. The *event loop* (black) is closely linked with the *temperature loop* and reacts on user-defined inputs. The two main inputs either close the program ('stop') or start a residual gas analyzer measurement ('RGA: on/off'). The other user-defined events set specific parameters for the 'temperature loop', i.e. which temperature sensors are

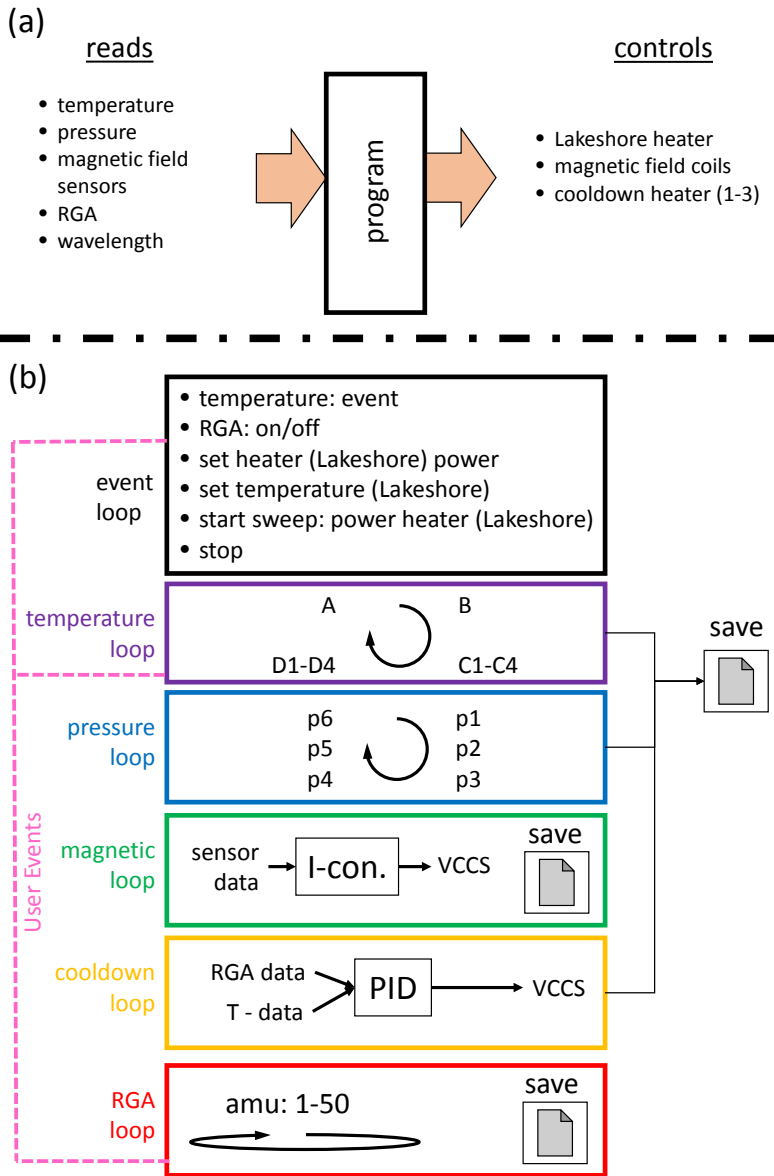


Figure 5.17: (a) Input and output diagram of the logging program. (b) Structure of the logging program, divided into 6 parallel control loops, see text for details.

read out, or the output power of the heater output of the controller. The *temperature loop* (violet) sequentially reads the different channels ('A, B, C1-C4, D1-D4') of the *LakeShore*-temperature-controller and saves their date, time, temperature data and sensor resistance into a file. Similarly, the *pressure loop* (blue) sequentially reads the (up to) 6 pressure channels of the *MaxiGauge*-pressure controller and saves the data into the same file as the temperature values. Both loops run at an individual rate but the rate with which the data is saved is determined by the larger of both rates. The *magnetic field loop* (green) reads the data from the magnetic field sensors and implements the 6 parallel SISO controllers (Sec. 5.3.1). The measured magnetic field data and the control-potentials applied to the VCCS are saved in a separate file as the temperature data. The *cooldown loop* (yellow) receives the data on partial pressure from the 'residual gas analyzer loop' and the 'temperature loop' and controls the VCCS for the cartridge heaters with a digital proportional-integral-differential controller (Sec. 5.2.4). The potentials applied to the VCCS are saved in the same file as the temperature and the pressure data. The *RGA loop* measures the partial pressures from the residual gas analyzer and saves them into a separate file.

The measurement program ('HybridSweep'), i.e. the custom-made *National Instruments:LabView*-code that runs on the 'measurement computer', is dedicated to sweep different measurement instruments (e.g. microwave sources, delay generators, ...) and synchronously acquire data from one of 3 acquisition instruments, i.e. the oscilloscope, the MCP camera or the FPGA. As indicated in Fig. 5.18(a), the program reads (inputs) data from the oscilloscope or FPGA traces, acquires camera images, reads the dye-laser wavelengths, the set delays of the delay generators, potentials of the low-voltage sources and the parameter configurations of the microwave sources. The program controls the oscilloscope, camera, FPGA, dye laser wavelength, microwave sources, low-voltage sources, delay generators, the 500-MHz-AWG and it interfaces to the LabView program 'CleanSweep' that is typically used in our group to conduct microwave experiments.

The measurement program consists of 4 parallel loops. The 'main control loop' (black) is constantly working off a task queue, the possible tasks of which are summarized in the list depicted in the black box. For every event, e.g. if a measurement is started, one or more tasks are added to this queue that define a sequence of operations that need to be carried out by the program. The important tasks are the 'idle state'-task, and 'process', 'analyze', 'measurement' and 'save'-tasks.

If the task list is worked off, the 'idle status'-task calls the 'process:keys' task, that calls again the 'idle status'-tasks, unless a user event triggers a measurement (possibilities shown in the inset). A user event [e.g.: start microwave (MW) frequency scan] defines the type of measurement by adding the corresponding 'measurement-task' (e.g. '1D measurement started') to the task queue. The

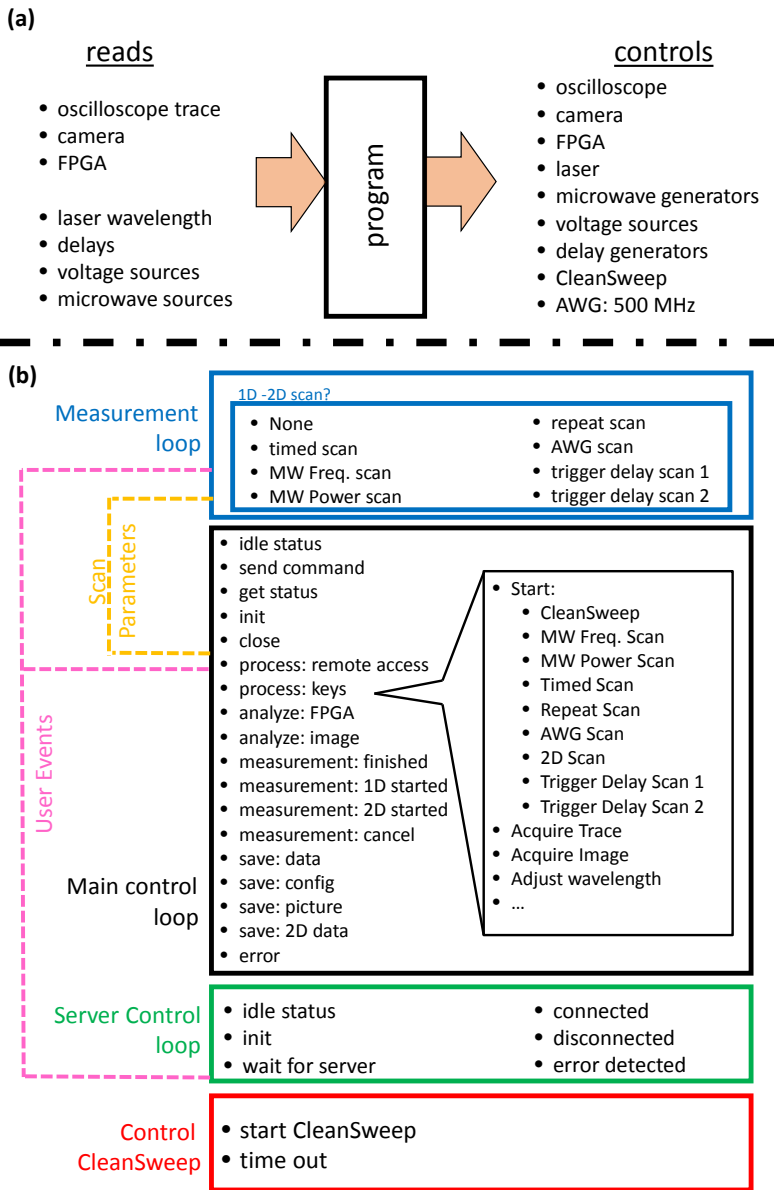


Figure 5.18: (a) Input and output diagram of the measurement program. (b) Structure of the measurement program, divided into 4 parallel control loops, see text for details.

'measurement'-task then creates a list with scan parameters (yellow dashed line, e.g. 10 1-MHz steps starting from 18 GHz) and starts the 'measurement loop' (blue). The measurement loop acquires the data and after finishing, adds the 'measurement:finished'-task and one or more analyze tasks to the queue, depending on whether data was acquired from the oscilloscope, the camera or the FPGA. The 'measurement finished' task then adds 'save'-tasks which save the data and do not call additional tasks.

The *measurement loop* first checks whether a scan was started that sweeps one instrument (1D) or two (2D). Then, depending on which measurement was started in the 'process:keys' task, it works off the scan parameter queue, applying the current scan-parameter value to the instrument which is swept (e.g. the microwave source) and waits for measurement data from the acquisition instrument. For every data point that is acquired, the measurement is analyzed and saved in parallel by adding the corresponding tasks to the tasks queue.

The *server control loop* is an additional server that provides external access to the current parameters, such as instrument settings and measured laser wavelength.

The *control CleanSweep* loop starts CleanSweep with the measurement-instrument-, and FPGA-parameters that are set in the program.

IMPORTANT SAMPLES

It is particularly important that the sample surfaces in the vicinity of which the Rydberg atoms are interfaced with microwave radiation emanate a minimal amount of electric stray fields. The sources of stray fields are manifold and include extrinsic sources such as surface adsorbates [*Tauschinsky et al. (2010); Hattermann et al. (2012); Thiele et al. (2014)*] or charges in the isolating gaps of coplanar waveguides (CPW) [*Carter et al. (2012); Thiele et al. (2015)*], and intrinsic sources, for example polycrystalline surface patches [*Carter and Martin (2011)*]. The samples we used during the course of this thesis have undergone a constant development to minimize intrinsic sources of stray fields. Four of the most important samples are described in Sec. 6.1. The design of the final, optimized sample is strongly linked with the design of a special sample holder (Sec. 6.1.1), that allows to establish electrical contact to superconducting chips by clamping. The characterization of the superconducting films (NbTiN) we use and typical performance of over- and undercoupled resonators is described in Sec. 6.2.

6.1 From printed circuit boards to superconducting chips

The different samples we use [Fig. 6.1(a-d)] have a width of 12 mm along the atom beam propagation (z) direction (yellow arrow) and extend between $\sim 24 - 40$ mm in x direction.

The printed-circuit-board(PCB)-based samples, sample design 1 [Fig. 6.1(a)], we used in our first experiments (Sec. II) contain a coplanar waveguide [*Hogan*

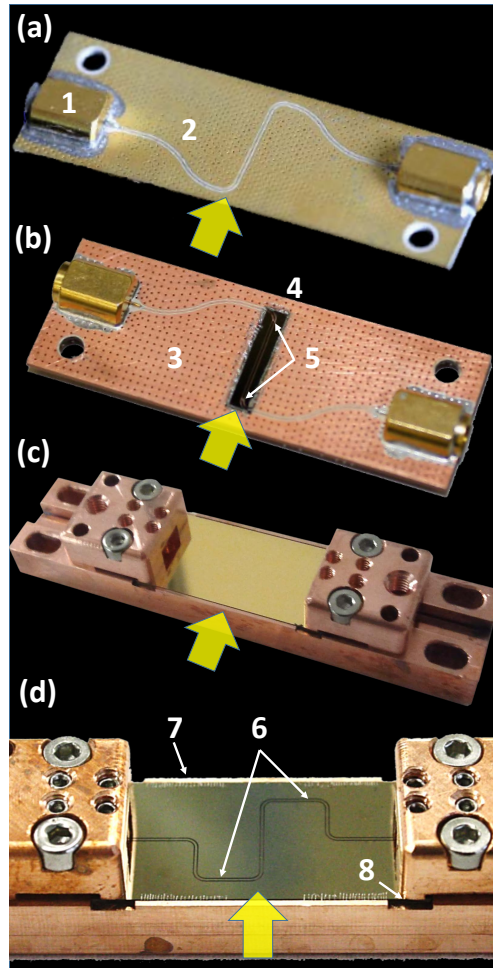


Figure 6.1: Different types of samples with the flight direction of the atoms indicated by the yellow arrow. (a) PC-board with soldered MMPX-connectors (1) containing a transmission line (2). (b) Similar PC-board with via-holes (3) containing a chip (4) with a resonator [gap-capacities at (5)]. (c) New sample holder for pure clamping of the chips, here a plain gold surface. (d) Same sample holder containing a superconducting chip with a transmission line. Resonator capacities are typically placed at (6), the copper walls are bondable (7) and the ground from the connectors can be isolated at (8) if the chip surface needs to be voltage biased.

et al. (2012a)]. The structure is patterned (fabrication: *OPTIPRINT*) into a 30- μm -thick copper surface with a chemically deposited silver/gold surface finish on fiber reinforced plastic (*ARLON: AD1000*) substrate of thickness 0.508 mm and relative permittivity $\epsilon_r \approx 10$. The coplanar waveguide has a 160 μm wide center conductor separated by 100 μm from the ground planes of the PCB. Via holes [see also label (3) in panel (b)] in the ground planes suppress parasitic microwave modes in the PC-board by connecting the top and bottom metal surfaces (thickness 120 μm). Microwave coaxial connectors [*Huber&Suhner:MMPX*, labeled (1)] couple microwave radiation from the coaxial microwave cables to the s-shaped transmission line [labeled (2)]. The connectors are soldered to the PCB using solder paste heated by hot air. The transmission line is designed to maximize the length in the region where the atoms interact with the surface (yellow arrow). At the same time the curvature of the coplanar waveguide is reduced to suppress out-coupling of microwave radiation to the metallic ground planes of the PC-board.

First tests of Rydberg atoms interacting with superconducting surfaces have been done using PC-board-based samples similar to the one depicted in Fig. 6.1(b). We also characterized the microwave properties of superconducting resonators and transmission lines in these samples. The design of the PC-boards is identical to the design presented in panel (a), but with immersion silver finish and pockets of either $2.2 \times 9.5 \text{ mm}^2$ or $4.2 \times 9.5 \text{ mm}^2$ (fabrication:*HUGHES INC.*). The pockets reach through the Arlon material to the backmetallization of the PC-boards and are large enough to encase the superconducting chips [label 4] we use. The chips are glued into the pocket using polymethylmethacrylat (PMMA) and consist of a 0.5 mm sapphire ($\epsilon_r \sim 10$) substrate with a magneto-sputtered 150-nm-thick film of niobium-titanium-nitride (NbTiN) (sputtering: *STARCRYO*). The grain size of the NbTiN film is $\sim 50 \text{ nm}$. To compensate for the different substrate properties, the width of the center conductor of the coplanar waveguide was changed to 180 μm and the width of the gaps to 80 μm . Electrical connection between the ground planes of the chip and the PCB is established using aluminum bond wires placed at separations of $\sim 50 \mu\text{m}$ along the long sides of the chip. The two gaps in the center conductor that cause the impedance mismatches defining the resonator (Sec. 1.4) are placed in the curves of the resonator to maximize the interaction length with the atoms [label (5)].

As discussed below, large stray fields emanated from the PC-board-based samples. In the new generation of samples, sample design 3 [Fig. 6.1(c)], used to interface Rydberg atoms with plain surfaces, we changed from the PC-boards to a copper sample holder to which the chips are fixed by clamping¹. The chips of dimensions $11.8 \times 24.2 \text{ mm}^2$ have a 200-nm-thick gold film evaporated onto the 0.5-mm-thick sapphire substrate. The grain size of the gold film was $\sim 40 \text{ nm}$.

¹For details on the sample holder design, see Sec. 6.1.1.

The sample design 4 we use to interface Rydberg atoms with patterned superconducting surfaces is depicted in Fig. 6.1(d). The contour of the transmission line was slightly adapted with respect to the design of the PC-boards. In the new designs all curves of the CPW have a radius of 0.8 mm such that the translationally invariant interaction region can have maximal dimensions $6.4 \times 6.4 \text{ mm}^2$, centered in the middle of the chip along the beam propagation direction (yellow arrow). The coupling capacities for resonators are inserted at positions labeled (6). Electrical connection between the copper sample holder and the ground planes of the chip is established by wire bonding at the long sides of the chip [label (7)], except for a $\sim 4 \text{ mm}$ long region in the center. If the ground planes are biased, no bonding wires are used and the chip surface is isolated from the copper clamps at the position labeled (8) with thin polyimide foil (*DUPONT:kapton*).

6.1.1 An optimized sample holder for Rydberg beam experiments

Sample designs 3 and 4 make use of a specially designed sample holder assembly which consists of two parts, a main holder and the chip sample holder (Fig. 6.2). The sample holder is designed to ensure clean sample surfaces, specifically:

1. The chips and connectors are fixed by clamping. Therefore, no glue (PMMA) or other organic (isolating) materials are used to assemble the sample, and no residues from the solder paste can condense on metallic surfaces (e.g. metallization of PC-board) during soldering.
2. The sample holders and the chips are fully reusable and can be reliably positioned² with a precision of $\lesssim 50 \text{ }\mu\text{m}$.
3. The fully assembled samples can be cleaned in solvents and/or in a reactive ion etcher (RIE) just before mounting into the cryostat. Depending on the allowed materials that are allowed to be etched in the RIE, the connectors may have to be added after the RIE-cleaning step.

The *main holder* is made of copper and is directly attached to the 3-K stage between electrode 2 and 3 with the surface in its positive y direction. Its extension along the y direction is chosen such that the chip surface is positioned 1 mm above the symmetry axis of the experiment. Additional thin plates can be inserted between main holder and the 3-K-stage such that the chip surface is positioned closer to the symmetry axis. The temperature of the sample assembly is measured using a temperature sensor and controlled using a heater inserted into the main holder.

²In contrast to the presented clamped design, the chips move after gluing because of the viscous re-flow of the glue during curing.

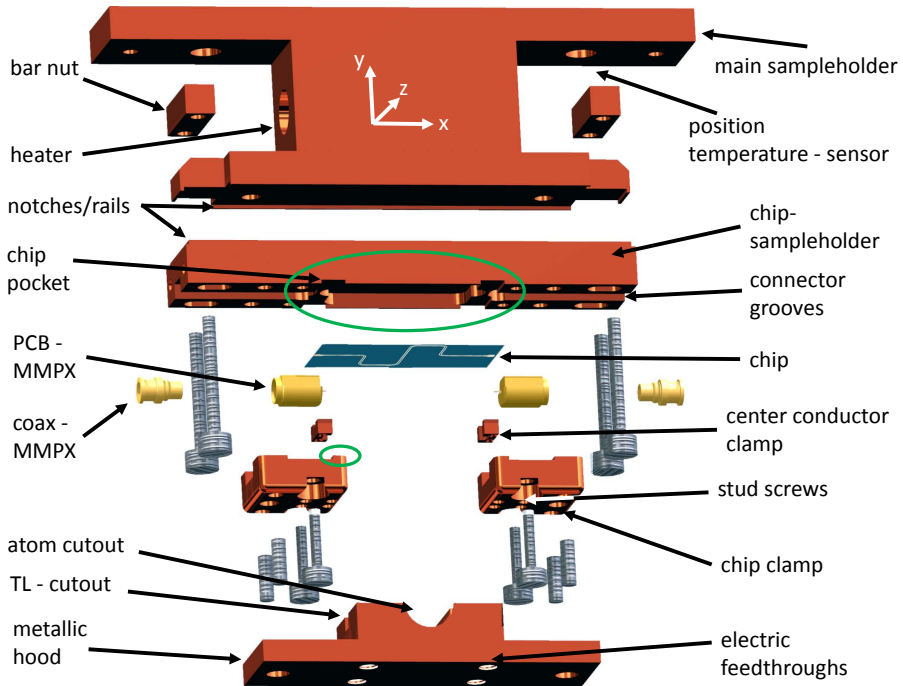


Figure 6.2: Explosion-view of sample holder, as explained in the text, containing a superconducting chip with a transmission line. Green circles denote areas that are machined with precision of $\sim 10 \mu\text{m}$.

The *chip sample holder* is attached to the main holder by 4 screws that are screwed into bar nuts. The correct position of the chip sample holder with respect to the main holder is defined to $\lesssim 100 \mu\text{m}$ because of the rails in the lower part of the main holder that fit into the notches of the chip sample holder. The superconducting chip fits into a chip pocket with dimension $24.4 \times 12 \text{ mm}^2$ and a depth of $0.48(1) \text{ mm}$ (indicated by large green circle). The chip clamps press the chip tightly into the pocket with the contact surfaces indicated by the small green circle. They are positioned parallel to the chip surface using two studs in holes with precision H7 such that their pressure is distributed homogeneously over the chips contact surface. This design allows to tightly fix the chip into the pocket without breaking it.

Microwave signals are coupled into the transmission line on the chip using the PCB-MMPX-connectors which can be installed after the chip has been fixed into the chip pocket. The connectors are positioned on the surface of the chip sample holder with a precision of $\sim 25 \mu\text{m}$ with respect to the lateral dimensions of the chip surface because of the precisely-machined connector grooves. It is important

that the center conductor of the connector presses tightly onto the chip surface for best electrical conductance. This is achieved passively because of the 20- μm -height difference between the surface of the center conductor of the connector and the surface of the chip, and actively by pressing the center conductor onto the chip surface with center conductor clamps. The center conductor clamps are made of copper and are bridge-shaped with a droplet of cured (isolating) epoxy that presses onto the center conductor. Both the connector and the center conductor clamps are fixed with stud screws in the chip clamps.

A metallic hood made of copper covers the space above 0.1 mm from the chip surface. Above the transmission line, a rectangular channel of 2 by 2 mm ensures that the microwave mode can propagate in the CPW undisturbed. The atoms pass the chip surfaces within a channel of a semi-circle-shaped crosssection of diameter 6.5 mm.

Electric potentials are applied to the metallic chip surfaces directly through the metallic shield with 4 specially designed electric feedthroughs (Fig. 6.3). The feedthroughs consist of connectors (yellow) in an isolating insert (light gray) in the metallic hood (brown). A spring is attached to a circular extension of the connector that pushes onto the sample surface and establishes electrical connection between the surface and the DC-wire (green).

6.1.2 Stray-field characterization of samples

The design changes between the samples presented in Fig. 6.1 were primarily motivated by minimization of stray electric fields that emanate from the chip surface. The PC-board-based samples presented in panel (a) and (b) exhibited very large stray fields that could be reduced for the sample designs presented in panel (c) and (d). Large stray electric fields above chip surfaces lead to significant changes

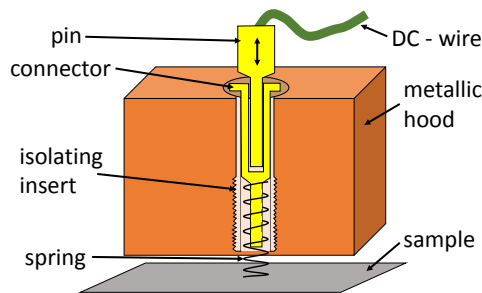


Figure 6.3: Sketch of the DC-connection to the sample. The DC-wire (green) is connected to a spring (black) that pushes toward the sample (gray) via a plug connection (yellow), which is pressed into an isolating insert (white) threaded into the metallic hood (brown).

in the Rydberg spectra of atoms flying over the surface. In the following we discuss typical spectra of Rydberg atoms, taken under standard conditions (Tab. 4.1), as they propagate above the different sample surfaces at distances below ~ 1 mm [Fig. 6.4(a-d)].

Large stray fields above the chip surface are indicated by an enhanced lifetime of np states for $n \leq 50$ and a reduction of the ionization limit, as also discussed in Sec. 4.1 and Sec. 5.2.4. Additionally, large stray fields from the chip surface can leak into the excitation region and therefore lead to broadening and (Stark) shifts of the resonance frequencies of the transition to Rydberg states.

The spectrum for Rydberg atoms flying above a PCB-based transmission line indicates characteristics of strong stray electric fields [Fig. 6.4(a)]. On the one hand, the lifetimes of the Rydberg states with $n \leq 50$ are strongly enhanced. For example, compare the relative strength of the detected $n^* \geq 33$ state (light red) with the relative strength of the same state measured in Fig. 4.2(c). Additionally, no states are detected above $n^* \approx 65$ ($\sim \Delta E_I \approx -800$ GHz), corresponding to an ionization field of ~ 18 V/cm. The large stray fields leak from the experimental region into the excitation region and create small fields. This is observed by the shifts of the transitions for the $n = 50$ and $n = 60$ state from the field-free positions (red lines) closer to the ionization limit, and from the broad linewidths of the states $n^* = 33$. A characterization measurement³ indicated, that the fields in the excitation region are smaller than ~ 1.5 V/cm. The large stray fields are attributed to the rough surface of the PC-Board and possibly charging of isolating patches on the surface.

The spectrum for atoms flying above a superconducting, PCB-based chip surface, exhibits smaller effects of stray fields [Fig. 6.4(b)]. The strength of the $n^* = 33$ state is reduced with respect to the PC-board sample but still stronger than in Fig. 4.2(c). Also, the ionization limit ($\sim \Delta E_I \approx -230$ GHz, $n^* \approx 120$) indicates that the maximal field through which the Rydberg atoms pass is ~ 1.5 V/cm. The Stark shifts for the states $n \geq 50$ are smaller. The improvement of the stray fields with respect to the PCB-based transmission line, is attributed to the cleaner surface of the superconducting chip over which the Rydberg atoms fly. Remaining stray fields may be residuals from the strong stray fields emanating from distant surfaces of the PC-board.

The spectrum for atoms flying above a gold surface, exhibits minimal effects of stray fields [Fig. 6.4(c)]. The relative strength of the $n^* = 33$ state is reduced to similar strengths as observed in the sample-free configuration [Fig. 4.2(c)]. Also, the ionization limit ($\sim \Delta E_I \approx -180$ GHz, $n^* \approx 140$) indicates that the maximal field

³A potential of ~ 1.6 V, applied to electrode 1 transfers a detectable amount of population to the ns states for $n \gtrsim 60$

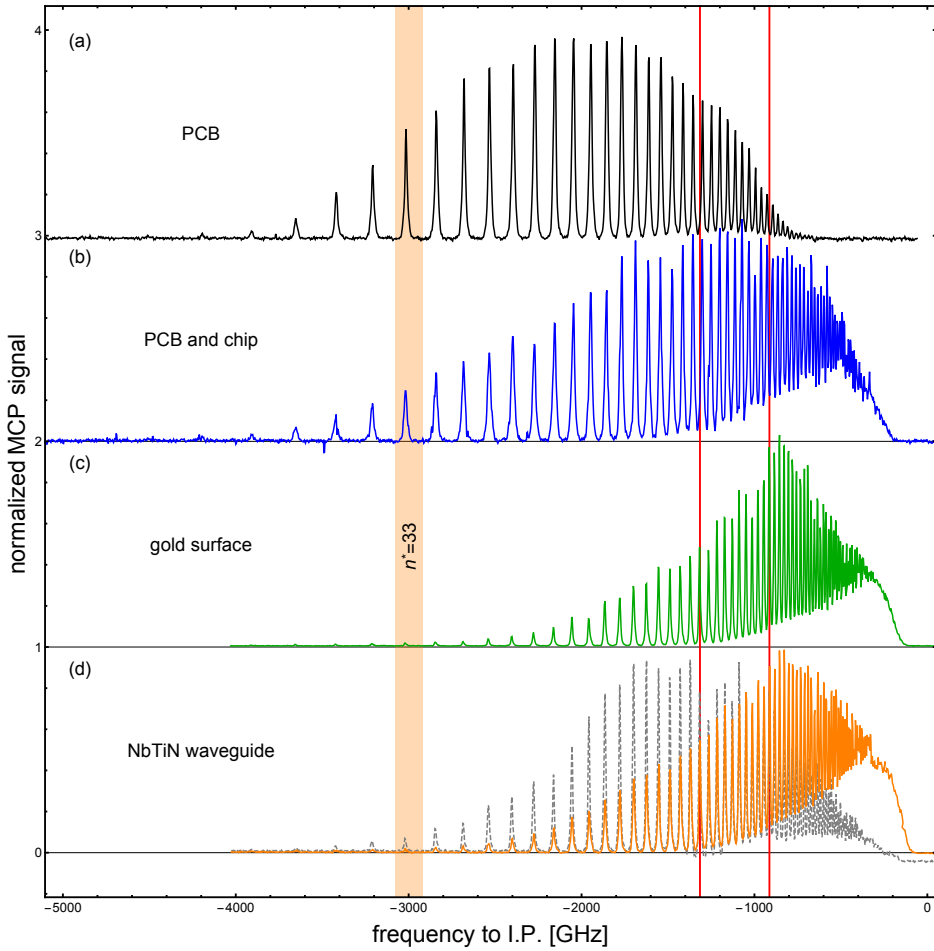


Figure 6.4: (a-d) Typical spectra corresponding to the different samples in Fig. 6.1(a-d) taken immediately after cool-down. The red lines indicate field-free positions for $n = 50$ and $n = 60$, respectively.

through which the Rydberg atoms pass is ~ 0.8 V/cm. Additionally, no Stark shift is observed for the states $n \geq 50$ and the widths of the transitions to levels with $n^* \leq 40$ are smaller. The spectra above plain gold surfaces correspond to spectra with the smallest effects of stray fields observed which is attributed to the minimal surface roughness of the gold film and the absence of other rough surfaces, e.g. of a PC-board. The drop in signal close to the ionization limit can be reproduced with a simple model (not shown) that takes into account stray fields that emanate normally to the surface with a field strength $F(h) = F_0 h^{-k}$ at height h above the surface. The fits revealed that the decay of the electric fields with the distance is quadratic ($k = 2$) and excluded decays with $k = 1, 3$. Typical fitted field constants were $F_0 = 0.004$ V cm. The quadratic decay of the stray electric fields is consistent with measurements presented in *Hogan et al. (2012a)*.

The effects of stray fields for a spectrum of Rydberg atoms flying above the superconducting chip surface containing a NbTiN waveguide [orange, Fig. 6.4(d)] are almost identical to the ones where atoms fly above plain gold surfaces [Fig. 6.4(c)] if the metastable atom beam never hit the surface (best case). The small change in the ionization limit ($\sim \Delta E_1 \approx -145$ GHz, $n^* \approx 150$, corresponding to ~ 0.6 V/cm) compared to the measured ΔE_1 for gold surfaces lies within the reproducibility range of the ionization limit over all chips. If the metastable beam is directed towards the surface (worst case), the insulating surfaces of the transmission line can charge and, as consequence, produce stray fields (dashed, gray data). As a result, longer lifetimes and a reduced ionization limit are observed.

6.2 Characterization of under and overcoupled NbTiN resonators

Using the samples presented in Fig. 6.1(b), we have characterized the properties of the superconducting NbTiN film and of coplanar microwave resonator modes. All tested samples had a center conductor of $160 \mu\text{m}$ width, separated by two gaps of $80 \mu\text{m}$ from the ground planes. The coupling capacitors that define the resonators were designed as gaps in the center conductor of different length. To characterize the superconducting films, we determined the critical temperature T_c and the electrical conductivity $\rho(T)$ at $T = T_c$. For the coplanar microwave resonator modes, we have determined the temperature-dependent kinetic inductance, internal and external quality factors and frequency shifts because of finite coupling capacities [*Waldburger (2012); Barmettler (2012)*].

A resonator mode n is described by a Lorentzian function, characterized by the resonance frequency ω_n and the full width at half maximum (FWHM) $\Delta\omega_n$. As also summarized in detail in *Waldburger (2012)*, the (temperature-dependent)

resonance frequency of the n^{th} mode of a superconducting resonator is given by [Göppl *et al.* (2008)]

$$\omega_n(T) = \frac{1}{\sqrt{L_n(T)(C + 2C^*)}}, \quad (6.1)$$

with $C = C_1 l / 2$ the resonators capacity, calculated from the (geometric) capacity per length C_1 [Simons (2001)] and the length of the resonator l . The effective coupling capacity

$$C^* = \frac{C_\kappa}{1 + \omega_n^2(T) C_\kappa^2 R_L^2} \quad (6.2)$$

is frequency-dependent, and depends on the load resistance ($R_L = 50 \Omega$) and the coupling capacity C_κ . The resonators inductance depends on the mode number n as

$$L_n(T) = \frac{2L_1(T)l}{n^2\pi}, \quad (6.3)$$

where the inductance per unit length $L_1(T) = L_1^m + L_1^k(T)$ has a temperature-independent magnetic (L_1^m) and a temperature-dependent kinetic (L_1^k) contribution [Watanabe *et al.* (1994)]. The magnetic inductance depends on geometric factors only [Simons (2001)], i.e. only on the chip design. The kinetic inductance is given by

$$L_1^k(T) = \mu_0 \frac{g(S, W, t)}{tW} \lambda^2(T), \quad (6.4)$$

with t the thickness of the superconducting film, W the width of the center conductor, S the width of the gaps between center conductor and ground planes, and $g(S, W, t)$ a geometric factor [Watanabe *et al.* (1994)]. The kinetic inductance depends on the London penetration depth $\lambda(T)$, the only part which varies with temperature, i.e. as

$$\lambda(T) = \lambda(0) \sqrt{\frac{1}{1 - (T/T_c)^4}} = 1.05 \times 10^{-3} \sqrt{\frac{\rho(T_c)}{T_c}} \sqrt{\frac{1}{1 - (T/T_c)^4}}. \quad (6.5)$$

with the expression for $\lambda(0)$ given for thin films and in the dirty limit, where the coherence length is larger than the mean free path of the electrons [Watanabe *et al.* (1994); Göppl *et al.* (2008)]. The critical temperature T_c and the resistivity at T_c , $\rho(T_c)$, depend on the used superconducting material and cannot be calculated easily.

The width of a resonator mode, $\Delta\omega_n$, is typically quantified in terms of the loaded quality factor $Q = \omega_n / \Delta\omega_n$. The loaded quality factor is a combination of the internal and external quality factors

$$Q = \left(\frac{1}{Q_{\text{int}}} + \frac{1}{Q_{\text{ext}}} \right)^{-1}. \quad (6.6)$$

The internal losses, characterized by Q_{int} , generally depend on material quality and fabrication. The external losses depend on the geometric design of the chips. They are characterized by $Q_{\text{ext}} = \omega_0/\kappa$, where $\Delta\omega_n = \kappa$ (compare Sec. 1.1.3) depends on the (designed) C_κ [Göppl *et al.* (2008)]. The Q-coupling ratio

$$g_Q = \frac{Q_{\text{int}}}{Q_{\text{ext}}} \quad (6.7)$$

determines whether the width of the mode's resonance $\Delta\omega_n$ is dominated by internal losses ($g_Q \ll 1$) or external ($g_Q \gg 1$) losses.

For successfully coupling Rydberg atoms to microwave photons in a transmission line, it is essential to have good knowledge about the properties of the resonator modes in the temperature and frequency range of the experiment. In our experiment, the 'working range' is given by the base temperature of the cryostat $T \approx 3$ K and the transition frequencies between np and ns states ($n \in [34, 38]$), i.e. $\sim 18 - 28$ GHz. Therefore, in the following, typical results are presented in which we

- a) characterize the frequency shifts of the resonator [Eq. (6.1)], resulting from temperature [Eq. (6.4)] or external coupling capacities [Eq. (6.2)],
- b) reach large enough internal Q-factors Q_{int} , such that the loaded Q is similar or smaller than the coupling of a microwave photon to Rydberg atoms [compare Fig. 1.8(b,c)],
- c) verify the values of the (designed) external coupling capacities C_κ and predict the measured external Q-factors Q_{ext} .

The temperature-dependent frequency shift of the resonator modes depends on the London-penetration depth [Eq. (6.5)], both decreasing the more the temperature T of the sample is decreased below the critical temperature T_c of the superconductor. T_c was determined in two independent transmission measurements of a coplanar microwave waveguide [Waldburger (2012)]. The data points (green and blue, Fig. 6.5) were normalized such that the largest and smallest measured values coincide for both measurements for direct comparison.

The blue data points correspond to a two-point, direct-current (DC) resistance measurement which was measured between the microwave output ports of the (cryogenic) chamber. The minimal measured resistance is $80.3(1) \Omega$ for temperatures below 12 K, and the maximal measured resistance is $114.4(1) \Omega$ for temperatures above 14 K. The offset of 80Ω is the DC-resistance of the microwave coaxial cables. The difference of $34.1(1) \Omega$ is the DC-resistance of the center conductor on the NbTiN-chip-part of the sample that vanishes for temperatures below $T_c = 12.95(2)$ K. The measured width of the transition is ~ 100 mK, a consequence of the temperature oscillations of the pulse-tube cooler (Sec. 5.2.5).

The green data points were acquired in a microwave transmission measurement through the coplanar waveguide [Waldburger (2012)]. The frequency-dependent transmission through a waveguide can be described by the function:

$$S_{21}(v, T) = -a(T)v^{b(T)} - c, \quad (6.8)$$

where S_{21} is the S-parameter describing transmission from port 1 to port 2, a, b are temperature-dependent pa-

parameter constants and c is a frequency-independent offset, e.g. from attenuators. The green data points correspond to the parameter a that was fitted to different transmission spectra acquired at different temperatures. The minimal measured value is 1 dB/GHz for temperatures below 12 K, and the maximal measured value is 22.5 dB/GHz for temperatures above 14 K. The transition temperature $T_c = 13.0(1)$ K was fitted with a heaviside function (red line).

Besides the geometric parameters L_1^m and C_l , a resonators mode-frequency at zero temperature $\omega_n(0)$ depends the residual kinetic inductance L_1^l at $T = 0$, which depends on T_c and $\rho(T_c)$. We determine $\rho(T_c)$ by measuring the temperature dependence of the kinetic inductance close to T_c for under and overcoupled resonators [Waldburger (2012)]. Specifically, we measure the temperature-dependence of the normalized frequency shift of up to 4 modes of three different resonators (Fig. 6.6, black, blue and green data points). The different modes have resonance frequencies ω_n distributed between 5 GHz and 30 GHz, and they differ in their Q-coupling ratios g_Q . As can be observed in Fig. 6.6, the relative shift of each resonance does not depend on g_Q . In fact, it only depends on the modes inductance per unit length, i.e. for the minimal measured temperature of 3 K

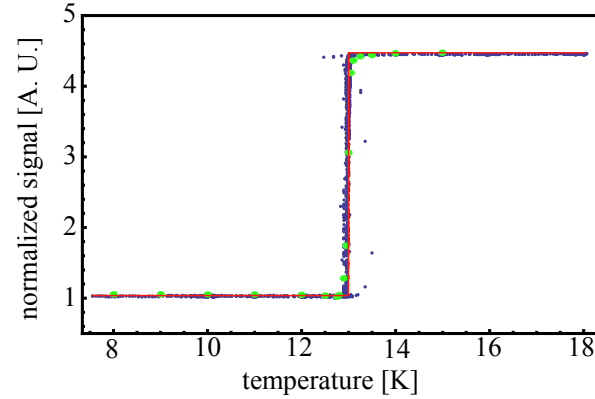


Figure 6.5: Measurement of resistivity (blue data points) and loss-parameter (green data points), see text, as function of temperature. The red line is a fit to stepfunction, determining the critical temperature of NbTiN. Data also presented in Waldburger (2012).

$$\frac{\omega(T)}{\omega(3)} = \sqrt{\frac{L_n(3)}{L_n(T)}}, \quad (6.9)$$

with $L_n(T)$ given by Eq. (6.3) and the temperature dependence contained in the kinetic inductance part [Eqs. (6.4,6.5)]. The red line corresponds to a fit of Eq. (6.9)

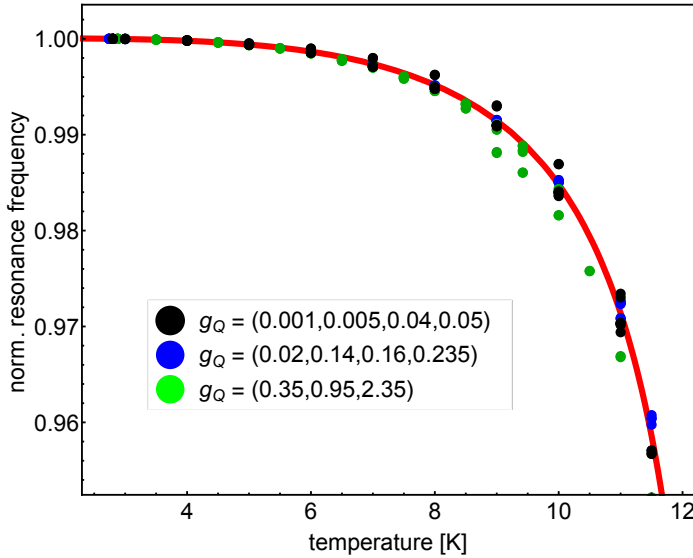


Figure 6.6: Normalized resonance frequency shift as a function of temperature for 3 different samples and 11 different over and undercoupled resonances [coupling ratios (g) given in picture] and resonance frequencies ranging from 5 GHz to 30 GHz. The red line is a fit to Eq. (6.9) of all data points. Data also presented in *Waldburger (2012)*.

to the undercoupled modes ($g_Q < 1$, black and blue data points). For this fit, we did not take into account the critically ($g_Q \approx 1$) and overcoupled modes ($g_Q > 1$, green datapoints), because of the additional temperature dependence of C^* . The fit revealed $\rho(T_c) = 93(3) \mu\Omega\text{cm}$ and $T_c = 13.11(4) \text{ K}$, consistent with numbers quoted by the company that produced the films (*STARCRYO INC.*).

The temperature-dependent frequency shift decreases with decreasing temperature. However, resonator modes with large loaded quality factors ($Q \geq 10000$) are sensitive to temperature fluctuations at temperatures below $T < 4 \text{ K}$. For $T = 3 \text{ K}$, the frequency shift [Eq. (6.9)] can be linearized as a function of temperature. In theory, we find

$$\frac{\omega(3 \pm \Delta T)}{\omega(3)} \approx 1 - 1.1288(2) \times 10^{-4} \Delta T, \quad (6.10)$$

which results for $\omega(3) \approx 5.1510 \text{ GHz}$ and for temperature fluctuations of $\pm 100 \text{ mK}$ in a shift of $\pm 50 \text{ kHz}$. This shift is observed when we do not compensate for the temperature fluctuations of the pulse-tube cooler (Sec. 5.2.5), i.e. the temperature of the sample holder oscillates by 100 mK (Fig. 6.7). The transmission data was acquired pointwise (blue data points) with a measurement rate that exceeded the

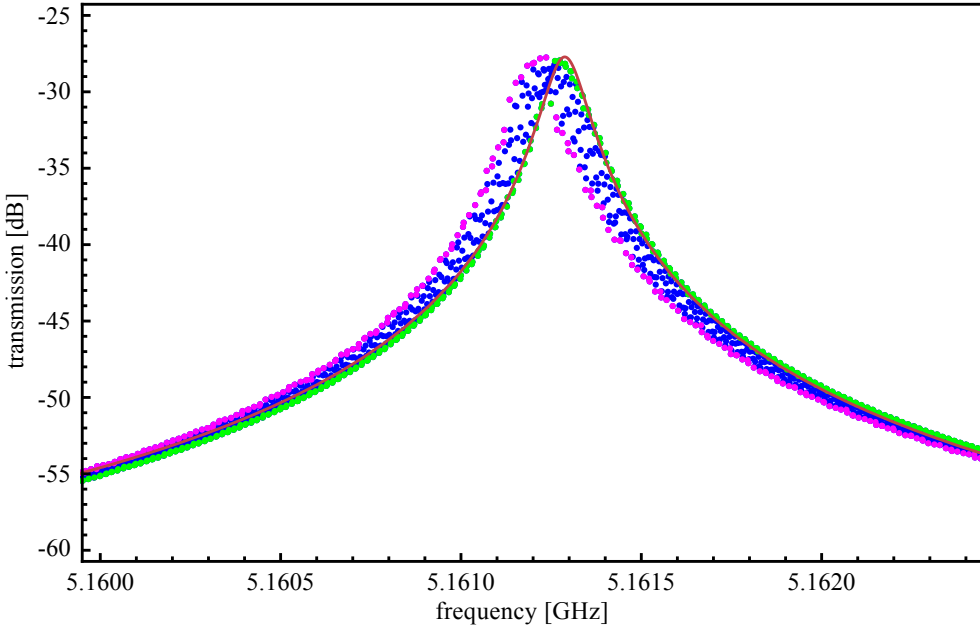


Figure 6.7: Measured transmission (blue data) of an overcoupled, high- Q resonator as a function of frequency. The resonance is shifted because of finite kinetic inductance of NbTiN and temperature fluctuations of the pulse-tube cooler. Post-selection of the data allows to fit (dark red line) the two extreme resonance positions (magenta and green data points). Data also presented in [Waldburger (2012)].

rate of 1.41 Hz at which the pulse-tube cooler operates. The data sets corresponding to the extremal points (green and magenta) were extracted by post-processing the measured data [Waldburger (2012)]. A fit of a Lorentzian function to both sets (fit for green points indicated in dark red) recovers the loaded $Q \approx 51000$, and the resonance shift of ~ 100 kHz.

Besides the resonance frequency, also the loaded Q -factor depends on temperature. In Fig. 6.8(a), we present temperature-dependent measurements of a typical, undercoupled ($g_Q < 0.2$) resonator mode ($n = 4$), the internal Q -factor and resonance frequency of which are suitable to couple to Rydberg atoms. The red data points correspond to the temperature-dependent frequency shift of the mode (indicated by right axis). The solid line is a fit to Eq. (6.1), with the only free parameters being $T_c \approx 10.1$ K, $\rho(T_c) \approx 93.6 \mu\Omega\text{cm}$ and the dielectric constant of the substrate $\epsilon_r = 9.4$. The resonance frequency at $T = 3$ K is $\omega_4 = 20.145$ GHz, which is part of the frequency range we aim to work in. The measured loaded quality factor $Q \approx 10000$ at $T = 3$ K indicates a width of the resonance frequency of $\Delta\omega_4 \approx 2$ MHz, which is slightly larger than the coupling rate g of a singlet he-

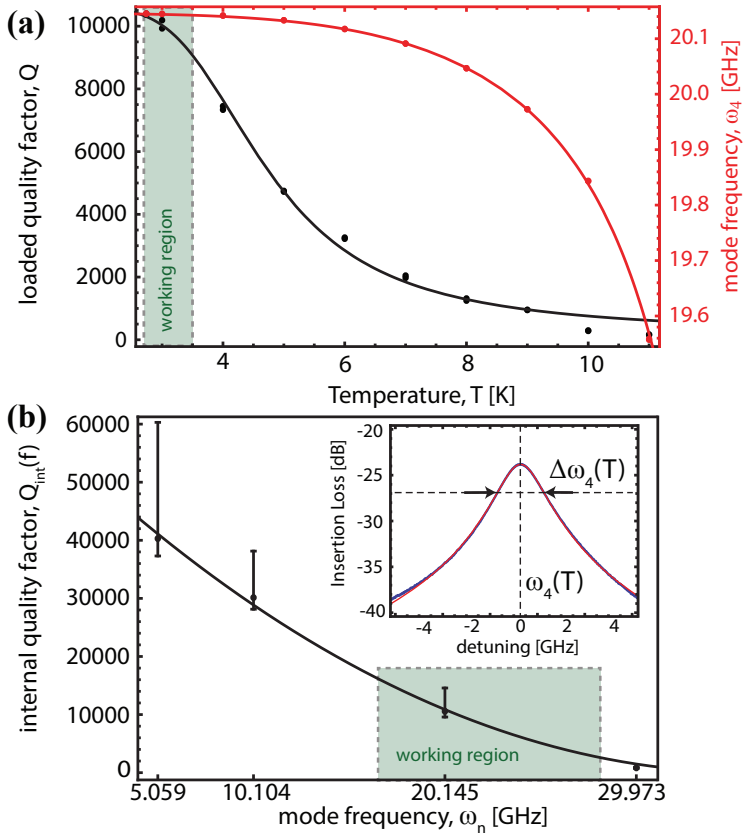


Figure 6.8: (a) Resonance frequency (red data, right axis) and corresponding loaded Q-factor (black data, left axis) of a resonance, suitable to reach strong coupling between ensembles of Rydberg atoms and a chip-based microwave photon, as a function of temperature with corresponding fits (black and red lines). The green region indicates the working region of the experiment. (b) Internal quality factor of the same resonator for different modes. The green area indicates the working region of the experiment. The inset shows a transmission measurement of the resonance that lies within the working regions of (a) and (b).

lithium atom in 34p to a coplanar transmission line resonator of the currently used design [compare solid black trace in Fig. 1.8(b)]. However, it is smaller than the coupling rate for of a single microwave photon to an ensemble of 100 Rydberg atoms [compare solid blue trace in Fig. 1.8(b)]. The dependence of the Q-factor on temperature is best described empirically by a Fermi-Dirac distribution (black line) [Waldburger (2012)]. The Fermi-Dirac distribution describes the exponential increase in Q_{int} for the temperature range $\sim 1 \text{ K} < T < T_c$, for which the losses in the resonator are dominated by quasi-particles, and it also takes into account saturation of the Q-factor for smaller temperatures.

We consistently observe internal Q-factors of $Q_{\text{int}} \gtrsim 10000$ for this frequency range. Also, Q_{int} decreases with increasing frequency, as presented in Fig. 6.8(b) for a typical resonator. The figure presents the internal Q-factors for the modes 1, 2, 4 and 6 of the resonator, the mode $n = 4$ of which is presented in panel (a). The black line is a guide to the eye. The inset presents the measured transmission of mode 4 (blue data) and a Lorentzian fit (red line).

Examination of spectra from 12 different, overcoupled resonators (6 different designs) allows to determine the agreement between simulated and measured coupling capacity C_κ [Barmettler (2012)]. The 6 different designs differed in length of the resonator, number of curves of the transmission line, and size of the chip. The two resonators the spectra of which are presented as examples by the black and blue datapoints in Fig. 6.9, differed in the size of the gaps of the coupling capacitors, only. The designed widths were $4 \mu\text{m}$ (black data) and $60 \mu\text{m}$ (blue data), respectively.

The insertion loss of the two spectra [Fig. 6.9(a)] was calibrated by subtraction of Eq. (6.8), fitted to the transmission of a transmission line of equivalent design. Every resonance in the spectrum was fitted separately with a Lorentzian function, and the center frequency ω_n and loaded Q-factor were extracted. From each measured resonance frequency we subtract the bare resonance frequency as calculated using Eq. (6.1) with $C^* = 0$, and plot the difference against the mode number [Fig. 6.9(b)]. The loaded Q-factor for each resonance [Fig. 6.9(c)] is separated into external [Fig. 6.9(d)] and internal Q-factor [Fig. 6.9(e)] using Eq. (6.6) and the insertion loss on resonance [Göppl *et al.* (2008)]

$$L_0 = \frac{gQ}{1 + gQ}. \quad (6.11)$$

The orange and red lines in all panels correspond to fits of a modified ABCD-matrix formalism, described in Göppl *et al.* (2008). For both spectra the fit parameters were the coupling capacities $C_{\kappa,1}$ and $C_{\kappa,2}$, and the attenuation constant α , respectively. The values of $C_{\kappa,1} = 24.9 \text{ fF}$ and $C_{\kappa,2} = 10.6 \text{ fF}$ correspond closely to the coupling capacities of $C_{\kappa,1} = 25.14 \text{ fF}$ and $C_{\kappa,2} = 10.18 \text{ fF}$, as simulated with

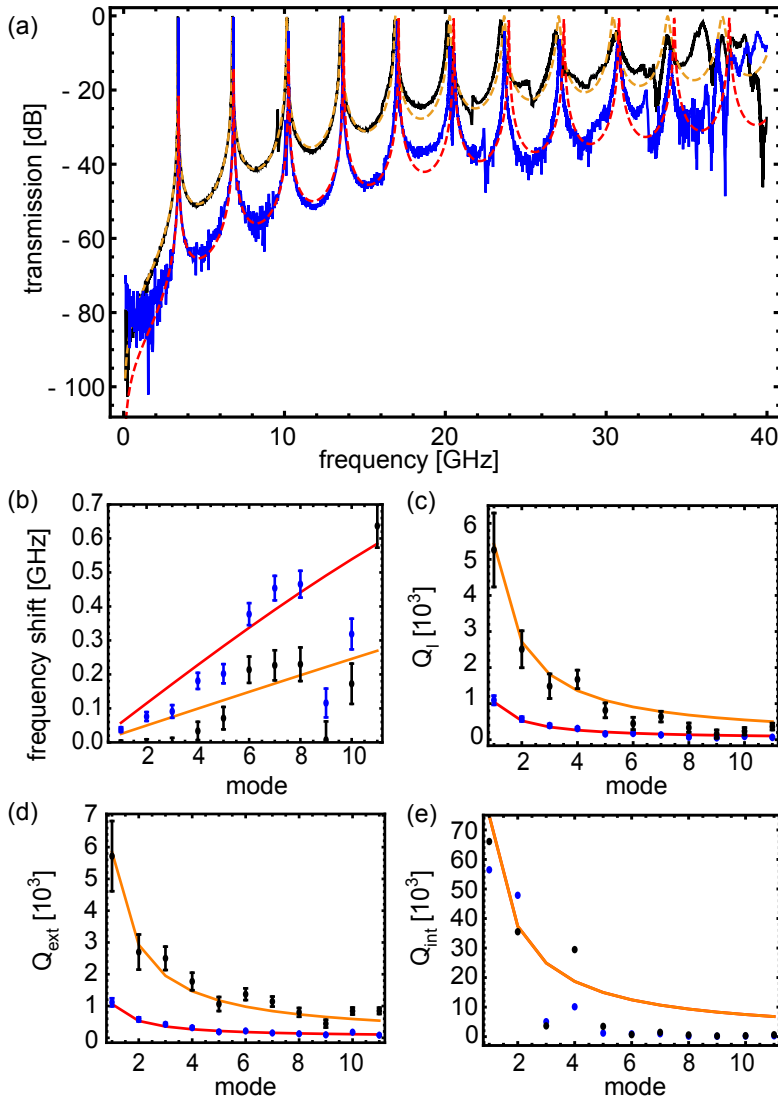


Figure 6.9: (a) Transmission spectrum of two overcoupled resonators (blue and black data) with fits (red and orange, dashed lines) to the ABCD-matrix formalism, see text. (b-e) Extracted frequency shifts and loaded, external and internal quality factors (blue and black data) with corresponding theoretical predictions from coupling capacities C^* , kinetic inductance L_1^k and fitted propagation constant (red and orange lines). Data from *Barmettler (2012)*.

finite element calculations. In fact, for all measured designs, the designed and measured coupling capacitances never differed by more than 1.5%. The coupling capacities affect the level of transmission between two resonances most, i.e. for example the insertion loss of ~ -65 dB at 5 GHz for the blue spectrum. Therefore the coupling capacities are fitted by overlapping the measured and ABCD-matrix-formalism-predicted insertion loss at 5 GHz. As a result, the ABCD-matrix formalism predicts well the measured resonance shifts [panel (b)] and the loaded and external Q -factors [panels (c,d)].

The attenuation constant α is design-independent and was fitted to the data in panel (e). Because the measurements are done at temperatures ($T=4.2$ K) for which the loss rates are limited by quasi-particle, we expect a strong dependence of the loss rate on the frequency. We found the (frequency-dependent) loss rate to be best described for all measured devices by [Barmettler (2012)]

$$\alpha = 1.3(3) \times 10^{-4} f^2. \quad (6.12)$$

In conclusion, we have reliably determined the parameters of the superconducting films on our chips. The large T_c of the chosen material, NbTiN, is large enough that internal Q -factors $Q_{\text{int}} \geq 10000$ at $\nu_4 \approx 20$ GHz can be reached. The large contribution from the kinetic inductance to the resonance frequency was characterized well and agreed perfectly with the prediction. Also the measured frequency shifts and coupling capacities agree well with simulations.

PART II

MEASUREMENTS

COHERENT MANIPULATION CLOSE TO SURFACES

The interest in coherent manipulation of Rydberg atoms has grown in recent years in several fields of physics. For example, coherent collective Rydberg excitations have been demonstrated in ultracold atom clouds (see Refs. [Tong *et al.* (2004); Singer *et al.* (2004); Pohl *et al.* (2011); Comparat and Pillet (2010)] and references therein), thermal vapor microcells [Kübler *et al.* (2010)], one-dimensional optical lattices [Viteau *et al.* (2011)], and on an atom chip [Tauschinsky *et al.* (2010)]. In the field of quantum information processing, Rydberg atoms have been proposed as a medium for quantum computation [Jaksch *et al.* (2000); Saffman *et al.* (2010); Lukin *et al.* (2001); Müller *et al.* (2009); Patton and Fischer (2013)] and quantum simulations [Buluta and Nori (2009); Weimer *et al.* (2010); Leung *et al.* (2011)] because of their large dipole moments, their tunable long-range interactions and their strong coupling to microwave fields. In cavity quantum electrodynamics, Rydberg atoms passing through high-quality microwave cavities are at the heart of fundamental quantum optics and quantum information processing experiments [Brune *et al.* (1994, 1996); Walther *et al.* (2006); Haroche and Raimond (2006); Gleyzes *et al.* (2007)].

The long coherence times of Rydberg states make Rydberg atoms attractive for hybrid systems in combination with solid-state devices that operate in the quantum regime. In the microwave regime, it has been proposed to couple Rydberg atoms to superconducting circuits [Sørensen *et al.* (2004); Petrosyan and Fleischhauer (2008); Petrosyan *et al.* (2009)]. Also the interactions between Rydberg atoms and surfaces have been studied experimentally [Nordlander and Dunning (1996); So *et al.* (2011); Pu and Dunning (2013)]. In experiments involving Rydberg atoms close to surfaces, the adsorption of atoms at the surface leads to inhomogeneous stray fields, which impose a severe limitation to the coherent manipulation of Rydberg atoms [Hattermann *et al.* (2012)], as has been described theoretically [Carter and Martin (2011)] and observed in experiments with alkali-metal atoms at room temperature [Obrecht *et al.* (2007); Tauschinsky *et al.* (2010); Carter *et al.* (2012); Carter and Martin (2013)]. These harmful effects may be mitigated

using microwave frequency dressing [Jones *et al.* (2013)]. Such experiments are even more challenging if the surface is held at cryogenic temperatures because adsorption of atoms is enhanced [Chan *et al.* (2013)] and typical surface cleaning procedures are not easy to implement.

In the experiments presented in the following chapters Rydberg atoms have been manipulated close to surfaces [Hogan *et al.* (2012a); Thiele *et al.* (2014, 2015)]. The microwave radiation emanated either from coplanar waveguides on superconducting chips or from horn antennas [compare Fig. 4.6(a)] while the sample was held at cryogenic temperatures. Reaching coherent evolution of an atomic ensemble close to a coplanar waveguide is an essential step to realize a hybrid system of Rydberg atoms and chip-based microwave resonators (Sec. 1.4).

DRIVING RYDBERG-RYDBERG TRANSITIONS FROM A PRINTED-CIRCUIT-BOARD-BASED COPLANAR MICROWAVE WAVEGUIDE

CONTENT BASED ON *Hogan et al. (2012a)*

In initial measurements, described in *Hogan et al. (2012a)*, we observed helium Rydberg atoms interacting coherently with microwave photons in a printed-circuit-board(PCB)-based coplanar transmission line. The observed coherent population transfer between two Rydberg states was subject to large decoherence - the observed contrast between the population in the two states never exceeded $\sim 2\%$ of the initial state - because the experiment suffered from a number of imperfections. In this chapter, we first discuss the measurements and then conclude with a list of challenges that need to be overcome to coherently manipulate the atoms close to cryogenic surfaces.

7.1 Determination of stray field strength using microwave spectra

The experiments were carried out in a beam of metastable singlet $(1s)^1(2s)^1S_0$ He Rydberg atoms in a simpler version of the experiment described in part 1 of

this thesis. Specifically, the He^* atoms were excited to Rydberg np states in zone 1 (Fig. 2.1) of an electrode stack consisting of 4 cylindrical electrodes. The Rydberg atoms propagated within a distance of 1 mm to the PCB-board containing a transmission line (sample design 1 as described in Sec. 6.1). Microwave radiation transferred population between np and ns states and the population in the Rydberg states was detected in zone 3 using ramped ionization. Due to the small energy difference of the two states, the two discrimination of the two states in detection was not perfect.

Because no measures were taken against adsorption of residual gases during and after cooldown, gas adsorbed at the surface, impeding experiments on a timescale of only a few hours after cooling the sample below 100 K. We observed slow drifts of the microwave transition frequencies and slowly increasing line widths whenever the Rydberg-atom beam propagated within 1 mm of the sample surface. To avoid this, the following experiments were carried out at temperatures $T \approx 100$ K, i.e. above the adsorption temperature of N_2 (Tab. 5.1).

In a first step, the strength of the stray field has been determined by detecting $np \rightarrow ns$ transitions for states with principal quantum number n between 31 and 35 (Fig. 7.1). After excitation and a flight time of $6 \mu\text{s}$, Rydberg np states were transferred to the ns state with a $1\text{-}\mu\text{s}$ -long microwave pulse from the transmission line. The microwave power on the PCB was ~ 10 nW as estimated from cable losses and the applied microwave power at the microwave source. At the time of the transfer, the atoms were positioned in the center of zone 2, i.e. the middle of the PCB. The observed transitions (Fig. 7.1, black) were asymmetric, with a sharp rise close to the field-free transition frequency (blue arrows) and a tail towards larger frequencies. The full-width at half maximum (FWHM) of the transitions varied between 25 MHz for $n = 31$ to $\gtrsim 120$ MHz for $n = 35$. The increase in FWHM for increasing n and the asymmetric lineshape are a consequence of the large, inhomogeneous stray fields that emanate vertically from the PCB (Sec. 6.2).

The effect of these stray electric fields on the line shapes were elucidated by performing a numerical simulation in which the primary fit parameter was the magnitude of the stray electric field as a function of distance above the surface. This Monte-Carlo simulation involved the generation of an ensemble of atoms, with a spatial distribution matching that of the experiment. The atoms were randomly positioned in the x - y plane at the midpoint of the PCB in the z dimension, with a normal distribution of positions in the x dimension with a FWHM of 2 mm centered at the waveguide. In the y dimension, the atoms were described by a normal distribution of the same FWHM centered 0.5 mm above the surface, and which was cut off at a distance of 1 mm above the PCB to account for the collimation of the atomic beam.

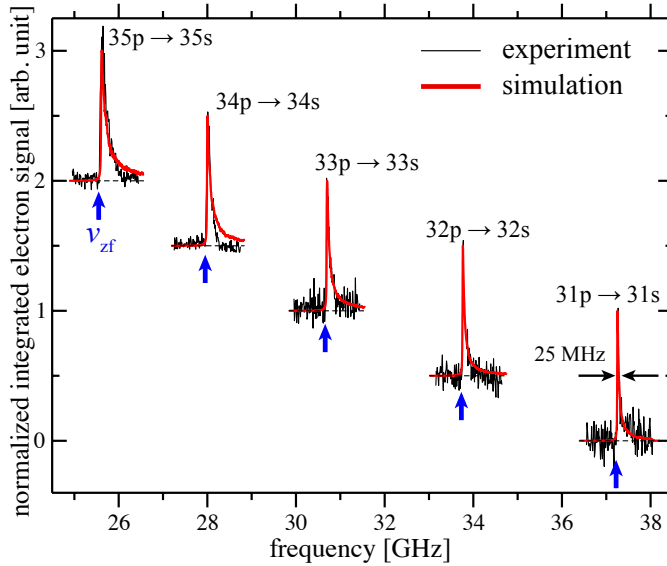


Figure 7.1: Microwave spectra of singlet $np \rightarrow ns$ transitions, in the range $n = 31 - 35$, for He atoms traversing the PCB-based coplanar waveguide. Simulated line shapes (red) are overlaid on the experimental data with the zero-field transition frequencies, ν_{zf} , indicated by arrows. Picture and caption from *Hogan et al. (2012a)*.

The stray electric field was assumed to have a spatial dependence¹ of $F = F_0/y^2$ with the free fitting parameter F_0 . We used the following model to fit F_0 to all spectra simultaneously.

The $np \rightarrow ns$ transition frequencies for different electric fields were calculated using the Stark shifts determined by matrix-diagonalization of the single particle Hamiltonian [*Zimmerman et al. (1979)*], see also Sec. 4.1. To account for the inhomogeneity of the microwave field distribution surrounding the waveguide, a finite-element calculation of this field was carried out in the x - y plane above the PCB. The microwave field strength F_μ experienced by each atom, and the field-dependent $np \rightarrow ns$ transition dipole moment $d_{np}^{ns}(F)$, were used to determine the degree of saturation $S_{np}^{ns} = [d_{np}^{ns}(F)F_\mu/(\hbar\gamma)]^2$ of the transition, where γ is the natural linewidth.

The transition dipole moments were calculated by summing the contribution of each dipole-allowed $\Delta l = \pm 1$ transition between the l -mixed np and ns states in the presence of the stray field. A Lorentzian homogeneous line shape with a

¹The assumed inverse-square dependence of the stray fields was suggested by *Carter and Martin (2011)* and is the same functional dependence found when simulating the drop in signal close to the ionization limit in Rydberg spectra (Sec. 6.2).

FWHM of $\gamma\sqrt{1+S_{np}^{2S}}$ (where $\gamma < 10$ MHz was associated with each atom). The simulated line profiles of an ensemble of 2×10^5 atoms were generated by summing these Lorentzian functions (thick red lines in Fig. 7.1). Best agreement with the experimental data was achieved for a field amplitude of $F_0 = (2.8 \pm 0.1) \times 10^{-5}$ V/m. The sharp rise close to the zero-field transition frequencies corresponds to atoms at large distances from the surface of the PCB in the y dimension where the stray field and its gradient are smallest.

7.2 Coherent population transfer with small contrast

The coherence of the atom-radiation interaction was investigated by selective detection of atoms in the 33s state as a function of microwave pulse duration at a fixed frequency and microwave power. The results obtained at a frequency of 30.76 GHz and microwave powers of 4 and 10 μ W are presented in Fig. 7.2. The mean (dots) and standard deviation (error bars) over six measurements are indicated for different pulse durations between 25 ns and 170 ns. For short pulse durations, population is transferred from the initially excited 33p state to the 33s state. Rabi oscillations are then observed in the fraction of atoms in the 33s state. For long pulse durations, the contrast of the oscillations is reduced because of ensemble dephasing and decoherence. Increasing the microwave power from 4 to 10 μ W results in a corresponding increase of the observed oscillation frequency.

This coherent population transfer between the 33p and 33s states was simulated in an extension of the procedure described above. Since each atom experiences a different microwave field (F_{μ}) and a different stray electric field, individual

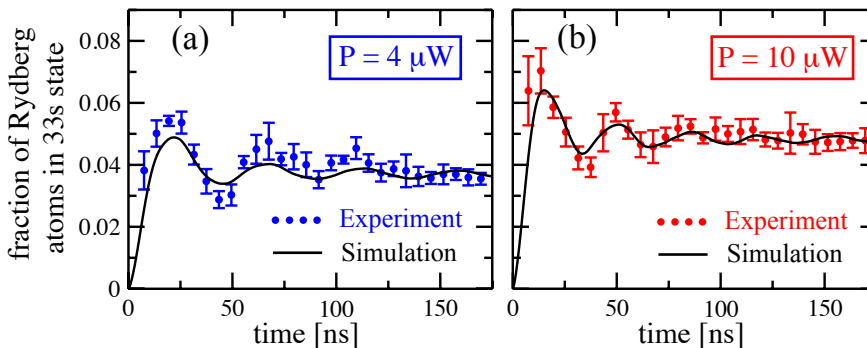


Figure 7.2: Fraction of Rydberg atoms in the 33s state as a function of microwave pulse duration for output powers of the microwave source of (a) 4 μ W and (b) 10 μ W. The solid black lines are the results of numerical simulations. Picture and caption from Hogan *et al.* (2012a).

Rabi oscillation frequencies, $\Omega = d_{33p}^{33s}(F)F_{\mu}/\hbar$, were determined. The fraction of the total ensemble of Rydberg atoms in the 33s state was then calculated by summing the contribution of each atom in the simulation. Because of the stray electric field each atom also experiences a different detuning Δ . Consequently, the single-atom oscillation frequency becomes

$$\Omega' = \sqrt{\Delta^2 + \Omega^2}, \quad (7.1)$$

and the contrast of the corresponding Rabi oscillations is reduced by a factor $(\Omega/\Omega')^2$ [Eq. (4.8)]. Because of the summation across the ensemble, the oscillations dephase with time.

Under the experimental conditions, T_1 (Sec. 1.1.3) is dominated by the fluorescence lifetime of the 33p state and is $> 1 \mu\text{s}$. The motion of the atoms ($v_0 \approx 1.7 \text{ mm}/\mu\text{s}$) above the PCB in regions of varying microwave field and stray electric field gives rise to a time dependence of Ω and Δ . The decoherence time was experimentally determined to be 250 ns. The results of the simulation, including this additional dephasing, are indicated by the black curves in Fig. 7.2. In changing the microwave power from 4 μW in Fig. 7.2(a) to 10 μW in Fig. 7.2(b) the microwave field strength and hence the Rabi frequency is expected to increase by a factor of 1.6 which is also observed in the simulations. However, the experiments revealed an increase in Rabi frequency by a factor of 1.4 ± 0.1 when increasing the microwave power from 4 μW to 10 μW . This discrepancy can be attributed to the limited knowledge of the spatial distribution of the static and microwave electric fields emanating from the surface of the PCB.

In the experiments described here, a number of serious limitations have been identified, that rendered an efficient, coherent coupling of Rydberg atoms to superconducting resonators impossible under the prevailing experimental conditions.

1. The adsorption of residual gases in the chamber (here N_2) onto the surface of the chip causes implantation of ions from Rydberg- and He^* -ionization in the matrix of frozen gas (Sec. 5.2.4). Consequently, the build-up of stray fields prohibits examination of persistent microwave transitions for temperatures below the adsorption temperatures of the gases, i.e. $\leq 100 \text{ K}$. This temperature range is incompatible with circuit QED experiments (Sec. 1.2,1.4) which need to operate at a temperature far below the critical temperatures of thin-film type II superconductors ($\sim 1 - 10 \text{ K}$)² (Sec. 6.2).

²In fact, typical circuit QED systems operate at $T \approx 10 \text{ mK}$ to suppress black-body radiation in the microwave regime.

2. The relative fraction of population transferred during coherent interaction can not be extracted from the data easily, but needs to be inferred from simulations. On the one hand, this is a consequence of the imperfect distinction of the np and ns states. On the other hand, an unknown (possibly large) fraction of Rydberg atoms in the $33p$ state has already decayed in zone 1 before reaching the PC-board, or decays after leaving zone 2, because of the small lifetime of this state ($\gtrsim 1 \mu\text{s}$). Both reasons prohibit measurement of the absolute fraction of transferred Rydberg atoms and decrease the detected Rydberg signal.
3. The measured spectra (Fig. 7.1) indicate strong stray electric fields emanating from the chip surface. Possible sources of stray fields are the rough surface (via holes) of the PC-Board (Sec. 6.1.2), surface adsorbates, potential differences between center conductor and ground planes of the transmission line, or from charging of the isolating surfaces of the coplanar waveguide [Carter *et al.* (2012); Thiele *et al.* (2015)]. Although consistent with an assumed y^{-2} -dependence from the surface, the exact origins and spatial distribution of the electric fields can not be determined. Hence, the stray fields can not be efficiently compensated.
4. The exact microwave electric field distribution could not be measured and might deviate from the simulated distribution because of spurious resonances in the metallic planes of the PCB.

The small contrast of the Rabi fringes ($\lesssim 2\%$) and the Rabi decay time much shorter than the physical limit of $2 T_1$ of the $33p$ state are a consequence of largely inhomogeneous stray electric fields and microwave fields. The characterization and compensation of these stray fields to observe robust coherent population transfer close to surfaces at (cryogenic) temperatures is an active and highly relevant topic in many atom systems such as ions, neutral ground-state- and Rydberg atoms, see introductions to next chapters.

In the following chapters we present measurements of Rydberg atoms close to plain and patterned surfaces where we can overcome all limitations listed above. Specifically, the presented experiments operate at cryogenic temperatures (overcoming limitation 1) and we efficiently detect the Rydberg-Rydberg population transfer (overcoming limitation 2). This is used to examine and compensate stray electric fields (overcoming limitation 3) and measure microwave electric field distributions (overcoming limitation 4). As a consequence we observe coherent Rabi oscillations with contrast $> 90\%$ in homogeneous, compensated static and microwave fields, and with contrast $> 80\%$ in inhomogeneous electric fields.

MANIPULATING RYDBERG ATOMS CLOSE TO SURFACES AT CRYOGENIC TEMPERATURES

CONTENT BASED ON *Thiele et al. (2014)*

In this chapter we present measurements in which helium atoms in Rydberg states have been manipulated coherently with microwave radiation pulses near a gold surface at a temperature of 3 K [*Thiele et al. (2014)*]. In the experiments we make use of the new experimental setup (Ch. 5) and the developed detection techniques (Sec. 4.2), characterizations (Sec. 4.3) and the optimal samples (Ch. 6) to improve on the limitations 1 – 4 formulated in the previous chapter (Sec. II).

Specifically, the experiments were carried out in a skimmed supersonic beam of metastable $(1s)^1(2s)^1^1S_0$ helium atoms (Sec. 3.1) excited with laser radiation to the 34p Rydberg level (Sec. 4.1). The separation between the cold surface and the center of the collimated beam was adjusted to 250 μm and the FWHM of the metastable beam was 250 μm (Sec. 4.3.3.3). As discussed in part 1 of the thesis, the adsorption of gases onto the sample surface was strongly reduced in the new setup through minimization of adsorption of residual gas onto the surfaces and the resulting slow build-up of stray fields by controlling the temperature of the surface and monitoring the partial pressures of H_2O , N_2 , O_2 and CO_2 in the experimental chamber during the cool-down procedure (Sec. 5.2.4). This measure stabilized the continuous build-up of stray fields due to ionization of the adsorbed layer of gas. Limitation 2 was relaxed by coherent transfer of the short-lived 34p

Rydberg states to the long-lived 34s state to avoid radiative decay of the Rydberg atoms between zone 1 and the region above the cold surfaces in zone 2 (Sec. 4.2).

In the following we discuss that pre-compensation of the stray electric fields emanating from the surfaces to levels below 100 mV/cm was achieved over a region of 6 mm along the beam-propagation direction (Sec. 8.1). We also discuss the stability and reproducibility of the (compensated) electric fields in the experiment on a daily basis. As discussed in Sec. 8.2, we perform coherent manipulation of the 34s Rydberg states with pulsed microwave radiation above the surfaces. This enabled measurements of electric and microwave field distributions and allowed us to study the decoherence of a coherent atomic ensemble in a region above the surface (Sec. 8.3).

8.1 Optimal compensation of static stray electric fields

Stray fields emanating from the surface of the chip represent a major source of decoherence for Rydberg atoms close to the surface and need to be avoided or compensated. In the following we present the results of microwave measurements and compensation of time-independent stray fields above the sample surface after adsorption-free cooling to 3 K using the methods presented in Sec. 5.2.4. The He* -beam propagates at a mean distance of 250 μm above a gold-coated chip, see Fig. 4.16(c) and explanations in the text.

In Sec. 4.2 we described a two-pulse microwave technique, which measures the center positions of spectral lines to determine stray electric fields along the beam propagation direction (z direction) without a sample in zone 2. Here, we use the same technique to determine electric fields above the gold-coated chip along the propagation axis of the atomic beam [Fig. 8.1]. The bottom and top axes in Fig. 8.1(a) represent the time delay between the two microwave pulses and the corresponding distance of the atoms from electrode 2, respectively. The chip surface is indicated by a yellow bar below the data points and the green bars represent electrodes 2 (left) and 3 (right).

The data points in Fig. 8.1(a) correspond to the fields (left axis) calculated from the observed center frequencies of the transitions (right axis). The vertical bars indicate the full-width-at-half-maximum (FWHM). Prior to compensation (full, red circles), these widths range from 20 MHz (≈ 0.25 V/cm) near the center of the chip (8 mm away from electrode 2, $t_\mu^{(2)} = 6 \mu\text{s}$), to 70 MHz (≈ 0.36 V/cm) near the edge of the chip (12.5 mm from electrode 2, $t_\mu^{(2)} = 9 \mu\text{s}$). The data reveal a rapid increase of the stray field and field inhomogeneities near the edges of the chip. As a result no transitions are observed at delay times of less than 5 μs and between 8.5 and 11 μs . At times greater than 11 μs , the Rydberg atoms are located in the field-free

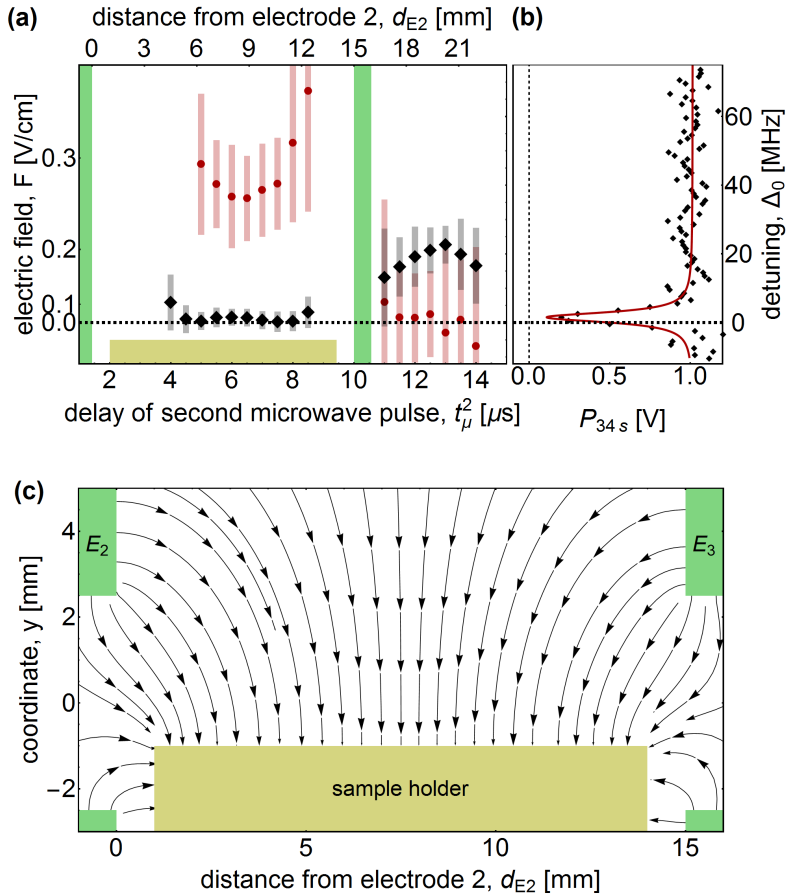


Figure 8.1: (a) Measurement of stray fields above the chip surface (yellow horizontal box) using the $34s \leftrightarrow 34p$ Stark shifts for atoms moving at a mean distance of $250 \mu\text{m}$ above the surface. The dots indicate the central positions of the transitions and the vertical bars indicate the corresponding width of the transitions. The data points indicate the measurement performed without (red dots) or with (black diamonds) stray-field compensation. Vertical green bars indicate the position of electrodes 2 and 3. (b) Spectrum of the $34s \leftrightarrow 34p$ transition with the stray-field compensation at a delay of $6 \mu\text{s}$. (c) Simulation of the direction of a compensation field without stray fields from the surface for $V_2 = 200 \text{ mV}$ and $V_3 = 255 \text{ mV}$. The sample holder is depicted by the yellow bar and the electrodes by the green bars.

region beyond electrode 3, in which the microwave power is above the saturation threshold of the transition such that it contributes to the observed linewidths.

To compensate the measured stray fields above the chip surface, we apply the potentials V_2 and V_3 (with respect to the sample holder ground) to electrodes 2 and 3, respectively. This results in a dominant component of the electric-field vector pointing in the direction perpendicular to the surface near the center of the chip (y direction) as calculated in a finite-element simulation not including stray fields [Fig. 8.1(c)]. The position along the beam-propagation axis at which the electric field is exactly perpendicular to the surface can be adjusted by applying different potential differences between electrodes 2 and 3.

Optimal stray-field compensation was achieved above the surface over a distance of ~ 6 mm along the beam-propagation direction by setting $V_2 = 300$ mV and $V_3 = 255$ mV. The observed Stark shifts are reduced to less than 1.5 MHz at distances between 5 and 11 mm (i.e. 4.5 and 8 μ s) from electrode 2 [Fig. 8.1(a); black diamonds], corresponding to residual fields of less than 55 mV/cm. These are of the same order of magnitude as the residual fields (F_{\perp}) observed after stray-field compensation in the absence of the sample [Fig. 4.7(b)]. The linewidths of the microwave transitions are in the range of 5 – 6 MHz, limited by the bandwidth of the pulsed microwave radiation [Fig. 8.1(b)]. Because of the compensation potential V_3 applied to electrode 3, the field in zone 3 of the experimental chamber is no longer zero.

At the cost of optimal compensation, the region in which the stray field is compensated can be increased to almost 9 mm and displaced by ~ 2 mm along the beam-propagation axis by changing the potentials V_2 and V_3 to 200 mV and 255 mV, respectively (Fig. 8.2). In this case, the observed Stark shifts after stray-field compensation are below 6 MHz. However, it was not possible to compensate the stray fields above the entire chip surface because of the stray-field inhomogeneities near the edges of the surface and the limited shaping capabilities when using two electrodes only.

The short-time stability and daily reproducibility of the electric fields and their compensation were examined in a series of spectroscopic experiments done within a period of 16 h. First, the electric field was determined six times within the first 5 hours, each time with the same potentials ($V_2 = 200$ mV and $V_3 = 255$ mV) applied to electrode 1 and 2, respectively. The first measurement is indicated black in Fig. 8.2. The level of fluctuation (stability) of the electric fields over a period of 5 h is below 4% of the maximal measured electric field in zone 2 (~ 0.1 V/cm). This can be concluded from the relative fluctuations of the fields measured when the atom cloud is positioned at ~ 11.5 mm within zone 2 ($t_{\mu}^{(2)} = 8$ μ s), as indicated in the inset. Second, the fields were measured two times after 16 h with the same compensation potentials applied and after the atom source, the laser and all ap-

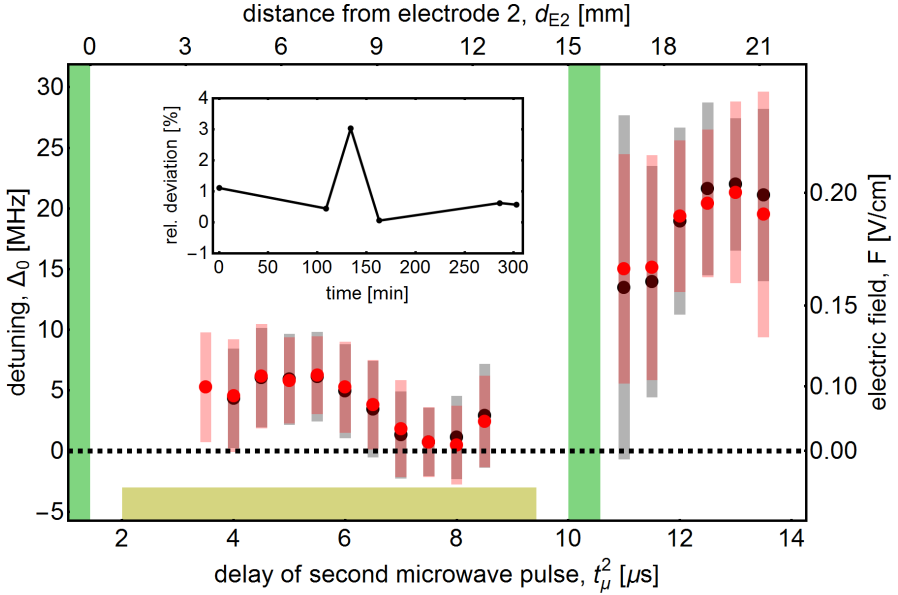


Figure 8.2: Measurement of electric field stability above the chip surface (yellow horizontal box) when the potentials $V_2 = 200$ mV and $V_3 = 255$ mV were applied to electrodes 2 and 3, respectively and determined using the $34s \rightarrow 34p$ Stark shifts for atoms moving at a mean distance of $250 \mu\text{m}$ above the surface. The red and black dots indicate the central positions of the transitions and the vertical bars indicate the corresponding width of the transitions from two measurements taken at times separated by ~ 16 h. The inset shows the relative deviation of the resonance at $t = 8 \mu\text{s}$ on a timescale of 300 min.

plied potentials had been switched off during a timespan of ~ 9 h. From this, the reproducibility of the stray fields on a daily basis can be concluded by comparing the measured electric fields after 16 h (red data) with the measured electric fields from the first dataset (black). The difference of ~ 10 mV/cm between $d_{E2} \approx 9$ and 12 mm ($t_{\mu}^{(2)} \approx 6.5$ to $8 \mu\text{s}$) are on the same order as the resolution limit of the voltage source with which the potential V_3 could be applied to electrode 3.

In conclusion, we have shown that compensation of stray fields (overcoming limitation 3) from a planar surface is possible over a distance of several millimeters. The spectroscopic results imply the possibility of coherent manipulation of Rydberg atoms near chip surfaces at cryogenic temperatures for several microseconds which will be studied in the next section.

8.2 Coherent population transfer to determine electric field distributions

The suppression of adsorption at the sample surface and the compensation of stray electric fields to levels much below 1 V/cm, demonstrated in the previous section, make it possible to observe coherent population transfer between the 34s and 34p Rydberg states of helium induced by microwave radiation pulses at a distance of less than 500 μm from a gold-coated surface. In this section, we present Rabi oscillations measured as a function of detuning Δ_0 from the field-free resonance frequency of $\nu_0 = 27\,965.77$ MHz, by either varying the microwave power at constant pulse length, or by varying the microwave pulse length at constant power. Specifically, we present how information about the static and microwave electric field distribution close to the surface can be extracted from the measured s-state population as a function of microwave power [Thiele *et al.* (2014)], i.e. we overcome limitations 3 and 4 as defined at the end of Sec. II.

In the first set of experiments, we applied the second, 160-ns-long microwave pulse at a delay of 6 μs , i.e. when the Rydberg atoms were located in zone 2 at a distance of ~ 8 mm from electrode 2 [Fig. 8.1(a)]. To compensate the stray field, we applied electric potentials of $V_2 = 200$ mV and $V_3 = 255$ mV to electrodes 2 and 3, respectively, resulting in a Stark shift of ~ 6 MHz corresponding to a residual field of ~ 110 mV/cm at the position of the atoms. For detunings $\Delta_0 = \nu - \nu_0$ varying between -5 MHz and 15 MHz from the field-free transition frequency ν_0 , the population transfer was monitored by pulsed field ionization in zone 3. The microwave power P_μ was varied at the microwave source between 0 to 5 mW, corresponding to microwave field amplitudes F_μ at the sample of 0 to 12 mV/cm.

$$F_\mu = \frac{\hbar\Omega_{\max}}{d_{34\text{p}}^{34\text{s}}} \quad (8.1)$$

was determined using the known transition electric-dipole moment $d_{34\text{p}}^{34\text{s}} = 917ea_0$ of the $34\text{s} \leftrightarrow 34\text{p}$ transition and the observed Rabi frequency Ω_{\max} determined at the maximal amplitude on resonance.

The experimental data in Fig. 8.3(a) shows the population in the 34s state as a function of detuning (Δ_0) and microwave amplitude (i.e. $\sqrt{P_\mu}$). Two regions in which the population transfer to the short-lived 34p state is efficient are observed. The first one is for detunings around 6.5 MHz and microwave powers around 0.3 mW, and the second one is for detunings around 4 MHz and microwave powers around 2.5 mW. The experimental data reveal a pronounced asymmetry which is caused by inhomogeneities of the stray electric and microwave fields across the volume of the 34s Rydberg-atom cloud. For the same reason the visibility of the

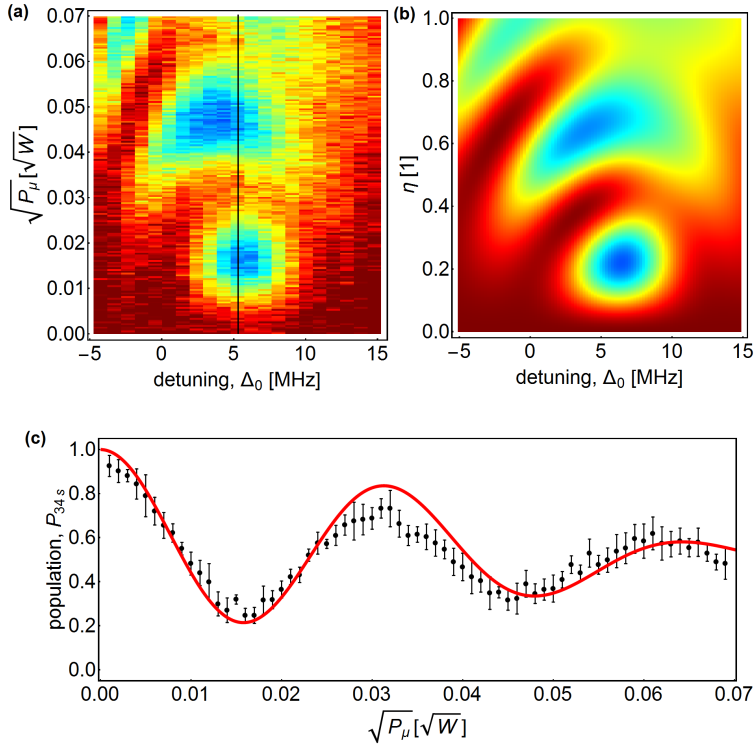


Figure 8.3: (a) Rabi oscillations measured as a function of microwave amplitude $\sqrt{P_\mu}$ and detuning Δ_0 from the field-free resonance frequency of the $34s \leftrightarrow 34p$ transition of singlet He, for a Rydberg atom cloud moving at a mean distance of $250 \mu\text{m}$ above the gold surface in a stray-field-free environment. (b) Corresponding simulation as described in the text. η is varied linearly from 0 to 1 when the experimentally set amplitude at the microwave source is varied as the square root of the power between 0 and 5 mW. In (a) and (b), the color scale indicates the population ranging from 0.14 (blue) to 1 (dark red). (c) Measured (black dots) and simulated (red line) Rabi oscillations at the detuning indicated by the dashed vertical line in (a). The vertical scale is normalized to the maximum field-ionization signal of the 34s Rydberg state observed at a detuning $\Delta_0 = -4.9$ MHz and microwave amplitudes below $0.04 \sqrt{W}$.

Rabi oscillations is less than unity, as exemplified by the data taken at $\Delta_0 \approx 5$ MHz [Fig. 8.3(c)].

In order to elucidate the influence of inhomogeneous electric fields, a simulation of the measurement was performed. We refine Eq. (4.9) by introducing a parametrization of the stray electric field and microwave field distribution over the atom cloud in order to derive the distribution $v_a(y)$ (y axis points perpendicular to the surface) of the atomic transition frequencies from the spatial distribution of the atoms $\rho(y)$. The s-state population is then calculated using

$$P_{34s}(v, \eta) = 1 - \int_0^{500 \mu\text{m}} \rho(y) p\left(v - v_a(y), \Omega(\eta, y), \Delta t_\mu^{(2)}\right) dy, \quad (8.2)$$

with $p(\Delta, \Omega, t)$ the excitation probability of the 34p state [Eq. (4.8)], and where we model the spatial distribution of the 34s Rydberg atoms in the y direction by a Gaussian distribution $\rho(y)$ with maximum at $y_{\text{max}} = 250 \mu\text{m}$ and a full width at half maximum of $250 \mu\text{m}$. The integration limits are dictated by the positions of the razor blades skimming the beam (Sec. 4.3.3.3). As a minimal model explaining our data we assume a linear dependence of the stray field [$F_{\text{stray}}(y)$] and the microwave field [$F_\mu(y)$] on the distance y from the surface according to

$$F_{\text{stray}}(y) = F_{\text{stray}}^0 + F_{\text{stray}}^1(y - y_{\text{max}}), \quad (8.3)$$

and

$$F_\mu(y) = \eta \left[F_\mu^0 + F_\mu^1(y - y_{\text{max}}) \right], \quad (8.4)$$

respectively. η , varying linearly from 0 to 1, corresponds to the microwave amplitude varying linearly from 0 to $F_{\mu, \text{max}}$ when the experimentally set amplitude at the microwave source is varied as the square root of the power between 0 and 5 mW. The one-to-one correspondence between the Stark shift and the magnitude of the electric field [Eq. (4.10)] and Equations (8.3) and (8.4) imply a direct correspondence between the distance y of an atom from the sample surface, its transition frequency $v_a(y)$ and the Rabi frequency $\Omega \propto F_\mu \propto y$. For the relevant fields, d_{34p}^{34s} is independent of F_{stray} . Good agreement with the experimental data is obtained for $F_{\text{stray}}^0 = 0.110(5)$ V/cm, $F_{\text{stray}}^1 = -1.2(5)$ V/cm², $F_\mu^0 = 11.4(6)$ mV/cm, and $F_\mu^1 = 0.69(2)$ V/cm² [Eqs. (8.3) and (8.4)]. The DC electric field decreases with increasing distance from the gold surface whereas the microwave field increases with the distance from the gold surface.

The good agreement between the experimental and simulated data in Fig. 8.3 indicates that the measurement of coherent population transfer provides information not only on the stray-field distribution, but also on the distribution of microwave fields above the sample surface in the region of the atom cloud, i.e. they

provide a path to determine the local static and microwave electric field distributions.

In *Thiele et al. (2014)*, we also present measurements above a superconducting surface, where the microwave pulse length was varied between 0 and 500 ns for fixed microwave power. At the velocity of 1770 m/s of the supersonic beam, the atoms move almost 1 mm during the longest pulses (500 ns) used in these experiments. Hence, the gradient of the microwave field strength along the beam-propagation axis needed to be taken into account in the simulations.

Note that the extrapolation of the microwave field to $y = 0$ yields a value of ~ 0.12 V/cm for gold (and ~ 1.2 mV/cm for NbTiN), which is non-vanishing at the surface. In fact, the distribution of the microwave field in the sample region (zone 2) is fully determined by the geometry of the setup. In our experiment the microwave radiation penetrates into the experimental region and zone 2 through the 5-mm-diameter laser entrance holes of the heat shields (Sec. 5.1) and has non-zero amplitude in the chip. Whether the microwave field vanishes at the sample surface or not depends on the field distribution in zone 2 and is independent of the conductivity of the surface in a first approximation.

8.3 Rabi oscillations with optimized coherence

In this section, we present a series of measurements that identify the optimal configuration to measure coherent Rabi oscillations of Rydberg atoms close to a gold surface as a function of microwave pulse length $\Delta t_\mu^{(2)}$. In this optimized configuration we observe maximal contrast ($\geq 90\%$) of the Rabi-fringes.

As observed in Fig. 8.3 and also discussed in *Thiele et al. (2014)*, inhomogeneous stray electric fields and microwave fields limit the coherence and reduce the contrast of Rabi-fringes in our experiments. Because we cannot control the microwave field distribution in the experiment, we identify regions of homogeneous static and microwave electric fields above the chip with a modified version of the spectroscopic measurement procedure used to characterize the static electric fields above the chip surface (Sec. 8.1).

We perform the experiment at larger microwave powers, such that population is efficiently transferred from the 34s to the 34p state when the microwave frequency is detuned from the atomic resonance frequency of the Rydberg atoms. The efficient off-resonant population transfer is indicated in microwave spectroscopy by a triple-peak structure [Eq. (4.8)]¹. In the absence of inhomogeneous

¹For the data measured in Fig. 4.6(b) and (c) this means that the strength of the peaks at $\Delta_c \pm 8$ MHz increases, while the center peak at $\Delta_c \approx 0$ MHz decreases.

stray fields, the relative height of the peaks uniquely determines the Rabi frequency Ω and the microwave electric field strength F_μ [Eq. (8.1)] at the position of the atomic ensemble.

Optimal stray field compensation was achieved for $V_2 = 490$ mV and $V_3 = 290$ mV with $\Delta t_\mu^{(2)} = 140$ ns and the microwave power at the microwave source $P_\mu = 0$ dBm. In the spectroscopic data for fixed $t_\mu^{(2)}$ between $\sim 5.5 \mu\text{s}$ and $7.5 \mu\text{s}$, efficient population transfer is observed at the three distinct frequencies $\Delta_0 = \nu - \nu_0 \approx -5, 3$ and 10 MHz [blue regions in Fig. 8.4(a)]. After normalization of all measured traces to the largest measured population, Eq. (4.8) was fitted to each spectrum, and the detuning $\Delta_c = \nu_a - \nu_0$ of the atomic transition frequency ν_a with respect to ν_0 and the Rabi frequency Ω were extracted. The extracted detunings Δ_0 vary between 5 MHz at $t_\mu^{(2)} = 4.5 \mu\text{s}$ and 1 MHz at $t_\mu^{(2)} = 5 \mu\text{s}$ [Fig. 8.4(b)]. The Rabi frequencies could only be extracted reliably for $t_\mu^{(2)}$ between $5.5 \mu\text{s}$ and $7.6 \mu\text{s}$, i.e. where the three-peak structure was clearly visible [Fig. 8.4(c)]².

The observed variation in microwave field strength F_μ [indicated by the right axes in Fig. 8.4(c)] over a distance of ~ 4 mm (top axis) can be extracted from the fitted Ω using Eq. (8.1). The red line indicates a fit to an (assumed) standing wave pattern of the microwave field along the beam propagation direction according to

$$|F_\mu(t)| = F_\mu^{\max} |\sin(2\pi v_0(t - t_0)/\lambda)| + B, \quad (8.5)$$

with $v_0 = 1750$ m/s, $\lambda = c/v_0 = 10.72$ mm and the fit parameters $F_\mu^{\max} = 5.1(5)$ V/cm, $B = 1.2(5)$ V/cm and $t_0 = 5.02(3)$ μs .

The detunings between $\sim 5.8 \mu\text{s}$ and $7.5 \mu\text{s}$ are minimal for the applied electric potentials V_2 and V_3 , i.e. every variation of V_2 or V_3 increases Δ_c . In fact, Rabi-type measurements (as discussed in the following) indicate a linear correlation of Δ_c and Rabi-frequency Ω .

The correlation between detuning Δ_c and microwave power is investigated in a measurement where we applied the second, 200-ns-long microwave pulse at a delay of $6.5 \mu\text{s}$ when the excited atoms were located in zone 2 at a distance of ~ 9 mm from electrode 2 [Fig. 8.4]. Note that this measurement differs from the measurement presented in Fig. 8.3 in the compensation of the stray electric field only. For detunings Δ_0 varying between -5 MHz and 15 MHz, the population transfer was monitored for applied microwave powers P_μ ranging from 0 to 20 mW [Fig. 8.5(a)]. We observe that the resonance frequency of the Rydberg atoms is shifted to larger

²The correct spatial distribution of Ω was confirmed in an independent Rabi measurement, where, for fixed microwave amplitude and $t_\mu^{(2)}$, $\Delta t_\mu^{(2)}$ was varied between 0 and 200 ns and $P_{34\text{s}}$ was measured. A fit of Eq. (4.8) to the traces acquired when $t_\mu^{(2)}$ was varied between 5 and $8 \mu\text{s}$ resulted in the same spatial variation of Ω .

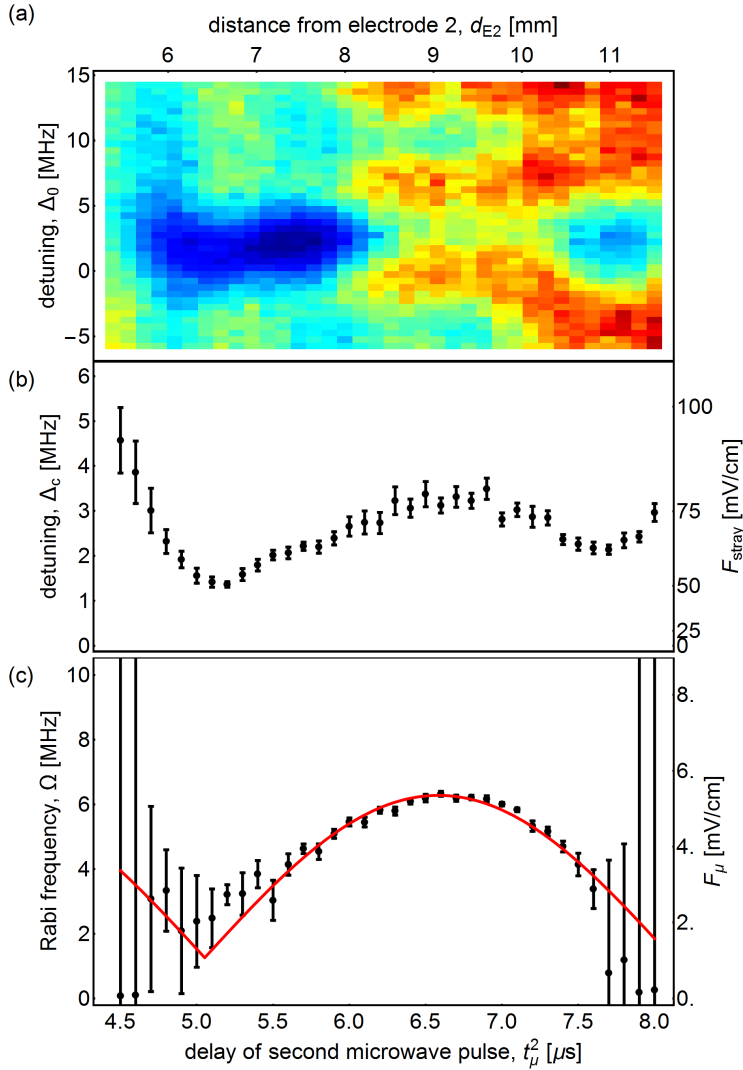


Figure 8.4: (a) 34s state population measured as function of detuning from field-free resonance frequency and position of the atom cloud in the experiment (top axis) or time delay of second microwave pulse (bottom axis), respectively. The driven Rabi angle at resonance ($\sim \Delta = 0$ MHz) exceeds $\pi/2$ for all measurements. (b) Fitted resonance frequency (left axis) and calculated, local stray electric field amplitude (right axis). (c) Fitted local Rabi rate (left axis) and calculated microwave electric field strength (right axis). The red line fits the microwave amplitude to a partially standing microwave with the microwave wavelength $\lambda = 10.72$ mm, see text.

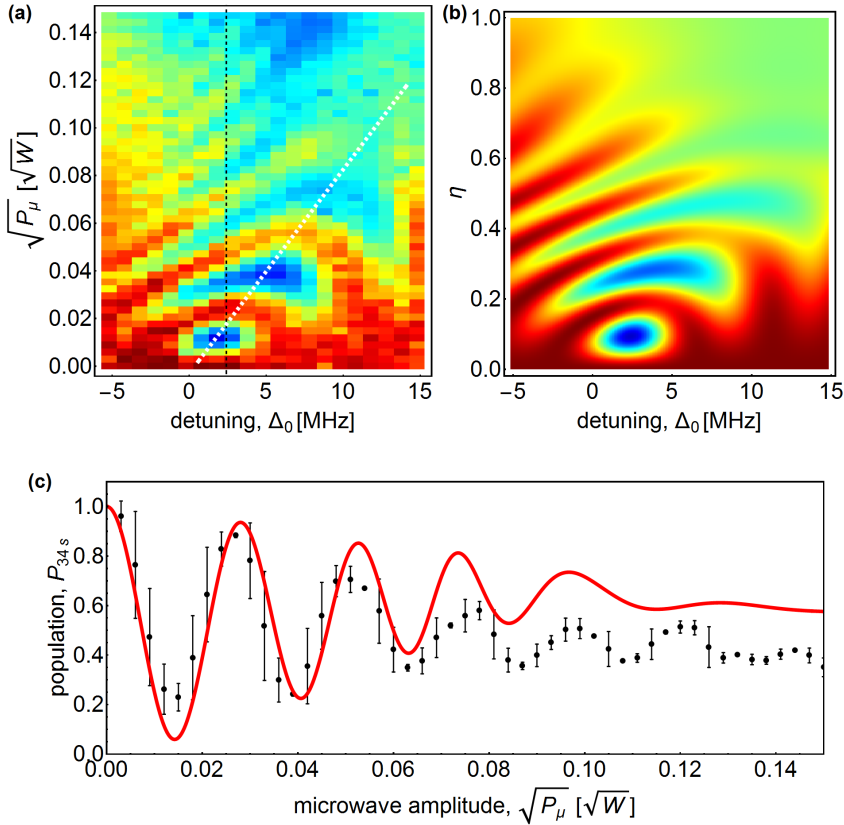


Figure 8.5: (a) Rabi oscillations measured as a function of microwave amplitude $\sqrt{P_\mu}$ and detuning Δ_0 from the field-free resonance frequency of the $34s \leftrightarrow 34p$ transition of singlet He, for a Rydberg atom cloud moving at a mean distance of $\sim 250 \mu\text{m}$ above the gold surface in a stray-field-free environment. The white line indicates the shift of the resonance frequency with amplitude. (b) Corresponding simulation as described in the text. η is varied linearly from 0 to 1 when the experimentally set amplitude at the microwave source is varied as the square root of the power between 0 and 20 mW. In (a) and (b), the color scale (indicating the population in 34s) ranges from 0.15 (blue) to 1 (dark red). (c) Measured (black dots) and simulated (red line) Rabi oscillations at the detuning indicated by the dashed vertical line in (a). The vertical scale is normalized to the maximum field-ionization signal of the 34s Rydberg state observed at a detuning $\Delta_0 = 3$ MHz and microwave amplitudes below $0.015 \sqrt{W}$.

frequencies for increasing microwave power (white line), which we attribute to an AC Stark effect.

The situation can be simulated using the same model as described above for Fig. 8.3 including an additional linear dependence of the atomic resonance on the microwave amplitude with proportionality constant β , i.e.

$$P_{34s}(\nu, \eta) = 1 - \int_0^{500 \mu\text{m}} \rho(y) p\left(\nu - (\nu(y) + \beta F_\mu(y)), \Omega(\eta, y), \Delta t_\mu^{(2)}\right) dy. \quad (8.6)$$

Good agreement with the experimental data is obtained for $F_{\text{stray}}^0 = 0.045(1)$ V/cm, $F_{\text{stray}}^1 = -0.90(5)$ V/cm², $F_\mu^0 = 22.0(2)$ mV/cm, and $F_\mu^1 = 0.25(1)$ V/cm² [Eqs. (8.3) and (8.4)], and for $\beta = 2\pi \times 19.1$ MHz/(Vcm⁻¹). The inhomogeneous variation of the microwave field over the Rydberg atom cloud renders coherent population transfer inefficient for $\sqrt{P_\mu} \geq 0.06\sqrt{W}$ as can be observed from the imperfect population transfer at $\Delta_0 = 10$ MHz in Fig. 8.5(a).

In the simulated data, the population in the 34s state approaches $P_{34s} \approx 0.5$ for microwave amplitudes $\sqrt{P_\mu} \geq 0.08\sqrt{W}$ and detunings $\Delta_0 \geq 5$ MHz (green area). However, in the measured data [Fig. 8.5(a)] the population $P_{34s} \lesssim 0.4$ (blue region for $\Delta_0 \geq 3$ MHz and $\sqrt{P_\mu} \geq 0.1\sqrt{W}$). A numerical simulation of a system with two coherently coupled states that can radiatively decay to a third state indicate that this is a consequence of the short lifetime of the 34p state ($\tau_{34p} \approx 2$ μ s) and the number of transfers the population has undergone within the duration of the pulse (200 ns). Lifetime effects are not taken into account in the numerical model we present in Fig. 8.5(b).

The strong correlation between microwave amplitude and atomic resonance frequency ν_a for well-compensated electric stray fields make it impossible to observe the microwave-field-free resonance frequency with the methods described so far, i.e. coherent spectroscopy. However, in a Ramsey-type experiment it is possible to observe the resonance frequency of the atoms in the absence of microwave fields.

To perform a Ramsey measurement, two microwave pulses of frequency ν are applied to the atoms with a variable time separation δt while monitoring the population transfer between the 34s and 34p state. The amplitude and duration of the microwave pulses are chosen such that for a detuning to the atomic resonance $\Delta = \nu - \nu_a = 0$ MHz, they correspond to $\pi/2$ -Rabi pulses. As a consequence, a full population transfer is observed independent of δt . If the two pulses are detuned, i.e. $\Delta \neq 0$ MHz the population has a sinusoidal dependence on δt with a frequency corresponding to the detuning Δ .

In the experiment presented here [Fig. 8.6], we extend the two-pulse microwave measurements (Sec. 4.2) by an additional third pulse at $t_\mu^{(3)} = t_\mu^{(2)} + \delta t$

through the second horn antenna. The first Ramsey pulse is applied at $t_\mu^{(2)} = 6.5 \mu\text{s}$ and the second Ramsey pulse at time $t_\mu^{(3)}$ at variable time delay $\delta t = 0$ to 1500 ns with respect to the first pulse. $t_\mu^{(2)}$ is chosen such that the microwave amplitude seen by the moving atoms varies slowly during the Ramsey sequence. From the Rabi measurement presented in Fig. 8.5(a), we conclude that for an applied pulse length $\Delta t_\mu^{(2)} = \Delta t_\mu^{(3)} = 35$ ns a microwave amplitude $\sqrt{P_\mu} \approx 0.04\sqrt{W}$ corresponds to a $\sim \pi/2$ rotation on resonance. The detuning Δ_0 is varied for both pulses simultaneously between $\Delta_0 \approx -8$ and 10 MHz and the population in the 34s state is monitored.

We observe rapid oscillations for large applied detunings Δ_0 from the field-free resonance [Fig. 8.6(a)]. The trace at $\sim \Delta_0 = 1$ MHz exhibits almost no population transfer as a function of δt [Fig. 8.6(b), top panel]. To each measured trace we fit a simple model [see also Eq. (1) in *Affolderbach et al. (2015)*] that is motivated by numerical simulations of the Bloch equations for a Ramsey experiment with an ensemble dephasing time T_2^* and a lifetime T_1 of the 34p state, i.e.

$$P_{34s}(\delta t, \nu) = A \exp\left[-\frac{\delta t}{T_2^*}\right] \sin[(\nu - \nu_a)\delta t + \phi] + B \exp\left[-\frac{\delta t}{T_1}\right]. \quad (8.7)$$

The model [red traces in Fig. 8.6(b)] describes the data well, as can be observed from the agreement of the red curves (fit) and the black data points in Fig. 8.6(b).

From the fits to all 19 traces we determine $A = 0.405(18)$, $T_2^* = 589(16)$ ns, $\nu_a = \nu_0 + 170(13)$ kHz (i.e. a residual field of 18 mV/cm), and $B = 0.43(2)$. T_1 varies between $\sim 10 \mu\text{s}$ for large detunings Δ and $\sim 3 \mu\text{s}$ for small detunings. This variation is expected because for $\Delta = 0$ MHz, the quantum mechanical state after the first Ramsey pulse is an equal superposition of 34p and 34s, hence we expect $T_1 = 2\tau_{34p} \approx 3.2 \mu\text{s}$. For large Δ , the population transfer to 34p is inefficient, and we expect $T_1 \approx \tau_{34s} \gg 2\tau_{34p}$.

From the Ramsey measurement we conclude that the electric field compensation is good enough that the Rydberg atoms can be coherently manipulated over a distance of more than 1 mm. The coherence time T_2^* is either limited by remaining stray electric fields from the gold surface or is an artefact of unequal Ramsey pulses because of the spatially varying microwave amplitude. We expect to observe longer T_2^* -times with a slower atom-beam velocity ν_0 .

The T_1 and T_2^* -times determined in the Ramsey measurements can be used to model Rabi oscillations, measured by variation of the pulse length ($\Delta t_\mu^{(2)}$ between 10 ns and 1000 ns) and the detuning (Δ_0 between -8 MHz and 17 MHz) of a single pulse with constant amplitude ($\sqrt{P_\mu} \approx 0.04\sqrt{W}$ or $P_\mu = 2$ dBm). For the same electric field compensation used for the Ramsey measurement, the pulse is applied at $t_\mu^{(2)} = 6.5 \mu\text{s}$ and the population in the 34s state, P_{34s} , is recorded [Fig. 8.7]. In panel (a), we observe P_{34s} to be symmetric with respect to an atomic resonance

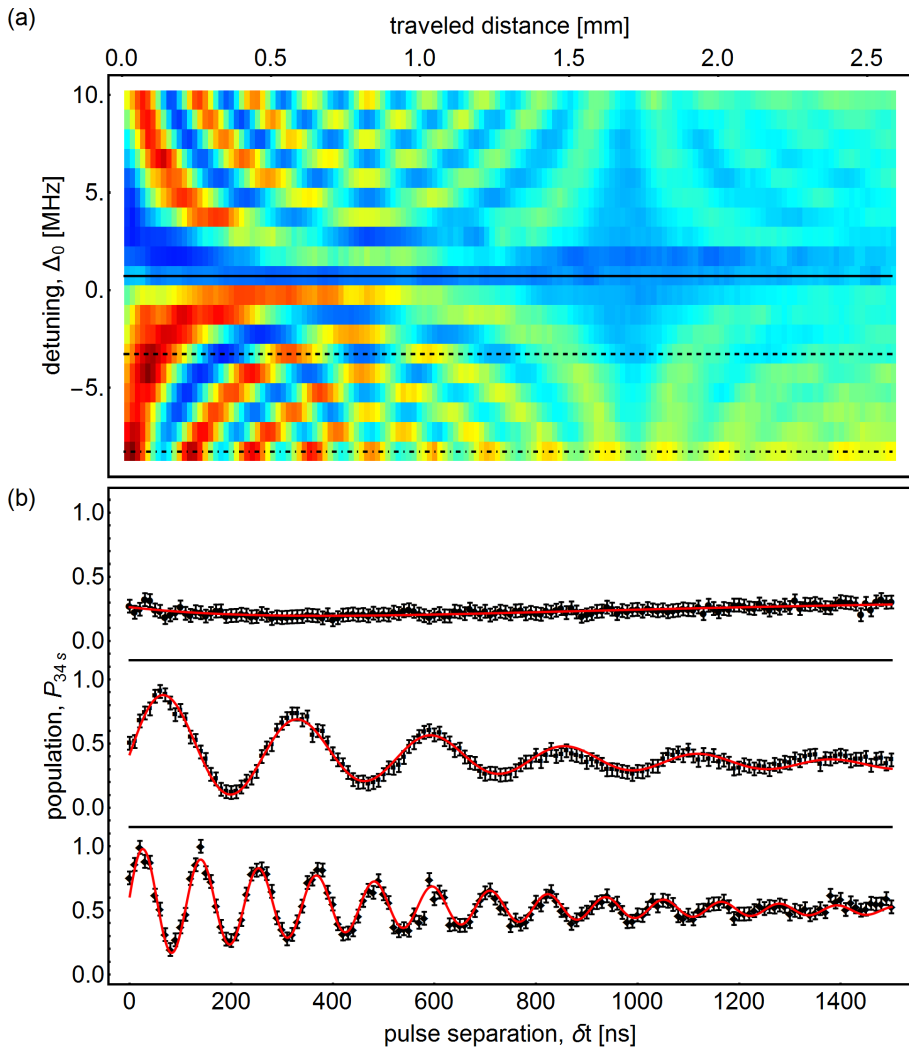


Figure 8.6: Ramsey-type measurement. (a) 34s state population is measured as function of detuning from field free resonance and the separation of two $\pi/2$ pulses (bottom axis). The top axis indicates the atom distance traveled between the pulses. (b) Cuts along the black solid (top panel), dashed (center panel) and dash-dotted (lower panel) lines in (a). The red lines are fits to Eq. (8.7), see text for details.

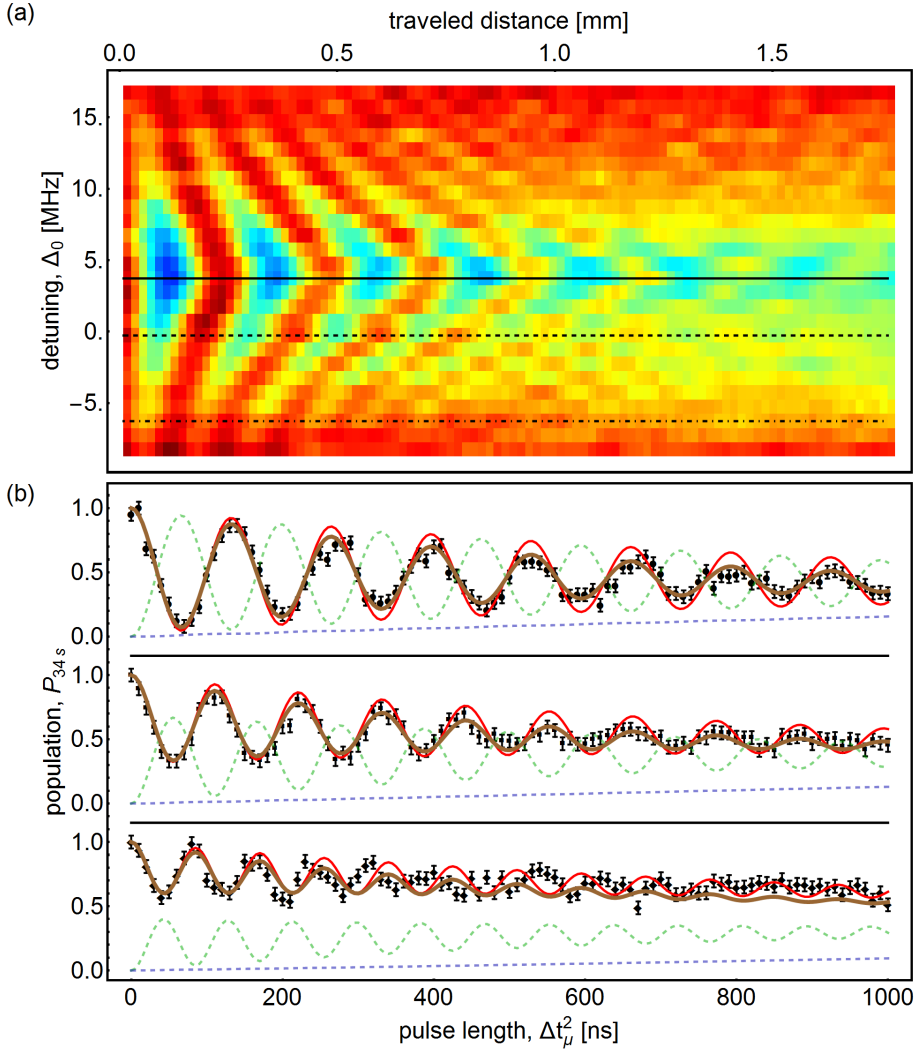


Figure 8.7: Rabi-type measurement. (a) 34s state population is measured as function of detuning from field free resonance and the microwave pulse length (bottom axis). The top axis indicates the distance traveled by the atoms during the microwave pulse. (b) Cuts (black data points) along the black solid (top panel), dashed (center panel) and dash-dotted (lower panel) lines in (a). The red lines are predictions from a master equation without free parameters, see text for details. Green and blue dashed lines indicate theoretical populations in the 34p and ground state, respectively. The brown line corresponds to the simulated 34s state population, when the predicted dephasing in the Master equation was adjusted to fit the data in the top panel.

frequency of $\nu_a = \nu_0 + 4.8(1)$ MHz (i.e. $\nu_a = 27.9706(1)$ GHz). The different shift of the resonance frequency in this Rabi measurement (4.8 MHz) compared to the shift in the Ramsey measurement (170 kHz) before is a consequence of the correlation between the atomic resonance frequency and the applied power (Fig. 8.5) because, during the Rabi experiment, the Rydberg atoms are (constantly) exposed to microwave radiation. Due to the well-compensated electric stray fields and the spatially slowly varying microwave field, we observe an initial contrast of the (resonant) Rabi fringes $\geq 90\%$.

The Rabi experiment is simulated without free parameters using a 3-state (Markovian) Kossakowski-Lindblad formalism [Lindblad (1976)]. Specifically, we consider the 34s and 34p-Rydberg states of helium, energetically separated by $h\nu_a = h 27.9706$ MHz, as determined from the measurement in Fig. 8.5. The states are coupled by a microwave drive at variable detuning Δ and Rabi frequency $\Omega = 2\pi \times 7.5$ MHz, as determined from the measured Rabi frequency ($\Omega = 2\pi \times 6$ MHz) at $t_\mu^{(2)} = 7 \mu\text{s}$ in Fig. 8.4(c) and considering the factor $1.26 = \sqrt{2 \text{ dBm}/0 \text{ dBm}}$ due to the difference in applied microwave power in the two experiments³. We add a third (groundstate) level that is far detuned from the Rydberg states. Damping in the system is induced by 3 Lindblad operators taking into account radiative decay of the 34p state ($\gamma_p = 1/T_1 = 1/3$ MHz), radiative decay of the 34s state ($\gamma_s = 1/\tau_{34s} = 1/98.2$ MHz) and dephasing of the atoms in the Rydberg state $\gamma_\phi = 1/T_2^* = 1/0.589$ MHz. γ_p and γ_ϕ are given by the T_1 and T_2^* values determined from the Ramsey measurement close to resonance.

The simulation agrees with the measured data. Black data points in the upper, middle and lower panel of Fig. 8.7(b) correspond to cuts along the black solid, dashed and dot-dashed lines in panel (a), respectively. The red lines indicate the predicted 34s state population as a function of the microwave pulse length $\Delta t_\mu^{(2)}$. The green and blue, dashed lines in each panel indicate the 34p and ground-state populations as predicted by the simulation. The disagreement between the measured data and the simulation for pulse lengths $\Delta t_\mu^{(2)} \gtrsim 500$ ns can be attributed to an additional dephasing because of the microwave field as motivated from the following arguments.

For $\Delta \ll \Omega$, the effective Rabi frequency is, see Eq. (7.1),

$$\Omega' = \sqrt{\Omega^2 + \Delta^2} \approx \Omega \propto F_\mu(y). \quad (8.8)$$

For a spatially inhomogeneous microwave field, the states of different atoms in the ensemble hence oscillate with different Rabi frequencies Ω' and dephase (i.e. decrease T_2^* and increase γ_ϕ). For $\Delta \gg \Omega$

$$\Omega' = \sqrt{\Omega^2 + \Delta^2} \approx \Delta \quad (8.9)$$

³7 μs correspond to the average time of the longest Rabi pulse.

is constant over the atom cloud in absence of stray electric fields. Consequently the states of different atoms in the ensemble oscillate with the same effective Rabi-frequency (i.e. Δ) and an inhomogeneous microwave field does not contribute to the dephasing. This effect can be observed also in the simulations. Increasing the dephasing by a factor of 2 (i.e. $\gamma_\phi = 3.4$ MHz) provides better agreement of the simulation (brown) and the measured data for small microwave detunings $|\Delta| = |\nu - \nu_a| \leq |\Omega/(2\pi)| = 7.5$ MHz (upper and middle panel) but disagrees for $|\Delta| \geq |\Omega/(2\pi)|$ (lower panel).

8.4 Conclusions

An atomic beam of singlet $(1s)^1(2s)^1S_0$ He Rydberg atoms has been manipulated coherently close to a gold surface at cryogenic temperature (3 K).

With microwave spectroscopy (Sec. 4.2), the stray electric fields above the surfaces were mapped out along the beam-propagation axis. The fields emanating from the surface were compensated to a level below 100 mV/cm over a distance of 6 mm and to a level below 20 mV/cm over a distance of 2 mm directly above the cold surface.

Rabi oscillations between the 34p and the 34s levels, for a He beam propagating 250 μm above the gold surface, were recorded by changing the frequency and either the amplitude or the length of microwave radiation pulses. The observed patterns of Rabi oscillations provide information on the distributions of microwave and stray electric fields above the surface. Exploiting a combination of spectroscopic and Ramsey measurements, we predicted the population transfer of a Rabi measurement and concluded that both, the inhomogeneous microwave and static electric fields, contribute to the dephasing.

The coherence of the Rydberg atom sample in the immediate vicinity of the gold surface, and the ability to manipulate Rydberg atoms with microwave radiation pulses above the surfaces is a prerequisite for experiments in which Rydberg states are coupled coherently to superconducting resonators embedded in solid-state devices.

For patterned surfaces, the inhomogeneities of the microwave and the static electric fields over the atom cloud are larger due to localized sources of stray fields, e.g. by charging of insulating patches. In the next chapter we present a novel technique to measure static and microwave electric field distributions that allows identifying sources of, and compensating stray electric and microwave fields above patterned, superconducting surfaces.

IMAGING ELECTRIC FIELDS IN THE VICINITY OF CRYOGENIC SURFACES USING RYDBERG ATOMS

CONTENT BASED ON *Thiele et al. (2015)*

In the last chapter we have identified the need to characterize the distribution of static stray and microwave electric fields across the atom cloud. Knowledge about the electric field distribution allows to identify and avoid sources of stray electric fields, and to create optimized electrode configurations to compensate electric field gradients. In this chapter we present techniques to characterize static and microwave electric field distributions varying across the atom cloud and observe coherent population transfer with initial contrast of $\gtrsim 80\%$.

In fact, the ability to characterize static and time-dependent electric fields *in situ* is an important prerequisite for most quantum-optics experiments with atoms close to surfaces. Especially in experiments which aim at coupling Rydberg atoms to the near field of superconducting circuits, as in our case, the identification and subsequent elimination of sources of stray fields is crucial. In this chapter, we present a technique that allows the determination of stray-electric-field distributions $(F_x^{\text{str}}(\mathbf{r}), F_y^{\text{str}}(\mathbf{r}), F_z^{\text{str}}(\mathbf{r}))$ at distances of less than 2 mm from (cryogenic) surfaces using coherent Rydberg-Stark spectroscopy in our pulsed supersonic beam of metastable $1s^1 2s^1 \ ^1S_0$ helium atoms. We demonstrate the capabilities of this

technique by characterizing the electric stray field emanating from a structured superconducting surface. Exploiting coherent population transfer with microwave radiation from a coplanar waveguide, the same technique allows the characterization of the microwave-field distribution above the surface.

Stray fields emanating from the patterned surfaces of solid-state devices in general are of major concern in hybrid systems involving ions [Seidelin *et al.* (2006); Ospelkaus *et al.* (2008)] and Rydberg atoms [Sørensen *et al.* (2004); Petrosyan and Fleischhauer (2008); Petrosyan *et al.* (2009)]. The sources of stray fields are manifold and include surface adsorbates [Tauschinsky *et al.* (2010); Hattermann *et al.* (2012); Chan *et al.* (2014)], polycrystalline surface patches [Carter and Martin (2011)], and charges in the isolating gaps of coplanar waveguides (CPW) [Carter *et al.* (2012)]. Although detrimental effects of electric stray fields might be mitigated in some cases, e.g., by microwave frequency dressing [Jones *et al.* (2013)], coating the surfaces with adsorbates [Hermann-Avigliano *et al.* (2014)] or choosing chemically inert atoms (such as helium) [Hogan *et al.* (2012a); Thiele *et al.* (2014)], techniques to measure stray fields are essential. A possible technique in this context is based on Rydberg-electromagnetically-induced transparency, with which also the microwave field in a glass cell [Holloway *et al.* (2014)] or of a coplanar waveguide (CPW) [Sedlacek *et al.* (2012); Fan *et al.* (2014)] has been characterized.

In this chapter, we show that measuring spatially varying quadratic Stark shifts

$$\begin{aligned}\Delta E_{\text{Stark}}^{(i)}(\mathbf{r}) &= h(\nu_a(\mathbf{r}) - \nu_0) = \frac{1}{2}\Delta\alpha|\mathbf{F}_{\text{tot}}^{(i)}(\mathbf{r})|^2 \\ &= \frac{1}{2}\Delta\alpha|\mathbf{F}^{(i)}(\mathbf{r}) + \mathbf{F}^{\text{str}}(\mathbf{r})|^2\end{aligned}\quad (9.1)$$

of the 34s to 34p Rydberg-Rydberg transition for different well-defined applied electric fields $\left[\left(F_x^{(i)}(\mathbf{r}), F_y^{(i)}(\mathbf{r}), F_z^{(i)}(\mathbf{r})\right), i = 1-4\right]$ allows the determination of the three components of an unknown stray field $\left(F_x^{\text{str}}(\mathbf{r}), F_y^{\text{str}}(\mathbf{r}), F_z^{\text{str}}(\mathbf{r})\right)$ emanating from the surface. Eq. (9.1) is obtained by combining Eqs. (4.10,4.11) and the generalization to field distributions. As determined in Sec. 4.2, $\Delta\alpha = 1078.03 \text{ MHz (V/cm)}^{-2}$ [Thiele *et al.* (2014)] is the polarizability difference between the 34p and 34s states. The stray field $\mathbf{F}^{\text{str}}(\mathbf{r})$ is uniquely determined at each point \mathbf{r} by a set of four independent equations [Eq. (9.1), $i = 1-4$]. Three equations are needed because of the three dimensions of the problem and an additional equation because of the quadratic nature of the Stark effect for fields below $F \lesssim 1 \text{ V/cm}$ [Fig. 4.5(a)]. The spatially varying Stark shift $\Delta E_{\text{Stark}}^{(i)}(\mathbf{r})$ is observed as the difference between the position-dependent resonance frequency $\nu_a(\mathbf{r})$ of the 34s to 34p transition and its zero-field transition frequency $\nu_0 = 27965.773 \text{ MHz}$, obtained from the known quantum defects [Drake (1999)].

9.1 Measurement of stray electric field distributions

We perform the measurements in the 6-mm-long experimental region [black rectangle, Fig. 9.1(a)] along the helium-beam propagation direction (z direction, yellow arrow) above the center of the transmission line sample (sample design 4, Sec. 6.1) in zone 2 cooled to ~ 3 K. In the (x, y) plane, the region is bounded by the surface of the patterned, superconducting NbTiN chip surface containing the coplanar waveguide aligned parallel to the z axis, and the metallic hood [Fig. 9.1(b)]. The special design of the sample holder (Sec. 6.1.1) allowed the chip to be cleaned with an Ar^+ plasma prior to mounting under nitrogen atmosphere. Charges Q_g and Q_s (surface charge densities σ_g and σ_s , respectively) can accumulate in the insulating gaps of the waveguide [Carter *et al.* (2012)] and on an insulating layer at the surface of the superconductor. The insulating layer could originate from adsorption of residual gases at the surface during an imperfect cooldown (Sec. 5.2.4) or from surface oxidation [Barends *et al.* (2010)]. These charges represent a potential source of stray fields $\mathbf{F}^{\text{str}}(\mathbf{r})$ in our experimental region.

The region above the chip where the stray electric field is measured coincides in the (x, y) plane with the cross section of the atomic beam, limited by collimating slits to the area marked by a dashed blue line in Fig. 9.1(b), and along z by the length of the Rydberg-atom cloud of 1 mm. Because of the translational invariance of the electrode configuration along z , $F_z^{(i)}(\mathbf{r}) = 0$, regardless of the potentials applied to the device, see Fig. 9.1(a,b). Moreover, $F_z^{\text{str}}(\mathbf{r})$ is constant and small enough that it does not cause shifts of the transition frequency of more than ~ 1 MHz, which is almost negligible compared to the shifts resulting from the x and y components of the stray field (see below). $F_z^{\text{str}}(\mathbf{r})$ can be determined from the Stark shift at a position where the stray field in x and y directions has been compensated. Consequently, only the x and y components of the stray-electric-field distribution need to be determined, and only three sets of measurements ($i = 1, 2, 3$) in Eq. (9.1) are required to determine $F_x^{\text{str}}(x, y)$ and $F_y^{\text{str}}(x, y)$.

Propagating along the CPW, the microwave square pulses of 200 ns length we use to monitor the 34s to 34p transition have a Fourier-transform-limited bandwidth of ~ 4.4 MHz centered around a chosen detuning Δ_0 from the field-free atomic resonance frequency ν_0 . These pulses allow us to probe and image atoms subject to specific Stark shifts and thus specific field strengths, see Fig. 9.2(a) for an example. Because the 34p state lifetime is less than $2 \mu\text{s}$, only atoms in the 34s state are detected using the Rydberg-atom-imaging technique presented in Sec. 4.3.3.3. The images therefore reveal regions of low intensities [dashed line in Fig. 9.2(a)] with a spatial resolution varying between $\leq 80 \mu\text{m}$ and $\sim 150 \mu\text{m}$ (Fig. 4.19) which reflect the positions where atoms are efficiently transferred to the 34p state in the experimental region.

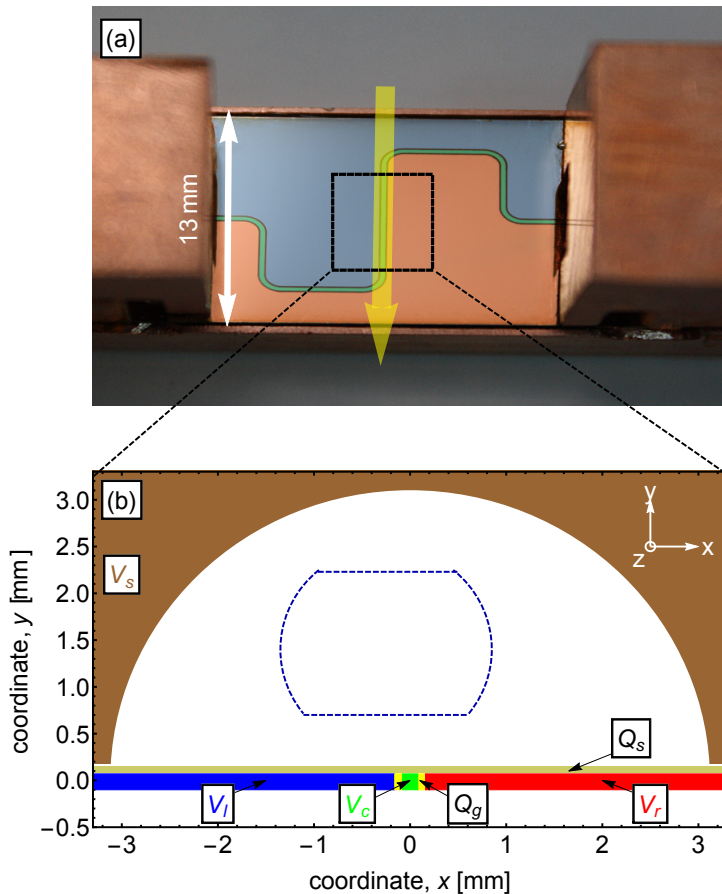


Figure 9.1: (a) Colorized, top-view photograph of a sample-design-4-chip (Sec. 6.1) as used in the experiments. Potentials V_c , V_r , V_l and V_s can be applied to the center conductor (green), the right (red) and the left (blue) ground plane of the coplanar waveguide (CPW) and to the metallic shield (brown, not shown). The direction of the atom beam is indicated by the yellow arrow and the experimental region by the black, dashed rectangle. (b) Cross section of the experimental region above the coplanar waveguide. Colors are the same as in (a). The thickness of the superconducting layer of the CPW is not to scale. Charges Q_g and Q_s (light and dark yellow) may accumulate either in the insulating gaps of the waveguide or on an insulating layer on the superconductor, respectively. The dashed blue line indicates the cross section of the Rydberg beam limited by the collimating slit apertures.

Well-defined electric-field distributions are generated by applying potentials V_c, V_l, V_r and V_s to the device (Fig. 9.1). The applied potentials are small enough that they do not change the stray electric fields. The stray-field-measurement procedure outlined below starts once the stray fields have been roughly compensated by varying the potential applied to the center conductor, a potential of 4 V being sufficient to reduce the Stark shifts to below 25 MHz over the entire experimental region marked by the dashed blue line in Fig. 9.1(b).

We determine $\Delta E_{\text{Stark}}(x, y)/h$ by varying the detuning Δ_0 of the microwave pulses between -7 MHz and 22 MHz and extracting the intensity at every pixel of the acquired camera images. This intensity corresponds to the relative population $P_{34s}(x, y)$ in the 34s Rydberg state after the microwave pulse. The amplitude of the microwave pulse is small enough to avoid coherent repopulation of the 34s state. The spectra at each pixel are fitted by Gaussian functions to determine the width and detuning (i.e., the Stark shift) of the 34s to 34p transition. Fig. 9.2(b) shows, as examples, the spectra recorded for $V_c = 4.00$ V, $V_l = -0.02$ V, $V_r = 0.00$ V and $V_s = -0.11$ V at the two pixels marked by red and blue arrows in the image depicted in Fig. 9.2(a). The fits yield the values $\Delta E_{\text{Stark}}/h = 0.15$ MHz and 9.48 MHz, respectively, with corresponding widths of 4.2 MHz and 14.67 MHz. The line broadening observed with increasing Stark shift is a consequence of the field inhomogeneity and the quadratic nature of the Stark effect at low fields, as explained in Fig. 4(a) of [Osterwalder and Merkt (1999)].

The measured distribution of Stark shifts [Fig. 9.2(c)] ranges from ≤ 0.1 MHz (point marked by the label ' Δ ') to 22 MHz (below the point labeled '+'), which is located close to the CPW. This range corresponds to electric-field strengths between ≤ 16 mV/cm and 200 mV/cm, see Fig. 9.2(e). Because of the relationship between Stark shift and Stark broadening mentioned above, the observed distribution of linewidths depicted in Fig. 9.2(d) provides an independent measurement of the stray-field distribution.

Over a large fraction of the cross section of the atomic beam, the observed microwave transitions exhibit a full-width-at-half-maximum of ~ 4.5 MHz [Fig. 9.2(d)], close to the Fourier-transform limit of ~ 4.4 MHz of the microwave pulse. This observation implies that the effects of inhomogeneous broadening that eventually limit coherence are negligible on the 200 ns timescale of the measurement.

Using a 2 dimensional finite-element calculation, we simulate the electric-field distribution [Fig. 9.2(f)] using the applied potentials V_c, V_l, V_r and V_s and fitting the surface charge densities σ_g and σ_s (extracted best fit values given in the caption). The simulated field distribution is in good agreement with the experimental results and the comparison indicates that σ_g and σ_s are defined with an accuracy of about 1%. Small discrepancies between the measured and simu-

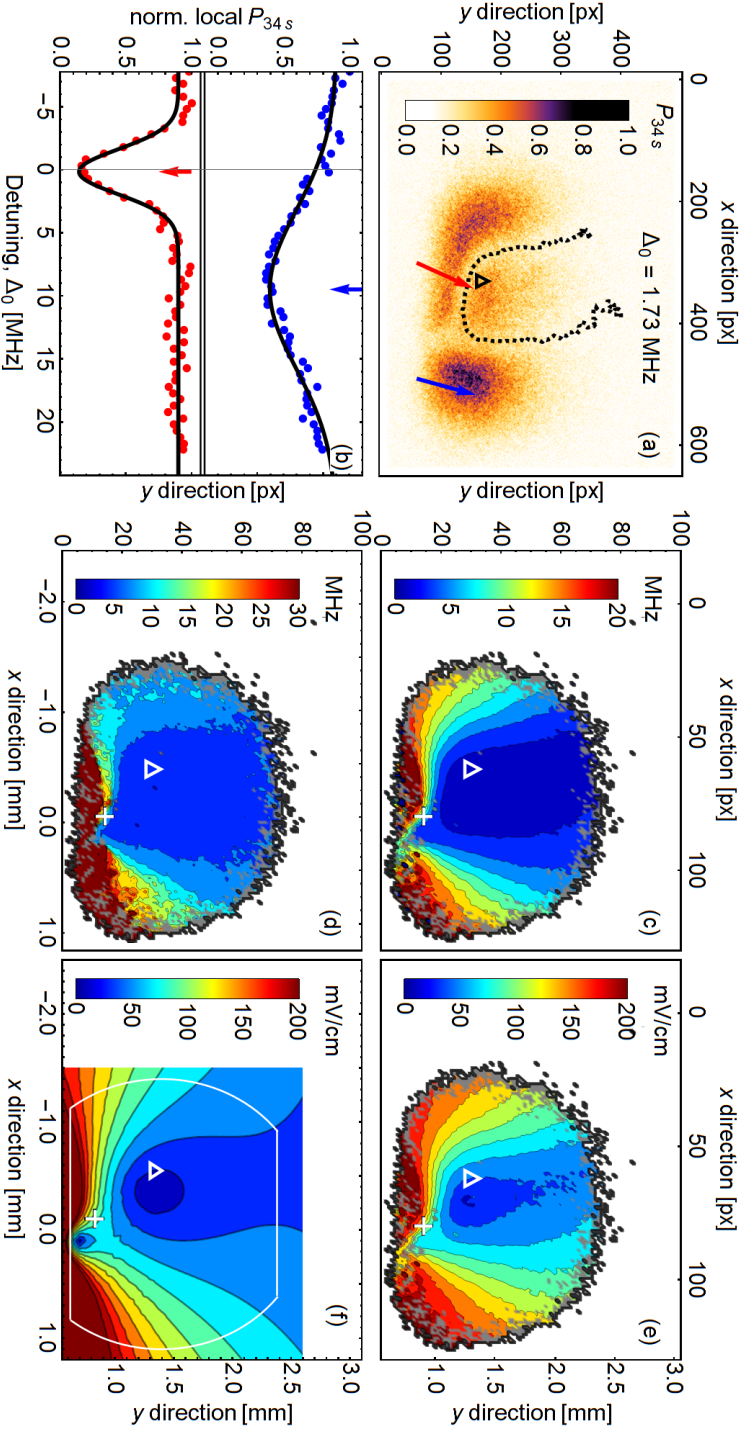


Figure 9.2: Distribution of electric-field strengths for potentials $V_C = 4.00$ V, $V_I = -0.02$ V, $V_S = 0.00$ V and $V_S = -0.11$ V. (a) Measured distribution of 34s Rydberg atoms after driving the 34s to 34p transition at a microwave detuning of 1.73 MHz. The spatial resolution of the images is $150 \mu\text{m}$ (see panels (c)-(f) for length scales). The dots mark the positions where the field-ionization signal is minimal and represent the positions where the 34s to 34p transfer is maximal and hence the field strength (extracted from the Stark shift) is 55 mV/cm. (b) Experimental spectrum (dots) and Gaussian fit (solid line) of the 34s to 34p transition for He atoms located at the positions marked by the blue (upper trace) and red (lower trace) arrows in (a) after binning over $5 \cdot 5$ pixels. (c) Spatial distribution of 34s to 34p transition frequencies (Stark shifts) extracted from the spectra measured at the different pixels. (d) Corresponding distribution of full widths at half maximum. (e) Electric-field distribution derived from the observed Stark shifts. (f) Simulated electric-field distribution using $\sigma_g = -23.6(1)10^{-6} \text{ C/m}^2$ and $\sigma_s = -2.10(5)10^{-6} \text{ C/m}^2$, see text.

lated electric-field distributions result from the assumption that the charge density σ_s is homogeneous over the chip surface, which is the least stringent assumption we can make on the spatial distribution of these surface charges. The simulation also confirms the conversion factor of $\sim 23 \mu\text{m}/\text{px}$ relating the camera pixels to the physical dimensions in the experimental region, determined independently from simulations of the metastable He beam propagation and from simulations of the electron trajectories. From Fig. 9.2(c-d), we extract an atom beam diameter of about 2.5 mm.

To determine the components of the electric stray field $(F_x^{\text{str}}(x, y), F_y^{\text{str}}(x, y))$, we measure three different electric-field distributions $(F_{\text{tot}}^{(i)}(x, y), i = 1, 2, 3)$, for three different potential configurations [see Fig. 9.3(a,b,c)]. The small homogeneous field component $F_z^{\text{str}} \approx 50 \text{ mV/cm}$ was determined from the Stark shift of $\sim 1 \text{ MHz}$ at the field minima in Figs. 9.3(a,b,c).

$(F_x^{\text{str}}(x, y), F_y^{\text{str}}(x, y))$ are extracted from a least-squares fit of the field strength $|\mathbf{F}^{(i)}(x, y) + \mathbf{F}^{\text{str}}(x, y)|$ to the measured electric-field strength $F_{\text{tot}}^{(i)}(x, y)$ for $i = 1, 2, 3$ using a random-search algorithm. The applied fields $\mathbf{F}^{(i)}(x, y)$ were obtained from finite-element calculations based on the applied voltages and the given geometry. The reconstructed stray-field vectors displayed in Fig. 9.3(d) all point toward the CPW, which reveals a negative potential difference between the CPW and the metallic shield and suggests an accumulation of negative charges (electrons) near the CPW.

To test the validity of the reconstructed stray-field vectors [Fig. 9.3(d)], a fourth potential configuration was explored, for which the field distribution depicted in Fig. 9.3(e) was measured. Comparison of this distribution with the field distribution displayed in Fig. 9.3(f) obtained by adding the measured stray field [Fig. 9.3(d)] and the calculated applied field indicates excellent agreement in the field strength, with deviations of at most 50 mV/cm in the region where the fields could be measured.

9.2 Measurement of microwave electric field mode

The electric-field distribution depicted in Fig. 9.3(c) corresponds to a situation where the stray electric field is almost perfectly compensated over the broad region located above the red dotted line. In this region, $\sqrt{F_{\text{tot},x}^2(x, y) + F_{\text{tot},y}^2(x, y)}$ does not exceed 30 mV/cm after compensation, which corresponds to a reduction by a factor of more than 50 compared to the uncompensated stray-field distribution [Fig. 9.3(d)]. The optimal compensation is a consequence of the electric fields, created from finite potentials V_s and V_c , that point in the same direction as the stray electric fields from the surface.

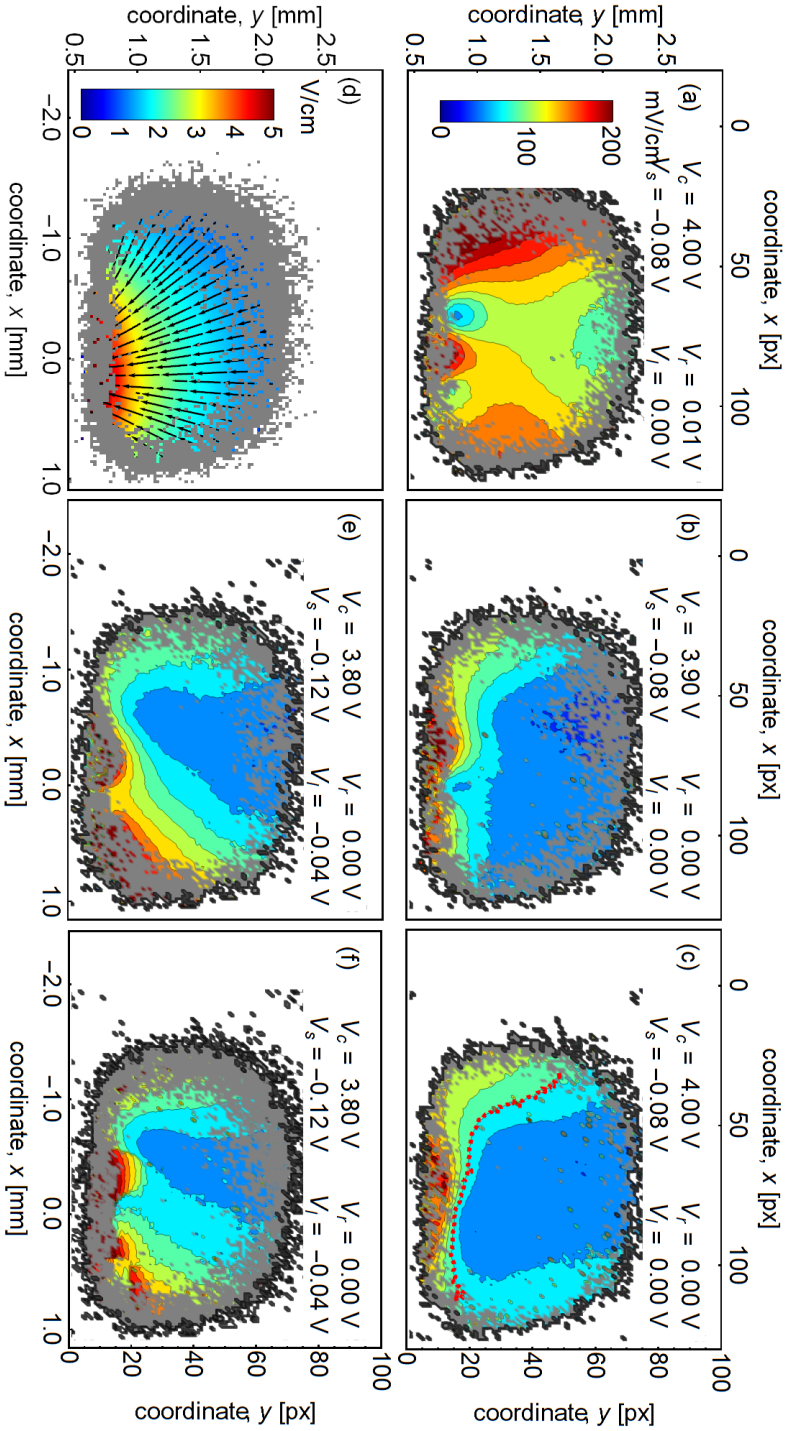


Figure 9.3: (a-c) Distribution of stray-electric-field strengths extracted from Stark shifts measured for the potential configurations defined in each panel. The dotted line in (c) indicates a region of well-compensated stray fields (see text). (d) Electric-stray-field vectors extracted from measurements (a-c). (e) Predicted electric-field distribution as measured in panel (e), see text. Except for panel (d) all color scales are described by the color legend given in (a).

A similar technique, based on measurements of the spatial variation of coherent population transfer, can be used to determine the distribution of the electric-field amplitude $F_\mu(\mathbf{r})$ of the microwave radiation generated by the CPW. Because of the translational invariance of the experimental region along z , the effective rate Ω' with which atoms are transferred from the 34s to the 34p state only varies in the (x, y) -plane and is given by Eq. (7.1) with spatially dependent parameters, i.e.

$$\begin{aligned}\Omega'(x, y) &= \sqrt{(2\pi\Delta(x, y))^2 + (dF^\mu(x, y))^2} \\ &= \sqrt{(2\pi\Delta(x, y))^2 + (s(x, y)\Theta)^2}.\end{aligned}\quad (9.2)$$

In Eq. (9.2), $\Delta(x, y) = \nu - \nu_a(x, y)$ is the detuning of the microwave frequency from the 34s to 34p resonance frequency $\nu_a(x, y)$, as determined from the stray-electric-field measurement, see Eq. (9.1). Because of the isotropy of the 34s state and the small static electric fields, the 34s to 34p transition intensity (dipole moment $d \approx 917ea_0$) does not depend on the polarization of the microwave field. $F^\mu(x, y)$ is determined by measuring $\Omega'(x, y)$ for a well-defined microwave amplitude Θ in the CPW and using the detuning $\Delta(x, y)$, known from the field distribution [see Fig. 9.3(c)]. Using Eq. (9.2), the microwave-field amplitude is determined from the single parameter $s(x, y)$, which scales the microwave amplitude in the CPW to its amplitude at the location (x, y) .

Fig. 9.4(a) presents two measurements of the 34s to 34p population transfer carried out at the positions marked with arrows in Fig. 9.4(b) by varying Θ from 0 V to $\Theta_{\max} \approx 560 \mu\text{V}$ in the center conductor and using a 400-ns-long microwave pulse of frequency 27.966 GHz. Because the stray-field distribution [Fig. 9.3(c)], i.e. the displacement of the 34s to 34p transition $\Delta(x, y)$ is known, $s(x, y)$ can be unambiguously determined using a simple model (black lines) based on Rabi's formula [Eq. (4.8)] using $\Delta t_\mu^{(2)} = 400 \text{ ns}$, i.e.

$$P_{34s}(x, y) = \left[0.5 - p \left(\Delta(x, y), s(x, y)\Theta, \Delta t_\mu^{(2)} \right) \right] \exp^{-\frac{\Theta}{\Theta_0(x, y)}} + 0.5. \quad (9.3)$$

The model accounts for decoherence with an exponential decrease of the Rabi contrast [fitparameter $\Theta_0(x, y)$] to $P_{34s} = 0.5$ with increasing microwave amplitude¹. The model is fitted to every pixel in the image using the fitparameters $s(x, y)$ and $\Theta_0(x, y)$. Therefore, multiplication of $s(x, y)$ with Θ_{\max} results in the microwave field distribution for the maximally applied microwave amplitude [Fig. 9.4(b)]. The large dipole moment of the 34s to 34p transition implies that a

¹We have proven, that this model can be reproduced with a rate equation model of the Rydberg states with the 34p state decaying to a third level, and a dephasing (based on detection) that originates from the finite resolution of the imaging system (not shown).

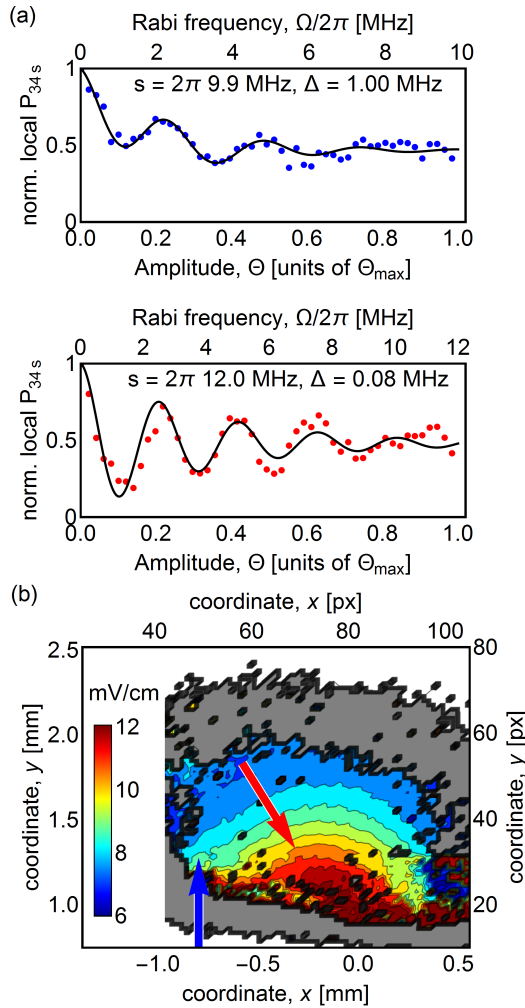


Figure 9.4: (a) Coherent population transfer between the 34s and 34p state as a function of CPW drive amplitude Θ for two spatially selected atom positions marked by the blue and red arrows in (b). The black lines are fits to a simple model, see text. (b) Microwave electric field distribution for Θ_{\max} extracted from the measured distribution of $\Omega'(x, y)$ using Eq. (9.2). The CPW is located at the origin (0, 0).

microwave field amplitude as weak as ~ 1.0 mV/cm suffices to fully transfer the population within 400 ns. The observed contrast for atoms that are close to resonant with the microwave pulse, a population transfer above 80% can be observed [e.g. lower panel in Fig. 9.4(a)].

Overall, the measured microwave field decreases with increasing distance from the CPW, as expected. However, the observed field maximum of the mode

does not exactly lie above the CPW, but $\sim 250 \mu\text{m}$ to its left. Motivated by numerical simulations, this shift could be explained by interfering even and odd modes of the CPW because of different ground potentials of the (super)conducting surfaces with lateral dimensions larger than the microwave wavelength.

9.3 Conclusions

In conclusion, we have presented a technique for measuring distributions of electric-field vectors with a spatial resolution of about $100 \mu\text{m}$ exploiting spatial variations of Rydberg Stark shifts and coherent population transfer in a supersonic beam of helium Rydberg atoms propagating above a cryogenic chip. By measuring several distributions of Stark shifts for the $34s$ to $34p$ transition resulting from different sets of potentials applied to the chip electrodes, the measured stray field could be accurately determined. The stray-field vectors allowed the identification of its source - in our case negative charges accumulating on the insulating surfaces in the vicinity of the CPW - and the determination of optimal potential configurations for stray-field compensation.

A similar technique allowed the measurement of the distribution of microwave amplitudes above the CPW. The reconstructed distribution of microwave field amplitudes did not exactly coincide with the expected mode of a CPW but revealed the effects of other interfering modes. By adding more microwave sources on the chip surface, it should be possible to fully characterize these spurious modes with the same technique as used to determine the stray electric-vector field.

In the absence of multiple microwave sources, the electric microwave-field vectors can also be determined by exploiting transitions that change the magnetic quantum number m of the contributing states. In current experiments, we apply a large, known static electric field that allows to separate the transition from the $(n, l, m) = (35, s, 0)$ to the $(35, p, 0)$ from the transition to the $(35, p, \pm 1)$ state in spectroscopy. The two transitions are driven by the parallel and perpendicular component of the total microwave field with respect to the static electric field, respectively. We apply the afore-mentioned method to determine microwave field strengths to characterize the strength of the two components of the microwave electric field at every position in the atom beam in the crosssection of the atom beam. Hence, it is possible to determine the angle between the electric and microwave field and the microwave field strength distribution [Köpsell and Thiele (2016)].

For experimental setups that are not translationally invariant, it is straightforward to characterize the electric field along the beam propagation axis (z direction). For different start times of the microwave pulse that are applied to the coplanar waveguide, the finite velocity of the atoms in z direction causes the atom cloud

to be localized at different positions along the beam propagation axis at which electric fields can be measured (Sec. 8.1). Also, the methods we presented are not limited to experiments with atomic beams but also applicable, e.g., to experiments using ensembles of ultracold atoms.

The techniques presented in this chapter have several advantages compared to previous works using (Rydberg) atoms to determine electric fields. The data can be acquired rapidly, because only a single spectrum is enough to measure a full 2-dimensional electric field distribution, and a minimal set of 4 spectra characterizes all stray fields. Electric-field distributions are determined on a mm-sized area, limited only by the cross-section of the atomic beam. The spatial resolution of the Rydberg-atom images above the surface is currently limited to $\sim 100 \mu\text{m}$ in both transverse dimensions by the transverse velocity spread of the Rydberg atom beam. Simulations of the electron-trajectories through optimized electron optics in combination with pulsed-field ionization indicate that laser cooling in the transverse dimension to the Doppler limit of $1s^1 2s^1 \ ^3S_1$ helium atoms (0.28 m/s) should enable an improvement of the resolution to $4 \mu\text{m}$. In contrast to other reported techniques, it does not alter the properties of the surface as it only requires low-frequency radiation (no laser radiation) close to the surface, and because of the use of an inert gas that does not adsorb to the surface. Finally, it is compatible with cryogenic temperatures.

Additionally, the spatial selection of atoms in field-free regions paves the way for precision measurements of atoms close to surfaces useful to study Van-der-Waals interactions [*Anderson et al. (1988)*] or surface ionization [*Nordlander and Dunning (1995)*; *Neufeld et al. (2008)*; *Pu and Dunning (2013)*]. Finally, the methods represent an important step toward coupling single Rydberg atoms to microwave photons on a chip.

P A R T III

CONCLUSIONS AND OUTLOOK

CONCLUDING REMARKS

In this thesis, experiments of ensembles of Rydberg atoms close to cryogenic surfaces have been presented. In the experiments, a supersonic beam of metastable $(1s)^1 (2s)^1 \ ^1S_0$ helium atoms was excited out of a supersonic beam to Rydberg states with principal quantum number between $n = 31$ and $n = 35$. The atom beam travelled in vicinity to plain and patterned surfaces and population was coherently transferred between two Rydberg states with large contrast. The coherent population transfer close to surfaces is a key developments when aiming at strong coupling (single) Rydberg atoms and microwave photons in a coplanar microwave resonator. Such a 'hybrid' system is ideal to achieve large atom-photon coupling ratios η , introduced in Ch. 1, and could serve as a quantum memory or a quantum router in a future quantum network. In this chapter, we will summarize the achievements presented in this thesis. For some achievements we present possible future experiments or applications additional or more specific to the ones already presented in the thesis.

A main development was the setup of an experiment optimized to observe coherent population transfer close to cryogenic surfaces. This setup was designed and characterized as discussed in part 1, including discussion of newly developed characterization methods (Ch. 2). Specifically, we have measured the transversal spread of the atomic beam in different parts of the experiment in Ch. 3. We developed a simple characterization method to determine the relative number of atoms, the longitudinal velocity and temperature of *all* possible metastable and Rydberg atom packets that can be generated for a specific valve configuration in a measurement where two parameters are varied only. This technique is not limited specifically to the setup described in this thesis, but can be employed in any atomic or molecular beam experiment, where Rydberg states are excited. Possible applications are, e.g., the fast and thorough characterization of (super)sonic beam expansions from a valve. Alternatively, the technique could be used to control the velocity of the Rydberg atom beam while still maintaining a cold Rydberg atom cloud. For example, in our case, we could vary the velocity of the Rydberg atom beam over a range of 600 m/s around a mean velocity of 2000 m/s with a resolution of 10 m/s. By cooling or heating the atom source, the mean velocity can

be coarsely adjusted. This might find applications in collision experiments, where the kinetic energy of an atom or molecule in a Rydberg state needs to be precisely adjusted with respect to another atom or molecule, with which it interacts.

In Ch. 4 we characterized laser and microwave spectra of Rydberg states in an atom beam of singlet metastable helium, propagating in free-space through the experimental setup. Specifically, in Sec. 4.1, we compared simulated positions and strengths of transitions from the metastable to Rydberg states between $n^* = 28$ to the ionization limit with measurements in almost field-free conditions. We also studied changes to Rydberg spectra of atoms propagating in electric fields. In Sec. 4.2 we exploited the particularly large polarizability of the $ns \leftrightarrow np$ transition of singlet He^* to develop a sensitive measurement method suitable to characterize static (stray and microwave) electric fields along the beam propagation direction. The use of metastable singlet helium to image electric fields in an atomic beam setup is ideal because of several reasons.

1. The noble character and absence of a solid phase of helium in low pressure conditions prohibits a persistent interaction with most surfaces, e.g. by physi- or chemisorption.
2. The sensitivity to magnetic fields is small because of the absence of a permanent spin.
3. The large and small energy differences of the ns and np states of singlet He^* with respect to the manifold of higher l -states allow to drive interband transitions in the microwave regime between low-lying Rydberg states. The large sensitivity of the transition frequencies to electric fields (2 to 3 orders of magnitude more sensitive as transitions between similar states of alkali atoms), the large Inglis-Teller-field of low-lying Rydberg states and the stability of typical microwave frequencies (linewidth ≤ 1 Hz for typical microwave sources) make the $np \rightarrow ns$ transition the ideal candidate to sensitively determine electric fields by Stark-spectroscopy over a large range of electric fields.

In Ch. 5, we described technical aspects of the newly designed experimental setup. The chamber was specifically optimized to minimize adsorption of gas onto the sample surface during and after cooldown of the experiment. Careful optimization of the design of the cryostat including the control lines allowed to reach base temperatures of the sample below 3 K. We expect the developed technique for adsorption-free cooldown to become a necessary tool to be employed in all experiments that manipulate atoms or ions close to cryogenic surfaces that are cooled by a closed-cycle refrigerator. It may also be used to identify residual gases that,

after adsorption, are particularly harmful for the coherence of atoms or ions close to surfaces, because the cooldown procedure can be altered such that a specific gas only adsorbs at the surface.

In Ch. 6 different sample designs were discussed, and in extension of the measurements described in Sec. 4.1, characterized with respect to their stray fields. Specifically, a new sample holder was designed that does not rely on gluing the chip sample into a printed-circuit-board and thus allowed to clean the mounted chip sample by solvents and reactive ion etching (Sec. 6.1.1). We identified thin-film NbTiN as the ideal superconducting material to use in experiments that aim at coupling Rydberg atoms to chip-based microwave resonators, because of its high critical temperature and minimal oxidation layer. Finally, we characterized designs of suitable coplanar resonators taking into account the large kinetic inductance of NbTiN.

Part 2 presents three sets of measurements where coherent population transfer was exploited to study the coherence of Rydberg atoms close to surfaces at cryogenic temperatures. In initial experiments (Ch. 7), we identified a set of challenges (imperfections) that impede coherent population transfer and render a strong coupling of Rydberg atoms to microwave photons in transmission line resonators impossible. With the new setup, we could remove two technical challenges, i.e. we reduced the adsorption of residual gas onto the sample to a negligible amount and we could efficiently detect the populations in the two energetically-close-lying Rydberg states.

The other imperfections were related to electric field inhomogeneities and studied in the other experiments. Specifically, in experiments close to ($250 \mu\text{m}$ above) plain gold surfaces (Ch. 8) we learned how to characterize and efficiently compensate stray electric fields along the beam propagation direction, that emanate from the chip surface. Furthermore, we characterized the strengths and gradients of static and microwave electric fields exploiting coherent population transfer (Rabi oscillations) between Rydberg states. From Rabi and Ramsey measurements at optimal positions, the effect of inhomogeneous static and microwave electric fields on the standard ensemble-decoherence times (T_1 and T_2^*) could be measured as a function of microwave-pulse-atom detuning. We concluded from these measurements, that the coherence of the Rydberg atom cloud is limited by the inhomogeneous character of the static and time-dependent microwave electric fields only. In a future measurement, we can use an up-conversion board to counteract the effect of spatially varying microwave amplitude to perform Ramsey-, and Rabitype measurements where for every position the microwave field strength is adjusted [Köpsell (2014); Köpsell and Thiele (2016)].

Because of the stronger inhomogeneities of microwave and static electric field above a coplanar transmission line, we developed a new and simple technique to

determine stray electric field and microwave field distributions as a tool to first measure and then compensate impeding electric fields (Ch. 9). We also determined that, currently, the most impeding source of decoherence in a strong coupling experiment will be charging of the isolating surfaces of the coplanar waveguide. First measurements indicate, that we can efficiently compensate these stray fields with an electrode configuration that produces fields that match the symmetry of the stray field.

The possible applications of the technique to measure electric field distribution are manifold. For example, one could imagine to build a setup that is specifically designed to measure static and microwave stray electric fields emanating from a chip surface at temperatures down to cryogenic levels. At the end of Ch. 9 we have presented that the possible resolution of such a machine could be as low as $\sim 4 \mu\text{m}$. Unlike in the experiments presented here, the electrodes we use to apply the known static or microwave electric fields do not need to be integrated into the chip surface, but can be positioned on the sample holder. This would release any demands on the chip's design. By rotating the chip within the experiment, it is possible to tomographically reconstruct electric fields that vary over distances that are smaller than the length of the atom pulse in the flight direction of the atomic beam.

Another application could be precision measurements in field-free conditions of Rydberg atoms close to surfaces from which strong electric stray fields emanate. For this, a quadrupole minimum can be generated at a certain distance from the surface. The atoms that are detected in the center of the quadrupole field have not been subject to stray electric fields. As a consequence, small shifts of the resonance, e.g. from a mirror dipole in the surface, could be measured precisely. These shifts could also be examined as a function of the distance of the atoms from the surface, for example by repeating the experiment for different heights of the center of the quadrupole field.

In a next step, we plan to use the results and techniques developed in this thesis to detect Rydberg atoms non-destructively using a superconducting coplanar waveguide as will be discussed in the next chapter.

NON-DESTRUCTIVE DETECTION OF RYDBERG ATOMS USING CHIP-BASED MICROWAVE RESONATORS

In this chapter, we sketch the next experiment that shows the interaction of a Rydberg atom with a quantized light-field in the chip-based microwave resonator. Specifically, we present the necessary steps to perform an experiment which reads out the Rydberg atom state non-destructively by means of the microwave photons in a coplanar waveguide resonator. A non-destructive readout would serve as a proof-of-principle that Rydberg atoms and artificial atoms can be entangled, or that their states can be swapped (Sec. 1.4). As will be shown, this requires an atom beam, which is slower and colder than the one presented in the main part of this thesis, and the propagation direction of which can be controlled precisely. We have set up a suitable source in parallel to the setup presented in this thesis, and the setup and preliminary results are presented shortly in Sec. 10.1.

In Sec. 4.1, it was shown, that we can generate helium atoms in well-defined Rydberg states up to states $n = 75p$. Following the calculations presented in Sec. 1.4, and with the current resonator designs (Sec. 6.1) a Rydberg transition between 70s and $n = 71p$ (~ 18 GHz) can be coupled to a resonator with $g_{\text{Ry}} \approx 2\pi \times 1$ MHz if the atom is positioned at distances smaller than $80 \mu\text{m}$, and with $g_{\text{Ry}} \approx 2\pi \times 0.1$ MHz if the atom is positioned at a distance of $\sim 300 \mu\text{m}$ from the gap of the transmission line. The smallest observed linewidth of our resonators,

so far, is ~ 2 MHz at ~ 20 GHz and $T \approx 3$ K (Sec. 6.2). This is not enough to observe the quantization of the light-field in the resonator by a vacuum-Rabi-mode splitting of $2g_{\text{Ryd}}$ of the vacuum field interacting with a single atom, according to the Jaynes-Cummings interaction [Eq. (1.3)]. Using the enhancement of g_{Ry} by $\sqrt{N_{\text{atoms}}}$, a (moderate) number of $N_{\text{atoms}} \approx 30$ below $80 \mu\text{m}$, or a larger number of $N_{\text{atoms}} \approx 3000$ at a distance of $\sim 300 \mu\text{m}$ would suffice to observe a Rabi-mode splitting. However, as an additional complication, for the current sample temperatures (3 K), the average occupancy per mode at 20 GHz is $n_{\text{th}} \approx 2.7$, given by the Bose-Einstein distribution. For $n_{\text{th}} \geq 1$ and an atom resonant to the cavity, the vacuum Rabi-mode splitting cannot be observed anymore [Fink *et al.* (2010)].

The problem of thermal occupation of the resonator can be overcome if experiments are performed in the dispersive limit of the Jaynes-Cummings Hamiltonian, where the atomic transition is detuned from the resonator frequency, i.e. $|\Delta_{\text{Ry},\mu}| = |\omega_{\text{Ry}} - \omega_{\mu}| \gg g_{\text{Ry}}$, with ω_{Ry} being the frequency of the Rydberg-Rydberg transition, ω_{μ} the transition of the resonator, and g_{Ry} the coupling strength between resonator and atom. In this case, following the notation of Sec. 1.4, the system Hamiltonian is

$$\frac{H_{\text{hy}}^{\text{disp.}}}{\hbar} = \frac{1}{2}\omega_{\text{Ry}}\sigma_{\text{Ry}}^z + \left(\omega_{\mu} + \frac{g_{\text{Ry}}^2}{\Delta_{\text{Ry},\mu}}\sigma_{\text{Ry}}^z \right) \left(a_{\mu}^{\dagger}a_{\mu} + \frac{1}{2} \right), \quad (10.1)$$

which allows a non-destructive detection of the Rydberg atoms via the dispersive shift $\chi \approx g_{\text{Ry}}^2/\Delta_{\text{Ry},\mu}$ of the resonator frequency, the sign of which depends on the state of the Rydberg atom. The dispersive approximation breaks down for resonator occupation numbers larger than the critical photon number in the resonator [Gambetta *et al.* (2006)]

$$n_{\text{crit}} = \frac{\Delta_{\text{Ry},\mu}^2}{4g_{\text{Ry}}^2}. \quad (10.2)$$

For $g_{\text{Ry}} = 2\pi \times 1$ MHz, and $\Delta_{\text{Ry},\mu} = 2\pi \times 10$ MHz, the dispersive shift of a single atom below $80 \mu\text{m}$ is $\chi = 2\pi \times 100$ kHz, whereas the critical photon number is $n_{\text{crit}} = 25$, which is well above $n_{\text{th}} \approx 2.7$.

In an experiment, one would measure the phase response of a critically-coupled resonator ($Q_{\text{int}} \approx 10^4$, Sec. 6.2) to an intentionally applied microwave signal as a function of frequency. The microwave amplitude of the drive signal needs to be low enough that the average occupation number of the resonator $n_{\text{r}} < n_{\text{crit}}$. The maximum change of the phase signal is expected when the frequency of the microwave signal equals the undisturbed resonator frequency. An estimation of the noise at this frequency in the currently used microwave setup indicates that

a signal-to-noise ratio of 10 in the power of the signal can be achieved by averaging over 100 repetitions only, when $n_r = 10 + n_{\text{th}}$. To estimate the noise in the acquisition, the mean photon occupation number for all temperature stages, all signal amplifications of the cold-amplifier and the down-conversion board, and all cable losses of the resonator output to the measurement computer were taken into account [Pozar (2011); Stammeier (2015)]. For the signal we assumed that the atoms at velocity of 1800 m/s interact for $2 \mu\text{s}$ with the cavity field, the amplitude of which changes sinusoidally with the wavelength [compare Sec. 1.1.1 and Eq. (1.6) in Sec. 1.4].

For an experimental repetition rate of $R_{\text{Exp}} = 25 \text{ Hz}$, averaging over 100 repetitions is very promising. However, the following limitations add additional decoherence that was not taken into account in the simple estimation above.

In the present setup, we cannot excite a single atom at a well-defined position. Because of the finite transversal temperature of the metastable atoms after skimmer 2 [expansion angle $\alpha_{\text{max},2} \lesssim 1.15^\circ$, Eq. (3.6)], the dimension of the atom cloud in y -direction (i.e. orthogonal to the sample surface) in the center of zone 2 is $\sim 0.2 \text{ mm}$ in the worst case and only when we assume an optimally focused laser beam (Sec. 4.3.1). In the x -direction, the extension of the Rydberg atom cloud is given by the extension of the metastable atom cloud in the center of zone 2, i.e. $\sim 2 \text{ mm}$. In the flight-direction of the atoms (z -direction), the Rydberg atom cloud extends over a distance $\lesssim 1 \text{ mm}$, because of the longitudinal temperature of the Rydberg atom beam (Sec. 3.2). Additionally, we cannot adjust the beam direction, which is defined by the axis through the centers of the two skimmers (Sec. 3.1), that are tightly connected to the vacuum chamber and the cryostat and cannot be adjusted easily.

The large extension of the atom cloud above the resonator and the limited control over its flight direction imposes the need for static and microwave electric fields, that are homogeneous enough within the volume during which the Rydberg atoms fly within the (assumed) $2\text{-}\mu\text{s}$ -interaction time with the resonator field (compare measurements concerning decoherence in Sec. 8.2 and 8.3). We have shown that static stray electric fields that emanate from plain chip surfaces can be compensated over large distances in z -direction [compare black data points in Fig. 8.1(a)]. We do not need to achieve a homogeneous microwave electric field in the same direction, because the standing wave pattern of the microwave field was taken into account in the estimation of the signal. Concerning the homogeneity of both the microwave and static electric fields in the (x, y) -plane the following limitations are identified:

1. The isolating gaps of the resonator and a (potentially small) layer of oxide on the superconductor can charge up and form strongly inhomogeneous electric fields, to which the singlet state transitions are very sensitive (Sec. 4.2).

We have suggested in Ch. 9, that the negative charging might be caused by secondary electrons created from the high-power Rydberg-excitation laser being absorbed by metallic surfaces. Other measurements (not shown) also indicated, that positive charging can occur when the metastable atoms ionize at the surface, or when other charges that copropagate with the He^* -beam, created in the discharge process, adsorb at the surface. Compensation of these stray electric fields using the current metallic surfaces as electrodes works well at distances that are larger than the transversal dimensions of the transmission line, i.e. $\geq 250 \mu\text{m}$. For smaller distances initial measurements and simulations indicate that it is only possible to compensate the field at up to three separate locations with diameter $\sim 100 \mu\text{m}$. These locations are positioned above the center conductor and above the gaps of the transmission line.

2. From the simulations of the microwave field mode [Fig. 1.8(a) in Sec. 1.4] and the measured microwave field strength (Ch. 9), we conclude that the maximal coupling is achieved only if we position all atoms of the atom cloud closer than $80 \mu\text{m}$, i.e. the size of the gap of the transmission line. At larger distances or for larger atom clouds, the inhomogeneity of the microwave field reduces the average coupling strength of the Rydberg atom.

In the current setup, the lacking possibilities to define the spatial extension of the Rydberg atom cloud and the lack of control over the distribution of stray and microwave electric fields close to the microwave resonator are incompatible with clean experiments in the dispersive regime. To overcome these limitations, on the one hand, we are currently working on a modified chip-design, where we deep-etch the substrate of the transmission line resonator to a depth of $\sim 100 \mu\text{m}$ [Bruno *et al.* (2015)], thus removing insulating material from the surface to reduce charging. On the other hand, we have constructed a new metastable helium source in parallel to the setup presented in this thesis [Thiele *et al.* (2016)]. The new source is optimized for Rydberg-atom experiments close to cryogenic surfaces. Because initial measurements and characterizations are well-described in a number of different master and semestertheses supervised by me [Hambitzer (2012); Gerster (2014); Melchner von Dydiowa (2014); Friese (2014, 2015); Phillip (2015); Möller (2015)], the idea and results are sketched only shortly in the following section.

10.1 An optimized metastable helium source for Rydberg experiments close to cryogenic surfaces

In parallel to the experiments presented in this thesis, we have built a new atom source that is optimized to perform experiments with metastable helium close

to surfaces at cryogenic temperatures [Hambitzer (2012); Gerster (2014); Melchner von Dydiowa (2014); Friese (2014, 2015); Phillip (2015); Möller (2015); Thiele et al. (2016)]. Specifically, we generate a beam of metastable $(1s)^1(2s)^1\ ^3S_1$ helium atoms (called 2^3S_1 or triplet He^* hereafter) at a forward velocity of ~ 900 m/s and with repetition rates of up to 1000 Hz. The metastable triplet beam is then transversally cooled and selectively separated from other species or helium atoms in other states (e.g. ions, ground-, or singlet states) co-propagating with the triplet He^* atoms. The propagation direction of the metastable triplet helium beam can be adjusted and measured precisely. Rydberg excitation is then performed using a two-photon Rydberg excitation with close-to-optical wavelengths with narrow-bandwidth diode-lasers. In Fig. 10.1(a) and (b), we present a sketch and a CAD-drawing of the final setup after combination of the improved source and the setup described in this thesis, respectively. The colored parts correspond to the chambers of the new source and will be discussed sequentially in the following subsections. The parts colored gray correspond to setup parts described in the main part of this thesis and will not be discussed.

10.1.1 A cryogenically cooled, pulsed valve for high repetition rates

The chamber indicated green in Fig. 10.1 contains a new valve for generating a supersonic beam of metastable atoms, developed by A.-J. Agner and H. Schmutz and characterized in Phillip (2015). The operation principle of the valve is similar to the one discussed in Sec. 3.1 and close in design to the valves sold by U. Even [Even et al. (2000); Even (2014); Luria et al. (2009, 2011)]. The duration of the atom pulse is limited to $\sim 19\ \mu\text{s}$ and can be reduced to below $10\ \mu\text{s}$ at variable repetition rates up to $R_{\text{Exp}}^{\text{max}} \approx 1$ kHz. A current pulse applied to a coil opens the valve by pulling a magnetic kernel which is connected to a metallic poppet. The current is triangular shaped with a maximum of 100 A and a potential-difference of 220 V, generated by the homemade valve-driver. The body of the valve is made from copper and is inserted into a bath of liquid nitrogen at a temperature of 77 K. We measure typical longitudinal velocities of the supersonic beam varying between $v_0 \approx 900$ m/s and $v_0 \approx 1120$ m/s, depending on the repetition rate. These velocities correspond to helium-bath temperatures varying between $T_0 \sim 80$ K and $T_0 \sim 120$ K for $R_{\text{Exp}} = 25$ Hz to $R_{\text{Exp}} = 1000$ Hz. For larger repetition rates, T_0 is larger than the temperature of the liquid nitrogen which can be attributed to temperature gradients within the valve-body due to the additional excess heat produced in the coil.

The metastable atoms are excited in a dielectric barrier discharge [Luria et al. (2009, 2011)]. A potential pulse of ~ 4 kV for durations of 100 ns or a pulse exceeding ~ 5 kV for durations of $3\ \mu\text{s}$, generated either by a homebuilt pulser or a

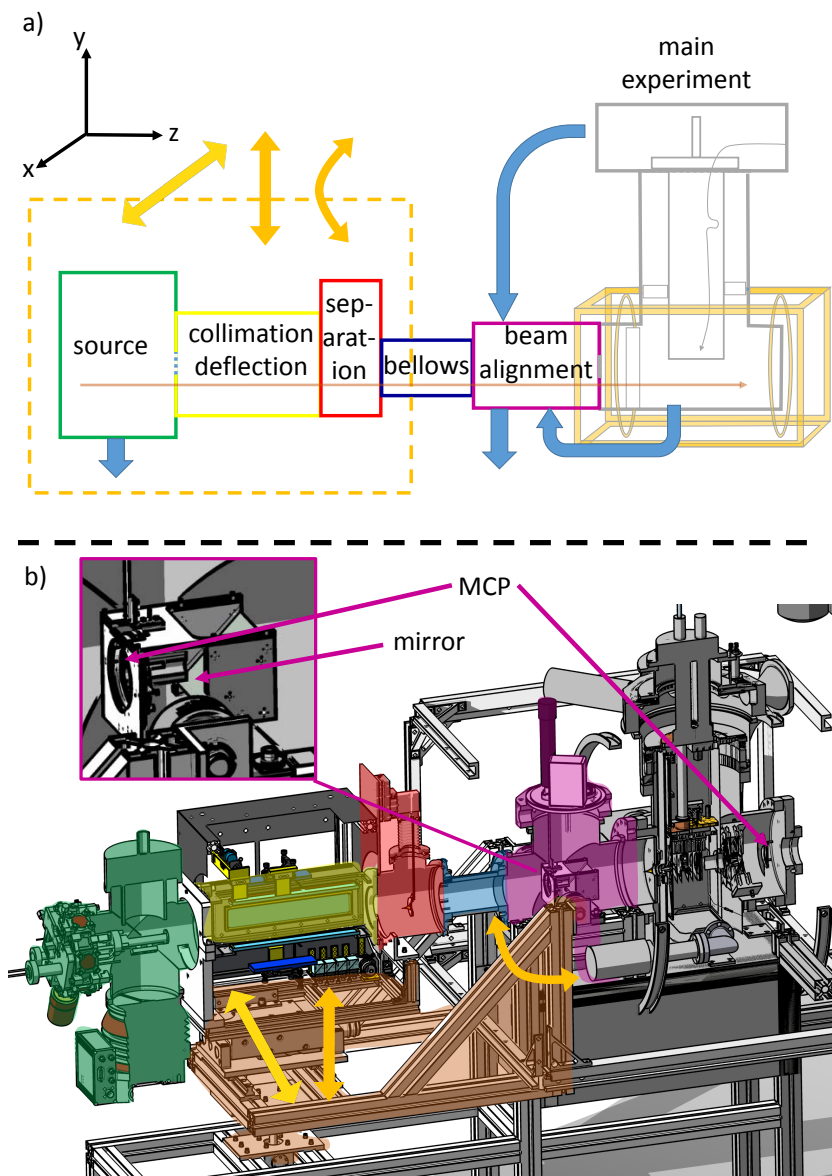


Figure 10.1: (a) Sketch and (b) CAD illustration of the planned combined experimental setup, consisting of the new source setup and the cryostat. The metastable atom beam (brown) is generated in the source chamber (green) and collimated and deflected in the collimation chamber (yellow) after passing a differential pumping stage [dashed, blue in panel (a)]. A movable pinhole in the separation chamber (red) separates the collimated triplet He $(1s)^1(2s)^1\ ^3S_1$ atoms from the singlet He $(1s)^1(2s)^1\ ^1S_0$ and $(1s)^2\ ^1S_0$ states. The three chambers and the beam can be moved in x and y direction and rotated in the $y-z$ plane (orange arrows) with respect to the imaging MCP assembly in the alignment chamber (magenta) that is movable along y direction. With an additional skimmer, the beam then enters experimental chamber of the main setup (gray), discussed in the main part of this thesis.

commercially available push-pull pulser (*BEHLKE: GHTS 60A*), excites the ground-state atoms to the metastable states. The pulse is applied to a circular electrode (diameter ~ 4 mm) that embraces a ceramic channel positioned immediately after the nozzle of the valve. With the homebuilt pulser we observe translational He^* temperatures of $\lesssim 1$ K, because of the short excitation pulse of ~ 100 ns duration. For the excitation with the push-pull pulser, we observe metastable beam temperatures of ~ 3 K. Using the short excitation pulse, we consistently observe smaller number of metastable atoms in the pulse than with the long pulse, which can be explained by the shorter pulse length and by the lower excitation potential. With both pulses we observe a strong decrease in the number of metastable atoms per pulse for repetition rates exceeding ~ 500 Hz, which is attributed to Penning-ionization of the metastable atoms with the background gas during their travel between the valve and the skimmer, positioned 6 cm after the nozzle.

For optimal operation of the new valve, we need to increase the number of atoms per pulse for repetition rates approaching $R_{\text{Exp}} = 1$ kHz. This is possible, for example, by pumping helium more efficiently from the source chamber or by decreasing the gas-load from the nozzle, either by generating even shorter atom-pulses (currently: ~ 10 μs) or by decreasing the diameter of the nozzle (currently: 0.18 mm).

10.1.2 Collimation of metastable 2^3S_1 helium atoms using laser cooling techniques

In the first part of the beam-manipulation chamber indicated yellow in Fig. 10.1, we collimate the metastable 2^3S_1 atoms in the (x, y) -direction using doppler cooling techniques. The technique we use was suggested theoretically [*Aspect et al. (1990)*], employed experimentally [*Simonet (2011)*; *Keller et al. (2014)*], and is explained in detail for our experimental setup in *Hambitzer (2012)* and *Melchner von Dydiowa (2014)*.

Specifically, we use the scattering force to manipulate the external degrees of freedom of the metastable atoms. For this, we use 3% of the output power ($P_{\text{FL}} \approx 2$ W) of a narrow-bandwidth (70 kHz) fiber laser with wavelength $\lambda \approx 1083$ nm. The laser is stabilized to the (cycling) $2^3\text{S}_1 \rightarrow 2^3\text{P}_2$ transition of helium using saturated absorption spectroscopy on triplet He^* in a glass-cell in combination with a Pound-Drever-Hall lock [*Hambitzer (2012)*; *Gerster (2014)*]. To collimate the atomic beam in x -direction, we retro-reflect the laser multiple times in the (x, z) -plane between two mutually inclined mirrors which are slightly tilted by a small angle Θ_m with respect to the beam propagation axis (z -direction). Because the laser beam hitting the mirror in the first place at a finite angle $\Theta_L > \Theta_m > 0$, the angle between retro-reflected instances of the laser beam decreases from $2\Theta_L$ to 0, and the atom and laser beam cross multiple times on a length of ~ 14 cm, see,

e.g., Fig. 3 in *Keller et al. (2014)*. As the laser is resonant with the (doppler-free) atomic transition, only atoms that propagate orthogonal to the laser beam at each intersection point with the atomic beam are pushed by the laser. For a correctly adjusted Θ_L and Θ_m , the laser beam always pushes the atoms with the largest transversal velocity to the center, continually decreasing their transversal velocity until the transversal temperature of the atoms is at the Doppler limit. For the transition we use, the Doppler temperature is $T_{\text{dop}} \approx 39 \mu\text{K}$, corresponding to a transversal velocity of $v_{\perp} = 0.28 \text{ m/s}$. The same procedure is applied for collimation of the atoms in y -direction.

In the experiments described in *Melchner von Dydiowa (2014)*, we observed transversal beam temperatures of $T_{\perp} \approx 1 \text{ mK}$ ($v_{\perp} \approx 1.6 \text{ m/s}$) which corresponds to a full beam divergence of 0.1° for $v_0 = 1800 \text{ m/s}$ for the valve presented in Sec. 3.1, and to a full beam divergence of 0.2° for $v_0 = 900 \text{ m/s}$ of the cooled valve presented above. Recently we could reduce this spread to values $T_{\perp} \lesssim 2T_{\text{dop}}$, which is below the resolution limit of our detection scheme. This was achieved by reduction of the laser power in each direction to about $100I_{\text{sat}} = 17 \text{ mW/cm}^2$ (40% of the initial power of $\sim 60 \text{ mW}$ are lost by fiber-coupling). A transverse temperature of $T_{\perp} = T_{\text{dop}}$ would correspond to a full beam divergence of 0.02° for $v_0 = 1800 \text{ m/s}$ for the valve presented in Sec. 3.1, and to a full beam divergence of 0.04° for $v_0 = 900 \text{ m/s}$ of the cooled valve presented above. Additionally, as a consequence of the collimation, the atom flux is increased. In the experiments described in *Melchner von Dydiowa (2014)*, a ~ 500 -fold increase of the atom flux was observed with respect to the uncollimated beam.

10.1.3 Deflection and separation of metastable 2^3S_1 helium atoms from a supersonic helium beam

A variety of different excitation states of helium are produced during the discharge process. Using the procedure above, only atoms in the triplet 2^3S_1 -state are collimated. All other atoms expand freely by $\alpha_{\text{max},2}$ (Sec. 3.1) and therefore might crash into the sample surface. The states produced most commonly besides the triplet state are singlet metastable states, groundstates and ions in neutral plasmas. Because of the purity of 99.996% of the helium we use, also other gases co-propagate with the atom pulse. Co-propagating ions and residual gases can charge or adsorb at the sample surface, leading to increased stray fields. The large abundance of groundstate atoms in the helium beam can lead to additional turbulences if manipulated with skimmer or razorblades. Therefore, after collimation, we deflect the metastable 2^3S_1 atoms in the y -direction using resonant laser force in the second part of the beam-manipulation chamber indicated yellow in Fig. 10.1 [*Friese (2014)*]. Using a movable skimmer positioned in the chamber in-

indicated red, we can then spatially separate the triplet states from the remaining atoms in the beam [Möller (2015)].

For the deflection, we use the remaining $\sim 97\%$ of the laser power of ~ 2 W, produced by the 1083-nm fiber laser¹ and split it into 4 separate beams. This is achieved by the laser beam passing a set of 3 beam cubes and a mirror [Friese (2014)], the first two of which have splitting ratios of 30 : 70, and the third has a splitting ratio of 50 : 50. The resulting beams have powers varying between 21% and 30% of the initial beam and are directed in negative y -direction through the second part in the collimation chamber over a distance of ~ 8 cm (in z -direction), such that they intersect the atomic beam almost perpendicular in 4 places, see Fig. (3.6) in Friese (2014). The intersection length each time is ~ 1 cm. Similar to the collimation, each laser beam pushes the triplet-state atoms only in the laser beam propagation direction by the resonant optical force. Using the beam cubes and the mirror, the direction of these laser beams can be individually adjusted, such that the 2^3S_1 -state atoms are maximally deflected in negative y -direction. We observe an average deflection for atoms with mean velocity of $v_0 \approx 1700$ m/s of 0.11° per laser beam, i.e. a total deflection of the metastable beam of $\sim 0.45^\circ$ from the original beam propagation direction. This value is smaller than the theoretical maximum of $\sim 1^\circ$, which is expected, since the value of 1° was calculated assuming a beam that constantly pushes the atoms over the full distance of 8 cm. For a beam with $v_0 \approx 900$ m/s, a deflection of $\sim 0.9^\circ$ of the triplet-state atom beam is expected.

A deflection angle of 0.5° or 0.9° is not enough to separate the collimated 2^3S_1 -state beam from the other atoms, because of their expansion with a dispersion angle of $\alpha_{\max,2} = 1.15^\circ$. Therefore, we have installed an additional skimmer ~ 100 mm after the last deflection beam in the separation chamber, indicated red in Fig. 10.1 [Möller (2015)]. The skimmer has a diameter of 2 mm, can be freely moved in the (x, y) -plane, and can therefore be precisely overlapped with the collimated atom beam. At the position of the skimmer, the center of the collimated and uncollimated atom beam have separated by 0.7 mm (for a deflection of 0.5°) because of the slightly different propagation directions due to the deflection. Therefore, the two beams (maximal diameter 2 mm) the skimmer extracts from the collimated and uncollimated beam overlap spatially at the position of the skimmer, but are fully separated after the free propagation of ~ 0.5 m [Friese (2014); Möller (2015)] and when they reach the skimmer on the 3-K state of the cryostat of the main experiment (Sec. 5.2). Consequently, the skimmer at the 3-K stage of the cryostat extracts only the metastable triplet states, whereas atoms from the uncollimated atom beam do not enter the electrode stack. We have observed, that the

¹The remaining 3% are used for collimation.

presence of the skimmer heats the transversal direction of the atomic beam from $v_{\perp} \approx 0.4$ m/s to ~ 0.8 m/s.

We detect the propagation direction and the position of the collimated, deflected metastable triplet-state atom beam using two imaging microchannel-plate detector assemblies (Sec. 4.3.3.1), one is positioned in the center of the alignment chamber (indicated magenta in Fig. 10.1) and the other being the detector used in the main setup. The detector in the alignment chamber can be moved in and out of the atomic beam with a translation-stage. The phosphor screen is imaged by a CCD-camera orthogonal to the beam propagation direction using a mirror positioned at an angle of 45° [Künzli (2015)]. To control the position in the (x, y) -plane and the propagation direction in the (y, z) -plane of the metastable triplet helium beam after collimation and separation, a beam-alignment system was built by Jonas Kuenzli [Künzli (2015)]. It allows to move the part of the vacuum chamber consisting of the source chamber, the collimation-and-deflection chamber and the separation-chamber with respect to the fixed position of the alignment chamber and the experimental chamber. The orientation of these vacuum-chamber parts determine the position and the propagation direction of the 2^3S_1 -state atoms and are connected to the main setup using a flexible bellows (indicated blue in Fig. 10.1). As a result, the atom beam can be moved with respect to the cryostat (and the sample surface) by ± 15 mm in the (x, y) -plane with a resolution below 0.1 mm, and can be rotated by an angle of $\pm 2^{\circ}$ in the (y, z) -plane, i.e. with respect to the surface, with a resolution of 0.05° .

10.1.4 Important properties and two-photon excitation of 2^3S_1 helium

We excite the metastable triplet atoms to Rydberg states using a resonant, two-photon transition with two spatially overlapped, narrow-bandwidth (~ 200 kHz) lasers of fixed (389 nm) and variable ($\lesssim 790$ nm) wavelengths, respectively [Lancuba and Hogan (2013); Friese (2015)]. The laser radiation with wavelength 389 nm is generated from an amplified, frequency-doubled, continuous-wave (cw) diode laser, locked to the $2^3S_1 \rightarrow 3^3P_2$ transition using saturated absorption spectroscopy and the Pound-Drever-Hall locking scheme. The laser with wavelength ~ 790 nm is generated from an amplified, continuous-wave (cw) diode laser that is running freely. It is used to excite the atoms from the 3^3P_2 state to ns or nd -Rydberg states varying between $n \approx 25$ to the ionization limit. Because of the cw-operation of the lasers, the available excitation intensities (maximal laser powers: ~ 0.5 W and ~ 1.6 W for the blue and red laser, respectively) are smaller than for the dye-laser system (Sec. 4.3.1), and the transitions can only be saturated for quantum numbers $n \lesssim 40$ if both lasers are focused to ~ 0.1 mm. We control the length of the two-photon excitation pulse using an acousto-optic deflector (400 MHz) in the blue laser beam, which has a (measured) rise time of 15 ns (limited by the

bandwidth of the detector) in which the signal increases from 10% to 90% of its final value (specified risetime ~ 5.5 ns).

The properties of the Rydberg states of triplet helium are different to the Rydberg states of singlet helium. Two of them will be discussed in the following. On the one hand, the quantum defects for the s and p Rydberg-states of triplet helium are $\delta_s^{\text{He}}, \delta_p^{\text{He}} \approx 1.3, 1.07$ [Drake (1999)] (instead of $\delta_s^{\text{He}}, \delta_p^{\text{He}} \approx 1.13, 0.98$ for the singlet state). Therefore, both the s and p state lie below the next lower Rydberg manifold and have smaller polarizabilities α_s^3, α_p^3 . From diagonalization of the single-particle Stark Hamiltonian [Zimmerman *et al.* (1979)], we conclude that the intraband transition of the triplet $ns \rightarrow np$ transition has a polarizability difference of $\Delta\alpha^{(3)} = \alpha_s^{(3)} - \alpha_p^{(3)} = -n^{*7} 1.8 \times 10^{-9}$ MHz/(V/cm)², which is more than a magnitude smaller than the polarizability difference for the singlet state ($\Delta\alpha^{(1)} = \alpha_s^{(1)} - \alpha_p^{(1)} = n^{*7} 25.26 \times 10^{-9}$ MHz/(V/cm)²) [Friese (2015)]. On the other hand, the lifetime of the p state of helium is much longer in the case of triplet helium than for singlet helium [Theodosiou (1984)]. In fact, where the lifetimes of the s-states for singlet and triplet helium are almost identical, the lifetime of the p-state in triplet helium is almost twice as long as the s-state lifetime. The decay rate of the p-state of singlet helium is dominated by the decay to the (low-lying) $(1s)^2 \ ^1S_0$ ground state of helium, whereas in the case of triplet helium, it is dominated (because of the spin) by the transitions to the $(1s)^1(2s)^1 \ ^3S_1$ metastable state that lies about 20 eV above the ground state of helium. As the decay rate of a state is proportional to the cube of the energy-difference of the dominating decay channel (Eq. (1.13)), the lifetime of the (singlet) p-state is therefore smaller.

10.1.5 Conclusions

The new setup should allow to perform the experiments presented in the introduction to this chapter, because of different advantages of the new source which we will discuss in the following.

The smaller velocity of the new metastable atom beam ($v_0 \approx 900$ m/s versus 1800 m/s) has two positive effects. On the one hand, it doubles the interaction time of the Rydberg atoms with the resonator, which provides more measurement time and larger achievable signal-to-noise ratio within the same measurement time. On the other hand, slower atoms are less subject to decoherence because of static and microwave electric fields varying along the flight-direction (z -direction). The longitudinally colder metastable atom beam (≤ 1 K versus ≥ 7 K) reduces longitudinal dispersion of the metastable and of the excited Rydberg atom packet, i.e. the size of the Rydberg atom packet in z -direction in the center of zone 2 will be reduced. Finally, the larger repetition rates (1 kHz versus 25 Hz) also help to increase the signal-to-noise ratio within a fixed measurement time.

The collimation reduces the divergence of the metastable and Rydberg atom beam from $\alpha_{\max,2} = 1.15^\circ$ to a measured divergence of 0.1° , with the potential to reduce it to 0.02° . A divergence of 0.1° causes the Rydberg atom to expand in the (x, y) -plane from the excitation in zone 1 to the center of 2 by $20 \mu\text{m}$, a divergence of 0.02° by $4 \mu\text{m}$. Both values are smaller than the field-free regions that can already be generated by biasing the metallic planes available in the experimental region (Ch. 9). Furthermore, the density of metastable atoms at the excitation spot is being increased by collimation, because of the minimized expansion in transversal directions due to the collimation. Because of the finite longitudinal temperature of the metastable atom beam, however, the increase in density is reduced again by the longitudinal dispersion of the metastable atom packet due to the longer flight time of the metastable atoms from the source to the Rydberg excitation because of the collimation chamber.

The deflection of the metastable triplet atom beam together with its separation from the other atoms produces a (clean) beam of metastable atoms in triplet states. This minimizes adsorption of residual gas onto, or charging of the surface from residual gases in the helium beam and ions that are produced in the discharge process. Additionally, the precise control over the position and direction of the collimated atom beam allows to certify that only a small amount of metastable or Rydberg atoms hit the surface.

As seen above, the triplet states are less sensitive to electric fields, and we can expect better coherence than for singlet states (for otherwise similar parameters). Additionally, the metastable states are not subject to radiative decay even for low- n -states ($n \leq 40$) and for typical durations of the experiments ($\leq 5 \mu\text{s}$). Finally, the two-photon-excitation can be used to define Rydberg atom packets that have lateral dimensions on the order of $\sim 50 \mu\text{m}$ when they intersect in the excitation (zone 1) at an angle, i.e. they are not perfectly overlapped. This is because both Rydberg excitation lasers are fiber-coupled, i.e. the laser modes occupy gaussian TEM_{00} -modes that can be optimally focused to mode waists $\leq 50 \mu\text{m}$, and the excitation to Rydberg states is only efficient at location where the two laser beams cross. Also, the use of Rydberg excitation lasers with wavelengths in the visible region and smaller powers reduce the creation of secondary electrons when hitting a metallic surface.

BIBLIOGRAPHY

- Affolderbach C, Du G, Bandi T, Horsley A, Treutlein P and Mileti G. 'Imaging Microwave and DC Magnetic Fields in a Vapor-Cell Rb Atomic Clock'. arXiv:1505.07739 (2015) (p. 196)
- Ahn C, Doherty A C and Landahl A J. 'Continuous quantum error correction via quantum feedback control'. Phys. Rev. A **65**, 042301 (2002) (p. 23)
- Allmendinger P, Agner J A, Schmutz H and Merkt F. 'Deceleration and trapping of a fast supersonic beam of metastable helium atoms with a 44-electrode chip decelerator'. Phys. Rev. A **88**, 043433 (2013) (pp. 43 and 49)
- Allmendinger P, Deiglmayr J, Agner J A, Schmutz H and Merkt F. 'Surface-electrode decelerator and deflector for Rydberg atoms and molecules'. Phys. Rev. A **90**, 043403 (2014) (p. 49)
- Altaisky M V, Zolnikova N N, Kaputkina N E, Krylov V A, Lozovik Y E and Dattani N S. 'Towards a feasible implementation of quantum neural networks using quantum dots'. arXiv:1503.05125 (2015) (p. 24)
- Alton D. *Interacting single atoms with nanophotonics for chip-integrated quantum networks*. Ph.D. thesis, CalTech (2013) (pp. 9 and 12)
- Alton D J, Stern N P, Aoki T, Lee H, Ostby E, Vahala K J and Kimble H J. 'Strong interactions of single atoms and photons near a dielectric boundary'. Nature Physics **7**, 159 (2011) (pp. 18 and 22)
- Anderson A, Haroche S, Hinds E A, Jhe W and Meschede D. 'Measuring the van der Waals forces between a Rydberg atom and a metallic surface'. Phys. Rev. A **37**, 3594 (1988) (pp. 13 and 212)
- Andrews R W, Peterson R W, Purdy T P, Cicak K, Simmonds R W, Regal C A and Lehnert K W. 'Bidirectional and efficient conversion between microwave and optical light'. Nature Physics **10**, 321 (2014) (p. 25)

- Aoki T, Dayan B, Wilcut E, Bowen W P, Parkins A S, Kippenberg T J, Vahala K J and Kimble H J. 'Observation of strong coupling between one atom and a monolithic microresonator'. *Nature* **443(7112)**, 671 (2006) (pp. 3, 18, and 22)
- Aoki T, Takahashi G, Kajiya T, Yoshikawa J i, Braunstein S L, van Loock P and Furusawa A. 'Quantum error correction beyond qubits'. *Nat. Phys.* **5**, 541 (2009) (p. 23)
- Arnoldus H F and George T F. 'Spontaneous decay and atomic fluorescence near a metal surface or an absorbing dielectric'. *Phys. Rev. A* **37**, 761 (1988) (p. 35)
- Aspect A, Dalibard J and Roger G. 'Experimental Test of Bell's Inequalities Using Time-Varying Analyzers'. *Phys. Rev. Lett.* **49**, 1804 (1982) (p. 2)
- Aspect A, Vansteenkiste N, Kaiser R, Haberland H and Karrais M. 'Preparation of a pure intense beam of metastable helium by laser cooling'. *Chemical Physics* **145**, 307 (1990) (p. 225)
- Authinarayanant A and Dudding R W. 'Changes in Secondary Electron Yield from Reduced Lead Glasses'. *Adv. Electron. Electron Phys.* **40A**, 167 (1976) (p. 95)
- Baglin V. 'Cold/sticky systems'. Tech. rep., CERN, Geneva, Switzerland (2001) (p. 132)
- Balmer J J. 'Notiz ueber die Spektrallinien des Wasserstoffs'. *Annalen der Physik* **261**, 80 (1885) (p. 2)
- Barends R, Kelly J, Megrant A, Veitia A, Sank D, Jeffrey E, White T C, Mutus J, Fowler A G, Campbell B, Chen Y, Chen Z, Chiaro B, Dunsworth A, Neill C, O'Malley P, Roushan P, Vainsencher A, Wenner J, Korotkov A N, Cleland A N and Martinis J M. 'Superconducting quantum circuits at the surface code threshold for fault tolerance'. *Nature* **508**, 500 (2014) (p. 24)
- Barends R, Lamata L, Kelly J, García-Álvarez L, Fowler A G, Megrant A, Jeffrey E, White T C, Sank D, Mutus J Y, Campbell B, Chen Y, Chen Z, Chiaro B, Dunsworth A, Hoi I C, Neill C, O'Malley P J J, Quintana C, Roushan P, Vainsencher A, Wenner J, Solano E and Martinis J M. 'Digital quantum simulation of fermionic models with a superconducting circuit'. arXiv:1501.07703 (2015) (p. 23)
- Barends R, Vercruyssen N, Endo A, de Visser P J, Zijlstra T, Klapwijk T M and Baselmans J J A. 'Reduced frequency noise in superconducting resonators'. *Appl. Phys. Lett.* **97**, 033507 (2010) (p. 203)

- Barmettler R. *Characterization of Overcoupled NbTiN Microwave Resonators up to 40 GHz*. Master's thesis, ETH Zurich (2012) (pp. 36, 163, 170, 171, and 172)
- Barreiro J T, Bancal J D, Schindler P, Nigg D, Hennrich M, Monz T, Gisin N and Blatt R. 'Demonstration of genuine multipartite entanglement with device-independent witnesses'. *Nat. Phys.* **9**, 559 (2013) (p. 21)
- Barrett M, Chiaverini J, Schaetz T, Britton J, Itano W, Jost J, Knill E, Langer C, Leibfried D, Ozeri R and Wineland D. 'Deterministic quantum teleportation of atomic qubits'. *Nature* **429**, 737 (2004) (p. 27)
- Bartkiewicz K, Beran J c v, Lemr K, Norek M and Miranowicz A. 'Quantifying entanglement of a two-qubit system via measurable and invariant moments of its partially transposed density matrix'. *Phys. Rev. A* **91**, 022323 (2015) (p. 21)
- Barzanjeh S, Milburn G J, Vitali D and Tombesi P. 'Optical Single Photons on Demand Teleported from Microwave Cavities'. arXiv:1205.6461 (2012) (p. 25)
- Barzanjeh S, Vitali D, Tombesi P and Milburn G J. 'Entangling optical and microwave cavity modes by means of a nanomechanical resonator'. *Phys. Rev. A* **84**, 042342 (2011) (p. 25)
- Beaudoin F, Gambetta J M and Blais A. 'Dissipation and Ultrastrong Coupling in Circuit QED'. ArXiv e-prints (2011) (p. 21)
- Bell J S. 'On the Einstein Podolsky Rosen Paradox'. *Physics (N. Y.)* **1**, 195 (1964) (p. 2)
- Bernardot F, Nussenzevig P, Brune M, Raimond J M and Haroche S. 'Vacuum Rabi splitting observed on a microscopic atomic sample in a microwave cavity'. *Europhys. Lett.* **17**, 33 (1992) (p. 13)
- Berry D W, Ahokas G, Cleve R and Sanders B C. 'Efficient Quantum Algorithms for Simulating Sparse Hamiltonians'. *Commun. Math. Phys.* **270**, 359 (2007) (p. 21)
- Beth T and Leuchs G (eds.). *Quantum Information Processing*. Wiley (2005) (p. 6)
- Bier K and Hagena O. 'Supersonic beam expansion'. *Rarefied Gas Dynamics 4th Symposium, Academic Press, New York* **2**, 260 (1966) (p. 52)
- Blais A, Gambetta J, Wallraff A, Schuster D I, Girvin S M, Devoret M H and Schoelkopf R J. 'Quantum-information processing with circuit quantum electrodynamics'. *Phys. Rev. A* **75**, 032329 (2007) (p. 30)

- Blais A, Huang R S, Wallraff A, Girvin S M and Schoelkopf R J. 'Cavity quantum electrodynamics for superconducting electrical circuits: An architecture for quantum computation'. *Phys. Rev. A* **69**, 062320 (2004) (pp. 3, 20, 22, 32, and 33)
- Böhi P, Riedel M F, Haensch T W, and Treutlein P. 'Imaging of microwave fields using ultracold atoms'. *Appl. Phys. Lett.* **97**, 051101 (2010) (p. 28)
- Böhi P and Treutlein P. 'Simple microwave field imaging technique using hot atomic vapor cells'. *Appl. Phys. Lett.* **101**, 181107 (2012) (p. 28)
- Bohr N. 'On the Constitution of Atoms and Molecules'. *Philos. Mag.* **26** (1913) (p. 1)
- Bourassa J, Gambetta J M, A A Abdumalikov J, Astafiev O, Nakamura Y and Blais A. 'Ultrastrong coupling regime of cavity QED with phase-biased flux qubits'. *Phys. Rev. A* **80**, 032109 (2009) (p. 12)
- Bravyi S B and Kitaev A Y. 'Quantum codes on a lattice with boundary'. *ArXiv* 9811052 (1998) (p. 24)
- Brennecke F, Donner T, Ritter S, Bourdel T, Kohl M and Esslinger T. 'Cavity QED with a Bose-Einstein condensate'. *Nature* **450**, 268 (2007) (p. 18)
- Brion E, Carlier F, Akulin V M and Mølmer K. 'Quantum repeater with Rydberg-blocked atomic ensembles in fiber-coupled cavities'. *Phys. Rev. A* **85**, 042324 (2012) (p. 27)
- Browaeys A. *Piégeage magnétique d'un gaz d'Hélium métastable: vers la condensation de Bose-Einstein*. Ph.D. thesis, Université de Paris VI (2002) (p. 49)
- Brune M, Nussenzveig P, Schmidt-Kaler F, Bernardot F, Maali A, Raimond J M and Haroche S. 'From Lamb shift to light shifts: Vacuum and subphoton cavity fields measured by atomic phase sensitive detection'. *Phys. Rev. Lett.* **72**, 3339 (1994) (p. 175)
- Brune M, Schmidt-Kaler F, Maali A, Dreyer J, Hagley E, Raimond J M and Haroche S. 'Quantum Rabi Oscillation: A Direct Test of Field Quantization in a Cavity'. *Phys. Rev. Lett.* **76**, 1800 (1996) (pp. 3 and 175)
- Bruno A, de Lange G, Asaad S, van der Enden K L, Langford N K and DiCarlo L. 'Reducing intrinsic loss in superconducting resonators by surface treatment and deep etching of silicon substrates'. *Applied Physics Letters* **106** (2015) (p. 222)

- Brutschy B and Haberland H. 'A high-intensity beam of metastable helium atoms with good velocity resolution'. *Journal of Physics E: Scientific Instruments* **10**, 90 (1977) (p. 56)
- Buck J J. *Cavity QED in Microspheres and Fabry-Perot Cavities*. Ph.D. thesis, Cal-Tech (2003) (pp. 12, 18, and 22)
- Buluta I and Nori F. 'Quantum Simulators'. *Science* **326**, 108 (2009) (p. 175)
- Bussi eres F, Clausen C, Tiranov A, Korzh B, Verma V B, Nam S W, Marsili F, Ferrier A, Goldner P, Herrmann H, Silberhorn C, Sohler W, Afzelius M and Gisin N. 'Quantum teleportation from a telecom-wavelength photon to a solid-state quantum memory'. *Nat. Photon.* **8**, 775 (2014) (p. 25)
- Carter J D, Cherry O and Martin J D D. 'Electric-field sensing near the surface microstructure of an atom chip using cold Rydberg atoms'. *Phys. Rev. A* **86**, 053401 (2012) (pp. 155, 175, 182, 202, and 203)
- Carter J D and Martin J D D. 'Energy shifts of Rydberg atoms due to patch fields near metal surfaces'. *Phys. Rev. A* **83**, 032902 (2011) (pp. 155, 175, 179, and 202)
- . 'Coherent manipulation of cold Rydberg atoms near the surface of an atom chip'. *Phys. Rev. A* **88**, 043429 (2013) (p. 175)
- Chan K S, Siercke M, Hufnagel C and Dumke R. 'Adsorbate Electric Fields on a Cryogenic Atom Chip'. arXiv:1312.5868 (2013) (p. 176)
- . 'Adsorbate Electric Fields on a Cryogenic Atom Chip'. *Phys. Rev. Lett.* **112**, 026101 (2014) (p. 202)
- Chiesa A, Santini P, Gerace D, Raftery J, Houck A A and Carretta S. 'Digital quantum simulators in a scalable architecture of hybrid spin-photon qubits'. arXiv:1504.05667 (2015) (p. 23)
- Chiggiato P. 'Coatings, Chemistry and Surfaces'. Tech. rep., CERN (2006) (p. 134)
- Childress L and Hanson R. 'Diamond NV centers for quantum computing and quantum networks'. *MRS Bulletin* **38**, 134 (2013) (p. 24)
- Childs A M and Chuang I L. 'Universal quantum computation with two-level trapped ions'. *Phys. Rev. A* **63**, 012306 (2000) (p. 23)
- Chuang I L, Vandersypen L M K, Zhou X, Leung D W and Lloyd S. 'Experimental realization of a quantum algorithm'. *Nature* **393**, 143 (1998) (p. 23)

- Chupka W A. 'Factors affecting lifetimes and resolution of Rydberg states observed in zero-electron-kinetic-energy spectroscopy'. *J. Chem. Phys.* **98** (1993) (p. 71)
- Cirac J I, Zoller P, Kimble H J and Mabuchi H. 'Quantum State Transfer and Entanglement Distribution among Distant Nodes in a Quantum Network'. *Phys. Rev. Lett.* **78**, 3221 (1997) (p. 24)
- Clader B D. 'Quantum networking of microwave photons using optical fibers'. *Phys. Rev. A* **90**, 012324 (2014) (p. 25)
- Class for Physics of the Royal Swedish Academy of Sciences. 'Measuring and Manipulating Individual Quantum Systems'. The Royal Swedish Academy of Sciences **The Nobel Prize in Physics 2012** (2012) (p. 3)
- Comparat D and Pillet P. 'Dipole blockade in a cold Rydberg atomic sample [Invited]'. *JOSA B* **27**, A208 (2010) (p. 175)
- Compton A H. 'A Quantum Theory of the Scattering of X-rays by Light Elements'. *Phys. Rev.* **21**, 483 (1923) (p. 1)
- Corcoles A, Magesan E, Srinivasan S J, Cross A W, Steffen M, Gambetta J M and Chow J M. 'Demonstration of a quantum error detection code using a square lattice of four superconducting qubits'. *Nat Commun* **6**, (2015) (p. 24)
- Crisafulli O, Tezak N, Soh D B S, Armen M A and Mabuchi H. 'Squeezed light in an optical parametric oscillator network with coherent feedback quantum control'. arXiv:1305.2239 (2013) (p. 24)
- Damburg R J and Kolosov V V. 'A hydrogen atom in a uniform electric field III'. *J. Phys. B: Atom. Molec. Phys.* **12**, 16 (1979) (p. 70)
- de Broglie L. *Recherches sur la théorie des Quanta*. Ph.D. thesis, Université Paris-Sorbonne (1924) (p. 1)
- De Michielis M, Ferraro E, Fanciulli M and Prati E. 'Universal Set of Quantum Gates for Double-Dot Exchange-Only Spin Qubits with Intradot Coupling'. arXiv:1404.2423 (2014) (p. 23)
- DeKock R L and Gray H B. *Chemical structure and bonding*. University Science Books (1989) (p. 135)
- Dennis E, Kitaev A, Landahl A and Preskill J. 'Topological quantum memory'. *Journal of Mathematical Physics* **43**, 4452 (2002) (p. 24)

- Devoret M and Schoelkopf R J. 'Superconducting Circuits for Quantum Information: An Outlook'. *Science* **339**, 1169 (2013) (pp. 21 and 22)
- DiCarlo L, Chow J M, Gambetta J M, Bishop L S, Johnson B R, Schuster D I, Majer J, Blais A, Frunzio L, Girvin S M and Schoelkopf R J. 'Demonstration of two-qubit algorithms with a superconducting quantum processor'. *Nature* **460**, 240 (2009) (p. 23)
- DiCarlo L, Reed M D, Sun L, Johnson B R, Chow J M, Gambetta J M, Frunzio L, Girvin S M, Devoret M H and Schoelkopf R J. 'Preparation and measurement of three-qubit entanglement in a superconducting circuit'. *Nature* **467**, 574 (2010) (p. 21)
- Dicke R H. 'Coherence in Spontaneous Radiation Processes'. *Phys. Rev.* **93**, 99 (1954) (p. 18)
- DiVincenzo D P. 'The Physical Implementation of Quantum Computation'. *Fortschritte der Physik* **48**, 771 (2000) (p. 23)
- . 'Fault-tolerant architectures for superconducting qubits'. *Phys. Scr.* **2009**, 014020 (2009) (p. 24)
- Drake G W F. 'High Precision Theory of Atomic Helium'. *Phys. Scr.* **83** (1999) (pp. 14, 16, 71, 73, 77, 202, and 229)
- Drexhage K H. *Progress in Optics* **XII**, 163 (1974) (p. 10)
- Drndic M, Johnson K S, Thywissen J H, Prentiss M and Westervelt R M. 'Micro-electromagnets for atom manipulation'. *Appl. Phys. Lett.* **5**, 2906 (1998) (p. 28)
- Dürst Y, Wilm B J, Dietrich B E, Vannesjo S J, Barmet C, Schmid T, Brunner D O and Prüssmann K P. 'Real-time feedback for spatiotemporal field stabilization in MR systems'. *Magnetic Resonance in Medicine* **73**, 884 (2015) (p. 144)
- Dutra S M and Knight P L. 'Spontaneous emission in a planar Fabry-Perot micro-cavity'. *Phys. Rev. A* **53**, 5, 3587 (1996) (pp. 9 and 11)
- Einstein A. 'On a heuristic viewpoint concerning the production and transformation of light'. *Ann. Phys.* **17**, 132 (1905) (p. 1)
- Einstein A, Podolsky B and Rosen N. 'Can Quantum-Mechanical Description of Physical Reality Be Considered Complete?' *Phys. Rev.* **47**, 777 (1935) (p. 2)

- Even U. 'Pulsed Supersonic Beams from High Pressure Source: Simulation Results and Experimental Measurements'. *Advances in Chemistry* **2014**, 636042 (2014) (pp. 49 and 223)
- Even U, Jortner J, Noy D, Lavie N and Cossart-Magos C. 'Cooling of large molecules below 1 K and He clusters formation'. *J. Chem. Phys.* **112**, 8068 (2000) (pp. 49 and 223)
- Fan H Q, Kumar S, Daschner R, Kübler H and Shaffer J P. 'Sub-wavelength microwave electric field imaging using Rydberg atoms inside atomic vapor cells'. arXiv:1403.3596 (2014) (p. 202)
- Fedorov A, Steffen L, Baur M, da Silva M P and Wallraff A. 'Implementation of a Toffoli gate with superconducting circuits'. *Nature* **481**, 170 (2012) (p. 23)
- Fink J M, Steffen L, Studer P, Bishop L S, Baur M, Bianchetti R, Bozyigit D, Lang C, Filipp S, Leek P J and Wallraff A. 'Quantum-To-Classical Transition in Cavity Quantum Electrodynamics'. *Phys. Rev. Lett.* **105**, 163601 (2010) (p. 220)
- Foletti S, Bluhm H, Mahalu D, Umansky V and Yacoby A. 'Universal quantum control of two-electron spin quantum bits using dynamic nuclear polarization'. *Nat. Phys.* **advance online publication** (2009) (p. 23)
- Forn-Díaz P, Lisenfeld J, Marcos D, García-Ripoll J J, Solano E, Harmans C J P M and Mooij J E. 'Observation of the Bloch-Siegert Shift in a Qubit-Oscillator System in the Ultrastrong Coupling Regime'. *Phys. Rev. Lett.* **105**, 237001 (2010) (p. 21)
- Fortagh J, Grossmann A, Zimmermann C and Hänsch T W. 'Miniaturized Wire Trap for Neutral Atoms'. *Phys. Rev. Lett.* **81**, 5310 (1998) (p. 28)
- Fortágh J, Ott H, Kraft S, Günther A and Zimmermann C. 'Surface effects in magnetic microtraps'. *Phys. Rev. A* **66**, 041604 (2002) (p. 28)
- Fowler A G, Mariantoni M, Martinis J M and Cleland A N. 'Surface codes: Towards practical large-scale quantum computation'. *Phys. Rev. A* **86**, 032324 (2012) (p. 24)
- Fowler A G and Martinis J M. 'Quantifying the effects of local many-qubit errors and nonlocal two-qubit errors on the surface code'. *Phys. Rev. A* **89**, 032316 (2014) (p. 24)
- Fowler A G, Stephens A M and Groszkowski P. 'High-threshold universal quantum computation on the surface code'. *Phys. Rev. A* **80**, 052312 (2009) (p. 24)

- Friese D. *Deflection of metastable Helium via Laser light*. Master's thesis, ETH Zurich (2014) (pp. 37, 222, 223, 226, and 227)
- . *Towards Continuous wave Rydberg Excitation for 2 3S1 Helium*. Master's thesis, ETH Zurich (2015) (pp. 37, 96, 222, 223, 228, and 229)
- Fuwa M, Toba S, Takeda S, Marek P, Mišta L, Filip R, van Loock P, Yoshikawa J i and Furusawa A. 'Noiseless Conditional Teleportation of a Single Photon'. *Phys. Rev. Lett.* **113**, 223602 (2014) (p. 27)
- Gabrielse G and Dehmelt H. 'Observation of inhibited spontaneous emission'. *Phys. Rev. Lett.* **55**, 67 (1985) (p. 10)
- Gallagher T F. *Rydberg Atoms*. Cambridge University Press (1994) (pp. 14, 15, 16, 69, 70, 71, 73, and 92)
- Gambetta J, Blais A, Schuster D I, Wallraff A, Frunzio L, Majer J, Devoret M H, Girvin S M and Schoelkopf R J. 'Qubit-photon interactions in a cavity: Measurement-induced dephasing and number splitting'. *Phys. Rev. A* **74**, 042318 (2006) (p. 220)
- Gao W B, Imamoglu A, Bernien H and Hanson R. 'Coherent manipulation, measurement and entanglement of individual solid-state spins using optical fields'. *Nat Photon* **9**, 363 (2015) (p. 24)
- Gerster L. *Metastable Helium Source*. Master's thesis, ETH Zürich (2014) (pp. 37, 53, 54, 55, 222, 223, and 225)
- Gilowski M, Wendrich T, Müller T, Jentsch C, Ertmer W, Rasel E M and Schleich W P. 'Gauss Sum Factorization with Cold Atoms'. *Phys. Rev. Lett.* **100**, 030201 (2008) (p. 21)
- Gisin N, Ribordy G, Tittel W and Zbinden H. 'Quantum cryptography'. *Rev. Mod. Phys.* **74**, 145 (2002) (p. 3)
- Gleyzes S, Kuhr S, Guerlin C, Bernu J, Deleglise S, Busk Hoff U, Brune M, Raimond J M and Haroche S. 'Quantum jumps of light recording the birth and death of a photon in a cavity'. *Nature* **446**, 297 (2007) (pp. 13, 18, 22, and 175)
- Goban A, Choi K S, Alton D J, Ding D, Lacroûte C, Pototschnig M, Thiele T, Stern N P and Kimble H J. 'Demonstration of a State-Insensitive, Compensated Nanofiber Trap'. *Phys. Rev. Lett.* **109**, 033603 (2012) (pp. 18, 22, and 28)
- Goban A, Hung C L, Yu S P, Hood J, Muniz J, Lee J, Martin M, McClung A, Choi K, Chang D, Painter O and Kimble H. 'Atom-light interactions in photonic crystals'. *Nature Communications* **5**, 3808 (2014) (pp. 18, 22, and 28)

- Goblot V. *Realization of an Active Magnetic Field Compensation*. Master's thesis, ETH Zürich (2014) (pp. 37, 103, 141, 142, 143, 144, 145, and 146)
- Göppl M, Fragner A, Baur M, Bianchetti R, Filipp S, Fink J M, Leek P J, Puebla G, Steffen L and Wallraff A. 'Coplanar Waveguide Resonators for Circuit Quantum Electrodynamics'. *J. Appl. Phys.* **104**, 113904 (2008) (pp. 164, 165, and 170)
- Goy P, Raimond J M, Gross M and Haroche S. 'Observation of Cavity-Enhanced Single-Atom Spontaneous Emission'. *Phys. Rev. Lett.* **50**, 1903 (1983) (pp. 10 and 11)
- Goy P, Raimond J M, Vitrant G and Haroche S. 'Millimeter-wave spectroscopy in cesium Rydberg states. Quantum defects, fine- and hyperfine-structure measurements'. *Phys. Rev. A* **26**, 2733 (1982) (pp. 14 and 16)
- Graham T M, Bernstein H J, Wei T, Junge M and Kwiat P G. 'SuperDense Teleportation using Hyperentangled Photons'. arXiv:1505.05615 (2015) (p. 27)
- Grover L K. 'A fast quantum mechanical algorithm for database search'. In *Proceedings of the twenty-eighth annual ACM symposium on Theory of computing*, 212–219. ACM, Philadelphia, Pennsylvania, United States (1996) (p. 23)
- Guerlin C, Bernu J, Deleglise S, Sayrin C, Gleyzes S, Kuhr S, Brune M, Raimond J M and Haroche S. 'Progressive field-state collapse and quantum non-demolition photon counting'. *Nature* **448**, 889 (2007) (pp. 13, 18, and 22)
- Gunter G, Anappara A A, Hees J, Sell A, Biasiol G, Sorba L, De Liberato S, Ciuti C, Tredicucci A, Leitenstorfer A and Huber R. 'Sub-cycle switch-on of ultrastrong light-matter interaction'. *Nature* **458**, 178 (2009) (p. 21)
- Haas A E. 'Über die elektrodynamische Bedeutung des Planck'schen Strahlungsgesetzes und über eine neue Bestimmung des elektrischen Elementarquantums und der Dimension des Wasserstoffatoms'. *Akademie der Wissenschaften Wien, Abt. IIa* **Bd. 119**, 119 (1910) (p. 1)
- Hafezi M, Kim Z, Rolston S L, Orozco L A, Lev B L and Taylor J M. 'Atomic interface between microwave and optical photons'. *Phys. Rev. A* **85**, 020302 (2012) (p. 25)
- Hagley E, Maitra X, Nogues G, Wunderlich C, Brune M, Raimond J M and Haroche S. 'Generation of Einstein-Podolsky-Rosen Pairs of Atoms'. *Phys. Rev. Lett.* **79**, 1 (1997) (p. 13)

- Halfmann T, Koensgen J and Bergmann K. 'A source for a high-intensity pulsed beam of metastable helium atoms'. *Meas. Sci. Technol.* **11**, 1510 (2000) (pp. 44, 48, 49, 54, and 56)
- Hambitzer A. *Design of a metastable helium source*. Master's thesis, ETH Zürich (2012) (pp. 37, 222, 223, and 225)
- Haroche S. 'Nobel Lecture: Controlling photons in a box and exploring the quantum to classical boundary'. *Rev. Mod. Phys.* **85**, 1083 (2013) (pp. 13, 18, and 22)
- Haroche S and Raimond J M. *Exploring the Quantum: Atoms, Cavities, and Photons*. Oxford University Press, New York, USA (2006) (pp. 7, 11, and 175)
- Harty T P, Allcock D T C, Ballance C J, Guidoni L, Janacek H A, Linke N M, Stacey D N and Lucas D M. 'High-Fidelity Preparation, Gates, Memory, and Readout of a Trapped-Ion Quantum Bit'. *Phys. Rev. Lett.* **113**, 220501 (2014) (p. 25)
- Hasegawa Y, Nakamura D, Murata M, Yamamoto H and Komine T. 'High-precision temperature control and stabilization using a cryocooler'. *Review of Scientific Instruments* **81**, 094901 (2010) (p. 138)
- Hattermann H, Mack M, Karlewski F, Jessen F, Cano D and Fortágh J. 'Detrimental adsorbate fields in experiments with cold Rydberg gases near surfaces'. *Phys. Rev. A* **86**, 022511 (2012) (pp. 155, 175, and 202)
- Heidemann R, Raitzsch U, Bendkowsky V, Butscher B, Low R, Santos L and Pfau T. 'Evidence for Coherent Collective Rydberg Excitation in the Strong Blockade Regime'. *Phys. Rev. Lett.* **99**, 163601 (2007) (p. 27)
- Heisenberg W. 'Über den anschaulichen Inhalt der quantentheoretischen Kinetik und Mechanik'. *Zeitschrift fuer Physik* **34**, Nr. 3, 172 (1927) (p. 2)
- Hennessy K, Badolato A, Winger M, Gerace D, Atature M, Gulde S, Falt S, Hu E L and Imamoglu A. 'Quantum nature of a strongly coupled single quantum dot-cavity system'. *Nature* **445**, 896 (2007) (pp. 19, 20, and 22)
- Hermann-Avigliano C, Teixeira R C, Nguyen T L, Cantat-Moltrecht T, Nogues G, Dotsenko I, Gleyzes S, Raimond J M, Haroche S and Brune M. 'Long coherence times for Rydberg qubits on a superconducting atom chip'. *Phys. Rev. A* **90**, 040502 (2014) (p. 202)

- Hogan S D, Agner J A, Merkt F, Thiele T, Filipp S and Wallraff A. 'Driving Rydberg-Rydberg Transitions from a Coplanar Microwave Waveguide'. *Phys. Rev. Lett.* **108**, 063004 (2012a) (pp. 38, 113, 155, 163, 176, 177, 179, 180, and 202)
- Hogan S D, Allmendinger P, Saßmannshausen H, Schmutz H and Merkt F. 'Surface-Electrode Rydberg-Stark Decelerator'. *Phys. Rev. Lett.* **108**, 063008 (2012b) (pp. 43 and 49)
- Hogan S D and Merkt F. 'Demonstration of Three-Dimensional Electrostatic Trapping of State-Selected Rydberg Atoms'. *Phys. Rev. Lett.* **100**, 043001 (2008) (p. 49)
- Hogan S D, Motsch M and Merkt F. 'Deceleration of supersonic beams using inhomogeneous electric and magnetic fields'. *Phys. Chem. Chem. Phys.* **13**, 18705 (2011) (p. 49)
- Hogan S D, Seiler C and Merkt F. 'Rydberg-State-Enabled Deceleration and Trapping of Cold Molecules'. *Phys. Rev. Lett.* **103**, 123001 (2009) (p. 49)
- Hogan S D, Wiederkehr A W, Andrist M, Schmutz H and Merkt F. 'Slow beams of atomic hydrogen by multistage Zeeman deceleration'. *Journal of Physics B* **41**, 081005 (2008) (p. 49)
- Holloway C L, Gordon J A, Schwarzkopf A, Anderson D A, Miller S A, Thaicharoen N and Raithel G. 'Sub-wavelength imaging and field mapping via electromagnetically induced transparency and Autler-Townes splitting in Rydberg atoms'. *Appl. Phys. Lett.* **104**, 244102 (2014) (p. 202)
- Hood C J, Lynn T W, Doherty A C, Parkins A S and Kimble H J. 'The Atom-Cavity Microscope: Single Atoms Bound in Orbit by Single Photons'. *Science* **287**, 1447 (2000) (pp. 12, 18, 20, and 22)
- Hua M, Tao M J and Deng F G. 'Fast universal quantum gates on microwave photons with all-resonance operations in circuit QED'. *Sci. Rep.* **5** (2015) (p. 23)
- Hulet R G, Hilfer E S and Kleppner D. 'Inhibited Spontaneous Emission by a Rydberg Atom'. *Phys. Rev. Lett.* **55**, 2137 (1985) (p. 10)
- Jaksch D, Cirac J I, Zoller P, Rolston S L, Côté R and Lukin M D. 'Fast Quantum Gates for Neutral Atoms'. *Phys. Rev. Lett.* **85**, 2208 (2000) (p. 175)
- Jaynes E and Cummings F. 'Comparison of quantum and semiclassical radiation theories with application to the beam maser'. *Proceedings of the IEEE* **51**, 89 (1963) (p. 5)

- Jin J, Saglamyurek E, Puigibert M I G, Verma V B, Marsili F, Nam S W, Oblak D and Tittel W. 'A telecom-wavelength atomic quantum memory in optical fiber for heralded polarization qubits'. arXiv:1506.04431 (2015) (p. 27)
- Jobez P, Laplane C, Timoney N, Gisin N, Ferrier A, Goldner P and Afzelius M. 'Coherent Spin Control at the Quantum Level in an Ensemble-Based Optical Memory'. *Phys. Rev. Lett.* **114**, 230502 (2015) (pp. 25 and 27)
- Jobez P, Usmani I, Timoney N, Laplane C, Gisin N and Afzelius M. 'Cavity-enhanced storage in an optical spin-wave memory'. arXiv:1404.3489 (2014) (p. 25)
- Jones L A, Carter J D and Martin J D D. 'Rydberg atoms with a reduced sensitivity to dc and low-frequency electric fields'. arXiv:1301.4170 (2013) (pp. 176 and 202)
- Julsgaard B, Sherson J, Cirac J I, Fiurasek J and Polzik E S. 'Experimental demonstration of quantum memory for light'. *Nature* **432**, 482 (2004) (p. 27)
- Kapit E. 'Universal two-qubit interactions, measurement and cooling for quantum simulation and computing'. arXiv:1502.02684 (2015) (p. 23)
- Keller M, Kotyrba M, Leupold F, Singh M, Ebner M and Zeilinger A. 'Bose-Einstein condensate of metastable helium for quantum correlation experiments'. *Phys. Rev. A* **90**, 063607 (2014) (pp. 225 and 226)
- Kiktenko E O, Fedorov A K, Strakhov A A and Moko V I. 'Single qudit realization of the Deutsch algorithm using superconducting many-level quantum circuits'. arXiv:1503.01583 (2015) (p. 21)
- Kimble H J. 'Strong interactions of single atoms and photons in cavity QED'. *Physica Scripta* **T76**, 127 (1998) (pp. 3, 9, 10, 18, and 22)
- . 'The quantum internet'. *Nature* **453**, 1023 (2008) (pp. 3 and 24)
- Kishimoto N, Nagamine M, Inami K, Enari Y and Ohshima T. 'Lifetime of MCP - PMT'. *Nuclear Instruments and methods in Physics Research A* **564**, 204 (2006) (p. 95)
- Kleppner D. 'Inhibited Spontaneous Emission'. *Phys. Rev. Lett.* **47**, 233 (1981) (pp. 10 and 11)

- Kogelnik H and Li T. 'Laser beams and resonators'. Proceedings of the IEEE **54(10)**, 1312 (1966) (p. 8)
- Könz M. *Design, Build-up and Control of Electronic Equipment for the Hybrid Rydberg Experiment*. Master's thesis, ETH Zurich (2014) (pp. 37 and 147)
- Köpsell J. *Up conversion board for amplitude and phase controlled microwave pulses on the 3-26.5 Ghz scale*. Master's thesis, Eth Zürich (2014) (pp. 37, 149, and 217)
- Köpsell J and Thiele T. 'Measurement of angle between DC and microwave electric fields in free-space'. (in preparation) (2016) (pp. 38, 83, 149, 211, and 217)
- Kotyrbá M. *Metastable-Helium-4 Source For Cold Atom Experiments*. Master's thesis, Universität Wien (2010) (pp. 49, 51, 52, and 53)
- Krüger P, Andersson L M, Wildermuth S, Hofferberth S, Haller E, Aigner S, Groth S, Bar-Joseph I and Schmiedmayer J. 'Potential roughness near lithographically fabricated atom chips'. Phys. Rev. A **76**, 063621 (2007) (p. 28)
- Kübler H, Shaffer J P, Baluktsian T, Löw R and Pfau T. 'Coherent excitation of Rydberg atoms in micrometre-sized atomic vapour cells'. Nat. Photon. **4**, 112 (2010) (pp. 27 and 175)
- Kuhn A, Hennrich M and Rempe G. 'Deterministic Single-Photon Source for Distributed Quantum Networking'. Phys. Rev. Lett. **89**, 067901 (2002) (p. 24)
- Künzli J. 'Documentation: Helium Source Alignment System'. Tech. rep., ETH Zürich (2015) (p. 228)
- Kurizki G, Bertet P, Kubob Y, Mølmer K, Petrosyan D, Rabl P and Schmiedmayer J. 'Quantum technologies with hybrid systems'. PNAS **112**, 3866 (2015) (pp. 3, 18, 25, 26, 27, 28, 29, 30, 32, and 35)
- Ladd T D, Jelezko F, Laflamme R, Nakamura Y, Monroe C and O'Brien J L. 'Quantum computers'. Nature **464**, 45 (2010) (p. 21)
- Lamb W E and Retherford R. 'Fine Structure of the Hydrogen Atom by a Microwave Method'. Phys. Rev. **72**, 241 (1947) (p. 2)
- Lancuba P and Hogan S D. 'Guiding Rydberg atoms above surface-based transmission lines'. Phys. Rev. A **88**, 043427 (2013) (pp. 43 and 228)

- Lanyon B P, Hempel C, Nigg D, Müller M, Gerritsma R, Zähringer F, Schindler P, Barreiro J T, Rambach M, Kirchmair G, Hennrich M, Zoller P, Blatt R and Roos C F. 'Universal Digital Quantum Simulation with Trapped Ions'. *Science* **334**, 57 (2011) (p. 23)
- Lanyon B P, Weinhold T J, Langford N K, Barbieri M, James D F V, Gilchrist A and White A G. 'Experimental Demonstration of a Compiled Version of Shor's Algorithm with Quantum Entanglement'. *Phys. Rev. Lett.* **99**, 250505 (2007) (p. 23)
- Las Heras U, Mezzacapo A, Lamata L, Filipp S, Wallraff A and Solano E. 'Digital Quantum Simulation of Spin Systems in Superconducting Circuits'. *Phys. Rev. Lett.* **112**, 200501 (2014) (p. 23)
- Lett P D, Watts R N, Westbrook C I, Phillips W D, Gould P L and Metcalf H J. 'Observation of Atoms Laser Cooled below the Doppler Limit'. *Phys. Rev. Lett* **61**, 169 (1988) (p. 60)
- Leung V Y F, Tauschinsky A, van Druten N J and Spreew R J C. 'Microtrap arrays on magnetic film atom chips for quantum information science'. arXiv:1104.3067v1 [quant-ph] (2011) (p. 175)
- Li L, O D Y and A K. 'Entanglement between light and an optical atomic excitation'. *Nature* **498**, 466 (2013) (p. 24)
- Li W and Lesanovsky I. 'Entangling quantum gate in trapped ions via Rydberg blockade'. arXiv:1306.5953 (2013) (p. 24)
- Lindblad G. 'On the Generators of Quantum Dynamical Semigroups'. *Commun. Math. Phys.* **48**, 119 (1976) (p. 199)
- Lloyd S, Garnerone S and Zanardi P. 'Quantum algorithms for topological and geometric analysis of big data'. arXiv:1408.3106 (2014) (p. 23)
- Lu C Y, Browne D E, Yang T and Pan J W. 'Demonstration of a Compiled Version of Shor's Quantum Factoring Algorithm Using Photonic Qubits'. *Phys. Rev. Lett.* **99**, 250504 (2007) (p. 23)
- Lu H, Liu C, Wang D S, Chen L K, Li Z D, Yao X C, Li L, Liu N L, Peng C Z, Sanders B C, Chen Y A and Pan J W. 'Universal digital photonic single-qubit quantum channel simulator'. arXiv:1505.02879 (2015) (p. 23)
- Lukin M D, Fleischhauer M, Cote R, Duan L M, Jaksch D, Cirac J I and Zoller P. 'Dipole Blockade and Quantum Information Processing in Mesoscopic Atomic Ensembles'. *Phys. Rev. Lett.* **87**, 037901 (2001) (p. 175)

- Luria K, Christen W and Even U. 'Generation and Propagation of Intense Supersonic Beams'. *Journal of Physical Chemistry* **115**, 7362 (2011) (pp. 49, 54, and 223)
- Luria K, Lavie N and Even U. 'Dielectric barrier discharge source for supersonic beams'. *Review of Scientific Instruments* **80**, 104102 (2009) (pp. 49 and 223)
- Lüthi F. *Active Magnetic Field Compensation*. Master's thesis, ETH Zurich (2013) (pp. 37, 140, 142, 143, and 144)
- Ma X S, Herbst T, Scheidl T, Wang D, Kropatschek S, Naylor W, Wittmann B, Mech A, Kofler J, Anisimova E, Makarov V, Jennewein T, Ursin R and Zeilinger A. 'Quantum teleportation over 143 kilometres using active feed-forward'. *Nature* **489**, 269 (2012) (p. 27)
- Marquardt E, Le J and Radebaugh R. 'Cryogenic Material Properties Database Cryogenic Material Properties Database'. Tech. rep., NIST (2000) (p. 128)
- Martin-Lopez E, Laing A, Lawson T, Alvarez R and O'Brien J L. 'Experimental realization of Shor's quantum factoring algorithm using qubit recycling'. *Nat. Photon.* **6**, 773 (2012) (p. 23)
- Marx S. *Realization of Temperature and Vibration Measurement Systems for Hybrid Cavity QED Experiments*. Master's thesis, ETH Zurich (2010) (pp. 127 and 128)
- Maxwell D, Szwed D J, Paredes-Barato D, Busche H, Pritchard J D, Gauguier A, Jones M P A and Adams C S. 'Microwave control of the interaction between two optical photons'. *Phys. Rev. A* **89**, 043827 (2014) (p. 25)
- Maxwell J C. 'A dynamical theory of the electromagnetic field'. *Phil. Trans. R. Soc. Lond.* **155**, 459 (1865) (p. 1)
- Melchner von Dydiowa M. *Collimation of metastable triplet state helium atoms using laser cooling techniques*. Master's thesis, ETH Zürich (2014) (pp. 37, 107, 222, 223, 225, and 226)
- Mergenthaler M. *Temperature Stabilization of a Cu-Sample-Holder on the 4 K-Stage of a Pulse Tube Cooler*. Master's thesis, ETH Zurich (2012) (pp. 37, 138, and 139)
- Merkt F and Zare R N. 'On the lifetimes of Rydberg states probed by delayed pulsed field ionization'. *Journal of Chemical Physics* **101**, 3495 (1994) (p. 71)

- Mezzacapo A, Casanova J, Lamata L and Solano E. ‘Digital Quantum Simulation of the Holstein Model in Trapped Ions’. *Phys. Rev. Lett.* **109**, 200501 (2012) (p. 23)
- Mezzacapo A, Las Heras U, Pedernales J S, DiCarlo L, Solano E and Lamata L. ‘Digital Quantum Rabi and Dicke Models in Superconducting Circuits’. *Sci. Rep.* **4**, 7482 (2014) (p. 23)
- Michelberger P S, Champion T F M, Sprague M R, Kaczmarek K T, Barbieri M, Jin X M, England D G, Kolthammer W S, Saunders D J, Nunn J and Walmsley I A. ‘Interfacing GHz-bandwidth heralded single photons with a room-temperature Raman quantum memory’. arXiv:1405.1470 (2014) (p. 25)
- Mikelsons G, Cohen I, Retzker A and Plenio M B. ‘Universal Set of Gates for Microwave Dressed-State Quantum Computing’. arXiv:1410.6720 (2014) (p. 23)
- Möller L. *Isolating a cold beam of metastable triplet helium states*. Master’s thesis, ETH Zürich (2015) (pp. 37, 222, 223, and 227)
- Morse M D. ‘Supersonic Beam Sources’. *ExMPS Vol. 29B* (1996) (pp. 49, 51, and 53)
- Müller M, Lesanovsky I, Weimer H, Büchler H P and Zoller P. ‘Mesoscopic Rydberg Gate Based on Electromagnetically Induced Transparency’. *Phys. Rev. Lett.* **102**, 170502 (2009) (p. 175)
- Nakamura Y, Terai H, Inomata K, Yamamoto T, Qiu W and Wang Z. ‘Superconducting qubits consisting of epitaxially grown NbN/AlN/NbN Josephson junctions’. *Appl. Phys. Lett.* **99**, 212502 (2011) (p. 138)
- Neufeld D D, Dunham H R, Wethekam S, Lancaster J C and Dunning F B. ‘Ionization of xenon Rydberg atoms at Au(111) surfaces: Effect of stray fields’. *Phys. Rev. B* **78**, 115423 (2008) (p. 212)
- Nielsen M A and Chuang I L. *Quantum Computation and Quantum Information*. Cambridge University Press (2000) (p. 3)
- Niemczyk T, Deppe F, Huebl H, Menzel E P, Hocke F, Schwarz M J, Garcia-Ripoll J J, Zueco D, Hümmer T, Solano E, Marx A and Gross R. ‘Circuit quantum electrodynamics in the ultrastrong-coupling regime’. *Nat. Phys.* **6**, 772 (2010) (p. 21)
- NIST. ‘NIST Atomic Spectra Database’. Website (2015) (p. 68)
- Nordlander P and Dunning F B. ‘Interaction of Rydberg atoms with a metal surface in the presence of an external electric field’. *Phys. Rev. B* **53**, 8083 (1995) (p. 212)

- . ‘Interaction of Rydberg atoms with a metal surface in the presence of an external electric field’. *Phys. Rev. B* **53**, 8083 (1996) (p. 175)
- Northup T E and Blatt R. ‘Quantum information transfer using photons’. *Nat Photon* **8**, 356 (2014) (p. 24)
- Obrecht J M, Wild R J and Cornell E A. ‘Measuring electric fields from surface contaminants with neutral atoms’. *Phys. Rev. A* **75**, 062903 (2007) (p. 175)
- O’Brien C, Lauk N, Blum S, Morigi G and Fleischhauer M. ‘Interfacing Superconducting Qubits and Telecom Photons via a Rare-Earth Doped Crystal’. arXiv:1402.5405 (2014) (p. 25)
- Ospelkaus C, Langer C E, Amini J M, Brown K R, Leibfried D and Wineland D J. ‘Trapped-ion quantum logic gates based on oscillating magnetic fields’. *Phys. Rev. Lett.* **101** (2008) (pp. 28 and 202)
- Osterwalder A and Merkt F. ‘Using High Rydberg States as Electric Field Sensors’. *Phys. Rev. Lett.* **82**, 1831 (1999) (pp. 80 and 205)
- Palittapongarnpim P. *Characterization of Magneto-optical Trap For Experiments in Light-Atom Interfacing*. Master’s thesis, Calgary (2012) (p. 60)
- Patton K R and Fischer U R. ‘Ultrafast Quantum Random Access Memory Utilizing Single Rydberg Atoms in a Bose-Einstein Condensate’. *Phys. Rev. Lett.* **111**, 240504 (2013) (p. 175)
- Pellizzari T. ‘Quantum Networking with Optical Fibres’. *Phys. Rev. Lett.* **79**, 5242 (1997) (p. 24)
- Petrosyan D, Bensky G, Kurizki G, Mazets I, Majer J and Schmiedmayer J. ‘Reversible state transfer between superconducting qubits and atomic ensembles’. *Phys. Rev. A* **79**, 040304 (2009) (pp. 28, 29, 32, 175, and 202)
- Petrosyan D and Fleischhauer M. ‘Quantum Information Processing with Single Photons and Atomic Ensembles in Microwave Coplanar Waveguide Resonators’. *Phys. Rev. Lett.* **100**, 170501 (2008) (pp. 18, 25, 28, 29, 175, and 202)
- Pfaff W, Hensen B J, Bernien H, van Dam S B, Blok M S, Taminiiau T H, Tiggelman M J, Schouten R N, Markham M, Twitchen D J and Hanson R. ‘Unconditional quantum teleportation between distant solid-state quantum bits’. *Science* **345**, 532 (2014) (p. 24)

- Phillip M T. *Characterization of a cold metastable helium source with a dielectric barrier discharge*. Master's thesis, ETH Zuerich (2015) (pp. 37, 222, and 223)
- Photonis. 'Chevron MCP and Detector Initial Start-up and Electrical Test Procedure'. Tech. rep., Photonis (2009) (p. 96)
- Pirandola S, Eisert J, Weedbrook C, Furusawa A and Braunstein S L. 'Advances in quantum teleportation'. *Nat Photon* **9**, 641 (2015) (p. 26)
- Planck M. 'Über irreversible Strahlungsvorgänge'. *Ann. Phys.* **306**, 69 (1900) (p. 1)
- . 'Über das Gesetz der Energieverteilung im Normalspectrum'. *Ann. Phys.* **309**, 553 (1901) (p. 1)
- Pohl T, Adams C S and Sadephpour H R. 'Cold Rydberg gases and ultra-cold plasmas'. *Journal of Physics B* **44**, 180201 (2011) (p. 175)
- Politi A, Matthews J C F and O'Brien J L. 'Shor's Quantum Factoring Algorithm on a Photonic Chip'. *Science* **325**, 1221 (2009) (p. 23)
- Pozar D M. *Microwave Engineering*. John Wiley & Sons, Inc., 4th ed. edn. (2011) (p. 221)
- Pritchard J. *Cooperative Optical Non-linearity in a blockaded Rydberg ensemble*. Ph.D. thesis, University of Durham (2011) (p. 80)
- Pu Y and Dunning F B. 'Ionization of Rydberg atoms at patterned electrode arrays'. *Phys. Rev. A* **88**, 012901 (2013) (pp. 175 and 212)
- Purcell E M. 'Spontaneous Emission Probabilities at Radio Frequencies'. *Phys. Rev.* **69**, 681 (1946) (p. 11)
- Rafac R J, Tanner C E, Livingston A E and Berry H G. 'Fast-beam laser lifetime measurements of the cesium $6p^2P_{1/2,3/2}$ states'. *Phys. Rev. A* **60**, 3648 (1999) (p. 7)
- Raimond J M, Brune M and Haroche S. 'Manipulating quantum entanglement with atoms and photons in a cavity'. *Rev. Mod. Phys.* **73**, 565 (2001) (pp. 20, 21, 22, and 35)
- Reed M D, DiCarlo L, Nigg S E, Sun L, Frunzio L, Girvin S M and Schoelkopf R J. 'Realization of three-qubit quantum error correction with superconducting circuits'. *Nature* **482**, 382 (2012) (p. 23)
- Reichel J and Vuletić V (eds.). *Atom Chips*. Wiley-VCH (2011) (p. 28)

- Reim K. 'Documentation on down-conversion-board to frequencies up to 26.5 GHz'. Tech. rep., ETH Zürich (2011) (p. 149)
- Reiserer A, Kalb N, Rempe G and Ritter S. 'A quantum gate between a flying optical photon and a single trapped atom'. *Nature* **508**, 237 (2014) (p. 27)
- Rempe G, Schmidt-Kaler F and Walther H. 'Observation of sub-Poissonian photon statistics in a micromaser'. *Phys. Rev. Lett.* **64**, 2783 (1990) (p. 10)
- Ristè D, Poletto S, Huang M Z, Bruno A, Vesterinen V, Saira O P and DiCarlo L. 'Detecting bit-flip errors in a logical qubit using stabilizer measurements'. *Nat Commun* **6**, 6983 (2015) (p. 24)
- Ritter S, Nolleke C, Hahn C, Reiserer A, Neuzner A, Uphoff M, Mücke M, Figueroa E, Bochmann J and Rempe G. 'An elementary quantum network of single atoms in optical cavities'. *Nature* **484**, 195 (2012) (pp. 24 and 27)
- Rothe E W, Neynaber R H and Trujillo S M. 'Velocity Dependence of the Total Cross Section for the Scattering of Metastable He(3S1) by Helium, Argon, and Krypton'. *J Chem Phys* **3310**, 42 (1965) (p. 49)
- Ruffieux S. *Towards cavity QED experiments with Rydberg atoms coupled to a 3D microwave cavity*. Master's thesis, ETH Zürich (2014) (p. 149)
- Rutherford E. 'The scattering of alpha and beta particles by matter and the structure of the atom'. *Philosophical Magazine* **21**, 669 (1911) (p. 1)
- Rydberg J R. 'On the structure of the line-spectra of the chemical elements'. *Philosophical Magazine* **5**, 331 (1890) (p. 2)
- Saffman M, Walker T G and Mølmer K. 'Quantum information with Rydberg atoms'. *Rev. Mod. Phys.* **82**, 2313 (2010) (p. 175)
- Salathé Y, Mondal M, Oppliger M, Heinsoo J, Kurpiers P, Potočnik A, Mezzacapo A, Las Heras U, Lamata L, Solano E, Filipp S and Wallraff A. 'Digital Quantum Simulation of Spin Models with Circuit Quantum Electrodynamics'. *Phys. Rev. X* **5**, 021027 (2015) (p. 23)
- Sames C, Chibani H, Hamsen C, Altin P, Wilk T and Rempe G. 'Antiresonance Phase Shift in Strongly Coupled Cavity QED'. *Phys. Rev. Lett.* **112**, 043601 (2014) (pp. 18 and 22)
- Sangouard N, Simon C, de Riedmatten H and Gisin N. 'Quantum repeaters based on atomic ensembles and linear optics'. *Rev. Mod. Phys.* **83**, 33 (2011) (p. 27)

- Sassmannshausen H, Merkt F and Deiglmayr J. 'High-resolution spectroscopy of Rydberg states in an ultracold cesium gas'. *Phys. Rev. A* **87** (2013) (p. 14)
- Sayrin C, Dotsenko I, Gleyzes S, Brune M, Raimond J M and Haroche S. 'Optimal time-resolved photon number distribution reconstruction of a cavity field by maximum likelihood'. *New J. Phys.* **14**, 115007 (2012) (p. 20)
- Scalari G, Maissen C, Turcinkova D, Hagenmüller D, De Liberato S, Ciuti C, Reichl C, Schuh D, Wegscheider W, Beck M and Faist J. 'Ultrastrong Coupling of the Cyclotron Transition of a 2D Electron Gas to a THz Metamaterial'. *Science* **335**, 1323 (2012) (p. 21)
- Schindler P, Nigg D, Monz T, Barreiro J T, Martinez E, Wang S X, Quint S, Brandl M F, Nebendahl V, Roos C F, Chwalla M, Hennrich M and Blatt R. 'A quantum information processor with trapped ions'. *New J. Phys.* **15**, 123012 (2013) (p. 21)
- Schrödinger E. 'An undulatory theory of the mechanics of atoms and molecules'. *Phys. Rev.* **28**, 1049 (1926) (p. 1)
- . 'Die gegenwärtige Situation in der Quantenmechanik'. *Naturwissenschaften* **23**, 807 (1935) (pp. 1 and 2)
- Schwinger J. *Selected papers on quantum electrodynamics*. Courier Dover Publications (1958) (p. 2)
- Sedlacek J A, Schwettmann A, Kübler H, Löw R and Shaffer T P J P. 'Microwave electrometry with Rydberg atoms in a vapour cell using bright atomic resonances'. *Nat. Phys.* **8**, 819 (2012) (p. 202)
- Seidelin S, Chiaverini J, Reichle R, Bollinger J, Leibfried D, Britton J, Wesenberg J, Blakestad R, Epstein R, Hume D, Itano W, Jost J, Langer C, Ozeri R, Shiga N and Wineland D. 'Microfabricated surface-electrode ion trap for scalable quantum information processing'. *Phys. Rev. Lett.* **96** (2006) (pp. 28 and 202)
- Seiler C, Hogan S D, Schmutz H, Agner J A and Merkt F. 'Collisional and Radiative Processes in Adiabatic Deceleration, Deflection, and Off-Axis Trapping of a Rydberg Atom Beam'. *Phys. Rev. Lett.* **106**, 073003 (2011) (p. 49)
- Shomroni I, Rosenblum S, Lovsky Y, Bechler O, Guendelman G and Dayan B. 'All-optical routing of single photons by a one-atom switch controlled by a single photon'. *Science* **345**, 903 (2014) (p. 24)

- Shor P W. 'Algorithms for Quantum Computation: Discrete Logarithms and Factoring'. In *Proceedings, 35th Annual Symposium on Foundations of Computer Science, Santa Fe*, 124. IEEE Computer Society Press (1994) (p. 23)
- . 'Polynomial-Time Algorithms for Prime Factorization and Discrete Logarithms on a Quantum Computer'. *SIAM Journal on Scientific and Statistical Computing* **26**, 1484 (1997) (p. 23)
- Simonet J. *Optical Traps for Ultracold Metastable Helium atoms*. Ph.D. thesis, ENS (2011) (p. 225)
- Simons R N. *Coplanar waveguide circuits, components and systems*. Wiley Series in Microwave and Optical Engineering. Wiley Inter-Science (2001) (pp. 32 and 164)
- Singer K, Reetz-Lamour M, Amthor T, Marcassa L G and Weidemüller M. 'Suppression of Excitation and Spectral Broadening Induced by Interactions in a Cold Gas of Rydberg Atoms'. *Phys. Rev. Lett.* **93**, 163001 (2004) (p. 175)
- Snels M, Horká-Zelenková V, Hollenstein H and Quack M. *High-Resolution FTIR and Diode Laser Spectroscopy of Supersonic Jets*. Wiley (2011) (p. 49)
- So E, Dethlefsen M, Ford M and Softley T P. 'Charge Transfer of Rydberg H Atoms at a Metal Surface'. *Phys. Rev. Lett.* **107**, 093201 (2011) (p. 175)
- Sørensen A S, van der Wal C H, Childress L I and Lukin M D. 'Capacitive Coupling of Atomic Systems to Mesoscopic Conductors'. *Phys. Rev. Lett.* **92**, 063601 (2004) (pp. 28, 175, and 202)
- Spillane S M, Kippenberg T J, Vahala K J, Goh K W, Wilcut E and Kimble H J. 'Ultra-high-Q toroidal microresonators for cavity quantum electrodynamics'. *Phys. Rev. A* **71**, 013817 (2005) (pp. 9 and 10)
- Stammeier M. 'Theoretical signal-to-noise ratio for cavity QED experiments with Rydberg atoms'. Tech. rep., Quantum Device Lab, ETHZ (2015) (p. 221)
- Staudt M U, Hoi I C, Krantz P, Sandberg M, Simoen M, Bushev P, Sangouard N, Afzelius M, Shumeiko V S, Johansson G, Delsing P and Wilson C M. 'Coupling of an erbium spin ensemble to a superconducting resonator'. *Journal of Physics B: Atomic, Molecular and Optical Physics* **45**, 124019 (2012) (p. 25)
- Steck D. 'Cesium D Line Data'. Tech. rep., Los Alamos National Laboratory (1998 2010a) (pp. 7 and 12)

- . ‘Rubidium87 D Line Data’. Tech. rep., Los Alamos National Laboratory (2010b) (p. 12)
- . ‘Sodium D Line Data’. Tech. rep., Los Alamos National Laboratory (2010c) (p. 12)
- . ‘Rubidium85 D Line Data’. Tech. rep., Los Alamos National Laboratory (2013) (p. 12)
- Steffen L, Salathe Y, Oppliger M, Kurpiers P, Baur M, Lang C, Eichler C, Puebla-Hellmann G, Fedorov A and Wallraff A. ‘Deterministic quantum teleportation with feed-forward in a solid state system’. *Nature* **500**, 319 (2013) (p. 26)
- Streltsov A, Singh U, Dhar H S, Bera M N and Adesso G. ‘Measuring Quantum Coherence with Entanglement’. arXiv:1502.05876 (2015) (p. 21)
- Stucki D, Legre M, Buntschu F, Clausen B, Felber N, Gisin N, Henzen L, Junod P, Litzistorf G, Monbaron P, Monat L, Page J B, Perroud D, Ribordy G, Rochas A, Robyr S, Tavares J, Thew R, Trinkler P, Ventura S, Voirol R, Walenta N and Zbinden H. ‘Long-term performance of the SwissQuantum quantum key distribution network in a field environment’. *New J. Phys.* **13**, 123001 (2011) (p. 24)
- Su Q and Yang C. ‘Circuit QED: Implementation of the three-qubit refined Deutsch-Jozsa quantum algorithm’. arXiv:1410.3049 (2014) (p. 23)
- Svelto O. *Principles of Lasers*. Springer (1998) (p. 6)
- Tame M S, Bell B A, Di Franco C, Wadsworth W J and Rarity J G. ‘Experimental Realization of a One-Way Quantum Computer Algorithm Solving Simon’s Problem’. *Phys. Rev. Lett.* **113**, 200501 (2014) (p. 23)
- Tauschinsky A, Thijssen R M T, Whitlock S, van Linden van den Heuvell H B and Spreuw R J C. ‘Spatially resolved excitation of Rydberg atoms and surface effects on an atom chip’. *Phys. Rev. A* **81**, 063411 (2010) (pp. 155, 175, and 202)
- Terhal B M. ‘Quantum error correction for quantum memories’. *Rev. Mod. Phys.* **87**, 307 (2015) (p. 23)
- Tey M K, Chen Z, Aljunid S A, Chng B, Huber F, Maslennikov G and Kurtsiefer C. ‘Strong interaction between light and a single trapped atom without the need for a cavity’. *Nat. Phys.* **advanced online publication**, (2008) (p. 6)

- Theodosiou C E. 'Lifetimes of singly excited states in He I'. *Phys. Rev. A* **30**, 2910 (1984) (pp. 79 and 229)
- Theuws P G A, Beijerinck H C, Verster N F and Schram D C. 'A hollow cathode arc as a high intensity beam source for ground state and metastable noble gas atoms in the eV translational energy range'. *J Phys E: Sci Instrum* **15**, 573 (1982) (p. 49)
- Thiele T. *Towards a Manipulation of Trapped Atoms in Optical Tweezers*. Master's thesis, ETH Zürich (2010) (p. 60)
- Thiele T, Deiglmayr J, Stammeier M, Agner J A, Schmutz H, Merkt F and Wallraff A. 'Imaging electric fields in the vicinity of cryogenic surfaces using Rydberg atoms'. *Phys.Rev. A* **92**, 063425 (2015) (pp. 38, 113, 155, 176, 182, and 201)
- Thiele T, Filipp S, Agner J A, Schmutz H, Deiglmayr J, Stammeier M, Allmendinger P, Merkt F and Wallraff A. 'Manipulating Rydberg atoms close to surfaces at cryogenic temperatures'. *Phys. Rev. A* **90**, 013414 (2014) (pp. 35, 38, 71, 113, 129, 155, 176, 183, 188, 191, and 202)
- Thiele T, von Dydiowa M, Hambitzer A, Friese D, Stammeier M, Agner J A, Schmutz H, Philipp M T, Möller L, SFilipp, Merkt F and Wallraff A. 'Optimized source for microwave experiments using Rydberg atoms close to surfaces'. in preparation (2016) (pp. 222 and 223)
- Thompson J D, Tiecke T G, de Leon N P, Feist J, Akimov A V, Gullans M, Zibrov A S, Vuletić V and Lukin M D. 'Coupling a Single Trapped Atom to a Nanoscale Optical Cavity'. *Science* **340**, 1202 (2013) (pp. 18 and 22)
- Thompson R J, Rempe G and Kimble H J. 'Observation of normal-mode splitting for an atom in an optical cavity'. *Phys. Rev. Lett.* **68**, 1132 (1992) (pp. 3 and 12)
- Tiecke T G, Thompson J D, de Leon N P, Liu L R, Vuletić V and Lukin M D. 'Nanophotonic quantum phase switch with a single atom'. *Nature* **508**, 241 (2014) (pp. 18, 22, 25, and 28)
- Todorov Y, Andrews A M, Colombell R, De Liberato S, Ciuti C, Klang P, Strasser G and Sirtori C. 'Ultra-Strong Light-Matter Coupling Regime with Polariton Dots'. arXiv:1301.1297 (2012) (p. 21)
- Tong D, Farooqi S M, Stanojevic J, Krishnan S, Zhang Y P, Côté R, Eyler E E and Gould P L. 'Local Blockade of Rydberg Excitation in an Ultracold Gas'. *Phys. Rev. Lett.* **93**, 063001 (2004) (p. 175)
- Vaidman L. 'Teleportation of quantum states'. *Phys. Rev. A* **49**, 1473 (1994) (p. 26)

- Van De Meerakker S Y, Bethlem H L and Meijer G. ‘Taming molecular beams’. *Nature Physics* **4**, 595 (2008) (p. 49)
- van Enk S J and Kimble H J. ‘Single atom in free space as a quantum aperture’. *Phys. Rev. A* **61**, 051802 (2000) (p. 6)
- Vandersypen L M K, Steffen M, Breyta G, Yannoni C S, Sherwood M H and Chuang I L. ‘Experimental realization of Shor’s quantum factoring algorithm using nuclear magnetic resonance’. *Nature* **414**, 883 (2001) (p. 23)
- Vetsch E, Reitz D, Sagua G, Schmidt R, Dawkins S T and Rauschenbeutel A. ‘Optical Interface Created by Laser-Cooled Atoms Trapped in the Evanescent Field Surrounding an Optical Nanofiber’. *Phys. Rev. Lett.* **104**, 203603 (2010) (pp. 18, 22, and 28)
- Viteau M, Bason M G, Radogostowicz J, Malossi N, Ciampini D, Morsch O and Arimondo E. ‘Rydberg Excitations in Bose-Einstein Condensates in Quasi-One-Dimensional Potentials and Optical Lattices’. *Phys. Rev. Lett.* **107**, 060402 (2011) (p. 175)
- Vliegen E, Hogan S D, Schmutz H and Merkt F. ‘Stark deceleration and trapping of hydrogen Rydberg atoms’. *Phys. Rev. A* **76**, 023405 (2007) (p. 49)
- Vliegen E and Merkt F. ‘On the electrostatic deceleration of argon atoms in high Rydberg states by time-dependent inhomogeneous electric fields’. *Journal of Physics B* **38**, 1623 (2005) (p. 49)
- . ‘Normal-Incidence Electrostatic Rydberg Atom Mirror’. *Phys. Rev. Lett.* **97**, 033002 (2006) (p. 49)
- Vuletić V, Fischer T, Praeger M, Hänsch T W and Zimmermann C. ‘Microscopic Magnetic Quadrupole Trap for Neutral Atoms with Extreme Adiabatic Compression’. *Phys. Rev. Lett.* **80**, 1634 (1998) (p. 28)
- Waldburger D. *Temperature Dependent Measurements of Undercoupled Coplanar NbTiN-Resonators*. Master’s thesis, ETH Zurich (2012) (pp. 37, 163, 165, 166, 167, 168, and 170)
- Waldherr G, Wang Y, Zaiser S, Jamali M, Schulte-Herbrueggen T, Abe H, Ohshima T, Isoya J, Neumann P and Wrachtrup J. ‘Quantum error correction in a solid-state hybrid spin register’. arXiv:1309.6424 (2013) (p. 24)

- Wallraff A, Schuster D I, Blais A, Frunzio L, Huang R S, Majer J, Kumar S, Girvin S M and Schoelkopf R J. 'Strong coupling of a single photon to a superconducting qubit using circuit quantum electrodynamics'. *Nature* **431**, 162 (2004) (pp. 3, 19, 20, and 22)
- Walther H, Varcoe B T H, Englert B G and Becker T. 'Cavity quantum electrodynamics'. *Rep. Prog. Phys.* **69**, 1325 (2006) (p. 175)
- Wang X L, Cai X D, Su Z E, Chen M C, Wu D, Li L, Liu N L, Lu C Y and Pan J W. 'Quantum teleportation of multiple degrees of freedom of a single photon'. *Nature* **518**, 516 (2015) (p. 27)
- Wang Y, Minář J c v, Hétet G and Scarani V. 'Quantum memory with a single two-level atom in a half cavity'. *Phys. Rev. A* **85**, 013823 (2012) (p. 25)
- Watanabe K, Yoshida K, Aoki T and Kohjiro S. 'Kinetic Inductance of Superconducting Coplanar Waveguides'. *Jap. J. Appl. Phys.* **33**, 5708 (1994) (p. 164)
- Weimer H, Mueller M, Lesanovsky I, Zoller P and Buechler H P. 'A Rydberg quantum simulator'. *Nat. Phys.* **6**, 382 (2010) (p. 175)
- Weinstein Y S. 'Quantum Error Correction During 50 Gates'. arXiv:1312.1245 (2013) (p. 24)
- White G K and Meeson P J. *Experimental Techniques in Low-Temperature Physics; 4th ed.* Monographs on the Physics and Chemistry of Materials. Oxford Univ. Press, Oxford (2002) (pp. 127 and 128)
- Wilk T, Webster S C, Kuhn A and Rempe G. 'Single-Atom Single-Photon Quantum Interface'. *Science* **317**, 488 (2007) (p. 24)
- Wiza J L. 'Microchannel Plate Detectors'. *Nuclear Instruments and Methods* **162**, 587 (1979) (pp. 94 and 96)
- Woestenenk G R, Thomsen J W, van Rijnbach M, van der Straten P and Niehaus A. 'Construction of a low velocity metastable helium atomic beam'. *Rev. Sci. Instrum.* **72**, 3842 (2001) (p. 49)
- Wu H, Yang Z, Shen L and Zheng S. 'Quantum teleportation and computation with Rydberg atoms in optical lattice'. arXiv:1301.0089 (2013) (p. 27)
- Yin J, Ren J G, Lu H, Cao Y, Yong H L, Wu Y P, Liu C, Liao S K, Zhou F, Jiang Y, Cai X D, Xu P, Pan G S, Jia J J, Huang Y M, Yin H, Wang J Y, Chen Y A, Peng C Z and Pan J W. 'Quantum teleportation and entanglement distribution over 100-kilometre free-space channels'. *Nature* **488**, 185 (2012) (p. 24)

- Yin Z q, Yang W L, Sun L and Duan L M. 'Quantum network of superconducting qubits through an optomechanical interface'. *Phys. Rev. A* **91**, 012333 (2015) (p. 25)
- Yuan Z S, Chen Y A, Zhao B, Chen S, Schmiedmayer J and Pan J W. 'Experimental demonstration of a BDCZ quantum repeater node'. *Nature* **454**, 1098 (2008) (p. 27)
- Zhang J, Yung M H, Laflamme R, Aspuru-Guzik A and Baugh J. 'Digital quantum simulation of the statistical mechanics of a frustrated magnet'. *Nat. Commun.* **3** (2012) (p. 23)
- Zhou J, Yu W, Gao Y and Xue Z. 'Cavity QED implementation of non-adiabatic holonomies for universal quantum gates in decoherence-free subspaces with nitrogen-vacancy centers'. *arXiv:1505.05244* (2015) (p. 23)
- Zhu X, Saito S, Kemp A, Kakuyanagi K, Karimoto S i, Nakano H, Munro W J, Tokura Y, Everitt M S, Nemoto K, Kasu M, Mizuochi N and Semba K. 'Coherent coupling of a superconducting flux qubit to an electron spin ensemble in diamond'. *Nature* **478**, 221 (2011) (p. 25)
- Zimmerman M L, Littman M G, Kash M M and Kleppner D. 'Stark structure of the Rydberg states of alkali-metal atoms'. *Phys. Rev. A* **20**, 2251 (1979) (pp. 14, 73, 77, 80, 179, and 229)
- Zu C, Wang W B, He L, Zhang W G, Dai C Y, Wang F and Duan L M. 'Experimental realization of universal geometric quantum gates with solid-state spins'. *Nature* **514**, 72 (2014) (p. 23)

Curriculum Vitae

Personal Information

Full name Tobias Sebastian Thiele
Address Hofwiesenstrasse 262
CH – 8050 Zurich
Email tthiele@phys.ethz.ch
Tel. +41 79 502 25 99

Education

- | | | | |
|-------------|--|-------------------|----------------------|
| 2011 – 2015 | Dr. sc. ETH Zurich | ETH Zurich | Zurich (CH) |
| | <ul style="list-style-type: none">• Topic: Coherent manipulation of Rydberg atoms close to cryogenic surfaces• Supervisor: Prof. Andreas Wallraff (Quantum Device Lab, ETH Zurich)• Collaborator: Prof. Frédéric Merkt (Laboratorium fuer physikalische Chemie, ETH Zurich)• External Referee: Prof. Michel Brune (LKB, ENS, Paris) | | |
| 2010 | Internship | CalTech | Pasadena (CH) |
| | <ul style="list-style-type: none">• Setup of a magneto-optical trap, characterization and design of a setup for pulling tapered fibers (Prof. Jeff Kimble) | | |
| 2008 – 2010 | MSc ETH Physics | ETH Zurich | Zurich (CH) |
| | <ul style="list-style-type: none">• Major Subject: (Quantum) Optics, Solid State Physics• Semester Thesis: “Laser Stabilization using the Pound-Drever-Hall Technique” (Prof. Tilman Esslinger)• Master Thesis: “Towards Trapping of Single Atoms in Optical Tweezers” at the University of Oxford, UK.) (grade: 6¹)<ul style="list-style-type: none">◦ Supervisors: Prof. Tilman Esslinger (ETH Zurich), Dr. Axel Kuhn (University of Oxford)• Final Grade: 5.82¹ (with distinction, above 1 std. dev. from average) | | |
| 2005 – 2009 | BSc ETH Physics | ETH Zurich | Zurich (CH) |
| | <ul style="list-style-type: none">• Major Subjects: Solid State Physics, Nuclear and Particle Physics• Semester Thesis: “Knight-Field Enabled Nuclear Spin Polarization Decay and Co-Tunneling-Rates in a Single Quantum Dot” (Prof. Atac Imamoglu)• Final Grade: 5.66¹ (above 1 std. dev. from average) | | |

¹Grade: 1: lowest, 4: passed, 6: highest

Tobias Sebastian Thiele

1999 – 2005	Gymnasium (high school)	KSW	Zurich (CH)
	<ul style="list-style-type: none">• Major subject: latin and english, according to MAR• Final thesis: "Construction of a Scanning Tunneling Microscope" (grade: 6¹)• Final grade: 5.39¹		
1994 – 1999	Primary school	Mettlen	Wettswil a. Albis (CH)
1993 – 1994	Primary school	Ostschule	Saarbruecken (D)

Skills

Language:	German: mother tongue English: fluent (Advanced Cambridge certificate (ACE)) French: intermediate Spanish: intermediate
Practical:	Good knowledge in <ul style="list-style-type: none">• (atom) optics and LASER technology• (UHV, HV)-vacuum techniques• cryogenics• clean-room fabrication techniques• (high-voltage) electronics• microwave technique
Computer:	Selected list <ul style="list-style-type: none">• design: SolidWorks, Inventor, AutoCAD, AWR, Eagle• finite-element simulation: HFSS, Maxwell• experimental control: LabView• evaluation: Mathematica, Matlab
Teaching:	
2011 – 2016	Teaching assistant in: <ul style="list-style-type: none">• Physics I-II for chemists, biologists, ... (bachelor course)• Physics I for electrical engineers (bachelor course)• Physics (III-IV) for physicists (3 X physics III), (bachelor course)• 3 x Quantum Science and Information technology (masters course) Direct Supervision of: <ul style="list-style-type: none">• 9 x semester theses,• 1 x bachelor thesis,• 2 x master theses,• 4 x summer projects
2007 – 2008	Tutor in: mathematical methods of physics (I and II)
2003 – 2009	Private tutoring in: physics, chemistry, mathematics, english and latin

Tobias Sebastian Thiele

Organizational:	Selected list
2013	IONS conference ETH Zurich / EPFL Lausanne Local coordinator Zurich <i>International OSA (Optical Society of America) Network of Students</i>
2012	QSIT Junior Meeting Passugg, CH Main organizer (with A. Kuhlmann, Univ. Basel) <i>National competence center of Research - Quantum Science and Technology</i>
2008 – 2013 America	Student Chapter ETH of the Optical Society of ETH Zurich Vice-president and co-founder Organization of various outreach events

Awards

2005 – 2013 excellent students	Member of the Swiss National Academic Foundation for (Schweizerische Studienstiftung)
2010	MSc ETH, obtained with distinction
2005 Olympiad)	Participation at the IPHO 2005 (International Physics Salamanca, Spain Representative of Switzerland (1 of 5)

List of publications

Peer-reviewed articles	L. Brandt, C. Muldoon, T. Thiele , J. Dong, E. Brainis and A. Kuhn <i>Spatial light modulators for the manipulations of individual atoms</i> Appl. Phys. B 102 : 443-450 (2011)
	S. D. Hogan, J. A. Agner, F. Merkt, T. Thiele , S. Filipp and A. Wallraff <i>Driving Rydberg-Rydberg transitions from a coplanar microwave waveguide</i> Phys. Rev. Lett. 108 , 063004 (2012)
	A. Goban, K. S. Choi, D. J. Alton, D. Ding, C. Lacroute, M. Pototschnig, T. Thiele , N. P. Stern and H. J. Kimble <i>Demonstration of a state-insensitive, compensated nanofiber trap</i> Phys. Rev. Lett. 109 , 033603 (2012)
	T. Thiele , S. Filipp, J.-A. Agner, H. Schmutz, J. Deiglmayr, M. Stammeier, P. Allmendinger, F. Merkt and A. Wallraff <i>Manipulating Rydberg atoms close to surfaces at cryogenic temperatures</i> Phys. Rev. A 90 , 013414 (2014)

Tobias Sebastian Thiele

T. Thiele, J. Deiglmayr, M. Stammeier, J.-A. Agner, H. Schmutz, F. Merkt and A. Wallraff
Imaging electric fields in the vicinity of cryogenic surfaces using Rydberg atoms
Phys. Rev. A **92**, 063425 (2015)

Conference Contributions

Talks:

Coherent manipulation of Rydberg atoms close to surfaces
Seminar Talk, Boulder, CO, USA, April 2016 (invited)

Coherent manipulation of Rydberg atoms close to surfaces
Seminar Talk, Boston, MA, USA, April 2016 (invited)

Microwave transitions between Rydberg states above (patterned) surfaces at cryogenic temperatures
CCQED, Aarhus, Denmark, October 2014

Coherent manipulation of Rydberg states above surfaces at cryogenic temperatures
APS March Meeting, Denver, USA, March 2014

Manipulating Rydberg atoms close to surfaces at cryogenic temperatures
QSIT General Meeting, Arosa, CH, February 2014

Hybrid Cavity QED with Rydberg Atoms and Circuits
QSIT Junior Meeting, Passugg, CH, June 2011

Posters:

Coherent Manipulation of Rydberg States above Surfaces at Cryogenic Temperatures
NCCR QSIT Review Meeting, Zurich, 2014

Coherent Manipulation of Rydberg States above Surfaces at Cryogenic Temperatures
NCCR QSIT Review Meeting, Zurich, 2013

Towards Driving Rydberg-Rydberg Transitions from a Coplanar Microwave Waveguide in a Cryogenic Environment
CCQED Conference on Resonator QED, Munich, Germany, September 2013

Interfacing Rydberg Atoms and Circuits in a Hybrid System
NCCR QSIT Review Meeting, Zurich, 2012

Driving Rydberg-Rydberg Transitions from a Coplanar Microwave Waveguide
WE-Heraeus-Seminar, Bad Honnef, Germany, 2012
(Poster Price)

Driving Rydberg-Rydberg Transitions from a Coplanar Microwave Waveguide
QSIT Junior Meeting, Passugg, Switzerland, 2012

Driving Rydberg-Rydberg transitions from a coplanar microwave waveguide

Tobias Sebastian Thiele

QSIT General Meeting, Arosa, Switzerland, 2012

Driving Rydberg-Rydberg Transitions from a Coplanar Microwave Waveguide

AQUTE Winterschool, Obergurgl, Austria, 2012

Interfacing Rydberg Atoms and Circuits in a Hybrid System

NCCR QSIT Review Meeting, Zurich, 2011

Towards hybrid cavity quantum electrodynamics with atoms and circuits

Quantum Information Processing and Communication, Zurich, 2011

Hybrid Cavity QED with Rydberg Atoms and Circuits

QSIT General Meeting, Arosa, 2011

Peer review

Journals:

Scientific Reports (1)

New Journal of Physics (shared: 1)